

# **Design and Control of a Resonant, Flapping Wing Micro Aerial Vehicle Capable of Controlled Flight**

Submitted in partial fulfillment of the requirements for  
the degree of  
Doctor of Philosophy  
in  
Mechanical Engineering

David COLMENARES

B.S., Computer Engineering, University of Washington, USA  
B.S., Bioengineering, University of Washington, USA  
M.S., Mechanical Engineering, Carnegie Mellon University, USA

Carnegie Mellon University  
Pittsburgh, PA

August, 2017

© David Colmenares, 2017  
All Rights Reserved

**Keywords:** Micro Aerial Vehicle, Flapping wing, Resonant Actuator, DC motor, Thermal Model, Flexible Wing, Wing Twist



## Abstract

Small scale unmanned aircraft, such as quadrotors, that are quickly emerging as versatile tools for a wide range of applications including search and rescue, hazardous environment exploration, or just shooting great video, are known as micro air vehicles (MAVs). However, for millimeter scale vehicles with weights under 10 grams, conventional flight technologies become greatly inefficient and instead inspiration is drawn from biology. Flapping wing MAVs (FWMAVs) have been created based on insects and hummingbirds in an effort to emulate their extreme agility and ability to hover in place. FWMAVs possess unique capabilities in terms of maneuverability, small size, and ability to operate in dynamic environments that make them particularly well suited for environmental monitoring and swarm applications such as artificial crop pollination. Despite their advantages, significant challenges in fabrication, power, and control must be overcome in order to make FWMAVs a reliable platform. Current designs suffer from high mechanical complexity and often rely on off-board power, sensing, and control, which compromises their autonomy and limits practical applications. The goal of my research is to develop a simple FWMAV design that provides high efficiency and controllability.

An efficient, simple, and controllable vehicle design is developed utilizing the principles of resonance, emulation of biological flight control, and under-actuation. A highly efficient, resonant actuator is achieved by attaching a spring in parallel to the output shaft of a commercial geared DC micro-motor. This actuator directly drives the wings of the vehicle, allowing them to be controlled precisely and independently. This direct control strategy emulates biology and differs from other FWMAV designs that utilize complicated transmissions to generate flapping from rotary motor output. Direct control of the wings allows for emulation of biological wing kinematics, resulting in control based on wing motion alone. Furthermore, under-actuation is employed to mimic the rotational motion of insect wings. A rotational joint is added between the motor and wing membrane such that the wing rotates passively in response to aerodynamic forces that are generated as the wing is driven. This design is realized in several stages, initial prototyping, simulation and development of the actuator and wings, then finally a control system is developed.

First the system was modeled and improved experimentally in order to achieve lift off. Improvements to the actuator were realized through component variation and custom fabrication increasing torque and power density by 161.1% and 666.8% respectively compared to the gear-motor alone and increased the resonant operating frequency of the vehicle from 4 Hz to 23 Hz. Advances in wing fabrication allowed for flexible wings that increased translational lift production by 35.3%, aerodynamic efficiency by 41.3%, and the effective lift coefficient by 63.7% with dynamic twisting. A robust control architecture was then developed iteratively based on a data driven system model in order to increase flight time from 1 second (10 wing strokes) to over 10 seconds (230 wing strokes). The resulting design improves lift to weight by 166%, allowing for a payload capacity of approximately 8.7 g and offers the potential for fully autonomous operation with all necessary components included on-board. A thermal model for micro-motors was developed and tuned to accurately predict an upper limit of system operation of 41 seconds as well as to optimize a heatsink that increases operating time by 102.4%.



## **Acknowledgments**

I would like to thank my advisor Metin Sitti and all of the member of the NanoRobotics Lab for their help and support. Thank you to my committee: Professor Metin Sitti (Chair), Professor Thomas Daniel, Professor Peter Whitney, and Professor Koushil Sreenath. I would like to specifically thank Randall Kania, Wang Zhang, Miao Liu, Lindsey Hines, and Drew Bent for their work on the project as well as Dr. Aaron Johnson (CMU Robomechanics Lab) and Jesse Roll (Purdue Biorobotics Lab) for their contributions and advice. Finally, to my wonderful wife Corena and my family Laura, Pat, and Julio, I am so grateful for your love and support through this journey.

This work was supported by the National Science Foundation Graduate Research Fellowship Program under Grant No. DGE-1252522.

# Contents

- Abstract** **v**
  
- Acknowledgments** **vii**
  
- List of Figures** **x**
  
- List of Tables** **xv**
  
- 1 Introduction** **1**
  - 1.1 Motivation . . . . . 1
  - 1.2 Previous Work . . . . . 2
    - 1.2.1 Motor Driven Platforms . . . . . 3
    - 1.2.2 Piezoelectric Platforms . . . . . 4
    - 1.2.3 Controller . . . . . 6
  - 1.3 Rotary vs. Flapping Flight . . . . . 8
  - 1.4 Thesis Outline . . . . . 10
  - 1.5 Contributions . . . . . 10
  
- 2 System Dynamics and Aerodynamic Model** **12**
  - 2.1 Introduction . . . . . 12
  - 2.2 Dynamics Model . . . . . 12
  - 2.3 Aerodynamic Model . . . . . 13
  - 2.4 Model Validation . . . . . 15
  - 2.5 Conclusion . . . . . 21
  
- 3 Actuation: Motor Selection, Resonant Actuator Design, and Thermal Analysis** **22**
  - 3.1 Introduction . . . . . 22
  - 3.2 Brushed Motor Selection . . . . . 22
    - 3.2.1 GM15 Component Characterization . . . . . 28
  - 3.3 Brushless Motor Usage . . . . . 32
  - 3.4 Resonant Actuation . . . . . 35
  - 3.5 Power Density . . . . . 41
  - 3.6 Thermal Modeling . . . . . 43
    - 3.6.1 Model Parameter Fitting . . . . . 45

3.6.2	Temperature Dependent Winding Resistance . . . . .	45
3.6.3	Bushing Friction . . . . .	45
3.6.4	Speed-Dependent Convective Thermal Resistance . . . . .	47
3.6.5	Heatsink Design . . . . .	51
3.7	Conclusion . . . . .	53
<b>4</b>	<b>Wing Design</b>	<b>55</b>
4.1	Introduction . . . . .	55
4.2	Morphology of Biological Wings . . . . .	55
4.2.1	Planform Shape . . . . .	56
4.2.2	Area Distribution . . . . .	56
4.2.3	Aspect Ratio and Rossby Number . . . . .	58
4.2.4	Flexibility . . . . .	59
4.2.5	Camber . . . . .	61
4.2.6	Wing Twist . . . . .	62
4.3	Analytical Generation of Wing Shape . . . . .	62
4.4	Wing Shapes of FWMAVs . . . . .	63
4.5	Wing Shape Experiments . . . . .	65
4.6	General Wing Flexibility Experiments . . . . .	66
4.6.1	Modeling and Design . . . . .	68
4.6.2	Wing Fabrication . . . . .	70
4.6.3	Experimental Setup . . . . .	71
4.6.4	Resonance Testing . . . . .	72
4.6.5	Experimental Wing Characterization . . . . .	72
4.6.6	Results . . . . .	74
4.7	Wing Twist Experiments and Analysis . . . . .	79
4.7.1	Results and Discussion . . . . .	80
4.7.2	Wing Twist Computational Fluid Dynamics Simulation . . . . .	85
4.7.3	Particle Image Velocimetry Study of Twisted Wings . . . . .	88
4.8	Conclusion . . . . .	88
<b>5</b>	<b>Vehicle Design Improvements</b>	<b>91</b>
5.1	Introduction . . . . .	91
5.2	Improvement of the resonant actuator . . . . .	91
5.3	Flexure improvements . . . . .	94
5.4	Passive Stability . . . . .	97
5.5	Full System Summary . . . . .	97
<b>6</b>	<b>Closed-Loop Control Framework</b>	<b>100</b>
6.1	System Model . . . . .	100
6.2	Calibration . . . . .	105
6.3	Controller Framework . . . . .	109
6.4	Controller Tuning and Free Flight Results . . . . .	112
6.5	Conclusion . . . . .	123

<b>7 Contributions and Concluding Remarks</b>	<b>124</b>
7.1 Future Work . . . . .	125
<b>Bibliography</b>	<b>127</b>

# List of Figures

- 1.1 Motor driven FWMAVs: a)Purdue\* 3.9 g, b) Cornell, c) Delfly Micro, d)Nano Hummingbird. Black bar shows 1cm. . . . . 5
- 1.2 Piezo driven FWMAVs: a) Army Research Labs, b) Berkeley MFI, c) Harvard - Double. Black bar shows 1cm. . . . . 7
- 1.3 Small rotorcraft: a) Proto X Nano, b) Nano-falcon, c) Crazyflie, d) Black Hornet. 9
  
- 2.1 Spring-mass-damper system model . . . . . 13
- 2.2 Model of the passively rotating wing with coordinate systems representing transformations by the flapping and rotation angles respectively. All three coordinate systems are centered at the labeled origin point, but detached for clarity. The  $\vec{E}''$  coordinate system is attached to the wing. . . . . 14
- 2.3 Experimental setup with control computer, power electronics, half system, load cell, and camera. The motor control signal is shown in black, while measured data is shown in green. . . . . 16
- 2.4 Wing kinematics of the developed system captured from high-speed video analysis and those of *Drosophila* adapted from Fry *et al.* (2003). . . . . 17
- 2.5 a) mean lift comparison from measured kinematics and b) simulated instantaneous lift and force component breakdown . . . . . 18
- 2.6 Comparison of simulated vs actuated wing kinematics a) and resulting mean lift b) 18
- 2.7 Comparison of wing kinematics and resulting instantaneous force production) . . 19
- 2.8 a) For twist v1 no difference in rotation was measured, but there is a three times difference in the minimum lift peak, b) for twist v2 a 6% difference in rotational delay was measured, but the minimum lift peaks are of consistent magnitude. . . 19
- 2.9 Simulated results for the rigid wing operating at 21 Hz, flapping amplitude 132°, rotational amplitude 90° with stoppers. . . . . 20
- 2.10 Experimental results for the rigid wing operating at 21 Hz, flapping amplitude 132°, rotational amplitude 90° with stoppers. . . . . 20
  
- 3.1 Typical brushed DC motor design for small sizes . . . . . 23
- 3.2 Difference between motor power and aerodynamic power: a) Ideal GM15 performance, b) with estimated 60% gearbox efficiency . . . . . 24
- 3.3 Difference between motor power and aerodynamic power: a) Ideal FH0515 performance, b) with estimated 80% gearbox efficiency . . . . . 25

3.4	GM15 two stage planetary gearbox showing a) gearbox output shaft with top annular gear, b) planet gear, c) pin connecting planet gear and carrier, d) carrier, e) sun gear connecting motor to gearbox, f) shell that holds down output stage, g) motor output shaft, h) GM15 motor, i) bottom annular gear . . . . .	26
3.5	Plot of torque density versus weight for motors under 3 grams. Gearmotors are shown in red, while motors are shown in blue. The GM15 and 0515A are marked with Xs. . . . .	27
3.6	Histogram of unloaded current draw at 6 V for GM15 motors only. . . . .	28
3.7	Histogram of unloaded current draw at 3 V for the GM15 25:1 plastic gearhead. . . . .	29
3.8	Rated performance of the GM15 with respect to torque, current, mechanical power, and efficiency. . . . .	30
3.9	Worst case measured performance of the GM15 with respect to torque, current, mechanical power, and efficiency. . . . .	30
3.10	Best case measured performance of the GM15 with respect to torque, current, mechanical power, and efficiency. . . . .	31
3.11	Comparison of GM15 performance. Red represents rated, blue worst measured, and green best measured. . . . .	31
3.12	Brushless motors from left to right Micromo 0515A006B06A 25:1, Homefly 10-1-50T (1.5 g), HexTronik Brushless Outrunner 7700kv (2.0g). Dissassembled 10-150T shown below . . . . .	33
3.13	Electrical Power or thermal losses for the gearmotor during frequency sweep. . . . .	37
3.14	Electrical Power for the resonant actuator during frequency sweep. . . . .	37
3.15	Comparison of torque, effective speed, mechanical power, and efficiency for the gearmotor and resonant actuator across frequencies. . . . .	38
3.16	Comparison of efficiency for the gearmotor and resonant actuator across frequencies. . . . .	38
3.17	Performance of the gearmotor with respect to motor torque, current, mechanical power, and efficiency for 17 Hz operation at increasing voltage amplitudes. . . . .	39
3.18	Performance of the resonant actuator at 17 Hz with increasing voltage amplitudes. . . . .	39
3.19	Comparison of electrical power or thermal losses between the two actuators at increasing voltage amplitudes. . . . .	40
3.20	a) Reduced, lumped parameter, thermal circuit model of a DC motor with attached fin. b) Disassembled motor showing brushes, rotor windings, magnet, case, and bushing (left to right). Annotations indicate physical representation of the full thermal model, which includes distinct thermal bodies for each motor component and resistances between all bodies. . . . .	44
3.21	Experimental setup with custom dynamometer, non-contact tachometer, and IR thermometer. Dynamometer experiments allow speed and current dependent heating effects to be isolated. . . . .	46
3.22	Image of the fabricated dynamometer. . . . .	47
3.23	Case temperature vs. time with speeds indicated in the legend. . . . .	48
3.24	Pulse-spin experiment settling time vs. operating speed results. . . . .	48
3.25	Results of the pulse-spin experimental data from the motor only in blue, compared to the output of the trained simulation in red. . . . .	49

3.26	Comparison of experimental and model data for the resonant actuator operating at hover (0.24 A, 841 rpm) showing both core and case temperatures. Case temperature for the actuator with heatsink is also shown. . . . .	50
3.27	Measured wing downwash surface with motor location and wing flapping arc. . .	52
3.28	Results from the optimizations are displayed over the velocity contour: a) result from the MINLP C. b) is the original result with variable thickness fin segments.	52
3.29	Fabricated weight-optimal heatsink attached to motor. . . . .	53
4.1	Wing shapes of common birds and insects: (a) hummingbird, (b) fruit-fly, (c) hover-fly, (d) wasp, (e) hawk moth, and (f) cabbage white butterfly. . . . .	57
4.2	Schematic of our wing design with aspect ratio of 3.6 and Rossby number 8.58. .	59
4.3	a) Measurements of wing flexibility [1], b) wing deformation during flight [2]. . .	60
4.4	The thin cambered airfoil is shown as the black curve. Since the foil is of negligible thickness its shape corresponds to the mean camber line. The chord line shown in blue connects the leading and trailing edges. The red segment indicates the maximum displacement between the chord line and mean camber line. . . . .	61
4.5	Four cross-sections of a twisted propeller blade, each labeled with its position as a percentage of the total length. The largest section is at the base, located at 0%. The next section is located at 50%, half the distance to the tip. Proceeding out, the blade tapers and the chord line (shown as dashed line) rotates decreasing the angle of attack of the cross-sections, which is maximal at the tip (100%). . . . .	63
4.6	a) Beta distribution for $\hat{r}_2 = 0.5$ , $\hat{r}_1 = 0.4291$ using $p = 1.1664$ and $q = 1.5519$ , b) Beta distribution for $\hat{r}_2 = 0.55$ , c) Beta distribution for $\hat{r}_2 = 0.6$ . . . . .	63
4.7	Wings of the a) Nano Hummingbird, b) Delfly, c) Robobee, d) Cornell. . . . .	64
4.8	Current wing spline compared to the ideal second moment of area of 0.54 . . . . .	65
4.9	Wing mass model a) Using reinforcing spars, b) Using a rigid border. . . . .	66
4.10	a) Current wing design $AR = 3.5$ , $\hat{r}_2 = 0.54$ , b) $AR = 3.5$ , $\hat{r}_2 = 0.57$ , c) $AR = 3.5$ , $\hat{r}_2 = 0.57$ , d) $AR = 3.5$ , rectangular, e) $AR = 2$ , $\hat{r}_2 = 0.54$ . . . . .	67
4.11	Comparison of original wing and larger wing with double the area. . . . .	67
4.12	Lift and drag coefficients ( $C_L$ and $C_D$ ) determined from experiments by Dickinson <i>et al.</i> [3] as a function of angle of attack. At $90^\circ$ angle of attack, the wing is perpendicular to the airflow producing no lift and maximal drag. At $0^\circ$ , the wing is parallel to the airflow. . . . .	69
4.13	a) Right wing of a hoverfly, <i>Eristalis tenax</i> , b) our bio-inspired design for tuning overall wing stiffness. . . . .	69
4.14	Side (a) and top view (b) of twisted wing simulation. Displacement ranges from 0mm (red) to 34mm (dark blue). . . . .	70
4.15	Images of fabricated full wing assemblies with labels. . . . .	71
4.16	a) Determination of wing spanwise resonance mode, and b) leading edge stiffness.	73
4.17	Example of wing deflection for 0-90 laser. . . . .	75
4.18	Lift per power results of all wings tested. . . . .	76
4.19	a) Flat and b) fully twisted wing image, both with measured chordwise distances shown. . . . .	77
4.20	Normalized percent wing twist vs. wing length. . . . .	78

4.21	Wing structural-inertial efficiency. Figure of merit plot reproduced from [4], with added data for our fabricated wings . . . . .	79
4.22	(a) Rigid wing with $\hat{r}_2 = 0.54$ beta distribution shown in blue and the modeled wing spline shown in red, and flexible wing designs, Twist v1 (b) and Twist v2 (c), with distance $r$ and element $dr$ shown. . . . .	81
4.23	(a) Experimental lift results as a function of input aerodynamic power. (b) Calculated twist profiles from experimental high-speed video images. (c) Simulated lift and drag distributions based on twist profiles. Lift and drag are equal for the rigid-wing design, and appear as a single line. (d) Simulated lift per drag, aerodynamic efficiency, along the wing length based on twist profile. . . . .	82
4.24	Pareto frontier of simulated optimal twisted wing designs. . . . .	86
4.25	Simulated optimal wing twist profiles. Curves go from high lift (top, red) to high efficiency (bottom, green). . . . .	86
4.26	Laminar CFD simulation of wing twist. . . . .	87
4.27	Custom PIV setup at the Bio-Robotics Lab. . . . .	89
4.28	Processed PIV images showing vorticity magnitude at approximately 40, 60, 80% of the wing length . . . . .	90
5.1	Iterations of the resonant spring of increasing stiffness from left to right 2.8, 8.1, 18 N*mm/rad. . . . .	92
5.2	Measured torque differs by 22% for a 45 degree deflection of the spring. . . . .	93
5.3	Comparison of systems fabricated with various springs with respect to lift per power. . . . .	94
5.4	Resonant actuator revision that supports gearbox output shaft with a bearing. a) Prototype, b) final version, c) final top view, d) shaft coupler piece. . . . .	95
5.5	Efficiency comparison of the bearing system to an unstabilized system using twist v1 and v2 wings. . . . .	95
5.6	Proposed double spring bearing system. . . . .	96
5.7	All peices for fabrication of the two actuator robot body. . . . .	96
5.8	Picture of the FWMAV system with attached air dampers and Vicon markers. A) Wing rotation flexure, B) Torsional spring, C) GM15 gearmotor, D) Kapton and carbon fiber wing, E) Vicon marker, F) Air dampers . . . . .	98
5.9	a) Developed system compared to b) initial prototype. . . . .	99
6.1	Diagram of the independent wing control paradigm. The system is shown from a top-down view with the arc demonstrating the flapping amplitude. The location of the crossed circles indicates the mean angle of the stroke, while their size indicates the amount of lift production which is proportional to the flapping amplitude. The configurations demonstrate stable flight, negative roll torque, and negative pitching torque. . . . .	101
6.2	3D printed fixture for attaching robot to the ATI Nano17-Ti sensor. . . . .	105
6.3	Physical parameters of the vehicle along with the coordinate system. The concentric circle symbol denotes the wing center of lift. . . . .	107

6.4	Experimental setup with computer, electronics, FWMAV system, load cell, and tracking camera array. The motor control signal is shown with solid lines, while measured data is shown as dotted lines. The dashed box shows the two ways the system is run: fixed to the load cell for calibration, or free flying in the camera array for closed-loop control. . . . .	108
6.5	Example calibration run. The left side shows raw data for both wings over a single experiment. Solid line sections A-D indicate difference commanded amplitudes over which the data is averaged. The right side shows the full calibration surfaces consisting of the marked points based on averaged data. The quadratic surface is fit to the measured data using singular value decomposition. . . . .	110
6.6	Vicon Bonita tracking setup. . . . .	111
6.7	Free flight control framework consisting of three independent PID controllers for roll, pitch, and altitude. The Vicon tracking system provides measurements of the system angles and position. Errors are converted by the controllers to desired forces and torques. The calibration matrix converts these to the appropriate actuator driving signal based on the determined $V_{pp}$ and $V_b$ . . . . .	111
6.8	Representative open-loop test flight tracking data. The left side shows the 3D position with all axes in mm. The right side shows the time series for the parameters of interest, vertical position as well as pitch and roll angles. . . . .	112
6.9	Roll control vicon trajectory. The trajectory begins with blue markers and ends with red ones. . . . .	113
6.10	Roll control showing vertical position, pitch angle, roll angle, and roll control signal. . . . .	114
6.11	Pitch and roll control vicon trajectory showing short flight due to tether interaction. The trajectory begins with blue markers and ends with red ones. . . . .	115
6.12	Pitch and roll control time series for vertical position, pitch angle, roll angle as well as pitch and roll control signal for short flight due to tether interaction. . . . .	116
6.13	Pitch and roll control vicon trajectory showing long flight staying on tether. The trajectory begins with blue markers and ends with red ones. . . . .	117
6.14	Pitch and roll control time series for vertical position, pitch angle, roll angle as well as pitch and roll control signal for long flight staying on tether. . . . .	118
6.15	Full PD control vicon trajectory. The trajectory begins with blue markers and ends with red ones. . . . .	119
6.16	Full PD control time series for vertical position, pitch angle, roll angle as well as pitch, roll, and height control signal. . . . .	120
6.17	Representative closed-loop test flight tracking data for a trail lasting 8 seconds. The 3D trajectory is shown with all axes in mm. . . . .	121
6.18	Representative closed-loop experiment. The left side shows the controlled degrees of freedom, vertical position as well as the pitch and roll angles. On the right side, the control inputs applied to these degrees of freedom are shown. . . . .	122

# List of Tables

1.1	Survey of motor driven FWMAVs . . . . .	4
1.2	Survey of piezo driven FWMAVs . . . . .	6
1.3	Survey of small rotorcraft . . . . .	9
3.1	Detailed specifications for candidate motors . . . . .	26
3.2	Maximal performance for 20 Hz actuation . . . . .	35
3.3	Maximal performance comparison for 20 Hz actuation . . . . .	41
3.4	Maximal actuator power densities . . . . .	42
3.5	Thermal circuit model parameters . . . . .	45
4.1	Aspect Ratios of Biological Wings . . . . .	58
4.2	Predicted wing assembly weight vs. measured weights to quantify added glue mass. All weights in milligrams. . . . .	72
4.3	Resonance and stiffness testing results. A * indicates the dominant natural frequency, while other recorded peaks were conserved across trial, but appeared at lower magnitudes. . . . .	73
4.4	Lift/power (mN/Watt) results for all wings tested. . . . .	75
4.5	Relevant wing information. Lift per wing weight represents a figure of merit. Rotational delay percentage is measured from high speed video and should produce large aerodynamic effects (0% constitutes symmetric rotation, while delayed rotation is considered > 8% delay). Wing area is measured for the actual wings. Aspect ratio and Rossby number are for the ideal wing shapes produced in simulation. . . . .	76
4.6	Flexible Wing Simulation Results . . . . .	84
4.7	Details of ANSYS Fluent CFD simulation comparing rigid and twisted wings. . . . .	88
5.1	Variations in system resonant spring . . . . .	92
5.2	Summary of system improvements . . . . .	99
6.1	System Physical Parameters . . . . .	106
6.2	System Damping Coefficients and Trim Inputs . . . . .	106
6.3	Closed-loop Control Results . . . . .	119

# Chapter 1

## Introduction

### 1.1 Motivation

Drones, in particular quadrotors, have rapidly become a commercial technology driven by the miniaturization of electronics used in cellular technology. They are increasingly used for a variety of tasks such as agricultural monitoring, infrastructure inspection, surveillance, and aerial photography. They are able to excel at these tasks due to their ability of slow flight and sustained hover. These are key features of biological flight across a diverse range of organisms. The fairyfly, *Mymaridae*, is the smallest flier with a body length of 0.15 mm, and an estimated weight of only 25 ng [5]. The largest fliers capable of sustained hover are the giant hummingbird (*Patagona gigas*) and the flower bat (*Glossophagine phyllostomidae*) with weights of 22 g and 32 g respectively [6, 7]. Furthermore, biological fliers are extremely agile. The fruit fly (*Drosophila melanogaster*) is able to make 90 degree turns in less than 50 ms [8]. Dragonflies are formidable hunters that can fly forwards at speeds of 100 body lengths per second (up to 30 mph), backwards at 3 body lengths per second, and conduct rapid prey interception maneuvers that terminate with a ballistic flip that drops the prey directly into their clutches [9, 10].

Flapping wing micro air vehicles (FWMAVs) possess many unique capabilities compared to traditional aircraft. Their extreme maneuverability, small size, ability to operate in confined spaces, and quick takeoff or landing capabilities make them especially well-suited for applications such as search and rescue and environmental monitoring, where they can interact seamlessly with the natural world. Furthermore, their low cost and design flexibility open up the possibility for swarm application, such as artificial crop pollination [11]. Despite their advantages, significant challenges in actuation, power, control, and navigation must be overcome in order to make MAVs a reliable platform [12]. Simply designing a flapping mechanism that can generate enough lift to support its own weight is a challenging task, especially given that traditional actuators such as motors scale poorly to small sizes. Although MAVs are typically battery-operated due to the inherent power limitations of their small size, these technologies suffer from low power densities and require additional hardware to interface with flight actuators [13]. Furthermore, while these systems have the potential for extreme maneuverability, maintaining control during hover where instantaneous forces greatly exceed stroke averaged ones as well as during rapid maneuvers requires novel control mechanisms and strategies. Operating in confined spaces requires

low-latency sensors that conform to the strict space and power constraints of MAVs. Furthermore, these constraints prevent the use of traditional radio or GPS based navigation, requiring the development of innovative navigation strategies [14]. Bio-inspired engineering, where we gain insights from animal biology and behavior, provides a powerful approach to address these issues. In this work I will present an efficient, simple, and controllable FWMAV design that utilizes the principles of resonance, emulation of biological flight control, and under-actuation.

## 1.2 Previous Work

Biological flight has been studied extensively in order to elucidate the underlying aerodynamic mechanisms and with the hopes of generating design guidelines for manmade systems. Studies on model organisms such as the fruit fly [15, 16, 17], hawk moth [18, 19, 20, 21], dragonfly [22, 23, 24, 25, 26], hummingbird [27, 28, 29, 30], and bats [31, 32, 33, 34], have focused on many features such as physical properties of the wing discussed in chapter 4, flapping kinematics discussed in section 2.3.1, and behavior. Studies utilizing robotic test beds based on dynamic scaling of biological systems have also been invaluable, such as work on a robotic fly by Dickinson [3] and work by Lentink [35, 36], for controlled studies of flight aerodynamics. In addition to spanning a huge range of animal sizes and morphologies, biological flight also occurs over a wide range of aerodynamic regimes. These regimes are characterized by the Reynolds number ( $Re$ ), a dimensionless quantity that represents the ratio of inertial to viscous forces, which is used to predict similarity of flow behavior.  $Re$  is defined formally for flapping systems in section 4.1. The fairyfly operates near an  $Re$  of 1, essentially swimming through the air, while larger insects and hummingbirds operate above an  $Re$  of 10,000 similar to that of small birds, while even the smallest drones operate around  $Re$  of 100,000 [7, 37, 38]. This upper limit on the size of hovering organisms is likely due to a combination of changing aerodynamics and increasing energetics of wing motion [39]. The isometric scaling of wing area, which was found to be proportional to *organism mass*<sup>2/3</sup>, clearly demonstrates this trend [40]. This scaling indicates that there is some critical mass at which the wing size, and directly the lift production, of the organism will not be sufficient to sustain hover. This limit highlights the fundamental challenge of hovering, to drive the reciprocating motion of the wings, which can have significant inertia, against skin friction and high aerodynamic drag in order to support the weight of the vehicle. Novel unsteady aerodynamic mechanisms such as an attached leading edge vortex, rotational circulation, wake-capture, and clap-and-fling, have been identified to augment lift in the low Reynolds number aerodynamic regime [40, 41, 42, 43].

Flight at larger scales, such as birds and conventional aircraft, is based on classical aerodynamics characterized by forward motion with low angles of attack. In hovering flight the animal is primarily stationary with its body perpendicular to the ground with the wings flapping in a plane parallel to the ground at high angles of attack. Changes of the kinematics between the wings, or tilting of the flapping plane can be used to achieve translational motion, while the body and stroke plane can be rotated to allow for forward flight. Birds typically flap their wings in a plane perpendicular to the ground to generate forward motion, while lift production greater than the body weight is typically only needed during takeoff. Birds can utilize energy saving behaviors such as gliding and soaring on thermals that allow them to achieve much larger sizes,

up to 16 kg for the Kori bustard [41]. There has been successful work in bird-like flapping flight, ornithopters, that have even demonstrated improvements over fixed wing performance [44, 45, 46, 47]. However, in this work, I will focus on systems designed to be capable of hover.

### 1.2.1 Motor Driven Platforms

Motor torque decreases sharply with size, scaling with  $L^4$ , making it difficult for small motors to directly drive flapping wings. A survey of motor driven vehicles is shown in Table 1.1 and Figure 1.1. The Delfly vehicles and Nano hummingbird both utilize a single motor spinning continuously, with a crank-rocker transmission to convert the rotary output to flapping motion. This results in coupled wing kinematics, necessitating additional actuators for control and limiting the payload of these systems. Furthermore, non-linearity of the transmission limits efficiency and complicates control of the drive motor [48]. The Delfly systems have four flexible wings in an X-wing configuration that allow them to utilize clap-and-fling behavior. They use a conventional tail with rudder and elevator controls driven by magnetic actuators for control [49]. Although the Delfly are not capable of sustained hover, they are capable of very slow forward flight. The Nano Hummingbird uses a tailless control approach based on actively controlling wing rotation as well as membrane tension throughout the stroke that results in variable twisting and cambering of the wing [50]. The Delfly and Nano Hummingbird are fully integrated, including battery, camera, and wireless communication, allowing untethered operation. The vehicle developed by Cornell also features a four wing design with flexible 3D printed wings and is capable of untethered flight [51]. However, the vehicle does not have control built into its design and is only capable of passively stable hover with the aid of two aerodynamic dampers.

The design of our vehicle is based on concepts developed by Campolo et al. that demonstrates DC motors could directly drive flapping wings by adding a torsional spring in parallel with the motor output [48, 52, 53]. This allows for operation at resonance, a key feature of biological flight at small scales [40]. For a spring-mass-damper system with periodic actuation occurring at the resonant frequency, the elastic element stores the energy necessary to accelerate the load. Therefore, when operating at resonance, the actuator only needs to provide torque to overcome damping. For flapping, the torque needed to accelerate the wing is almost seven times larger than the torque needed to overcome aerodynamic damping [48]. Therefore, resonant actuation significantly decreases the power requirements of a flapping wing system, allowing a smaller motor to be used. Direct control over the wing motion has a key advantage of allowing control of the vehicle through independent control of the wing kinematics alone, as is done in biological systems. This allows the weight of the vehicle to be minimized as only one actuator per wing is needed to control the system. Our design also utilizes underactuation to minimize weight. A flexure joint at the base of the wing allows its rotation to be driven passively by aerodynamic forces. In addition, the elasticity of the flexure provides some restorative force to aid wing rotation. The original prototype capable of liftoff and controlling torques operated at 10 Hz, had a weight of 2.7 g, and a lift to weight ratio of 1.4 [54, 55]. The improved vehicle operates at 20 Hz, has a weight of 3.2 g, and a lift to weight ratio of approximately 3.7 [56]. The vehicles developed at Purdue have a similar design. While they also rely on passive wing rotation, only the smallest uses an elastic flexure while the other two simply use a pin joint with rotational stoppers [57, 58]. The two smaller vehicles are driven by a custom electromagnetic actuator that operate at reso-

Table 1.1: Survey of motor driven FWMAVs

System	Weight (g)	Wingspan (cm)	Flapping Frequency (Hz)
Purdue* [59]	0.55	3.5	160
CMU Prototype [54]	2.7	21.6	10
Delfly Micro [62]	3.07	10	30
CMU [56]	3.2	21.6	20
Cornell [51]	3.89	14.3	30
Purdue* [59]	3.9	10	80
Purdue [58]	3.89	15	33
Nano Hummingbird [50]	19	16.5	30
Delfly Explorer [63]	20	28	14

\*Utilizes a custom electromagnetic resonant actuator

nance using a virtual magnetic spring allowing for high frequency operation [59]. This design has allowed for a lighter, more powerful actuator than conventional motor designs for driving reciprocating wing motion. The addition of elastic energy storage to a flapping transmission has also been explored in works by Lau *et al.* as well as Beak *et al.*, although these systems have not been capable of liftoff [60, 61].

## 1.2.2 Piezoelectric Platforms

At scales less than 1 gram, the power available from piezoelectric actuators exceeds that of conventional motors [13]. A survey of piezo driven vehicles is shown in Table 1.2 and Figure 1.2. The Harvard Robobee utilizes a piezoelectric bimorph actuator. Small amplitude oscillations of the actuator tip are amplified and generate flapping motion through a four-bar linkage. The initial prototype of the system used a single power actuator, while later iterations use one power actuator per wing to allow for control through independent wing motion [64, 65]. Another iteration uses one power actuator to drive the wing stroke and another control actuator to crease a difference in angle of attack between the two wings [66]. These designs also rely on passive wing rotation to minimize system weight. However, significant challenges remain in making these systems fully autonomous. The piezoelectric actuator requires 200-300V requiring the system to be tethered for power and control. Incorporate a suitable high-voltage power source and associated electronics onboard has remained a challenge [13, 67]. Control is done off-board with the use of a Vicon motion capture system. Some recent studies have added single sensors to the vehicle, such as a magnetometer or photodiode, and demonstrated improved stability with this additional input [68, 69, 70]. However, such sensors consume significant vehicle payload and do not eliminate the need for ground truth measurements of position and orientation provided by the Vicon system. Despite advances in micro scale fabrication based on smart composite microstructures and folding, systems capable of liftoff are still constructed by hand, limiting possibilities for cheap mass production of such systems [71, 72]. Finally, its small size ultimately limits its payload capacity and ability to operate in real world environments. The Micromechanical Flying Insect, developed at UC Berkeley, utilizes four piezoelectric actuators to control the flapping and

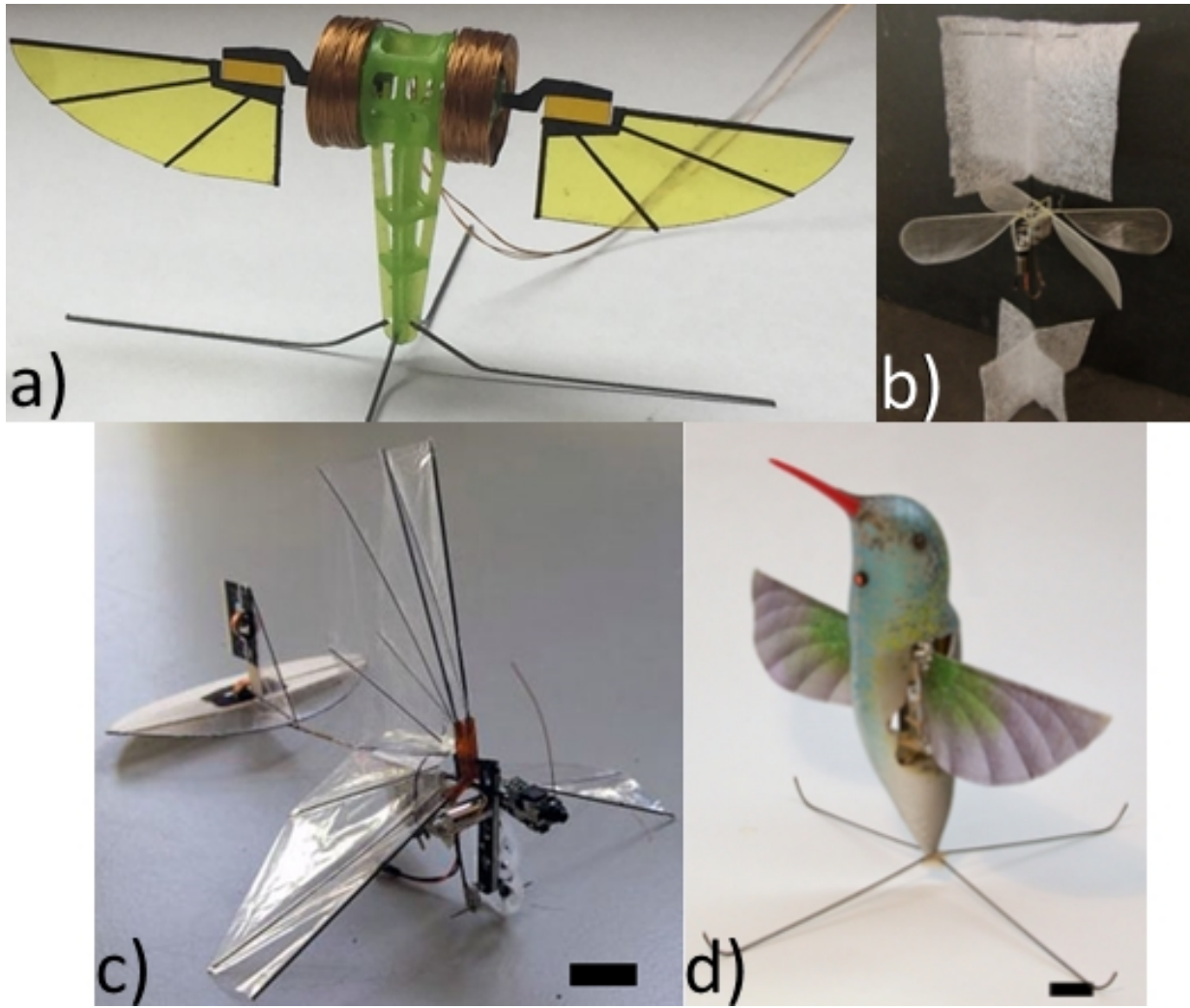


Figure 1.1: Motor driven FWMAVs: a)Purdue\* 3.9 g, b) Cornell, c) Delfly Micro, d)Nano Hummingbird. Black bar shows 1cm.

Table 1.2: Survey of piezo driven FWMAVs

System	Weight (g)	Wingspan (cm)	Flapping Frequency (Hz)
Army Research Labs [76]	n/a	0.2	n/a
Harvard - Single [64]	0.06	3	110
Harvard - Double [65]	0.08	3	120
Berkeley MFI [73]	0.1	1.1	150

rotation angles of both wings [73]. Although capable of hover in simulation, it has been unable to achieve liftoff due to the large actuator weight [74]. The Army Research Labs have released limited details on a PiezoMEMS flapping system, which uses thin film piezoelectric actuators to both drive and sense the wing flapping and rotation angles [75, 76]. The thin film piezoelectric actuators at these miniscule sizes can be driven at low voltages, in this case resonant operation occurred at 3.4V. To my knowledge, this remains a proof of concept design. Although other actuator types such as electrostatic, dielectric elastomer, shape memory alloy, or thermal can also be fabricated at small scales they have not been suitable for flapping flight since they cannot provide high force output at high frequencies.

### 1.2.3 Controller

Flapping flight is an inherently unstable form of locomotion based on highly dynamic and time-varying wing motions [77]. As discussed previously, significant work has studied biological flight in order to understand the aerodynamics and their control. However, due to the lack of FWMAVs capable of liftoff and control, many of the studies on controllers for these systems are based on simplified models and have been performed in simulation [78, 79]. In general, controllers are based on averaging theory, allowing the flapping system to be treated as time-invariant approximation. Under the condition where the flapping frequency is sufficiently high and the wing forces are sufficiently filtered by the body dynamics, wing forces and torques can be averaged over each flapping cycle. We will see later in this work that due to our low flapping frequency, a pitching oscillation at this frequency is generated that complicates control. Several groups have shown longitudinal control in simulation using non-linear control [80, 81]. However, the majority of controllers developed for FWMAVs are linear. The MFI demonstrated controlled hover in simulation using a linear-quadratic regulator (LQR) using fully controlled wing kinematics. Although effective in simulation, direct control over the wing stroke trajectory tends to dramatically increase the power consumption of the drive actuators [57, 58, 82]. For developed systems, cyclic actuation of parameters such as the flapping amplitude, mean stroke position, or wing twist are used to control roll, pitch, and yaw [50]. Significant work on a controller for the Robobee has been done based on off-board ground truth measurement of the vehicle state from the Vicon camera tracking system. Initial work demonstrated altitude control using a proportional-derivative (PD) controller, based on system dynamics linearized about hover, for a vehicle stabilized with aerodynamic dampers [83]. A model-free controller, where the system was considered to be linear time-invariant, used sequential parameter tuning to achieve upright stable flight, straight vertical flight, and finally stable hovering with altitude and position con-

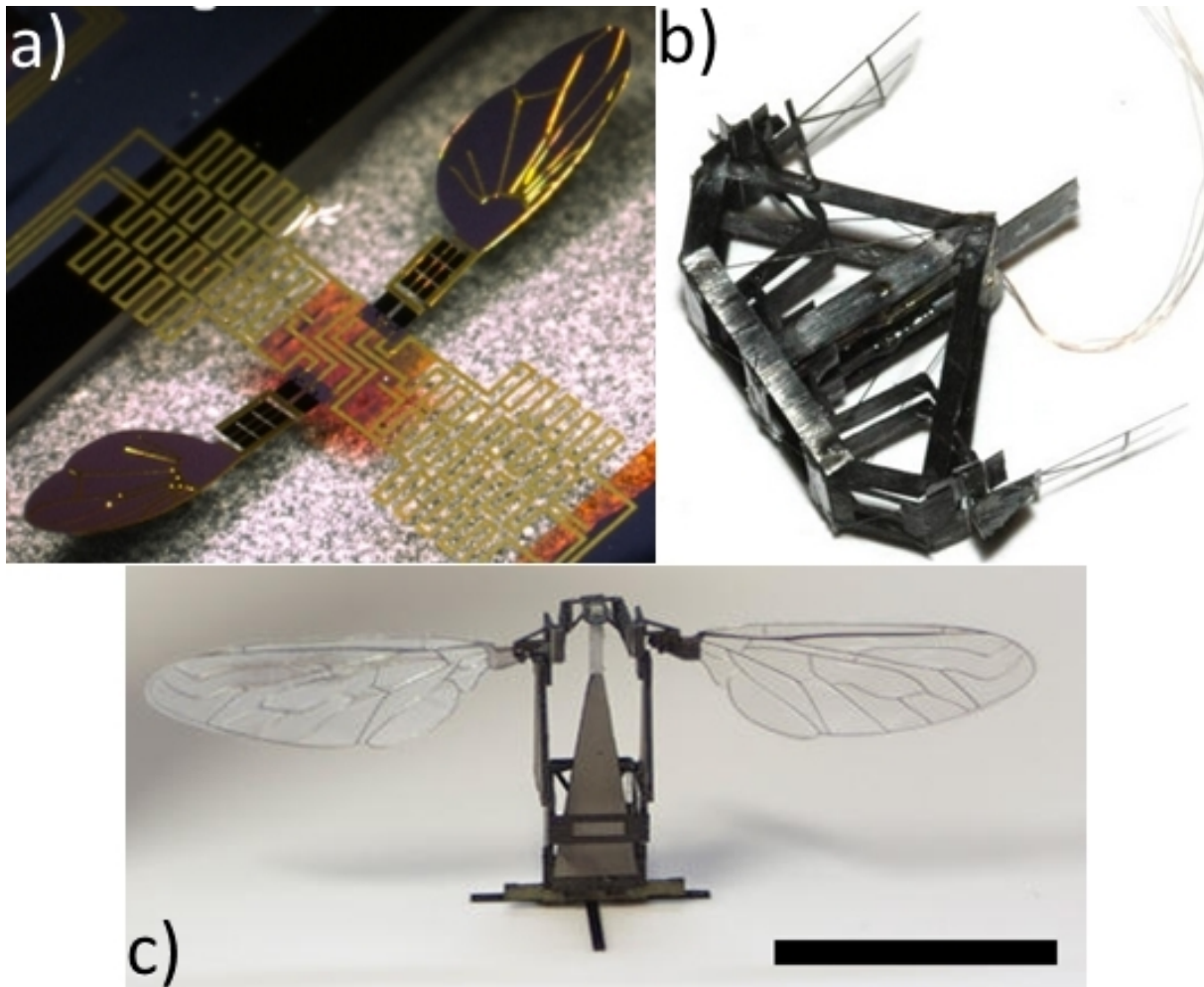


Figure 1.2: Piezo driven FWMAVs: a) Army Research Labs, b) Berkeley MFI, c) Harvard - Double. Black bar shows 1cm.

trol [84, 85]. An adaptive controller developed with Lyapunov's direct method reduced hovering RMS positional errors by approximately 50% after a set of open loop trimming and controlled test flights [86].

### 1.3 Rotary vs. Flapping Flight

It is important to address the distinctions between rotorcraft, primarily helicopters and quadrotors, and flapping flight since they possess similar operational capabilities with their ability to hover in place. Rotorcraft are comparatively a very mature technology as they rely on conventional electric motors and electronics. The smallest R/C quadrotor and helicopter, the Proto X Nano and Nano-falcon, are toys with a price point of approximately \$30. A detailed survey of small rotorcraft is presented in Table 1.3 and Figure 1.3. These toys have minimal capabilities and are quite fragile, however they represent a lower bound for the size of these types of vehicles with current technologies. Commercial and research platforms tend to be at least 60% heavier, but include more advanced communications, sensors, and flight capabilities. These vehicles are on the same scale as fully integrated flapping systems such as the Nano Hummingbird or Delfly Explorer. However, all other flapping systems are smaller than the toy rotorcraft. There are also key differences between rotary aerodynamics based on steady state actuation and flapping flight based on reciprocal motion. A simulation study by Zheng et al. concludes that with respect to power loading (N of lift per W of aerodynamic power) flapping wings exceed the performance of rotary wings over the range of Re from 50–6000 [87]. At Re = 100 power loading is a factor of two higher for flapping wings, while both types of actuation appear to reach an asymptote with similar performance around Re = 6000. For low Re, viscous drag dominates in rotary flight lowering its effectiveness. In a study conducted by Lentink and Dickinson using a scaled robotic system rotary performance exceeded that of a flapping wing with respect to power factor  $C_L^{3/2}/C_D$ , a measure of aerodynamic efficiency, for glide numbers greater than one over the range of Re from 110–14000 [35]. However, performance with respect to this metric remained equal for glide numbers less than one. Additionally flapping flight can take advantage of unsteady aerodynamic mechanisms that increase lift production such as the attached leading edge vortex, rotational circulation, added mass, wake capture, and clap-and-fling. Furthermore, for flapping flight utilizing a resonant actuator can significantly increase the efficiency of actuation compared to steady state rotation utilized for rotary flight. Current flapping systems have similar controllability to rotary platforms as they both utilize cyclic control inputs. Translation is achieved by tilting the vehicle in order to vector thrust towards the desired direction of motion. However, this limitation is due to the utilization of passive wing rotation. A fully controlled wing allows for almost arbitrary generation of forces and torques during a single wing stroke. Peak torques during the stroke have been measured to be an order of magnitude larger than stroke averaged values. Therefore, even small changes in the differential wing kinematics or rotation can generate large control inputs to the system. Multi-rotor systems with blades mounted at different angles can achieve translation without tilting, but require additional actuators. Other rotor designs such as a coaxial dual rotor in a spherical cage with a gimbal have improved autonomy, but limited controllability.

Table 1.3: Survey of small rotorcraft

System	Weight (g)	Blade Span (cm)	Endurance (min)	Type	Market
Nano-falcon [88]	11	15	5	Helli	Toy
Proto X Nano [89]	11.5	2.9	6	Quad	Toy
Black Hornet [90]	18	12	25	Helli	Military
Crazyflie [91]	19	4.5	7	Quad	Commercial
GRASP Lab Pico [92]	25	4.5	n/a	Quad	Research
muFLY [93]	80	17.5	6	Helli	Research

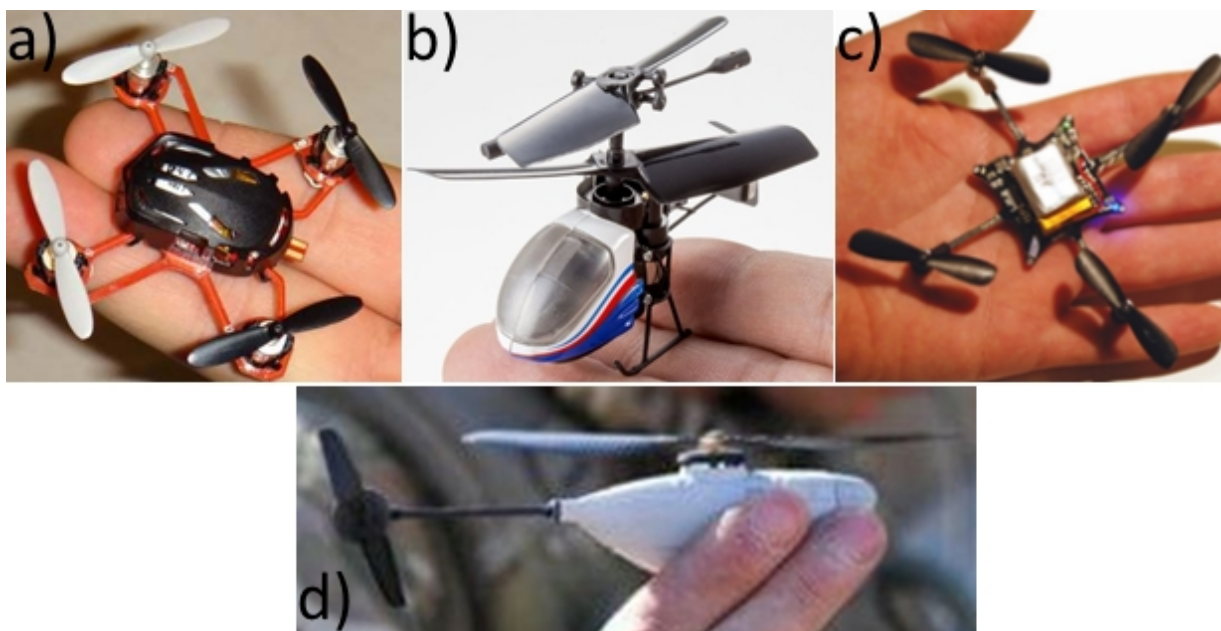


Figure 1.3: Small rotorcraft: a) Proto X Nano, b) Nano-falcon, c) Crazyflie, d) Black Hornet.

## 1.4 Thesis Outline

This document is divided into six chapters. Chapter 2 discusses the system dynamics model originally presented by Hines *et al.* and aerodynamic model adapted from work by Sane and Dickinson [54, 94]. Chapter 3 covers resonant actuation, motor selection, and thermal modeling of the actuator presented in [95]. Chapter 4 covers wing design and modeling of flexible, twisted wings presented in [56, 96]. Chapter 5 details improvements to the design of the system that resulted in an increase of the resonant operating frequency and system reliability. Chapter 6 deals with controller design and closed-loop flight performance presented in [55, 97]. Chapter 7 contains contributions and concluding remarks.

## 1.5 Contributions

The major contribution of this work is the development of an efficient, reliable, and controllable FWMAV platform that is capable of controlled flight and has the potential to be fully integrated. In summary, this work presents contribution to system modeling, actuator design, flexible wing design, system robustness, and control. The contributions are:

- Transformed a simple prototype into a robust flapping wing micro aerial vehicle testbed with a flapping frequency of 23 Hz, weight of 3.2 g, and peak lift to weight of 3.7 with reliability exceeding 50,000 cycles
- Developed a DC gearmotor based resonant actuator that increases torque and power density by 161.1% and 666.8% respectively, compared to just the motor, while decreasing current draw 25.8%
- Modeled actuator thermal performance, experimentally identifying novel parameters for micro motors, to predict safe operating parameters for the system and to optimize a heatsink that increased operating time by 102.4%
- Fabricated and tested flexible wings that increase translational lift production by 35.3%
- Extended a quasi-steady, blade element aerodynamic simulation to account for wing flexibility demonstrating that the flexible design increases aerodynamic efficiency by 41.3% and the effective lift coefficient by 63.7%
- Implemented control framework stabilizes the vehicle allowing for controlled flight experiments surpassing 10 second in duration

Publication summary:

- D. Colmenares, M. Sitti, Control of a Flapping Wing Micro Air Vehicle for Stable Flight Based on Independent Wing Motion, *International Journal of Advanced Robotic Systems*. In review.
- D. Colmenares, R. Kania, W. Zhang, M. Sitti, Bio-inspired Flexible Twisting Wings Increase Lift and Efficiency of a Flapping Wing Micro Air Vehicle, *Journal of Micro-Bio Robotics*. In review.
- D. Colmenares, R. Kania, M. Liu, M. Sitti, Characterization and Thermal Management

of a DC Motor-Driven Resonant Actuator for Miniature Mobile Robots with Oscillating Limbs, *IEEE/ASME Transactions on Mechatronics*. In review.

- D. Colmenares, R. Kania, W. Zhang, M. Sitti, Compliant Wing Design for a Flapping Wing Micro Air Vehicle, *Proc. Of the IEEE/RSJ Conference on Intelligent Robots and Systems*, Hamburg, Germany, September 2015. pp. 32-39.
- L. Hines, D. Colmenares, M. Sitti, Platform Design and Tethered Flight of a Motor-driven Flapping-wing System, *Proc. Of the IEEE International Conference on Robotics and Automation*, Seattle, WA, May 2015. pp. 5838-5845.

# Chapter 2

## System Dynamics and Aerodynamic Model

### 2.1 Introduction

This chapter presents modeling of system dynamics in section 2.2, originally presented by Hines *et al.*, and aerodynamic model in section 2.3 adapted from work by Sane and Dickinson [54, 94]. The dynamics model is used to estimate kinematics of the wing directly driven by a resonant actuator composed of a DC gearmotor with a torsional spring attached in parallel to the motor output. The aerodynamics model then estimates aerodynamic lift and drag generated by the wing. These basic models allow for determination of suitable values for system parameters in order to achieve liftoff. This model is validated for the initial prototype and developed system in section 2.4, but remains limited in scope.

### 2.2 Dynamics Model

The vehicle is represented as a spring-mass-damper system driven by a DC gearmotor shown in Figure 2.1. The Lagrangian, the difference in kinetic and potential energies, is given by

$$L = \frac{1}{2}m_w\vec{v}^T\vec{v} + \frac{1}{2}J_w\vec{\omega}^T\vec{\omega} - \frac{1}{2}K_w\phi^2 - \frac{1}{2}K_s\theta^2, \quad (2.1)$$

where  $m_w$  is the mass of the wing,  $\vec{v}$  is its translational velocity,  $\vec{\omega}$  is its angular velocity,  $J_w$  is its inertia,  $K_w$  is the flexure stiffness, and  $K_s$  is the motor spring stiffness. We can then formulate the Euler-Lagrange equations for our system by adding in non-conservative forces,

$$\frac{d}{dt} \left( \frac{\partial L}{\partial \dot{\theta}} \right) - \frac{\partial L}{\partial \theta} = \vec{M}_{aero} \cdot \vec{E}_3 - M_{act} \quad (2.2)$$

$$\frac{d}{dt} \left( \frac{\partial L}{\partial \dot{\phi}} \right) - \frac{\partial L}{\partial \phi} = \vec{M}_{aero} \cdot \vec{E}_1'' - b_w\dot{\phi}, \quad (2.3)$$

where  $\vec{M}_{aero}$  is the aerodynamic moment acting on the wing calculated from the model described in Section 2.3,  $\vec{E}_1''$  is the wing rotation axis,  $\vec{E}_3$  is the wing flapping axis as shown in

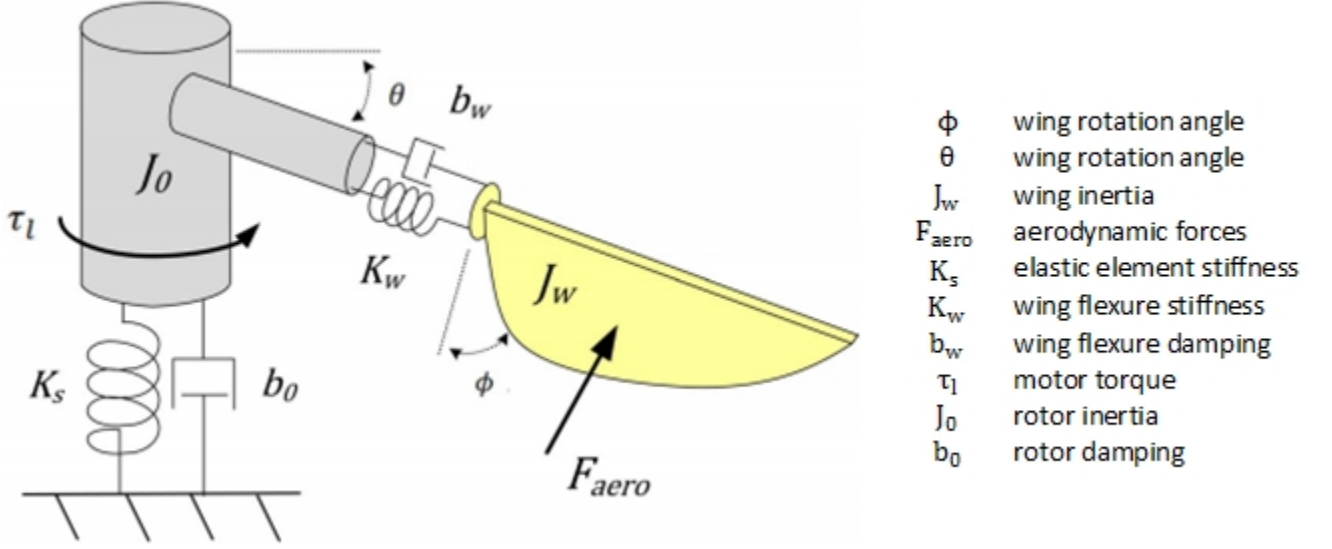


Figure 2.1: Spring-mass-damper system model

Figure ,  $b_w$  is the damping of the flexure, and  $M_{act}$  represents the actuator dynamics. For a DC gearmotor the equation is given by

$$M_{act} = \frac{\eta_g N_g k_a}{R_0} (V - k_a N_g \dot{\theta}) - \eta_g N_g^2 J_m \ddot{\theta} - b_m \dot{\theta}, \quad (2.4)$$

where  $\eta_g$  is the gearbox efficiency,  $N_g$  is the gear ratio,  $k_a$  is the motor constant,  $R_0$  is the armature resistance, and  $V$  is the input voltage. By specifying and input voltage the Euler-Lagrange equations can be solved to determine the time course of the wing kinematics. Substituting equation 2.4 into 2.2 results in the full equation of motion for the wing flapping angle. Under the assumption that the wing does not rotate  $\phi, \dot{\phi}, \ddot{\phi} = 0$  the equation simplifies to

$$\vec{M}_{aero} \cdot \vec{E}_3 + \frac{\eta_g N_g k_a V}{R_0} = (J_{33} + (R_{CG} + d_w)^2 m_w + \eta_g N_g^2 J_m) \ddot{\theta} + \left( \frac{\eta_g N_g^2 k_a^2}{R_0} + b_0 \right) \dot{\theta} + K_s \theta, \quad (2.5)$$

where  $J_{33}$  is a term in the wing inertia matrix,  $R_{CG}$  is the distance from the wing base to center of gravity, and  $d_w$  is the wing offset. The equation is in standard spring-mass-damper form with nonlinear aerodynamic damping. This can be used to calculate the ideal spring stiffness so that the system operates at resonance as follows,

$$K_{s,ideal} = (J_{33} + (R_{CG} + d_w)^2 m_w + \eta_g N_g^2 J_m) (2\pi f)^2, \quad (2.6)$$

where  $f$  is the flapping frequency and  $J_{33} + (R_{CG} + d_w)^2 m_w$  is the wing inertia about the flapping axis.

## 2.3 Aerodynamic Model

The total aerodynamic force on the wing ( $F_{tot}$ ) consists of

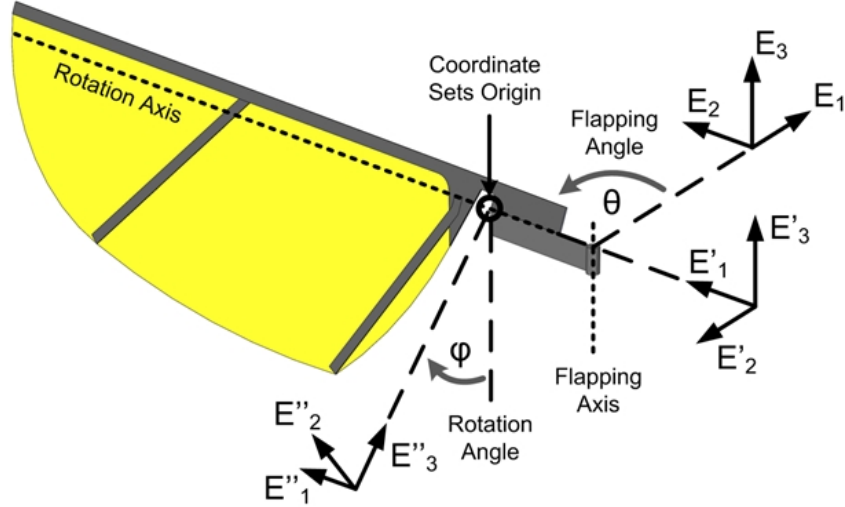


Figure 2.2: Model of the passively rotating wing with coordinate systems representing transformations by the flapping and rotation angles respectively. All three coordinate systems are centered at the labeled origin point, but detached for clarity. The  $\vec{E}''$  coordinate system is attached to the wing.

$$F_{tot} = F_{trans} + F_{rot} + F_{air} + F_{wc}, \quad (2.7)$$

where component forces arise from the effects of wing translation ( $F_{trans}$ ), rotation ( $F_{rot}$ ), added air mass ( $F_{air}$ ), and wake capture ( $F_{wc}$ ). These force components are modeled based on work by Sane and Dickinson [94]. A quasi-static, blade element model calculates the forces on each wing strip at independent time snapshots, which are then integrated along the wing length to calculate total force. Forces are normal to the wing surface and decomposed into lift and drag components based on the wing rotation angle. Wake capture occurs at the end of the stroke as the wing changes direction and interacts with its previous wake. We neglect this effect since it lacks a closed form expression, typically only contributes up to 10% of the total force, and for symmetric rotation generates only drag. Translational force is derived from thin airfoil theory and is based on the pressure distribution on the airfoil. This force is given by

$$F_{trans} = \frac{1}{2} \rho U(r)^2 c(r) \sqrt{C_l^2 + C_d^2} dr, \quad (2.8)$$

where  $C_l$  and  $C_d$  are the lift and drag coefficients,  $c(r)$  is the chord length at spanwise position  $r$ , and  $\rho$  is the fluid density.  $U(r)$  is the translational velocity at a spanwise position of  $r$ , taken to be the velocity of each wing strips mid-chord point in the  $\vec{E}'_2$  direction calculated as follows,

$$U(r) = r\dot{\theta} + \frac{c(r)}{2} \dot{\phi} \cos(\phi), \quad (2.9)$$

where  $\theta$  is the wing flapping angle,  $\phi$  is the wing rotation angle. The difficulty of using this standard aerodynamic equation is the correct determination of the force coefficients that represent

the effect of the pressure distribution. We are able to utilize equations developed by Dickinson [3] in order to calculate appropriate coefficients based on rotation angle. The equations were determined experimentally from a dynamically scaled model of a fruit fly at a Reynolds number (Re) of 136. An additional benefit of these equations is that they contain the contribution of the stable leading edge vortex (LEV) that is created at high angles of attack in this low Re regime. The rotational force is derived from the Kutta-Joukowski theorem and is based on the relative velocities of wing translation and rotation. As the wing rotates at the end of the stroke, the rotation angle decreases leading to expansion of the LEV as the flow separates. This circulation and the rotation of the wing generates net rotational flow around the wing producing a Magnus force. Rotational force is given by

$$F_{rot} = -\text{sign}(\dot{\phi}) C_{rot} \rho \left| \dot{\theta} \dot{\phi} \right| c(r)^2 dr, \quad (2.10)$$

where  $C_{rot}$  is the rotational force coefficient calculated based on the location of the wings axis of rotation. The relative phase shift between the wing translation and rotation determines if the rotation is advanced, symmetric, or delayed, which determines the sign and magnitude of this force. The force due to added air mass is generated by the boundary layer of fluid that effectively becomes coupled to the wing through its unsteady motion. This force is given by

$$F_{air} = -\frac{\rho\pi}{4} [(\ddot{\theta}\cos(\phi) - \dot{\theta}\dot{\phi}\sin(\phi))r - \ddot{\phi}(z_{RA} - \frac{c(r)}{2})]c(r)^2 dr, \quad (2.11)$$

where  $z_{RA}$  is the location of the wing rotational axis. Accelerating the fluid causes a negative force, but as the wing decelerates the inertia of the fluid results in positive force and aids wing rotation.

## 2.4 Model Validation

Model verification experiments were performed using a half-system consisting of a single motor and wing as shown in Figure 2.3. A control computer generated a sinusoidal reference voltage for the motor driver, which boosted the voltage and current to power the motor. The voltage and current output of the driver were also measured in order to calculate input power. The half-system was mounted on a six-axis load cell that was used to measure lift force. High-speed video of the system was also recorded in order to determine the wing flapping and rotation angles.

In the first experiment the validity of the aerodynamic model was addressed. The force coefficients were determined for an Re of 136, while our system operated around 7000. Although previous results have found that low Re results from Dickinson *et al.* show good agreement with inviscid models that are applicable to our Re regime, we wished to verify force agreement experimentally [98, 99, 100]. For this experiment we operated the motor with a range of input signals from 8 V peak-to-peak to 13 V. Lift force was measured directly from the sensor and averaged on a per wing stroke basis. The flapping and rotation angles were determined from the high-speed video, shown in Figure 2.4.

In the first experiment the validity of the aerodynamic model was addressed. The force coefficients were determined for an Re of 136, while our system operated around 7000. Although previous results have found that low Re results from Dickinson *et al.* show good agreement

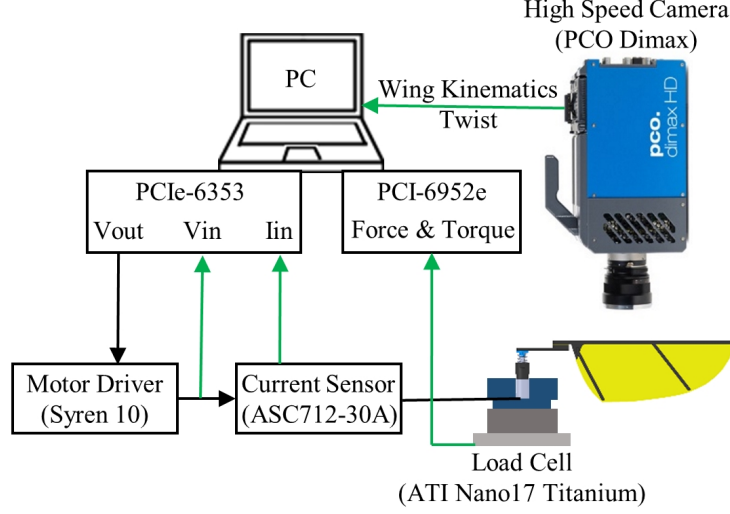


Figure 2.3: Experimental setup with control computer, power electronics, half system, load cell, and camera. The motor control signal is shown in black, while measured data is shown in green.

with inviscid models that are applicable to our Re regime, we wished to verify force agreement experimentally [98, 99, 100]. For this experiment we operated the motor with a range of input signals from 8 V peak-to-peak to 13 V at 10 Hz. Lift force was recorded using a 6 degree of freedom force/torque sensor (ATI-Nano17Ti) at 50 kHz, block averaged to an effective sampling frequency of 5 kHz, and low pass filtered. The conditioned signal was averaged on a per wing stroke basis. The flapping and rotation angles were determined from the high-speed video tracking of three points on the wing, shown in Figure 2.4. The rotation angle  $\phi$  is calculated using the ratio of the projected and maximum chord length as follows

$$\phi = \arcsin\left(\frac{c_{proj}}{c_{max}}\right) \quad (2.12)$$

where  $c_{max}$  is known and  $c_{proj}$  is calculated as the distance of the point p3 from the line defined by p1 and p2 as follows

$$c_{proj} = \frac{|(y_2 - y_1)x_0 - (x_2 - x_1)y_0 + x_2y_1 - x_1y_2|}{\sqrt{(x_2 - x_1)^2 + (y_2 - y_1)^2}} \frac{R}{|p_2 - p_1|} \quad (2.13)$$

where  $\frac{R}{|p_2 - p_1|}$  is the conversion factor from pixels to millimeters. Flapping angle  $\theta$  is determined using a vector along the leading edge  $\vec{v}_{le} = p_2p_1$  and the nominal wing position vector  $\vec{v}_{le,nom}$  as follows

$$\theta = \arccos\left(\frac{\vec{v}_{le,nom} \cdot \vec{v}_{le}}{\sqrt{|\vec{v}_{le,nom}| |\vec{v}_{le}|}}\right) \quad (2.14)$$

These angles were then used as input to the aerodynamics simulation and the resulting force was averaged per wing stroke.

Figure 2.4 also provides a comparison of the system wing kinematics and those of *Drosophila* measured by Fry *et al.* [8]. The flapping amplitudes are remarkably similar and smooth, although

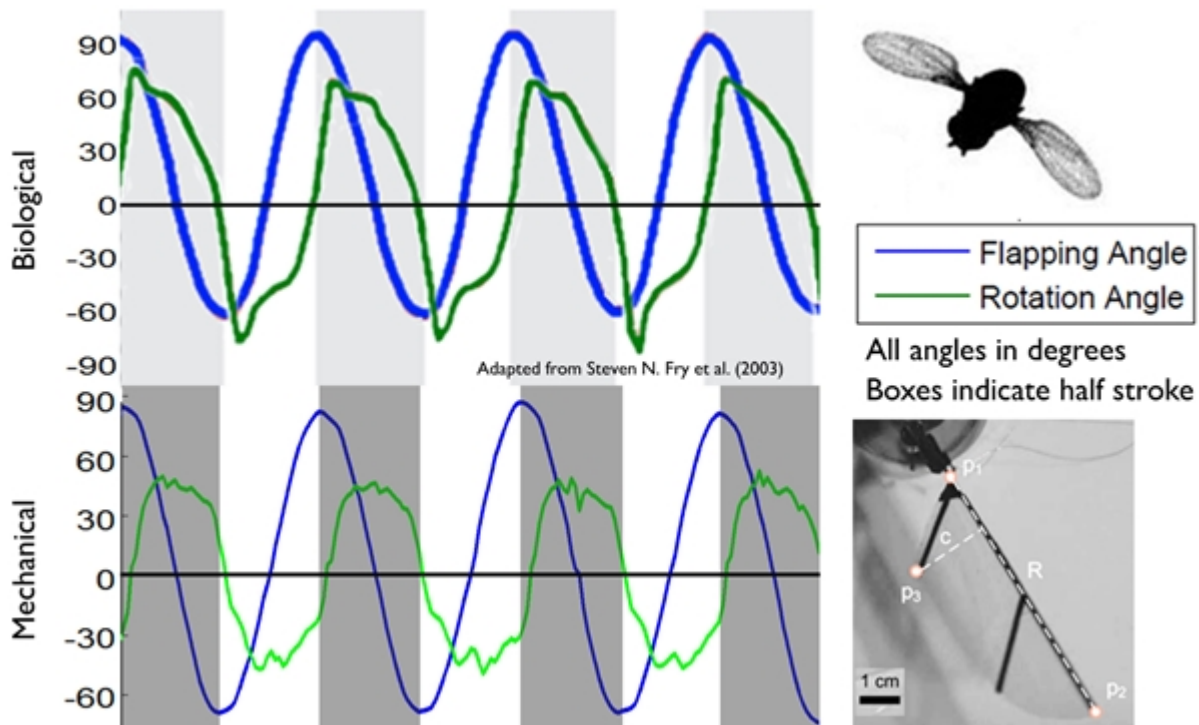


Figure 2.4: Wing kinematics of the developed system captured from high-speed video analysis and those of *Drosophila* adapted from Fry *et al.* (2003).

a significant asymmetry is measured that effectively shifts the midpoint of the stroke. Due to active control of rotation, *Drosophila* is able to change alter wing rotation and on average operates at a lower angle of attack for aerodynamic efficiency. In our system, stoppers were used to limit the wing rotation to  $\pm 45^\circ$  in order to maximize lift production. However, the wing had a tendency to rebound slightly after hitting the stoppers causing some deviations in the rotation. Despite the passive dynamics, rotation is only slightly delayed, whereas in *Drosophila* it is symmetric or slightly advanced.

Results of the aerodynamic simulation are shown in Figure 2.5. The trend in mean lift was well captured across the range of flapping amplitudes and is estimated within 10%. From b we see that total lift is dominated by the translational component. In the case of a perfectly symmetric wing stroke and rotation the rotational and added mass components will average out over one cycle.

In the second experiment, both models were utilized. The only input to the simulation was the voltage signal. The flapping and rotation angles were determined and used to calculate aerodynamic forces. This was compared to the measured lift and wing kinematics as shown in Figure 2.6. The error in the rotation angle prediction is small, which is aided by the use of the rotational stops. The wing flapping angle was under-predicted, especially at higher voltages. This may be due to discrepancies in the calculation of the drag force or in the parameters of the electromechanical system. Due to this trend in flapping amplitude, mean lift is also under-predicted by the full model. When comparing instantaneous lift force production we saw that the simulated curve had a smooth sinusoidal shape, which deviates from measured lift at mid stroke and stroke

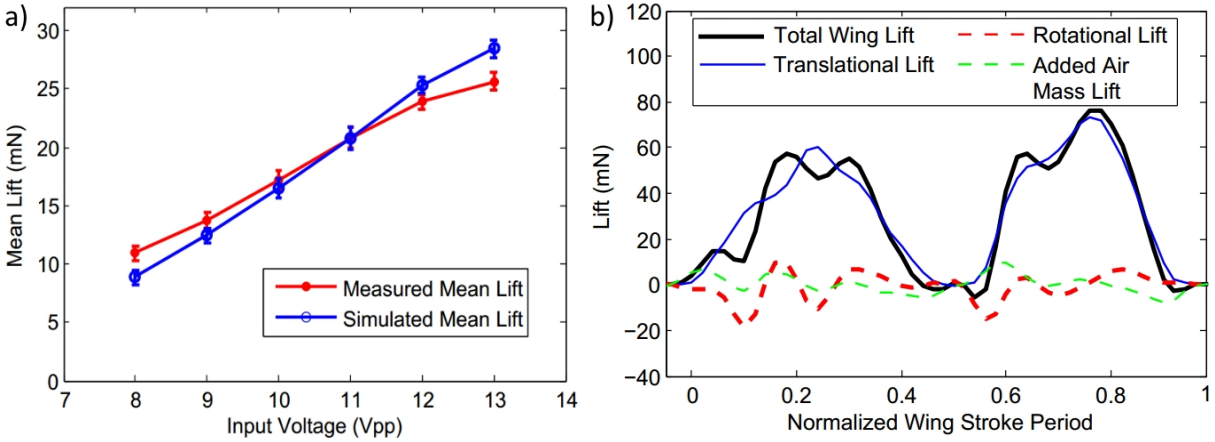


Figure 2.5: a) mean lift comparison from measured kinematics and b) simulated instantaneous lift and force component breakdown

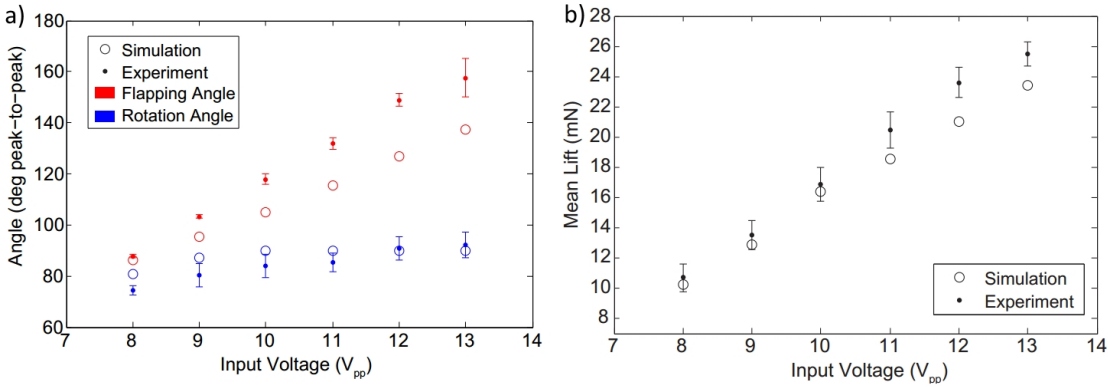


Figure 2.6: Comparison of simulated vs actuated wing kinematics a) and resulting mean lift b)

reversal as seen in Figure 2.7.

Although the shape of this deviation appears to be due to delayed rotation, its magnitude is much larger than would be expected. These negative dips contribute to under-prediction of the lift force and this trend was seen to continue as the system was improved to generate higher lift force. Experiments comparing rotational delay and the negative force features demonstrated that rotational lift is not the cause of these features. As seen in Figure 2.8a no difference in rotational phase was seen between upstroke and downstroke, while a significant difference in the minimum lift peak was measured. In 2.8b we measured a 6% difference in rotational phase, but consistent force peaks. Further examination of high-speed video revealed that at higher lift forces the stiffness of the system is not sufficient to constrain the motion of the wing in the vertical plane. Therefore the wing moves upward during the stroke, pushed up by the generated lift, rebounds in the middle once it hits the end of possible travel or bending, and drops at the end of the stroke where lift is negligible creating a triangular profile. The drop at the end of stroke is most significant and recorded on the force sensor as negative lift production, but is an inertial and not an aerodynamic force. Removing this inertial artifact reconciles the simulated and measured

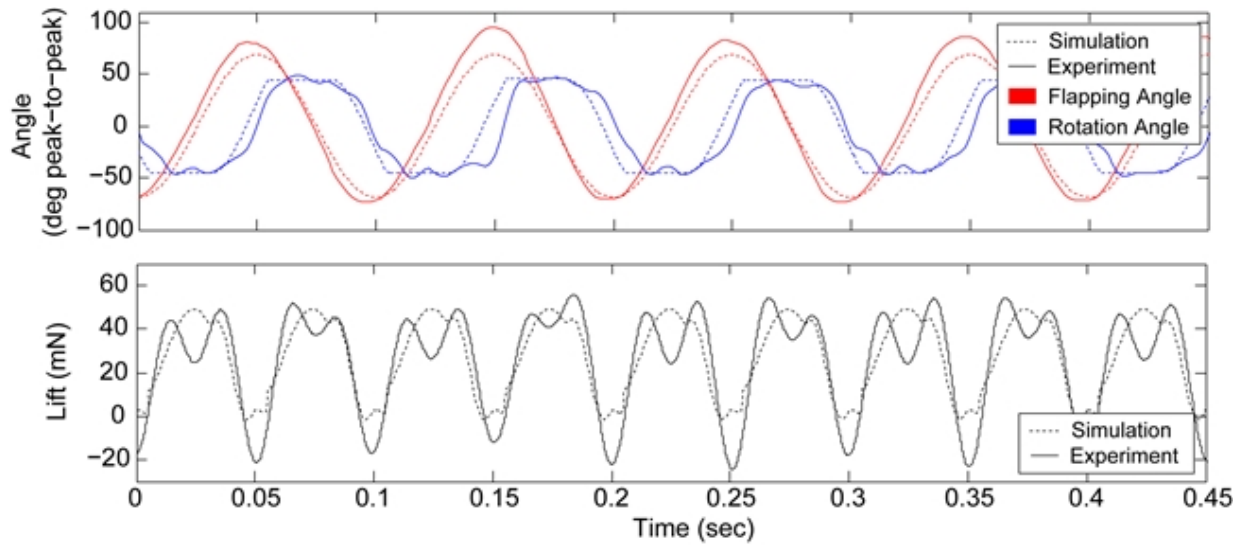


Figure 2.7: Comparison of wing kinematics and resulting instantaneous force production)

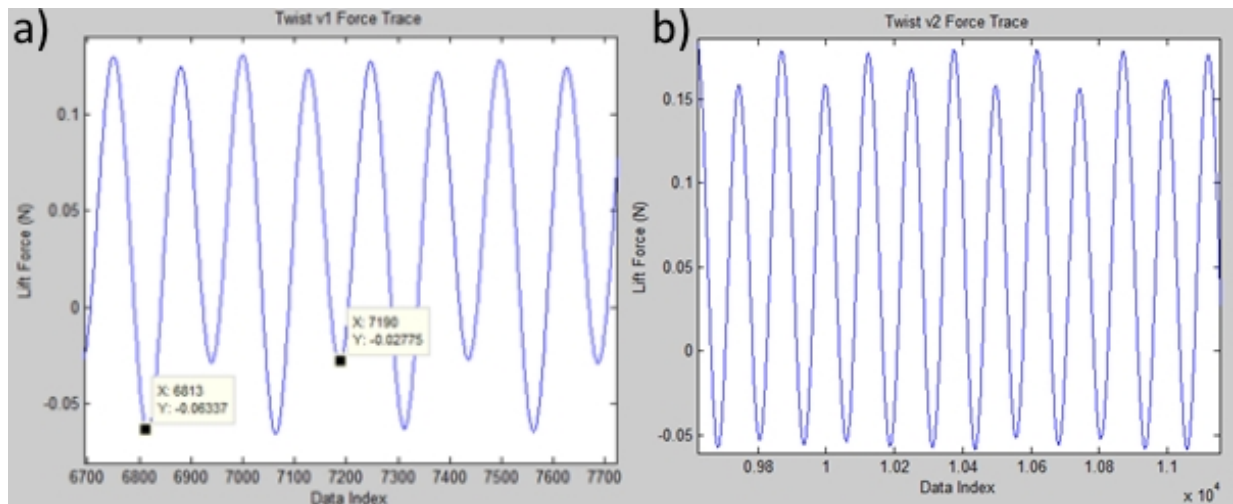


Figure 2.8: a) For twist v1 no difference in rotation was measured, but there is a three times difference in the minimum lift peak, b) for twist v2 a 6% difference in rotational delay was measured, but the minimum lift peaks are of consistent magnitude.

lift. The lift production of the system tested at 21 Hz and flapping amplitude of  $132^\circ$ , a Reynolds number of approximately 12600 average and 20000 peak, is correctly estimated within 10%. Simulated results with the lift breakdown are shown in Figure 2.9. We see that interaction with the stopper does cause drops in lift following stroke reversal. This is due to the discontinuous behavior of the rotational angle, and therefore a large derivative, which causes a negative contribution from rotational lift. However, this contribution is relatively small compared to the inertial effects seen in the experimental data shown in Figure 2.10. Note that some upstroke/downstroke asymmetry is seen in experiment. A detailed simulation comparison is shown in Section 4.7, tables 4.6.

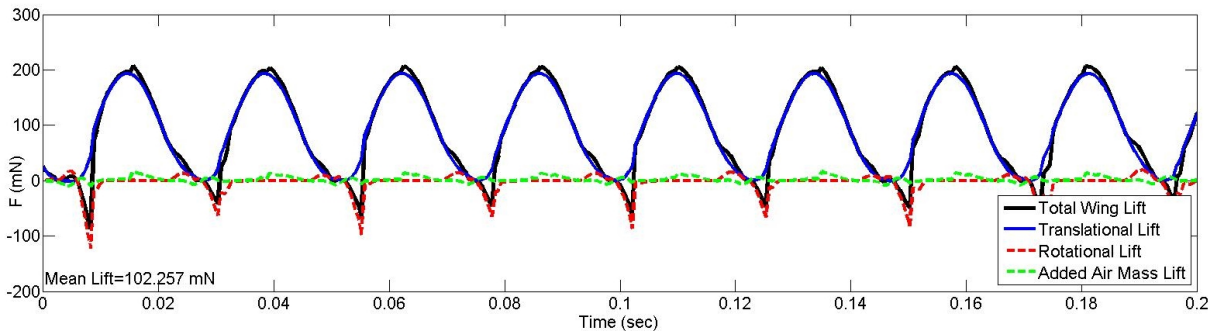
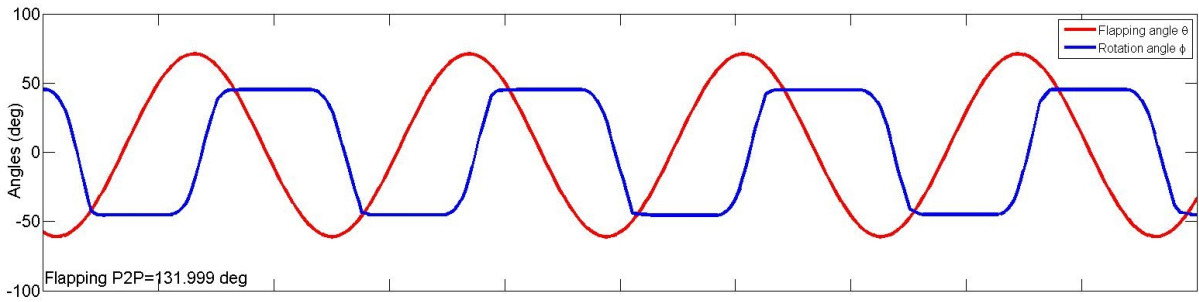


Figure 2.9: Simulated results for the rigid wing operating at 21 Hz, flapping amplitude  $132^\circ$ , rotational amplitude  $90^\circ$  with stoppers.

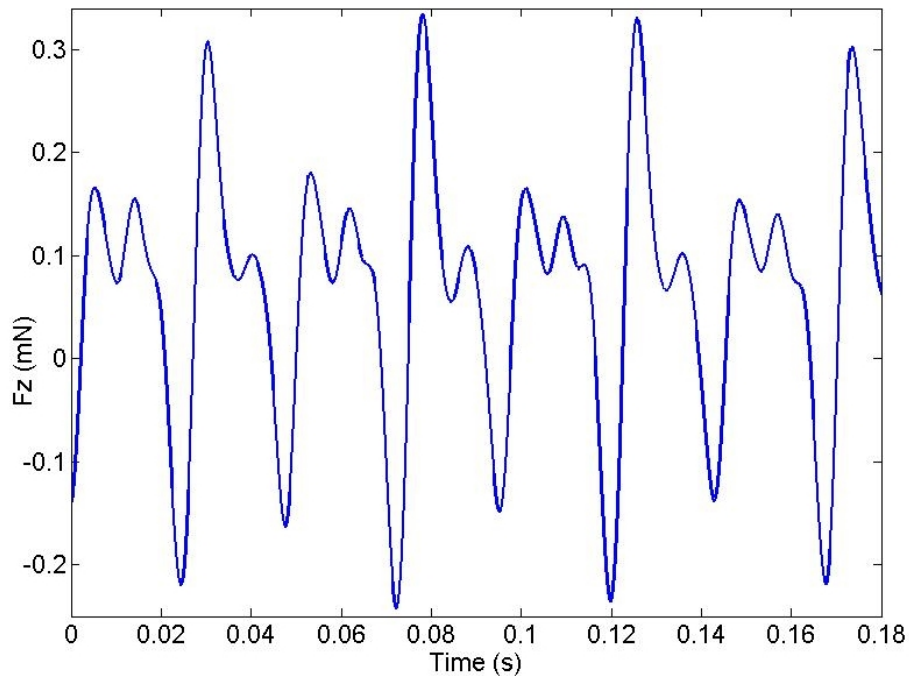


Figure 2.10: Experimental results for the rigid wing operating at 21 Hz, flapping amplitude  $132^\circ$ , rotational amplitude  $90^\circ$  with stoppers.

## 2.5 Conclusion

The described model is capable of accurately predicting mean lift of the initial prototype operating at 10 Hz (average Re of 7000) as well as the developed system operating at 21 Hz (average Re of 12600). This confirms other works indicating that aerodynamic force coefficients determined by Dickinson *et al.* remain applicable at our higher Re regime. Although the model has proven useful for predicting performance of the system, using it to optimize wing shape or voltage input signal has been unsuccessful so far. Performance of wing shape was most strongly linked to mass distribution of the wing, with increasing performance as the center of mass was moved outward. In testing optimization of the input signal, the model was seen to be very sensitive to wing kinematics, particularly wing rotation. The optimizations often resulted in unrealistic motions that primarily generated lift through rotation. However, both of these results indicate that the optimizations were not carefully constrained and merit further investigation. Since translational lift dominates, such optimizations could be tested based on translational lift only. The model could be improved to include three-dimensional motion, which would better match the developed system kinematics. However, unless the out of plane motion is carefully controlled it is likely undesirable and minimizing its effect should likely be a target of actuator or vehicle design improvement.

# Chapter 3

## Actuation: Motor Selection, Resonant Actuator Design, and Thermal Analysis

### 3.1 Introduction

Now that modeling of the system has been covered, a suitable motor that is both light weight and has high torque output at moderate rpm must be found to drive the system. Section 3.2 covers motor selection based on the electromechanical and aerodynamic simulations presented in Chapter 2 and the impedance matching principle developed by Campolo *et al.* Section 3.3 discusses the use of brushless motors for driving flapping wings. Section 3.4 presents a characterization of the developed resonant actuation and 3.5 provides a comparison with other actuators in terms of power density. Section 3.6 discusses thermal modeling of the system, which is used to design a weight optimal heat sink and to determine safe operation limits for the system. A conclusion is given in section 3.7.

### 3.2 Brushed Motor Selection

DC motors are commonly used to power miniature robots capable of running [101, 102, 103], climbing [104], and flying [49, 50, 51, 61]. Such behaviors with periodic limb motion require significant torque to continuously accelerate and decelerate the limb. Transmissions have been used to convert rotary motor output into periodic limb motion and often use gearing to increase torque, which declines sharply with decreasing motor size. However, they can be complex and heavy [50], limit system energy efficiency [61], and complicate control [105]. In order to build smaller, more powerful robots, we utilize a resonant actuator inspired by biological muscles, which acts as an elastic actuator, storing energy to reduce inertial power needed to produce these behaviors. For a spring-mass-damper system with periodic actuation occurring at the resonant frequency, the elastic element stores the energy necessary to accelerate the load. Therefore, when operating at resonance, the actuator only needs to provide torque to overcome damping. For flapping, the torque needed to accelerate the wing is almost seven times larger than the torque needed to overcome aerodynamic damping [48]. Therefore, resonant actuation significantly decreases the power requirements of a flapping wing micro air vehicle. Furthermore, resonant actuators

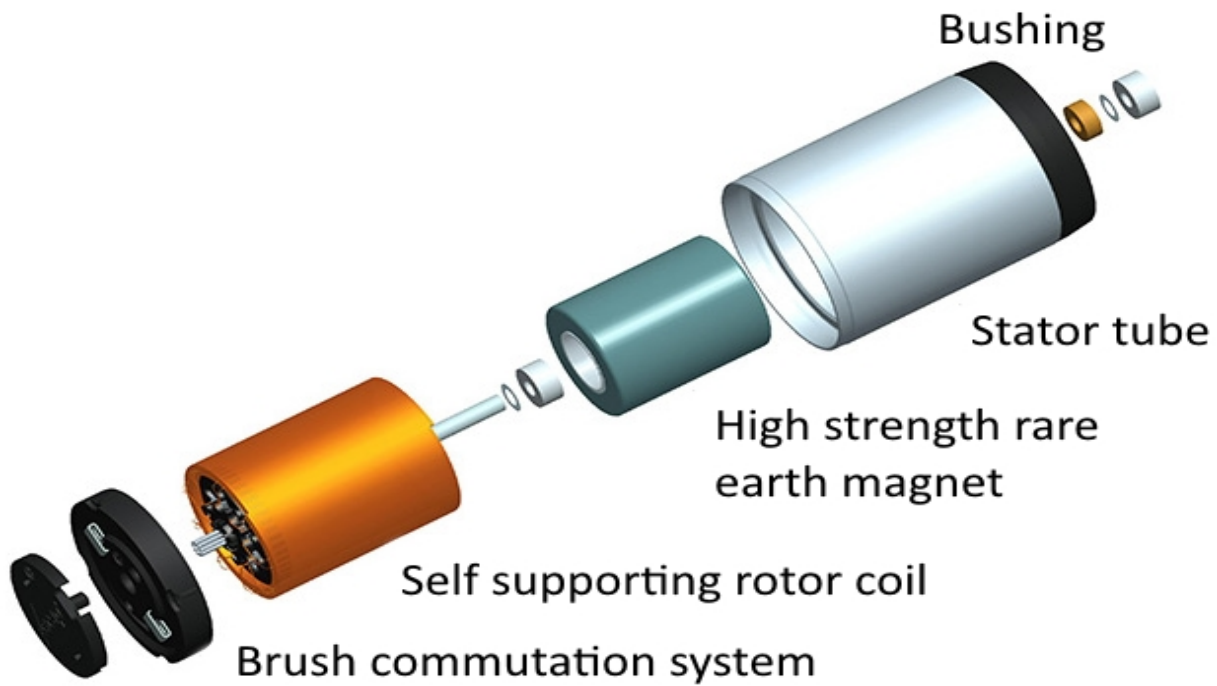


Figure 3.1: Typical brushed DC motor design for small sizes

can directly drive limbs to efficiently generate high force output with independent control. This is particularly useful for weight-constrained systems where maximizing actuator power density is critical for operation.

Despite the significant benefits from this actuation technique, finding a suitable motor for a small scale robot was still extremely challenging. The motor must be light weight in order to achieve the target vehicle weight around 3 g. It must also have high torque output in the range of 600–1800 rpm in order to achieve a large amplitude wing stroke in the range of 10–30 Hz. In search of a suitable commercial motor, over 166 models from a wide range of manufacturers were tested in simulation. Most of the surveyed motors were in the range of 0.3 to 5 grams, although several others weighing up to 20 grams were tested. Most of the small motor designs consist of brushed motors in an inrunner configuration where the rotor spins inside the motor casing. Although typical brushed motors contain the permanent magnet outside the windings, in these small motors the magnet is a cylindrical two-pole magnet placed inside the windings as shown in Figure 3.1 adapted from [106]. For this small size the rotor can be self-supporting and is coreless, also called ironless, since the wire does not need to be wound around a central core. The resulting rotor has very low inertia and allows for rapid accelerations, which will be essential for directly driving a flapping wing. However, these long and thin motors are designed for high speeds and are not able to generate large torques due to the small lever arm between the rotor windings where the electromagnetic force is applied and the central axis of rotation. Therefore a gearbox is needed so that the motor runs at low speeds with high torque. Motors were tested in geared configurations when available, although most gearboxes were made of steel, with the gearbox often having the same weight, or exceeding, the weight of the motor itself. An alternative to the geared inrunner design, is an outrunner motor design. These motors

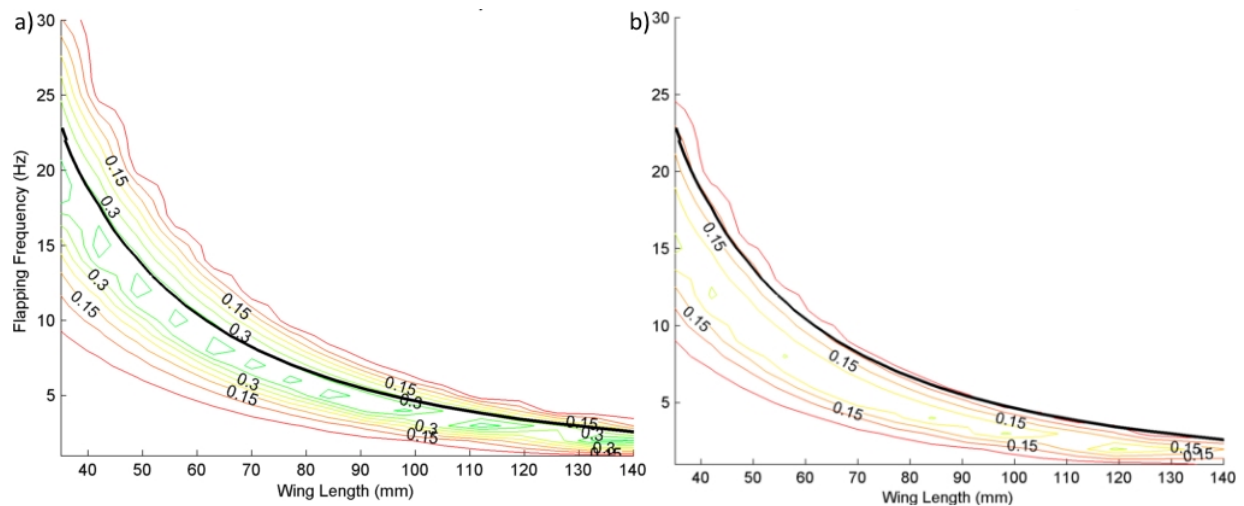


Figure 3.2: Difference between motor power and aerodynamic power: a) Ideal GM15 performance, b) with estimated 60% gearbox efficiency

produce high torque without a gearbox due to the large radius of the rotor. However, the rotor tends to have high inertia since it contains the permanent magnet elements, while the stator and windings remain stationary. At our size scale, these motors tend to be brushless and are popular for hobby aircraft. Unfortunately detailed specifications for these motors are not available and are based on how much thrust is generated with a prop of a given size. They are also designed for use with lithium polymer so they feature low windings resistance and high current draw, which caused issues in simulation. Pancake motors offer an inrunner design, with the large radius common to outrunner motors. This allows for low rotor inertia as well as a brushed design. While this solution seems optimal for our application. At the time of this survey the smallest brushed pancake motor available was from Micromo with a weight of 4.3 grams and could not generate sufficient power for liftoff.

Motor performance was evaluated in simulation based on operating voltage, stall torque, torque constant, winding resistance, motor damping, gear ratio, and gearbox efficiency. The available motor power was then calculated based on these parameters, as well as the impedance matching ratio between the winding resistance and the mechanical damping, represented as an equivalent resistance, due to internal frictional and aerodynamic drag calculated based on wing size and model kinematics following [48]. These kinematics are used to calculate lift using the aerodynamic model described in section 2.3. The difference in available motor power and required aerodynamic power to achieve the prescribed kinematics was then plotted against the wing length and flapping frequency. A black line was plotted to indicate system lift to weight equal to 1. Only operating points above this line allow for the system to lift off. Only two candidate motors were identified as a result of this simulation, the GM15 from Solarbotics and 0515A006B from Micromo/Faulhaber. Results for these motors are shown in Figures 3.2 and 3.3, showing an ideal and estimated gearbox efficiencies.

The GM15 is a brushed motor with a fully plastic 25:1 gearbox and a total weight of 1.2 grams. It is important to note the distinction between the different gearbox options for this motor.

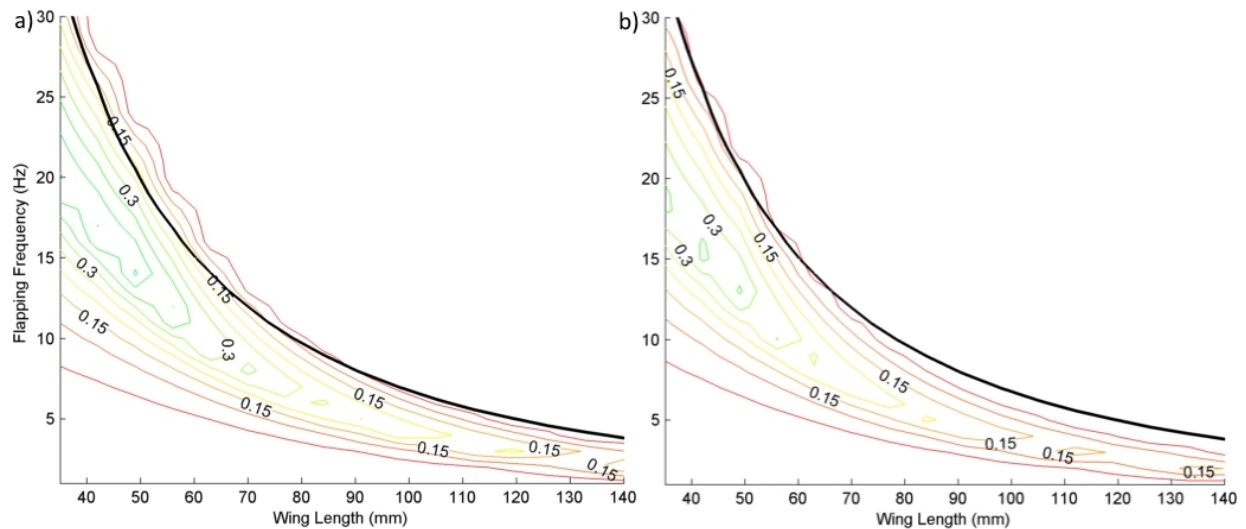


Figure 3.3: Difference between motor power and aerodynamic power: a) Ideal FH0515 performance, b) with estimated 80% gearbox efficiency

The standard version has a pulley shaft output is well constructed and fully back drivable [107]. The GM15A features a D shaft output, but the gearbox was highly prone to failure since it is not fully back drivable and uses a softer plastic material. Due to the reciprocal driving of the motor to generate flapping, backdriveability of the gearbox is desired for smooth operation and to avoid gearbox damage. While the GM15A operated smoothly in the forward direction, it experienced degraded performance in the reverse direction and switching directions could cause binding or failure of the gearbox. Unfortunately the GM15A was used to initial tests and prototype since the D shaft was more convenient for attachment of the wing assembly. The pins connecting the planetary gears to the carrier assembly, Figure 3.4, have half the diameter of those in the standard version and would often shear off during operation of the system. Switching gearboxes allowed the resonant spring stiffness to be increased from 2.8 to 18 N\*mm/rad. With the A version the gearbox failed frequently even with such a weak spring. The new gearbox has had no failures indicating that it could potentially tolerate even stiffer springs. The 0515B is a brushless motor with a bronze gearbox in a plastic shell with a 25:1 ratio and a total weight of 2.72 grams. A detailed comparison of motor specifications can be seen in Table 3.1. Although switching to this motor would more than double the weight of the vehicle, it was considered at the time before the standard GM15 had been discovered and seemed to be one of the only possible alternatives for improving the vehicle.

The result of the simulation is that gearmotors with high torque are selected. The two selected models have the advantage of a lightweight, high ratio gearbox. Figure 3.5 plots torque density versus weight for motors under 3 g, with gearmotors in red and motors in blue. The two identified models are marked with Xs. Two other candidates are clear, but did not perform as well in the impedance matching simulation, not crossing into the region of lift to weight greater than 1. However, motor characteristics may vary from the nominal spec sheet values and can be intermittently driven above their rated power. Therefore, these motors should be considered viable candidates for future work. It is clear that the small inrunner motors alone do not operate



Figure 3.4: GM15 two stage planetary gearbox showing a) gearbox output shaft with top annular gear, b) planet gear, c) pin connecting planet gear and carrier, d) carrier, e) sun gear connecting motor to gearbox, f) shell that holds down output stage, g) motor output shaft, h) GM15 motor, i) bottom annular gear

Table 3.1: Detailed specifications for candidate motors

Product	Solarbotics GM15	Micromo 0515A006B+06A 25:1
Design	DC Brushed	DC Brushless
Price	\$14.25	\$232.40
Weight	0.9 g + 0.3 g (gearbox) = 1.2 g	1.5 g + 1.22 g (gearbox) = 2.72 g
Gearbox	25:1 planetary - plastic	25:1 planetary bronze gears, plastic shell
Size	6 mm diameter, 20.1 mm length	5.8 mm diameter, 25.6 mm length
Rated Voltage (V)	6	6
No load speed (rpm)	2450 ± 350	1611 ± 12
Stall torque (N*mm)	6.8	10

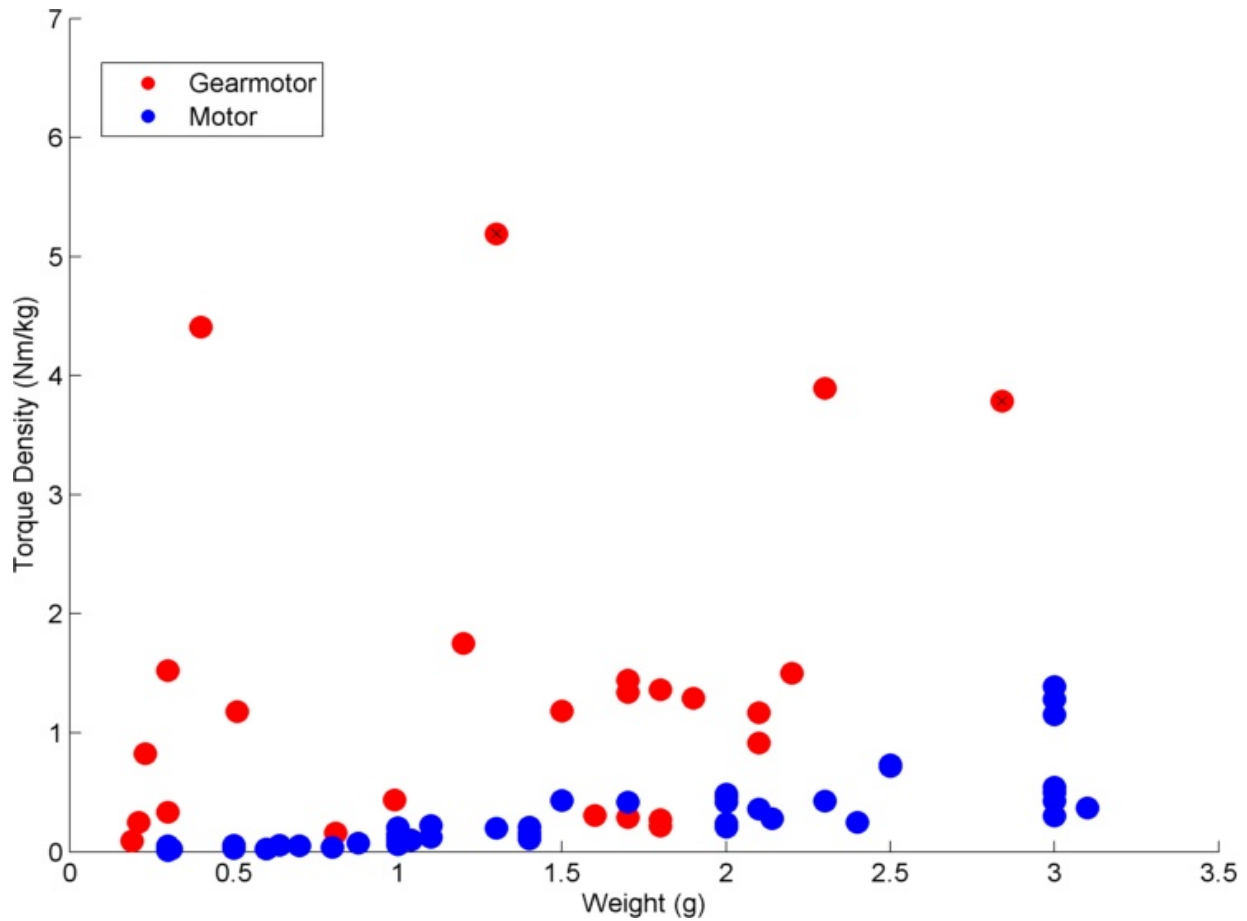


Figure 3.5: Plot of torque density versus weight for motors under 3 grams. Gearmotors are shown in red, while motors are shown in blue. The GM15 and 0515A are marked with Xs.

with high torque at low speed as is necessary to flap the wings. The steel gearboxes typically offered, often had larger weight than the motor itself, making them too heavy for our desired vehicle size. Using a 3D printed connector for the motor shaft and outer shell may make it possible to connect the GM15 gearbox to almost any other motor, another possibility for future work along with optimization of the gear ratio, which could also improve impedance matching and performance.

The GM15 is run with power electronics shown in Figure 2.3. LabVIEW code is used to generate the sinusoidal analog drive signal via a NI PCIe-6353 DAQ board. The signal is sent to a Syren10 motor driver, which boosts the voltage and power of the measured signal to drive the motor [108]. Although this driver would be too large to integrate into the vehicle, with a weight of 26 g, it has been used for its convenience and robustness. Driving of the motor can be accomplished with an op-amp circuit as done by Campolo et al. or with an H bridge circuit using MOSFETs or transistors, which could easily be made to conform to the size and weight requirements of the vehicle [52]. Designing and testing a custom, or small commercial, driver circuit remains future work tied to the task of fully integrating the vehicle.

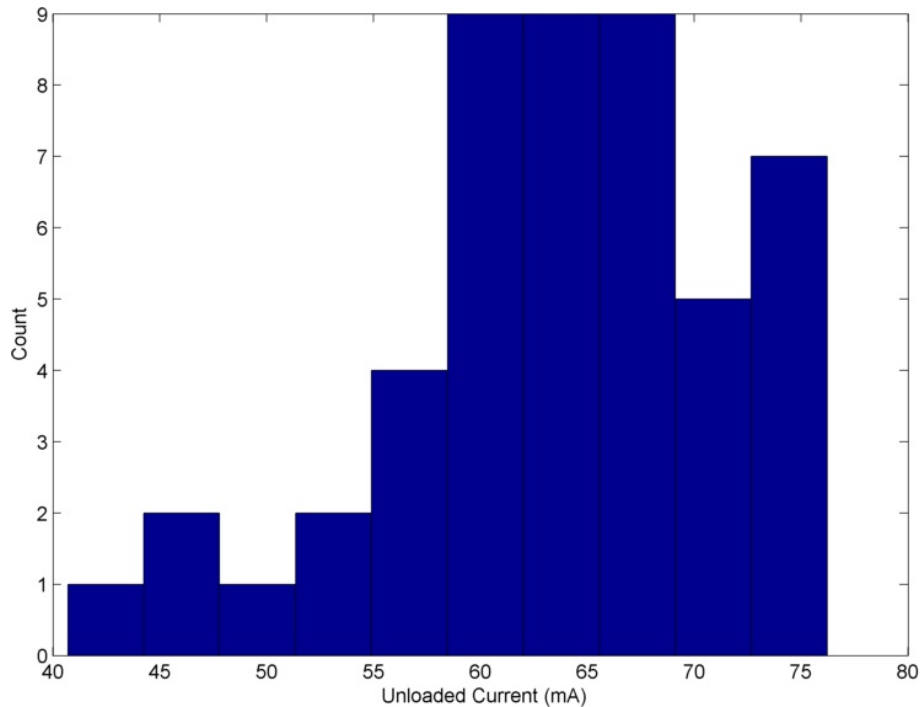


Figure 3.6: Histogram of unloaded current draw at 6 V for GM15 motors only.

### 3.2.1 GM15 Component Characterization

We see from initial testing that the performance of the GM15, with respect to no load speed, varies significantly. The rated value is 1550 rpm and the measured speeds ranged from 2100 to 2800 rpm. Since these motors are cheap and mass produced it is not unexpected that they are not well characterized and exhibit significant variation. Therefore, it is possible to improve system performance by measuring the performance of each motor and choosing those with the best performance for use in our system. Furthermore, the performance of the motor and gearbox will vary independently. Characterizing them separately allows for the best of each to be paired together resulting in a gearmotor with the highest possible performance.

Several methods were tested to directly measure torque production: lifting a weight, attachment to the torque sensor, and acceleration of a mass. However, the results were not as consistent as desired and the tests were time consuming. Speed testing using a non-contact tachometer (CyberTech tach-mtr-01) were done, but also seen to have significant variability. The chosen method was measurement of the unloaded current at 6 V operation averaged over one second. Since the motors are seen to have very similar electrical properties, measured resistance, unloaded current provides a direct measurement of the internal friction. Results for 50 motors are shown in Figure 3.6. The mean current is  $63.7 \pm 8.1$  ma. This differs significantly from the 200mA rating. Although the rated value is with the gearhead attached, we will see that this did not significantly change current draw in our tests. We see that about 10% of tested motors had current draw less than 55 mA and these are chosen for system fabrication. The percent increase in current draw between the best and worst motor was 87.22%. Gearboxes were tested attached to a single motor and measured for one second at 3 V. The draw of the motor was subtracted out to yield the

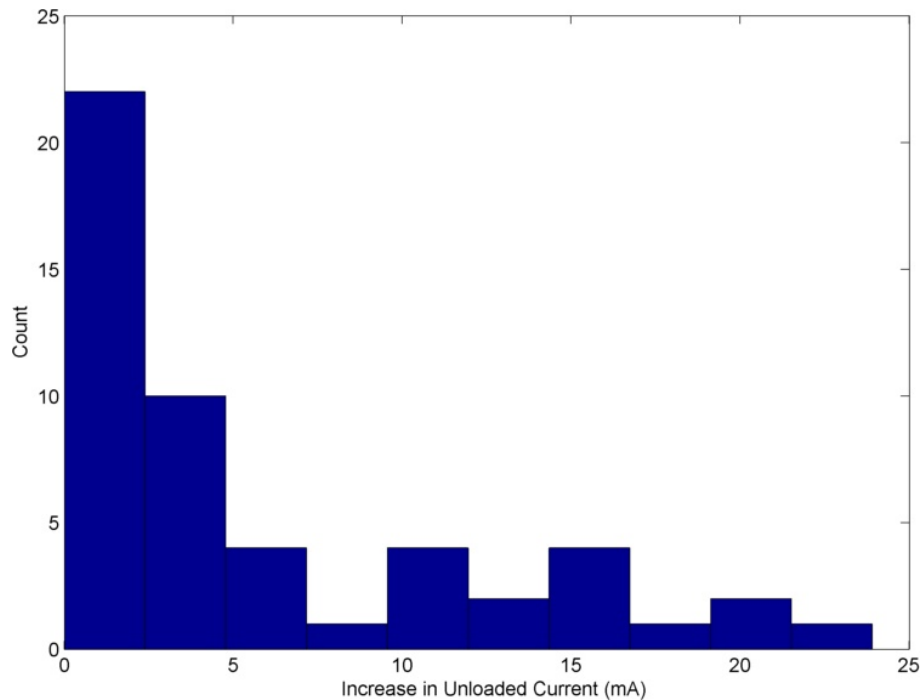


Figure 3.7: Histogram of unloaded current draw at 3 V for the GM15 25:1 plastic gearhead.

increase in draw due to the gearbox. 3 V was chosen due to a discontinuity in speed seen at 6 V operation. The gearbox would initially run at a lower speed, as verified by tachometer tests, and jump to a higher speed after a short period of time causing a similar discontinuity in current. Although this may affect the startup transient of the system, it is not expected to impact steady state operation. Results are shown in Figure 3.7. The gearhead adds a mean draw of  $6 \pm 6.5$  ma. However, in this case the majority, 63%, add a draw of less than 5 mA. While the majority of the gearheads have good performance, the difference between the best and worst is extremely high. These experiments indicate that testing and proper selection of gearmotor components is essential for ensuring fabrication of effective systems. This variation in system performance is visualized in the following figures. Figure 3.8 shows the rated performance of the GM15 with respect to torque, current, mechanical power, and efficiency. Figure 3.9 shows the worst case performance of the tested motors. We see that torque is similar, but the unloaded speed is higher resulting in larger torque output and that the unloaded current draw is lower resulting in higher efficiency. Figure 3.10 shows the best case performance of the tested motors with increased torque and unloaded speed combined with further decreased current demonstrating significantly higher performance than represented by the spec sheet. This improved performance is directly compared in Figure 3.11. We see that it is primarily the increase in operating speed that produces performance improvements by dramatically increasing the power curve of the system.

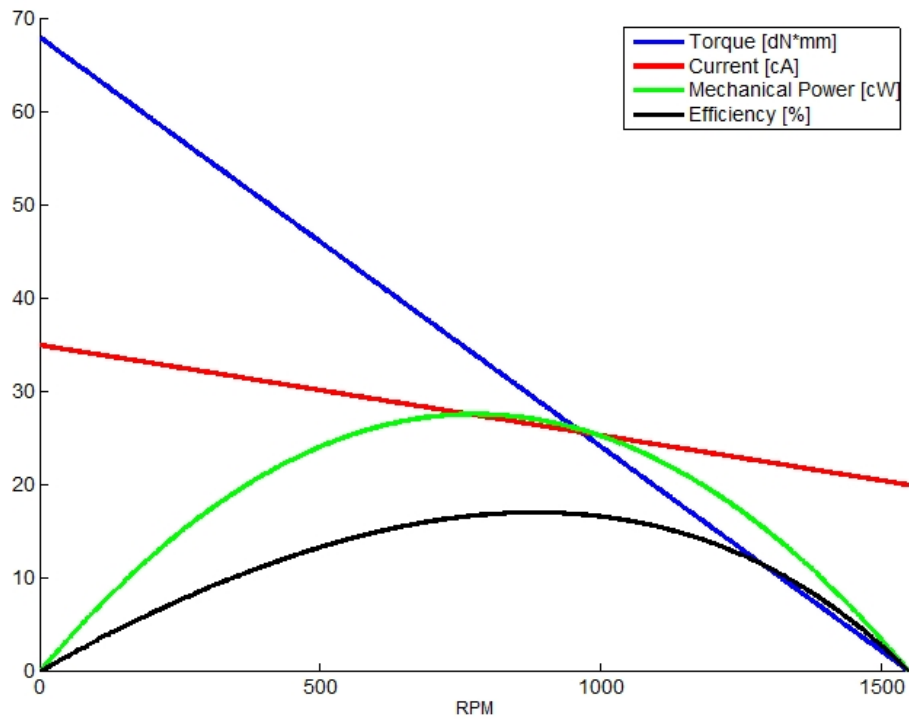


Figure 3.8: Rated performance of the GM15 with respect to torque, current, mechanical power, and efficiency.

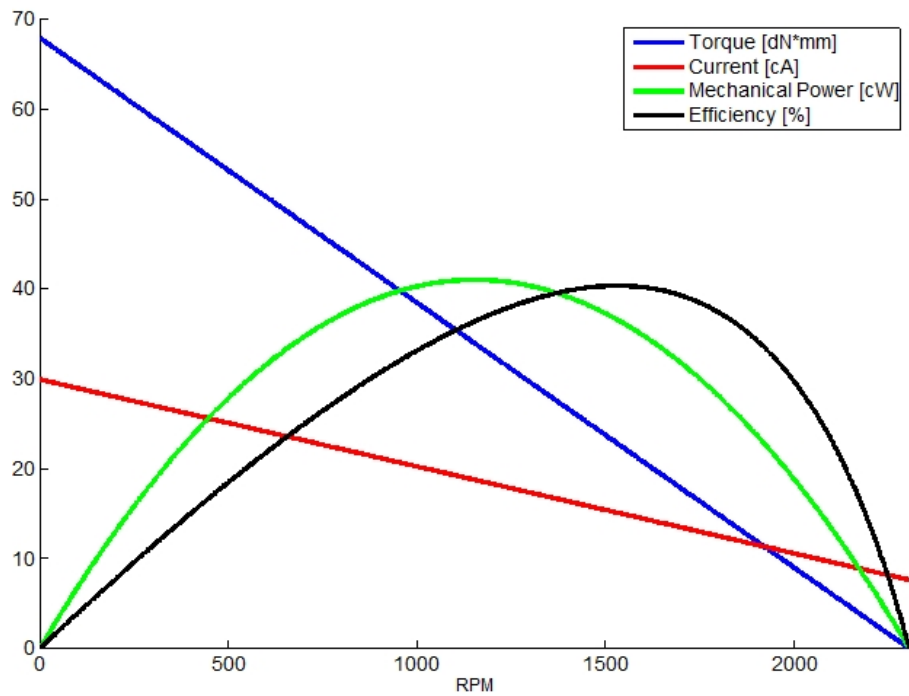


Figure 3.9: Worst case measured performance of the GM15 with respect to torque, current, mechanical power, and efficiency.

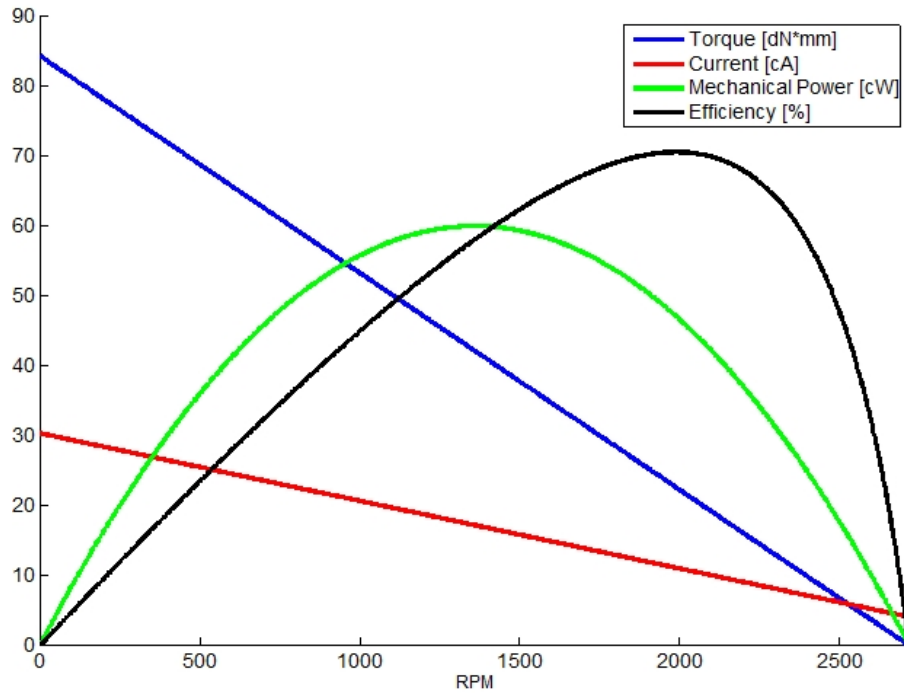


Figure 3.10: Best case measured performance of the GM15 with respect to torque, current, mechanical power, and efficiency.

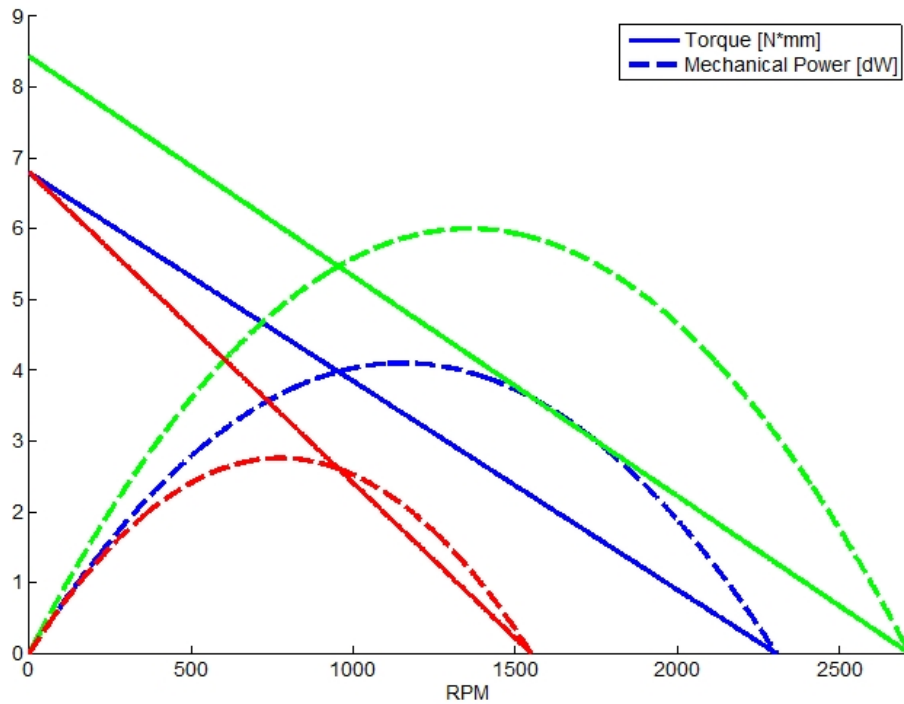


Figure 3.11: Comparison of GM15 performance. Red represents rated, blue worst measured, and green best measured.

### 3.3 Brushless Motor Usage

Although the GM15 provides remarkable torque density for its size, its main drawback is wear of the plastic gearbox. Although brushed motors are typically cited as having low life-span and high maintenance due to physical wear on the brushes, this has not been the case at the small size of the GM15. While switching to the standard gearbox has greatly improved the system performance and eliminated acute failures, the gearbox does wear over time. This is noticed with a decrease in power output, likely due to decreasing efficiency with wear. Another issue is the play in the output shaft that becomes worse with wear, and leads to out of plane stroke deviations during the flapping cycle. The current solution is to use a bearing to isolate the gearbox from off axis loading generated by the aerodynamic forces on the wing. However, another option that was considered was using brushless motors such as the Micromo 0515A006B06A, which has a bronze gearbox that is bearing supported, or using ungeared outrunner motors shown in Figure 3.12. Since outrunner motors are used for hobby aircraft, they lack detailed specifications and are often rated based on how much thrust they generate with a given propeller. The two motors Homefly 10-1-50T and HexTronik Brushless Outrunner 7700kv were both selected due to their small size, 1.5 and 2 g respectively.

Initial testing was performed with a basic sensorless brushless driver, the HK-30A from HobbyKing. Sensorless drivers use the back electromotive force (EMF) to estimate the motor operation speed and determine the commutation sequence. Maximum stall torque was measured as 1.02 mNm for the 0515, 0.43 mNm for the 50T, and 0.13 mNm for the Hextronik. This is much lower than expected for the 0515. However, the driver had problems consistently starting the motors, especially the Hextronik, which could lead to unreliable results for the stalled tests. Furthermore, the driver was not capable of consistently switching motor direction at speeds above 1 Hz and was abandoned. The ESC32 from AutoQuad was chosen as a replacement as it is open source and would allow for direct firmware modifications for high frequency switching needed for flapping. The two outrunner motors were no longer considered as they did not seem to offer sufficiency high torque densities for their size.

The ESC32 allowed for high frequency switching with modified firmware, but could not maintain consistent flapping amplitudes with an attached wing. The firmware was modified so that the motor was commanded to switch direction after a fixed number of commutation steps. This allows driving to be performed in open-loop analogous to driving the brushed motors. The driver settings were modified to make the controller more aggressive, but also to decrease the control effort, by reduced the PWM frequency and commutation period, to improve switching performance. The timing advance of commutation in electrical degrees was increased from 10 to a maximum of 30 or half a commutation cycle. The minimum commutation period allowed was increased from 50 to 400 microseconds. The number of microseconds to ignore back EMF after commutation was increased from 30 to 100. The voltage applied during motor startup was increased from 1.1 V to 6 V. The number of good, in order zero crossing of the back EMF before the motor is considered to be running was decreasing from 75 to 50. The number of missing zero crossings allowed before the driver disarmed the motor was increased from 48 to 75. The PWM switching frequency was decreased from 20 kHz to the minimum value of 4 kHz. The maximum commutation period allowed in microseconds was decreased from 12000 to 4000. These modifications allowed flapping of a wing up to 20 Hz, with maximum flapping amplitude

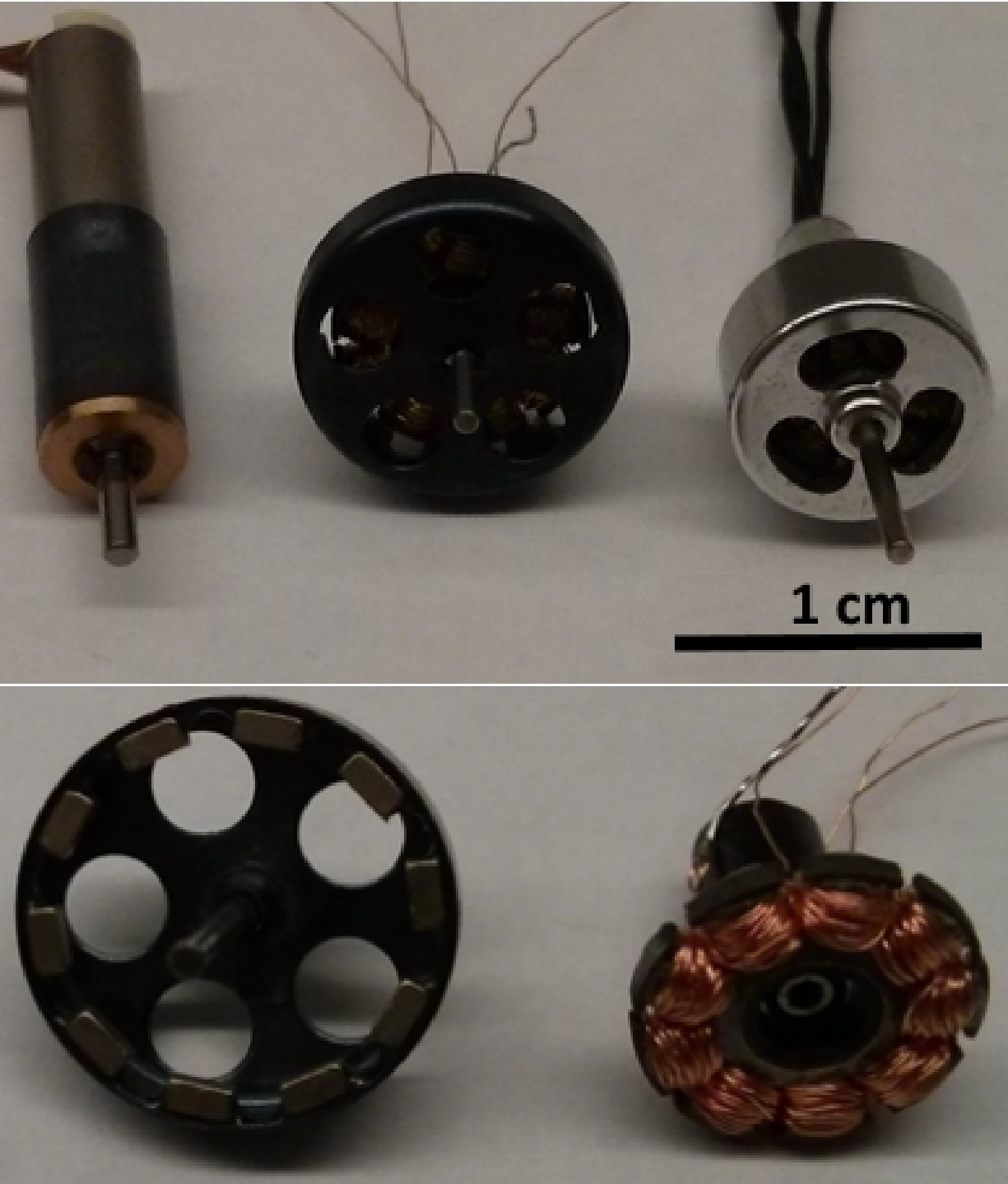


Figure 3.12: Brushless motors from left to right Micromo 0515A006B06A 25:1, Homefly 10-1-50T (1.5 g), HexTronik Brushless Outrunner 7700kv (2.0g). Dissassembled 10-150T shown below

close to 180 degrees. However, the full amplitude could not be maintained consistently with some strokes achieving full amplitude, while others had small amplitudes. Lift measurements were inconclusive as testing with the system appeared to excite a resonant mode of the force sensor resulting in unreasonable high force measurements. A guide wire test failed, but had issues with keeping the wires taught and balancing the aerodynamic torques on the wire carriage. Although it may have been possible to improve performance by developing custom commutation code, we chose to switch to a sensored brushless driver instead.

Use of a sensored motor driver was not able to produce reliable performance and damaged motors. The sensored driver uses Hall Effect sensors integrated into the motor to detect the rotor position to determine the commutation sequence. Such sensors are normally not available for small motors so they were added to the 0515 motor. Linear hall effect sensors (GMW EQ-730L), with 130 mV/mT sensitivity and fast response time of 2 s were utilized along with the MCBL 3002 Motion Controller V2.5 Sensored Brushless Position Controller from Micromo (MCBL3002SRS). Even with the high sensitivity sensors, the signal from the rotor was not strong enough with the sensors attached directly to the case. Three notches were filed into the case to allow for consistent mounting and increased signal strength from the decreased distance between the magnet in the rotor and the sensor. Switching of the motor with no load was successful, but shortly after the motor failed. Increased winding resistance suggested thermal failure of the motor.

There were several reasons for such a failure to have occurred, even with the motor unloaded. The motor rating provided on the spec sheet, especially the maximum rated current, indicated that the thermal resistance of the case was reduced by 55% in testing. This is a significant reduction of case resistance, which I was told by Micromo engineers was a feature of their test fixture that they could not provide specifics on. Therefore, the data from the spec sheet did not represent performance of the motor without a significant heat sink. Misalignments of the hall sensors could also have contributed to thermal failure. Finally, other groups have shown that commanding position control of the entire flapping cycle significantly increased the power required compared to open-loop driving [57, 58, 82]. The 7.5 g motor driven FWMAV from Purdue uses a similar motor from Micromo that includes an encoder and custom brushless driver to achieve flapping motion based on position control. However, the motors still fail frequently and the system has not had a clear demonstration of lift off. It is also possible that at this scale the thermal performance of brushed motors exceeds that of brushless. For brushed motors the heat generated in the windings is dissipated evenly to the case by convection generated by spinning of the rotor. In the brushless case the windings are embedded in an epoxy layer attached to the case. Heat is dissipated by conduction through the epoxy and casing. However the epoxy likely increases the thermal resistance of the steel casing and may not result in even heating.

The Delfly provides an example of successfully utilizing a brushless motor for an FWMAV [49]. However, the motor is run continuously with flapping motion is generated with the crank rocker transmissions and had to be modified extensively. The motor is a modified version of the Homefly 10-1-50T, which uses a 9 phase, 10 pole design to reduce cogging torque and allow for consistent operation at lower speeds. In development with two companies a custom motor driver that included higher accuracy EMF measurement and filtering was developed that allow for consistent operation despite the uneven loading during the flapping cycle generated by the transmission. Finally two stage gearing was used to achieve a 20:1 ratio between the motor

Table 3.2: Maximal performance for 20 Hz actuation

	GM15	Resonant Actuator
Torque ( $N \cdot mm$ )	$4.04 \pm 2.00$	$11.87 \pm 0.57$
Efficiency (%)	$4.29 \pm 0.45$	$48.14 \pm 1.6$
Pk-Pk Amplitude ( $^\circ$ )	$100.0 \pm 7.6$	$154.7 \pm 4.7$
RMS Voltage (V)	$4.53 \pm 0.06$	$4.70 \pm 0.08$
RMS Current (A)	$0.299 \pm 0.016$	$0.222 \pm 0.006$

output and the input link to the transmission. This example shows the difficulty of utilizing a brushless motor for a non-standard applications. Despite still being run continuously, significant modifications to the motor and drive electronics were needed to allow for low speed operation with the uneven loading generated by the flapping transmission.

### 3.4 Resonant Actuation

The resonant actuator is based on work by Campolo *et al.* [48, 52, 53], where a torsional spring was connected in parallel with the shaft of a brushed DC motor. Addition of elastic energy storage to flapping transmission mechanisms has been tested in work by Lau *et al.* as well as Beak *et al.*, although these systems have not been capable of liftoff [60, 61]. Recent work by Roll *et al.* demonstrates liftoff of a vehicle using a custom electromagnetic actuator that achieves resonance with a virtual magnetic spring [109]. However, analysis of the actuator isolated from nonlinear aerodynamic loading has never been performed. Such analysis is critical for improved modeling of the actuator and comparison to systems in the literature. Furthermore, it allows researchers to determine if their work could benefit from this actuation technique, extending its use to other applications.

The resonant actuator and gearmotor were characterized using a proof mass, a purely inertial load, in order to isolate the system from the complex aerodynamic loading generated by the flapping wing. The mass is chosen to have a similar moment of inertia to the FWMAV wings in [56]. They were driven bi-directionally with a sinusoidal voltage to produce periodic motion with a constant amplitude. First, the driving frequency was swept from 10 to 30 Hz to identify the resonant frequency where load amplitude was maximized. Both systems were then characterized at 20 Hz with successive tests at increasing voltage amplitudes. The frequency range was set by the torsional spring stiffness, an average of  $18 N \cdot mm/rad$  over a  $180^\circ$  displacement. The spring was fabricated from 1080 steel wire and 87%-118% lighter than equivalent commercial springs [110]. This stiffness can be varied, although stiffening the spring would increase loading on the gearbox and could lengthen the startup transient, or the number of cycles before maximum amplitude is achieved.

Input power was calculated as the product of root-mean-square (RMS) current, measured using a current sensor (ASC712-30A), and RMS voltage, measured across the motor with a DAQ board (National Instruments PCIe-6353), at a resolution of  $40 \mu W$ . The electrical characteristics of the winding were considered purely resistive as inductance was negligible. Power factor was

approximately one as the current and voltage signals were seen to be in phase. Proof mass kinematics were measured from high-speed video (PCO Dimax). Mechanical power was calculated using inverse dynamics analysis as follows: angular velocity and acceleration are derivatives of load position, effective speed is the product of average angular velocity and frequency, torque is the product of load inertia and angular acceleration, power is the product of torque and angular velocity as shown in equation 3.2. Efficiency is the ratio of mechanical power to electrical power input

$$\eta = \frac{P_{mech}}{P_{el}} = \frac{I\omega}{I_e V + I_e^2 R} \quad (3.1)$$

where  $I$  is the load inertia,  $\omega$  is the angular velocity,  $I_e$  is the electrical input current,  $V$  is the applied voltage, and  $R$  is the resistance. Maximal performance is shown in Table 3.2. Calculations were based on 76 steady state cycles.

$$\begin{aligned} \theta(t) & \text{ measured} & (3.2) \\ \omega(t) & = \dot{\theta}(t) \\ \alpha(t) & = \ddot{\theta}(t) \\ \tau(t) & = I\alpha(t) \\ P(t) & = \tau(t)\omega(t) \end{aligned}$$

$$\text{Effective speed} = \bar{\omega}(t)f$$

Full comparisons of the gearmotor and resonant actuator are shown in the following figures. Note that this data is from an initial set of experiments and is not exactly represented of the final values presented, but provides additional information of the system performance across a range of frequencies and amplitudes. First we compare the frequency sweep. Figure 3.13 shows the thermal power for the gearmotor, calculated as  $I^2 R = IV$ . Approximately equal dissipation is seen over the tested range as expected since the motor is operated at constant voltage. Once the spring is introduced as seen in Figure 3.14 there is a clear minimum power draw at the resonant frequency. The two actuators are compared in Figure 3.15 with respect to torque, effective speed, mechanical power, and efficiency. We see that the gearmotor acts as a low pass filter. The resonant actuator displays several resonant peaks. Efficiency and speed appear to peak at 17 Hz, while torque and power peak at 21 Hz, with a sharp drop off afterwards. Just the efficiency curves are shown in Figure 3.16 so additional detail can be seen.

The following data is for the amplitude sweep. At the identified resonant frequency, both systems are run at increasing voltage amplitudes. Figure 3.17 shows the performance of the gearmotor with respect to motor torque, current, mechanical power, and efficiency. Although the system is able to produce increasing torque with increasing applied voltage the output is low and efficiency plateaus around 5%. Figure 3.18 shows the performance of the resonant actuator. The system provides increased torque and mechanical power output, just over 1 W compared to 0.35 W from the gearmotor alone. However, the most important feature is that this is accomplished with over 45% efficiency. The extreme difference in electrical power and therefore thermal losses generated by the two systems is highlighted in figure 3.19.

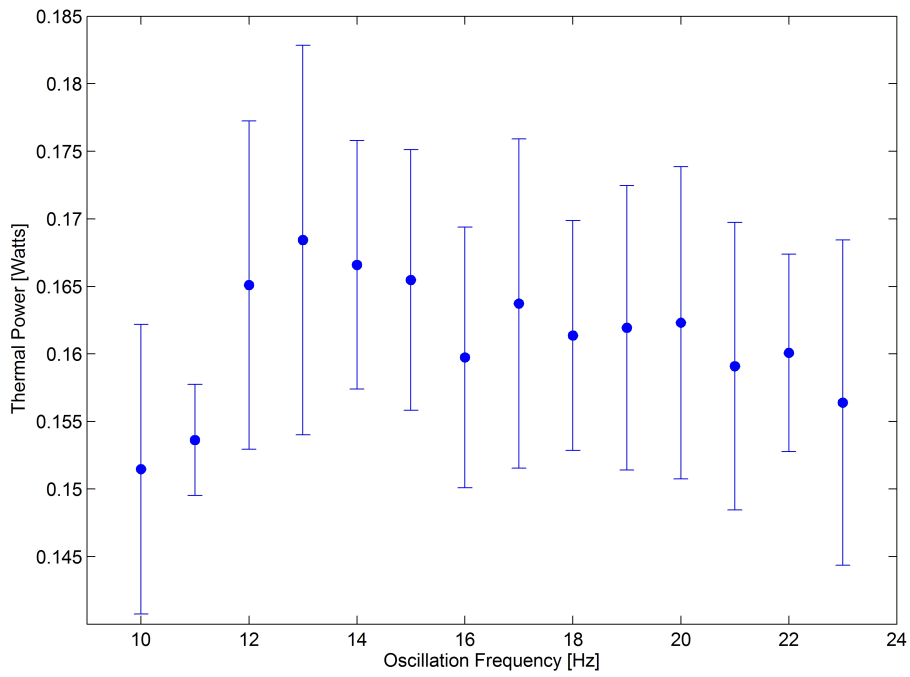


Figure 3.13: Electrical Power or thermal losses for the gearmotor during frequency sweep.

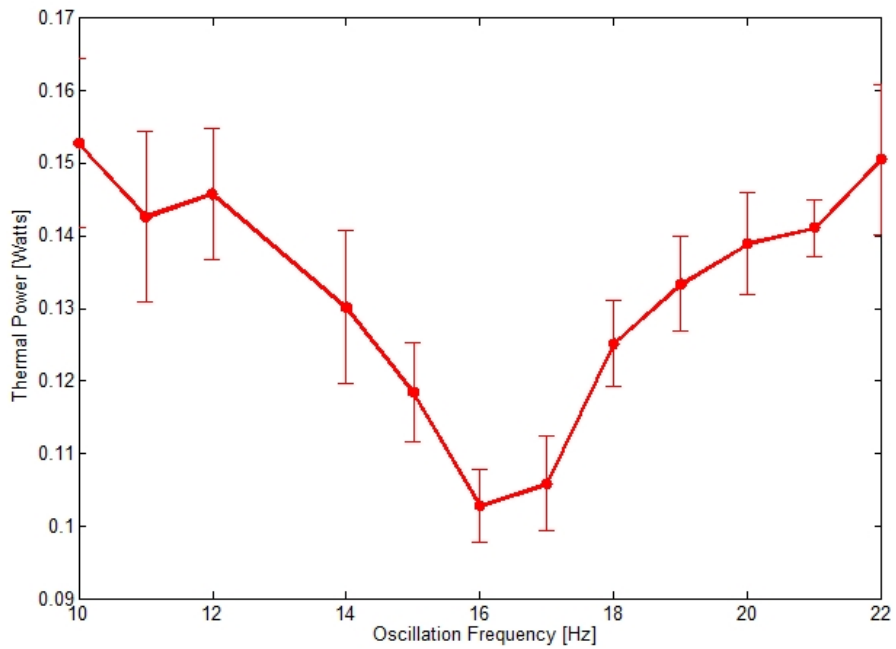


Figure 3.14: Electrical Power for the resonant actuator during frequency sweep.

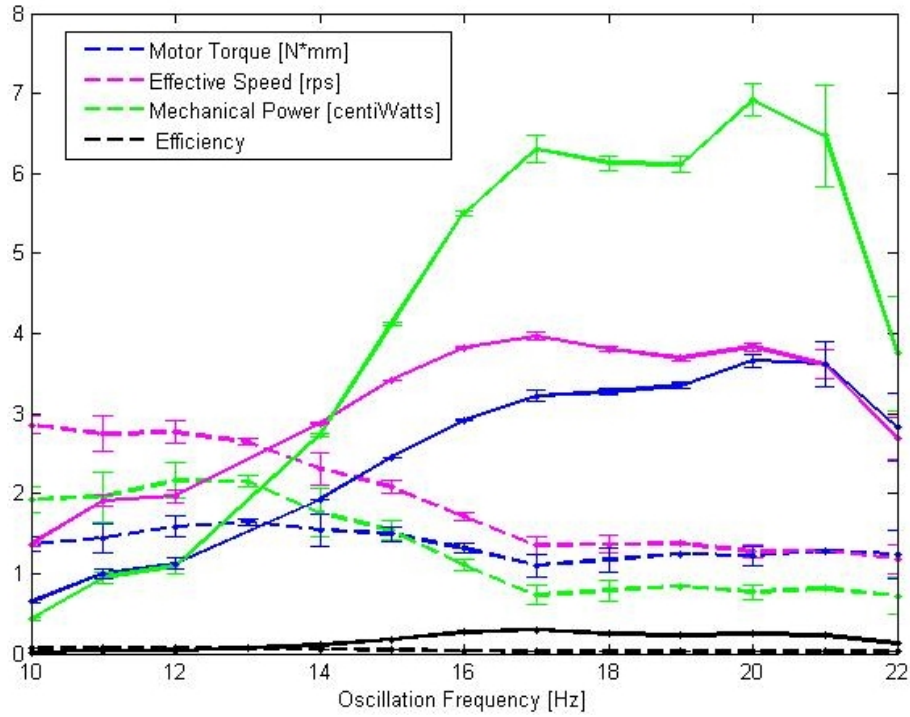


Figure 3.15: Comparison of torque, effective speed, mechanical power, and efficiency for the gearmotor and resonant actuator across frequencies.

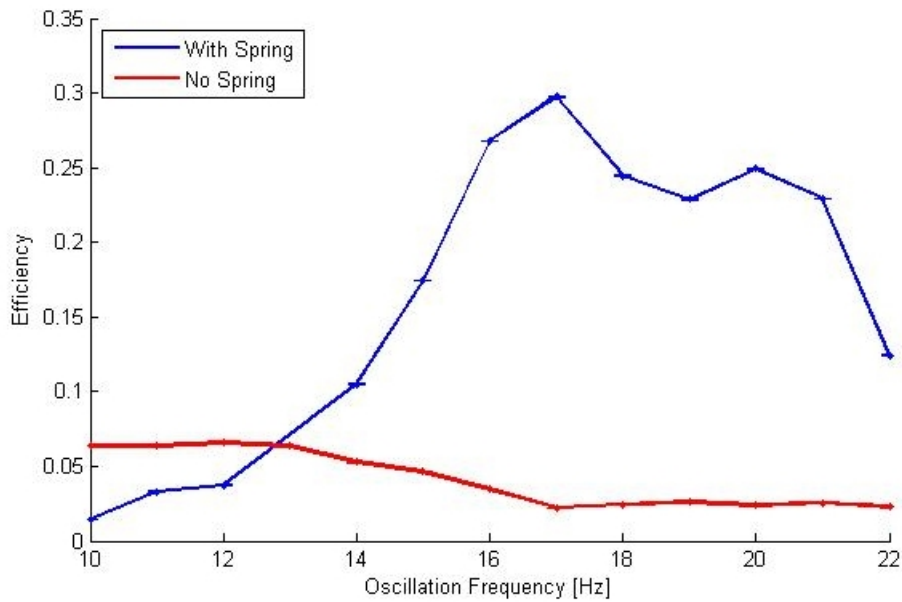


Figure 3.16: Comparison of efficiency for the gearmotor and resonant actuator across frequencies.

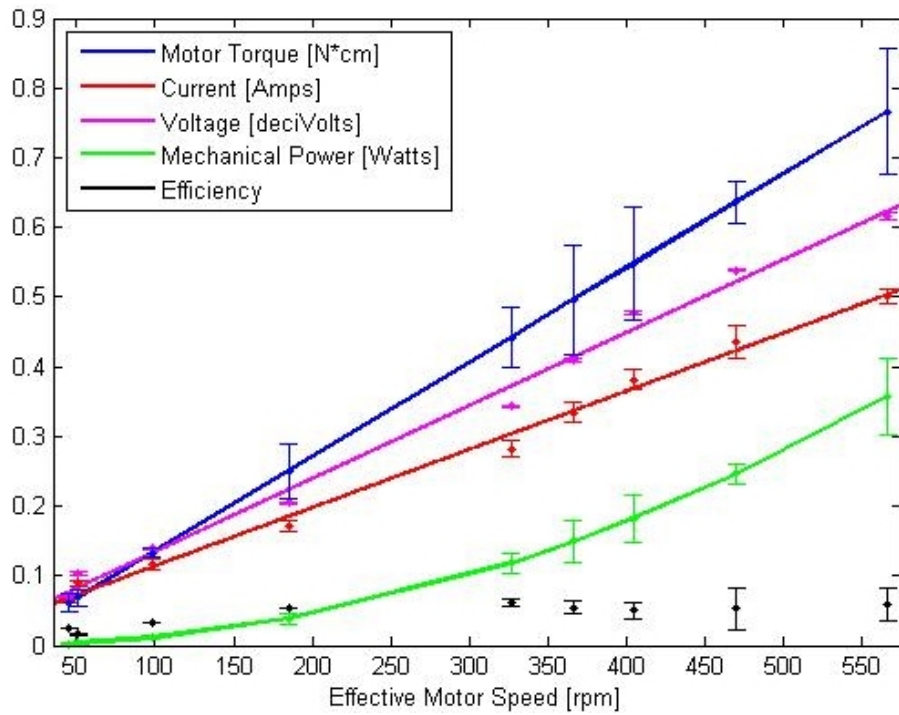


Figure 3.17: Performance of the gearmotor with respect to motor torque, current, mechanical power, and efficiency for 17 Hz operation at increasing voltage amplitudes.

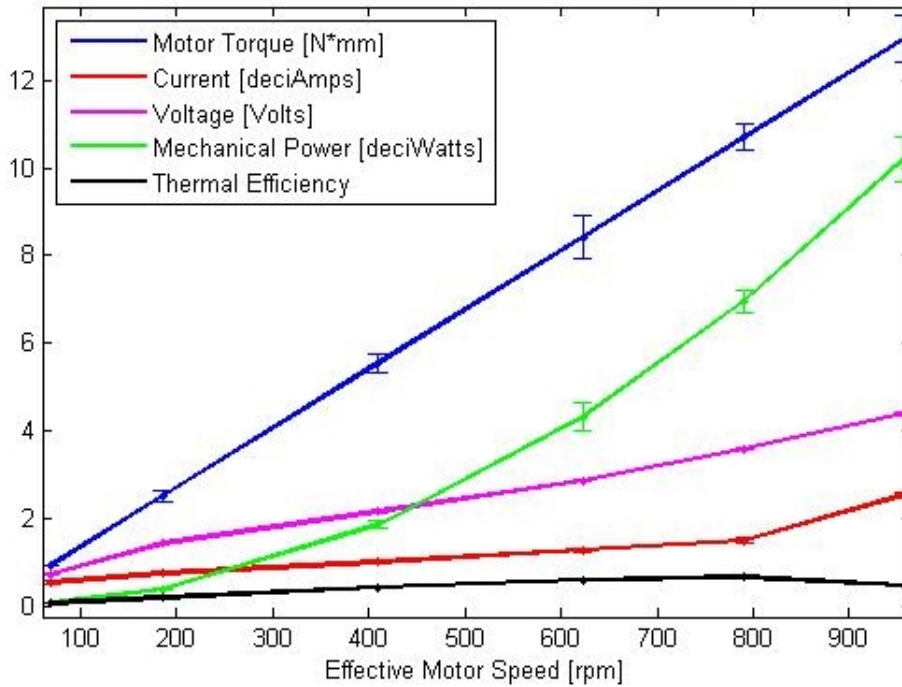


Figure 3.18: Performance of the resonant actuator at 17 Hz with increasing voltage amplitudes.

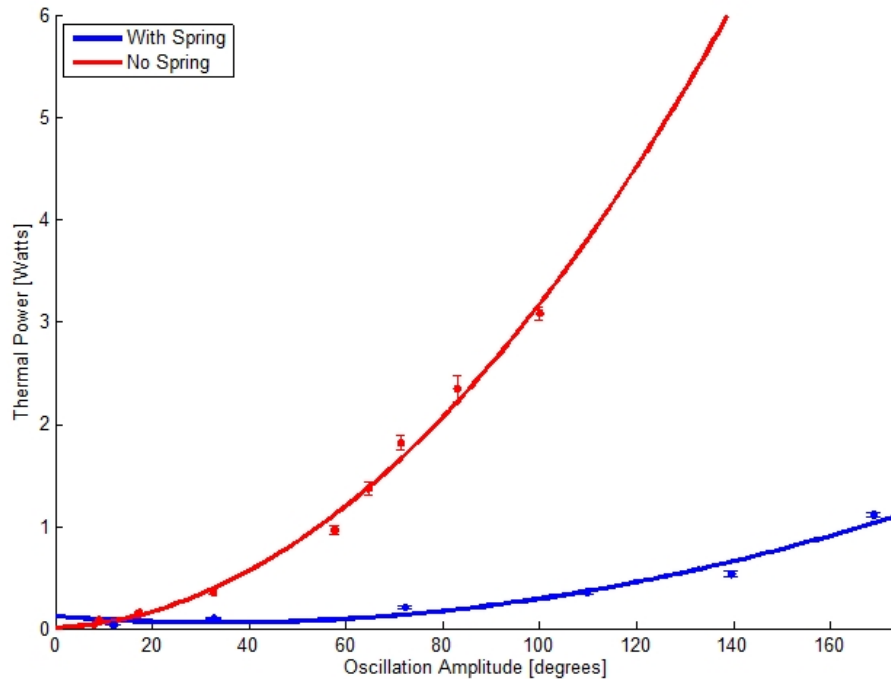


Figure 3.19: Comparison of electrical power or thermal losses between the two actuators at increasing voltage amplitudes.

The AC steady-state gearmotor data closely matches the DC ratings, although maximum torque is achieved with high amplitude oscillations instead of at stall. However, load position was not consistent and increasing the voltage above 4.5 V did not increase load amplitude. The resonant actuator produced 193.8% more torque than the gearmotor and achieved consistent and symmetric high amplitude oscillations. The resonant actuator achieved over 40% efficiency for peak-to-peak oscillation amplitudes above  $32.75^\circ$ , indicating that the spring effectively stores the energy to overcome inertial loading. Furthermore, the mechanical and electrical impedances of the load and motor were well matched. In the case of maximum power transfer, occurring at equal impedances, mechanical power is equal to the thermal losses as stated by the maximum power transfer theorem for linear networks [48]. This agrees with similar results from Campolo et al. showing over 45% dynamic efficiency for a resonant actuator driving a model wing [53].

Power density, torque density, and effective operating speed are used to compare the actuators as shown in Table 3.3. Although the GM15 motor achieved high power density, its coreless inrunner design provides low torque at high speed. A large gear ratio was needed to produce high torque at moderate speeds required for the flapping task. Metal gearboxes are commercially available and offer high efficiency, 78% for a 25:1 ratio [111]. However, their weight is prohibitive and significantly lowers the actuator power density. The 25:1 plastic gearbox of the GM15, despite a lower efficiency of 60% [54, 107], improves power and torque density by 66.8% compared to the metal option. The resonant design increased torque and power density by 161.1% and 666.8%, respectively. The speed is also increased by 193.7%, allowing the FW-MAV to generate more lift with larger wing stroke amplitudes. Furthermore, these performance improvements were achieved with over 40% efficiency and 25.8% less current, as stored elastic

Table 3.3: Maximal performance comparison for 20 Hz actuation

	GM15 Motor	GM15 Gearmotor	Metal Gearmotor	Resonant Actuator
Weight (g)	0.9417	1.169	2.535	1.316
Power Density ( $W/kg$ )	263	127	76	974
Torque Density ( $N \cdot m/kg$ )	0.29	3.45	2.07	9.02
Effective Speed (RPM)	8775	351	351	1031

energy drove acceleration of the load. The motor is estimated to have a peak efficiency of approximately 70 % from experiment. Given the peak measured efficiency of the system is 48%, this indicates that the gearbox efficiency may be as high as 68.8 %. Therefore the system losses are due to the motor and gearbox efficiencies, with the elastic energy storage in the spring occurring without measureable losses. This significantly reduced heat production, allowing the system to sustain peak output for longer durations. Finally, characterization of the actuator with standard metrics allows researchers to directly determine if it could improve the performance of their system.

### 3.5 Power Density

Power density is a proposed metric for comparing the performance of actuators in engineered systems as well as to biology, with data compiled in Table 3.4. Biological muscle is an elastic actuator capable of storing energy, reducing the inertial cost of periodic limb motion. Despite functional similarities, differences are seen between the muscle of the hummingbirds, insects, and cockroaches. On the other hand, the fraction of the body weight devoted to power muscles remains relatively consistent across organism body masses spanning four orders of magnitude. Actuators in robotic systems achieved on average 340% higher power density than their biological counterparts. However, the method of calculating these values produces misleading results. While muscle effectively fulfills the role of a battery, electronics, and actuator, calculations for robotic systems were based on the power actuator mass alone, excluding the weight of transmission elements and steering actuators. It was not possible to rectify these calculations based on published data.

The actuation principles vary amongst robotic systems: Delfly uses a brushless outrunner motor customized to reduce cogging torque, Robobee uses a piezoelectric bimorph, and DASH uses a commercial brushed motor. Our resonant actuator and piezoelectric bimorph produce bi-directional motion to directly drive the wing, although in each case a transmission is still used for torque or displacement amplification. Each wing has its own actuator allowing for differential motion to control the vehicle. Both the Delfly and DASH use large spur gears to increase output torque and include additional transmission mechanisms to convert continuous rotary motor output to limb motion. A single motor drives limb motion, while steering is achieved with additional actuators. Actuator mass fraction varies by system complexity. The Delfly is untethered carrying a battery, necessary electronics, and includes a camera for vision-based autonomy. DASH is also untethered, but lacks sensors for autonomy. Our vehicle and the Robobee are tethered with

Table 3.4: Maximal actuator power densities

	Task	Body Mass (g)	Percent Actuator Mass	Power Density (W/kg)
<b>Biological</b>				
Hummingbird [112] <i>Lampornis clemenciae</i>	Hover	8.4	29.0	309
Hummingbird [112] <i>Archilochus alexandri</i>	Hover	3.0	29.0	228
Moth [20, 113] <i>Manduca sexta</i>	Hover	1.52*	22.35	90
Fruit Fly [114, 115] <i>Drosophila melanogaster</i>	Hover	0.001*	30.0	80
Cockroach [116, 117] <i>Blaberus discoidalis</i>	Run	2.6	20.4	19-25
<b>Robotic</b>				
<b>CMU FWMAV (this study)</b>	<b>Hover</b>	<b>3.22</b>	<b>58.49</b>	<b>974</b>
Delfly II [49]	Hover	16.07	9.33	1000
Harvard Robobee [64, 65]	Hover	0.08	66.67	400
Berkeley DASH Hexapod [102]	Run	16.20	19.14*	105

\*Values calculated to the best of our ability using available data

off-board battery, electronics, and sensors.

Although our actuator and the brushless motor of the Delfly achieve high power density, the bio-inspired resonant actuation principle has several key advantages that reduce vehicle weight and complexity. Our vehicle is fully controlled by differential motion of the two wing actuators, while Delfly uses a power actuator to drive the wing stroke and two steering actuators to control pitch and yaw. Furthermore the crank-rocker transmission that converts motor rotation to reciprocal wing motion increases system weight, complexity, and lowers efficiency compared to the direct drive approach. Due to the lack of elastic elements, energy from wing deceleration cannot be recovered.

In this section we have quantified peak actuator output, which can only be achieved for limited time periods as heating exceeds the thermal dissipation capabilities of the motor. The following sections detail the development of a thermal model that predicts operating limits that allow for sustained hover, while avoiding damage to the actuator.

### 3.6 Thermal Modeling

Despite the benefits of resonant actuation, the capacity to dissipate thermal losses fundamentally limits motor performance. Therefore, maximizing output results in a thermal management problem. Although motors are commonly used in robotic systems, thermal considerations are often neglected when they are operated continuously within the motor specifications. However, thermal behavior is critical when intermittent, high-power operation is desired. While early studies focused on continuous operation of industrial-sized devices [118, 119, 120], recent work has addressed intermittent operation for motors at the 100 gram scale [121, 122]. The main source of thermal energy is Joule heating of the motor windings produced at a rate of  $I^2R$ , where  $I$  is the input current and  $R$  is the winding resistance. In large systems this is the dominant heat source and heat flow is limited by low air-gap convection due to internal laminar flow [123]. However, heat transfer through the motor varies substantially across designs and size scales [124].

The motor in this study weighs 1 gram, two orders of magnitude smaller than those previously characterized, and has been used in several miniature robotic systems [51, 54, 125, 126]. A second-order lumped parameter approach was used for the thermal model [93, 127]. Experimental model parameter fitting identified effects of variable winding resistance and bushing friction. Furthermore, high rotor velocities were found to substantially increase air-gap convection. The addition of a heatsink, which increases the surface area to volume ratio of the motor, was also included. While previous studies used temperature measurements from internal components, the following procedure uses only case temperature for fitting. The developed model is validated for dynamic operation of the FWMAV, used to predict safe operating limits, and to optimize a heatsink. This new small scale model and training approach can be applied to accurately characterize micro-motors used in miniature robotic systems.

Heat flow through the actuator was modeled as a second-order lumped parameter thermal circuit shown in Figure 3.20(a). The main input was Joule heating, produced at a rate of  $I^2R$  in the windings. Bushing friction was identified as a significant secondary source, produced linearly at a rate of  $\omega m$  where  $\omega$  is the motor speed. The bushing directly contacts the case and shaft, but no significant conductive heat transfer occurs to the windings due to the plastic commutator

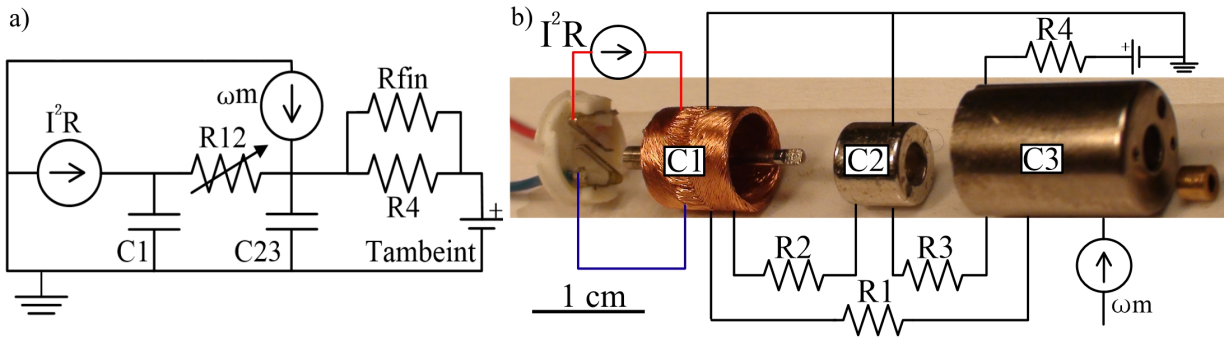


Figure 3.20: a) Reduced, lumped parameter, thermal circuit model of a DC motor with attached fin. b) Disassembled motor showing brushes, rotor windings, magnet, case, and bushing (left to right). Annotations indicate physical representation of the full thermal model, which includes distinct thermal bodies for each motor component and resistances between all bodies.

plate. Therefore bushing friction is treated as a heat input to the case. Each thermal body was modeled as a capacitor and heat flow between bodies as resistors as shown in Figure 3.20(b). Capacitance was estimated from measured component mass and specific heat capacity for each material. The dominant thermal resistances are convective, expressed as

$$R_{conv} = \frac{1}{hA} \quad (3.3)$$

where  $A$  is the relative surface area and  $h$  the heat transfer coefficient based on geometry and fluid flow [93]. Although the convective resistances from the windings to the magnet and the case vary due to differences in geometry, they are difficult to differentiate experimentally. The model combines the magnet and case into a single element, neglecting the conductive resistance between them. The resistance from the windings to this element are then treated as a single resistor. This circular flow travels over the internal cylindrical surfaces in a manner analogous to parallel flow over a flat plate. Therefore, this resistance was modeled as convection to a flat plate with the assumption that flow reaches a steady state velocity profile over each stroke due to the high gear ratio. High rotor velocities are expected to improve air-gap convection by increasing the contribution of forced convection. Forced convection dominates natural convection when the Archimedes number is much smaller than one [93]. At hover, the FWMAV has an effective speed of 841 rpm and an Archimedes number of  $1.37 \times 10^{-4}$ .

Convection from case to atmosphere was conservatively modeled as free convection, representing worst case performance where air around the motor is stagnant. Therefore, a heatsink, or fin, can improve case convection by increasing relative surface area. The heatsink resistance was added in parallel with the convective resistance from the case to atmosphere. This assumes that the heatsink and its connection to the case does not decrease overall flow from the case itself. If the heatsink resistance is too high, the model behaves as if there was no heatsink. Estimated model parameters are listed in Table 3.5.

Table 3.5: Thermal circuit model parameters

Symbol	Parameter	Estimate	Tuned
$R_{12}$	Windings to case & magnet	201.58	33.29
$R_4$	Case to atmosphere	622.37	154.76
$R_{fin}$	Heatsink resistance	9.88	467.38
$C_1$	Winding thermal mass	0.048	0.057
$C_{23}$	Case & magnet thermal mass	0.375	0.381

### 3.6.1 Model Parameter Fitting

The accuracy of lumped parameter models relies on experimental parameter fitting [123]. In order to isolate speed-dependent effects, a dynamometer was created by connecting two motors as shown in Figure 3.21 and 3.22. The left side, drive motor, was used to spin the right side, sensing motor, without powering it. The case temperature of the sensing motor was measured with a non-contact thermometer and the operating speed measured with a tachometer. The only modification to the motor was a spot of black paint, which increased the emissivity of the steel case for accurate temperature measurements. Previous studies relied on temperatures recorded from internal components for characterization [122]. However, it was not possible to modify the small motor to do so without significantly altering its thermal properties. Following, experimental fitting of parameters for temperature dependent winding resistance, bushing friction, and speed dependent forced convection are discussed.

### 3.6.2 Temperature Dependent Winding Resistance

Joule heating of the motor windings is expressed as

$$h(t) = I(t)^2 R(1 + \alpha(T_w(t) - T_0)) \quad (3.4)$$

where  $I(t)$  is the current,  $T_w(t)$  is the winding temperature, and  $R$  is the winding resistance at  $T_0 = 25^\circ\text{C}$ . The temperature coefficient of resistance  $\alpha$ , is typically assumed from material properties to be  $3.93 \times 10^{-3}$  for copper [128]. While this is sufficiently accurate for large systems where  $I > 1 \text{ A}$  and  $R < 1 \ \Omega$ , for our system the resistance term dominates since  $I < 0.3 \text{ A}$  and  $R > 12.5 \ \Omega$ . To improve accuracy,  $\alpha$  was measured experimentally over a relevant range of temperatures, 25 to  $155^\circ\text{C}$ , using an oven and determined to be  $3.42 \times 10^{-3}$ .

### 3.6.3 Bushing Friction

Friction between the motor shaft and supporting bushing was found to be a significant secondary heat source. This effect was characterized by running the drive motor at constant speeds and measuring the temperature of the sensing motor, which was connected to the power supply in high impedance mode to prevent current from flowing due to the back electromotive force. Experimental data is shown in Figure 3.23. The relationship between steady state temperature and speed was linear ( $R^2 = 0.99$ ) over the tested range. This effect was added to the circuit model

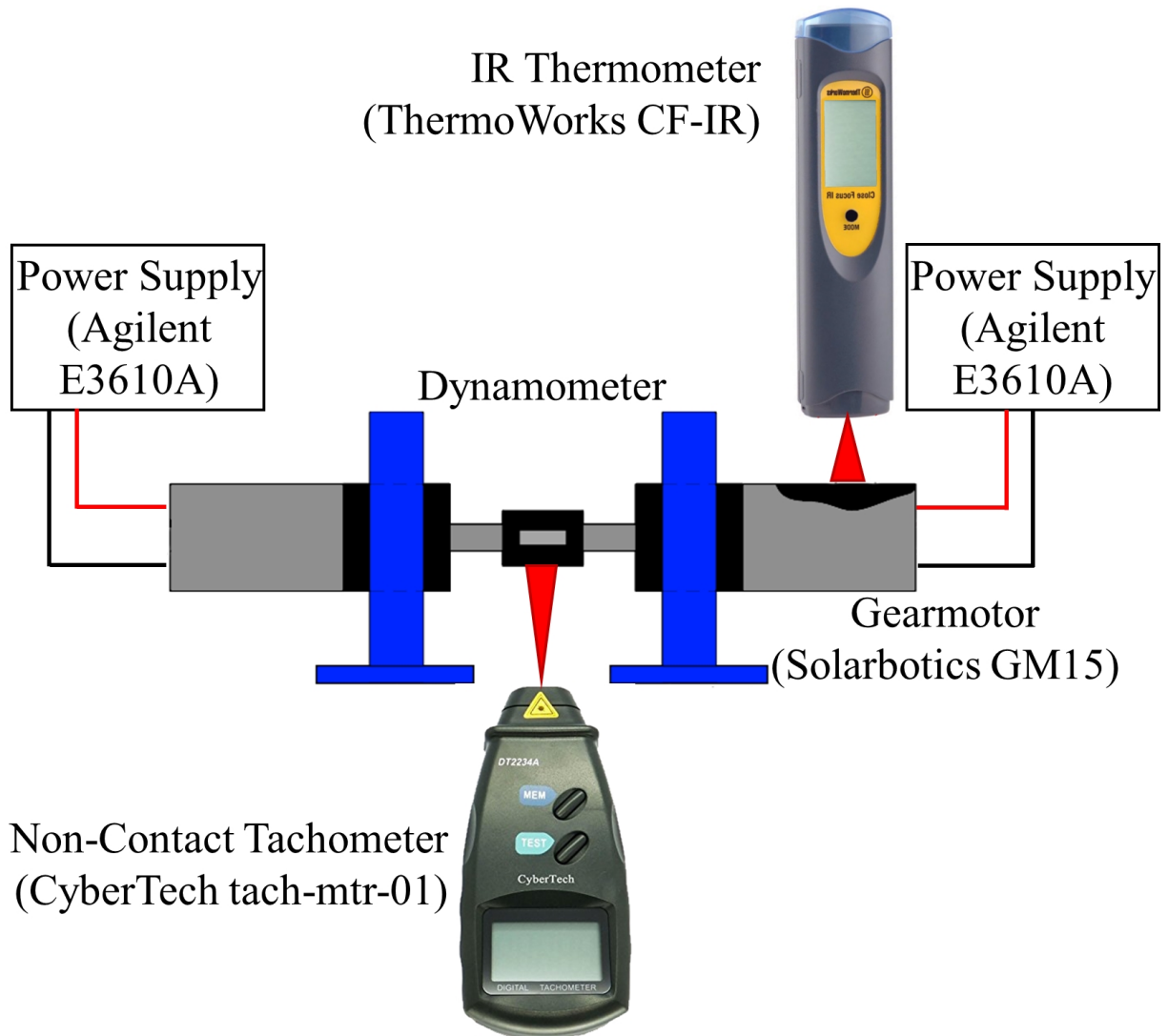


Figure 3.21: Experimental setup with custom dynamometer, non-contact tachometer, and IR thermometer. Dynamometer experiments allow speed and current dependent heating effects to be isolated.

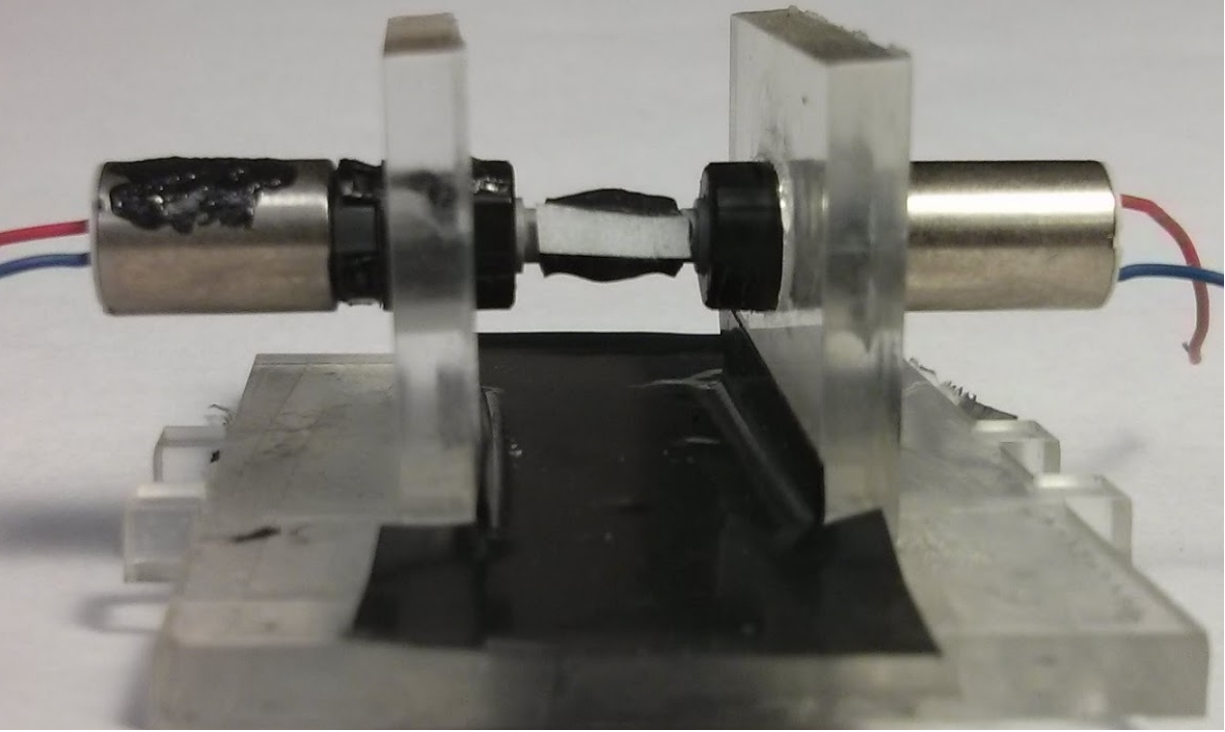


Figure 3.22: Image of the fabricated dynamometer.

as a heat source at the input of  $C_{23}$  proportional to speed with slope  $m$ . The steady state temperature depends only on the value of  $m$  and  $R_4$ . A linear expression for  $m$  as a function of  $R_4$  was experimentally determined using estimated values and used in the final parameter fitting.

### 3.6.4 Speed-Dependent Convective Thermal Resistance

At hover, the Archimedes number indicates significant forced convection. However, its effect on overall heat flow and dependence on speed needed to be characterized. For this, a pulse-spin experiment was used. First the sensing motor was stalled at a current of  $570\text{ mA}$  for  $5\text{ s}$ . This pulse was less than one-tenth of the system time constant and elevated case temperature to  $75\text{ }^\circ\text{C}$ . The drive motor was then run at a constant speed. The temperature of the sensing motor was recorded as it cooled to steady state, which varied with speed due to bushing friction. The settling time, which depends on the internal convective resistances  $R_{12}$ , was calculated as shown in Figure 3.24. Limitations of the dynamometer made it difficult to conduct precise replicate trials. Individual experiments are denoted by marker type. Each experiment was fit with a linear trend and the average of these was used to create the aggregate fit line shown in black. The strong trend of decreasing settling time indicates that  $R_{12}$  decreases linearly with increasing speed.

The circuit was implemented in Matlab Simulink using SimPowerSystems Specialized Technology library. Model parameters were trained with genetic optimization (Matlab *ga*) using the squared difference between case temperature from pulse-spin experiments and model as the fitness value. The optimization was initialized with the parameter estimates shown in Table 3.5.

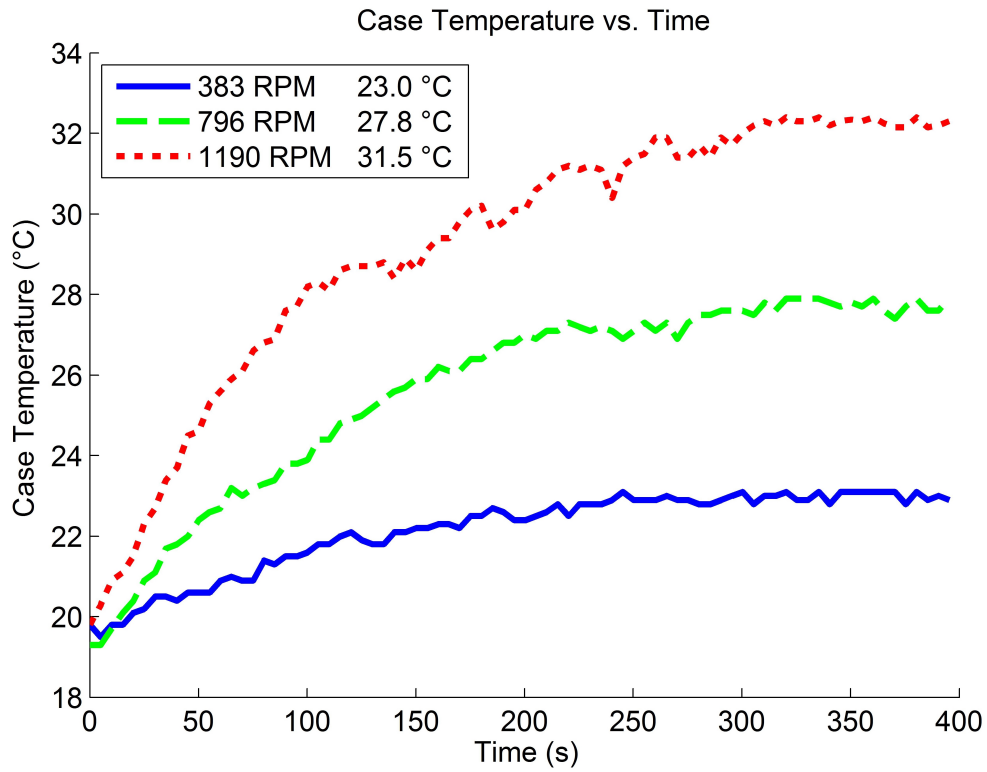


Figure 3.23: Case temperature vs. time with speeds indicated in the legend.

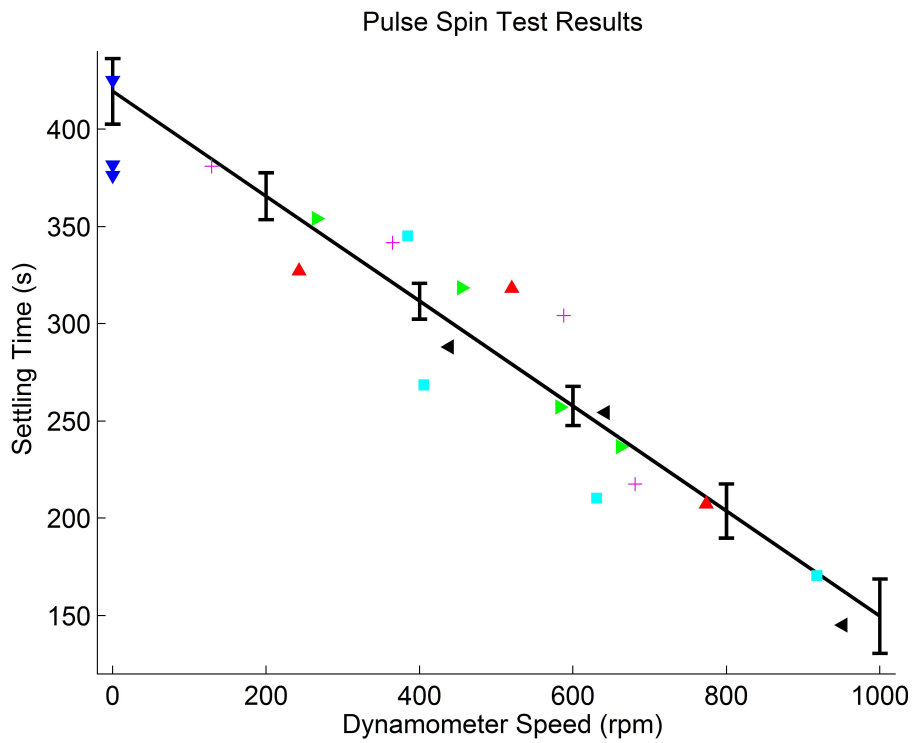


Figure 3.24: Pulse-spin experiment settling time vs. operating speed results.

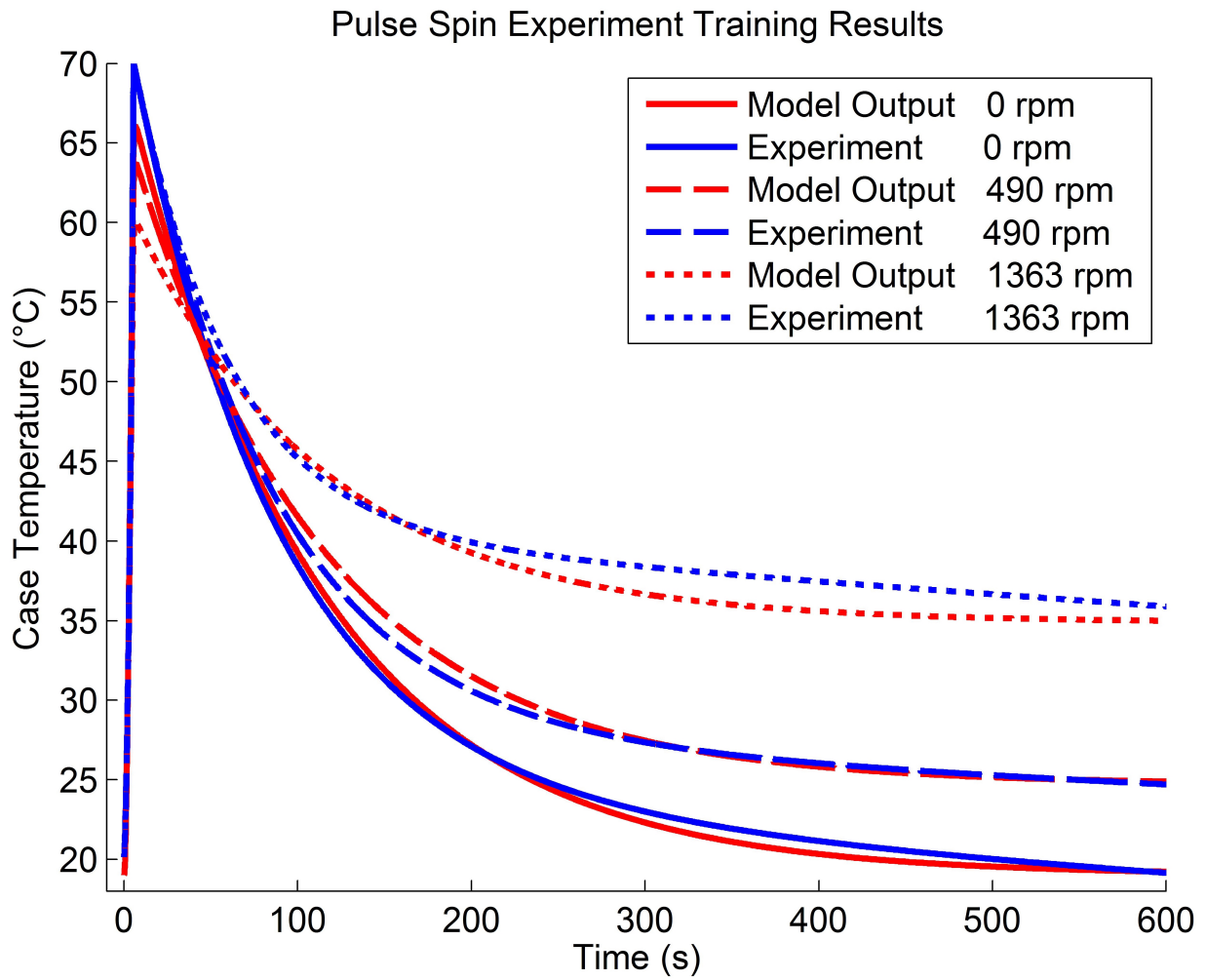


Figure 3.25: Results of the pulse-spin experimental data from the motor only in blue, compared to the output of the trained simulation in red.

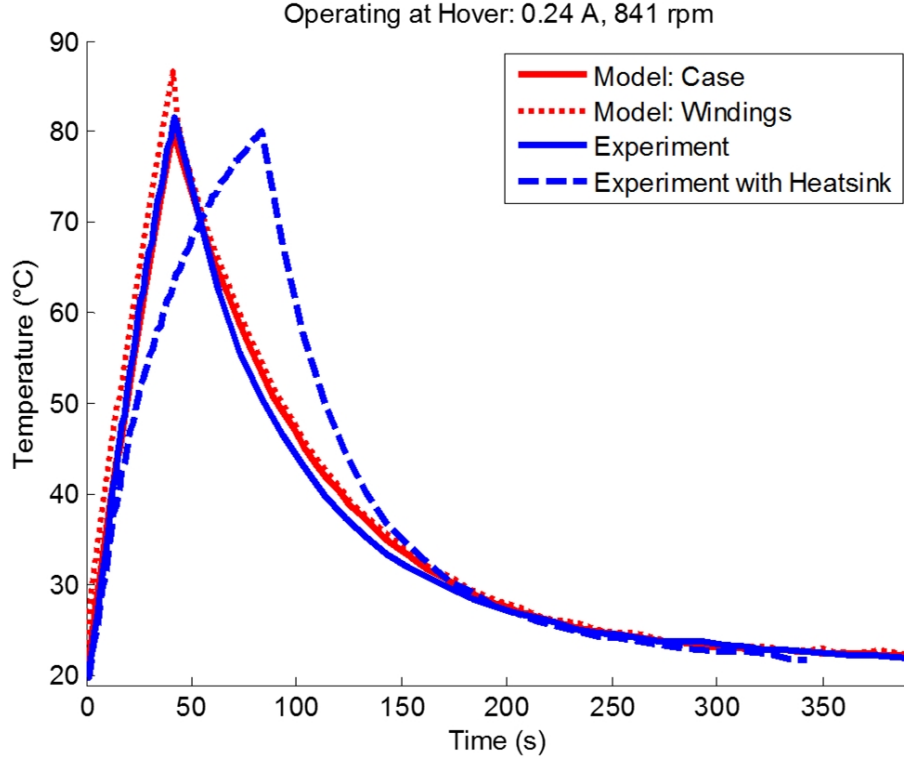


Figure 3.26: Comparison of experimental and model data for the resonant actuator operating at hover (0.24 A, 841 rpm) showing both core and case temperatures. Case temperature for the actuator with heatsink is also shown.

The bounds on capacitance values were set to  $\pm 20\%$  to account for variation in material properties. The resistance terms were allowed to vary from 1 up to the estimated value, since convective resistance tends to be over-estimated. Optimization was performed over three sets of pulse-spin data at 0, 490, and 1363 rpm.  $R_4$ ,  $C_1$ , and  $C_{23}$  showed close agreement between datasets and an averaged value was used for the final simulation. As predicted  $R_{12}$  was seen to vary linearly with speed and was fit as follows,

$$R_{12} = 33.29 - 0.034\omega \quad (3.5)$$

Results for the trained model are shown in Figure 3.25.

Training of the simulation resulted in the tuned parameters listed in Table 3.5.  $C_{23}$  is closely estimated since the case and magnet are both single materials.  $C_1$  was underestimated as the windings were assumed to be pure copper, but contain plastic wire coating and binding epoxy. Convective resistances  $R_{12}$  and  $R_4$  were significantly overestimated.  $R_{12}$  was difficult to estimate due to the unknown nature of the motors internal flow. The decrease in  $R_4$  is likely due the air around the motor not being fully stagnant. For training of the heatsink data,  $C_{23}$  was augmented by the heatsink mass, approximately doubling its value.  $R_{fin}$  was significantly higher than predicted indicating low conductive flow through the thermal adhesive used to attach it to the motor and also suggests that  $R_4$  was increased by the heatsink addition.

The trained simulation accurately predicts case temperature as shown in Figure 3.26. The

actuator is tested to a safe limit at the hover operating point, which corresponds to a current of 0.24 A and a speed of 841 rpm. It takes the system 41 s to reach critical temperature and 352 s to return to within two degrees of room temperature. The case temperature shows very close agreement, particularly during heating. A slight temperature offset can be seen during the midway through the cooling phase, however, the settling time is still captured correctly. The windings are predicted to have a slightly higher temperature than the case during heating, with a difference of 6 °C at the peak. During cooling, the windings quickly return to the case temperature due to the low thermal resistance and small thermal mass relative to the case. A case temperature upper bound was used for the safe operating envelope of the actuator. The case should not exceed 80 °C as this deforms and eventually melts the plastic gearbox. In practice, the windings should also not exceed 105 °C as this significantly degrades the wires insulating coating leading to permanent failure upon melting [129]. However, the simulation indicates that the case temperature limit also protects the windings.

In this section we have outlined a novel thermal model to accurately predict heating dynamics of a micro-motor. The critical effects of variable winding resistance, bushing friction, and speed-dependent forced convection were characterized experimentally. Furthermore, all model training data was collected with the motor alone operating continuously, while validation was performed with the resonant actuator undergoing reciprocal operation. The trained model accurately predicts case temperature for the resonant actuator at the hover operating point and sets a safe operating limit. Winding temperature is also predicted and indicates that a case temperature limit also protects the windings from thermal damage.

### 3.6.5 Heatsink Design

The circuit model was used to determine maximum total heatsink resistance that improved performance. For hover, corresponding to a current of 0.24 A, preliminary simulations indicated the threshold to be  $10 \frac{K}{W}$ . A design optimization was then performed to minimize the weight as follows,

$$\min_{segment\#} (\min_{\theta} (\text{Weight}_{array}))$$

$$\text{Subject to: Biot number of each segment} \leq 0.1 \tag{3.6}$$

$$\text{Heatsink resistance} \leq 10 \frac{K}{W}$$

The heatsink was modeled as an array of fins composed of as many connected segments, with heat transferred between them by conduction and to the atmosphere by convection. The Biot number constraint was needed to ensure a physically accurate solution where the heat being drawn out of each segment never exceeded that heat transferred in. Initial simulations focused on several long fins that took advantage of the high velocity downwash from the wings shown in Figure 3.27 and 3.28.

However, an array of many shorter fins was determined to be weight-optimal. A total resistance of  $9.88 \frac{K}{W}$  was predicted for an array of 42 copper fins, where each fin was 25 mm × 0.1 mm × 2 mm. The design was laser cut (LPKF ProtoLaser U3) from a copper sheet and attached to the motor with a thermal adhesive (Arctic Alumina AATA-5G) as shown in Figure 3.29. The total weight was 0.97 g per motor, which is within the payload of the vehicle.

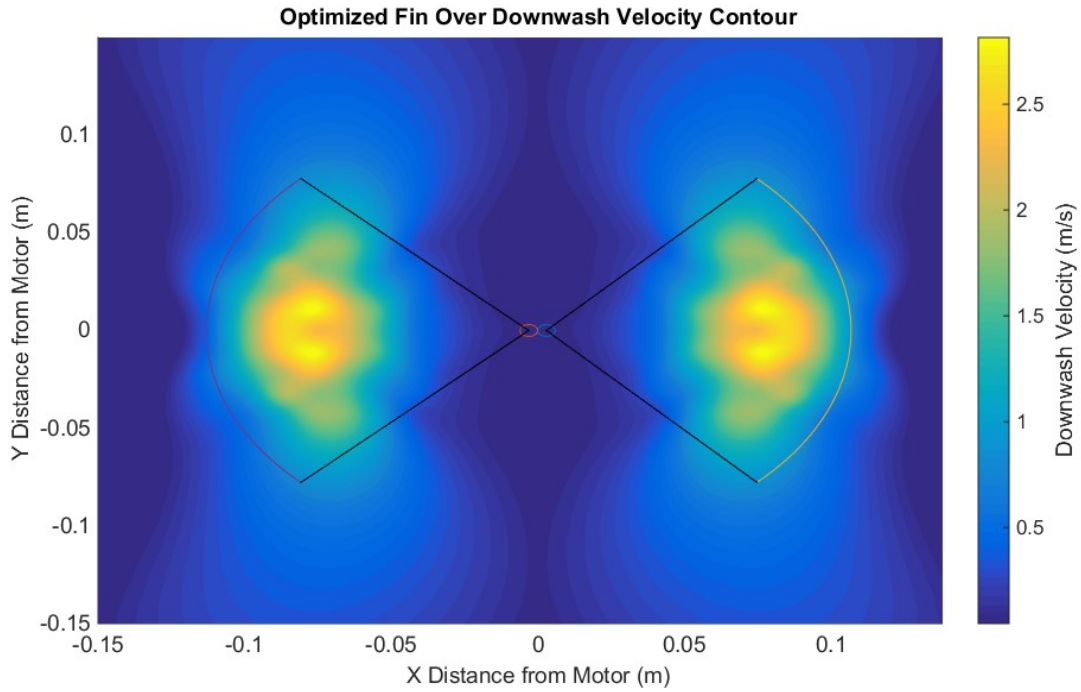


Figure 3.27: Measured wing downwash surface with motor location and wing flapping arc.

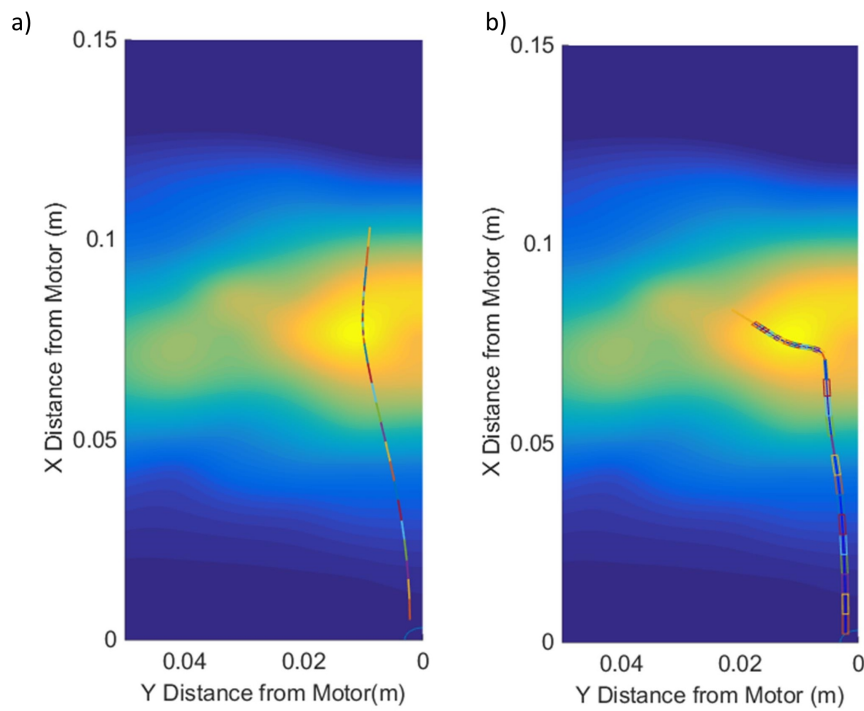


Figure 3.28: Results from the optimizations are displayed over the velocity contour: a) result from the MINLP C. b) is the original result with variable thickness fin segments.

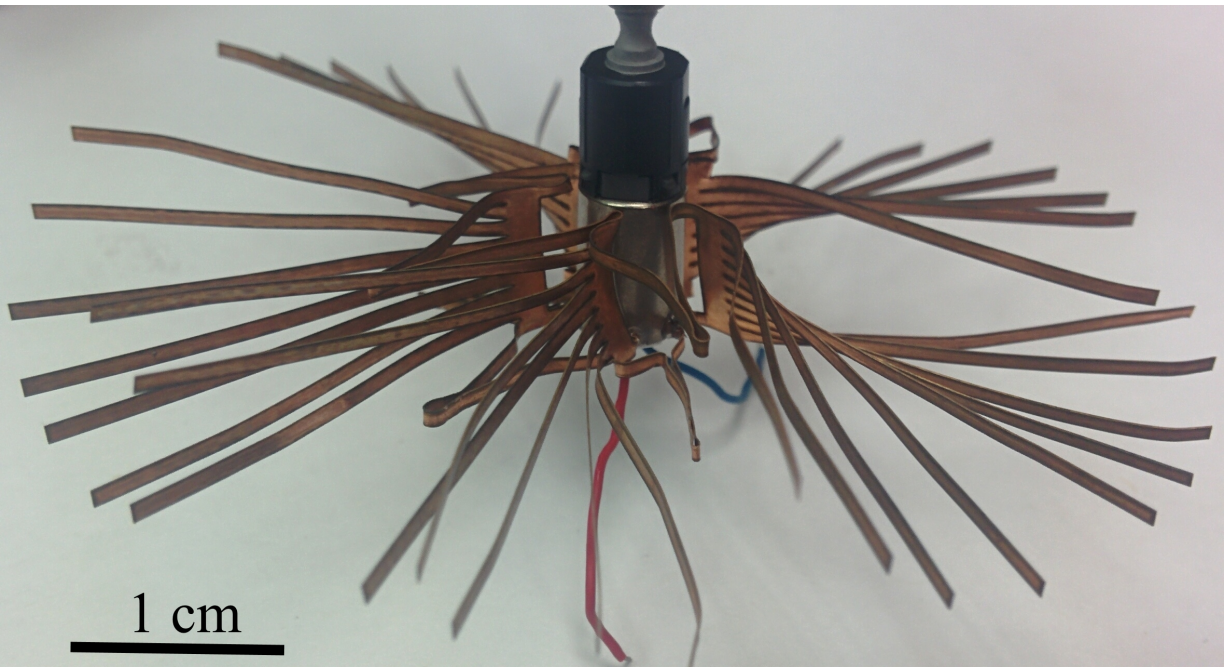


Figure 3.29: Fabricated weight-optimal heatsink attached to motor.

Given that this design relies on free convection alone, it could be generalized to other applications. With the heatsink the system takes 83 *s* to reach critical temperature and 260 *s* to return to within two degrees of room temperature. The fin increases system operating time by 102.4% and reduces cooling time by 26.1%.

### 3.7 Conclusion

In this chapter I have covered topics related to actuation of the vehicle. I demonstrate a simulation for evaluating the performance motors to drive a flapping wing. However, I show that for motor selection it is more effective to utilize the metric of torque density and carefully consider the performance of different motor designs. I also identify discrepancies between manufacturer supplied motor ratings and tested values. Significant variation in the components of the GM15 make it extremely valuable to measure the performance of all motors and gearheads and to select the best ones for system fabrication. Furthermore, I demonstrate improvements in performance due to resonant actuation. Therefore, an improved workflow for future studies is: identification of candidate motors based on first principles and torque/power density, estimate increase in torque and speed due to resonant actuation, use impedance matching modeling to determine resonant frequency and wing size.

Resonant actuation serves as a general principle by which oscillating limbs can be efficiently driven by motors in miniature robotic systems. Furthermore, directly driving independent limb motion can eliminate the need for complex transmissions and simplify control. Compared to the gearmotor alone, the resonant design is shown to increase torque and power density by 161.1% and 666.8% respectively, while decreasing the drawn current by 25.8%. Characterization with

standard metrics allows researchers to determine if such an actuator could be incorporated into their work. Measured actuator efficiency exceeds 40% for amplitudes above 33 *circ*. Increasing efficiency, resulting in decreased current draw, lengthens the time that peak performance can be sustained. However, for applications where continuous high torque is required, these improvements may not be sufficient for extended operation.

To determine a safe operating envelope for the system, a thermal modal of the actuator was developed. A lumped parameter thermal circuit was experimentally fit using current and speed as inputs and case temperature as the output. In order to accurately model the micro-motor, two orders of magnitude smaller than those previously characterized, the effects of temperature-dependent winding resistance, bushing friction, and speed-dependent forced convection were experimentally determined using a custom dynamometer. The trained model accurately predicts the time course of case temperature for hovering of the FWMAV and subsequent cooling. A safe operating envelope for the actuator is determined to prevent permanent damage. Furthermore, the model was used to design a weight-optimal heatsink that relies on free convection and increases system operating time by 102.4%. Resonant actuation and thermal modeling are powerful tools to better understand and maximize the performance of electromagnetic actuators in miniature mobile robots and could be considered by researchers for a variety of applications.

# Chapter 4

## Wing Design

### 4.1 Introduction

This chapter covers the design of the lifting surface of the vehicle, the wing. Biological flight displays an enormous variety of planform wing shapes and flexibility profiles over a large range of aerodynamic regimes. Section 4.2 discusses the morphology of biological wings including planform shape, area distribution, aspect ratio and Rossby number, flexibility, camber, twist, and venation. Section 4.3 covers analytical generation of wing shape, while section 4.4 surveys the wing shapes of FWMAVs. The remaining sections discuss wing design done for our FWMAV. Section 4.5 covers experiments varying wing size and shape and section 4.6 covers experiments with general wing flexibility. Section 4.7 covers improved experiment dealing with wing span-wise twist with an overall conclusion in section 4.8.

### 4.2 Morphology of Biological Wings

Wing in nature have a vast array of planform shapes and flexibility profiles over a range of Reynolds numbers from approximately 1 to 10,000 for hovering organisms. For hovering flight the  $Re$  can be defined based on the mean chord length of the wing  $\bar{c} = \frac{2R}{AR}$ , where  $R$  is the wing length and  $AR$  is the aspect ratio, and the mean wingtip velocity  $\bar{U}_t = 2\Phi fR$ , where  $f$  is the flapping frequency, and  $\Phi$  is the peak-to-peak flapping amplitude in radians [40]. The full expression is as follows,

$$Re = \frac{\bar{c}\bar{U}_t}{\nu} = \frac{4\Phi fR^2}{\nu AR}, \quad (4.1)$$

where  $\nu$  is the kinematic viscosity of the fluid in  $\frac{m^2}{s}$ . Over the range wing area is seen to scale with  $m^{2/3}$ , where  $m$  is the body mass. Flapping frequency is seen to scale with  $m^{-1/4}$ , increasing with decreasing body size. In general, it is thought that local maxima of lift product exist for combinations of wing planform shape, the flexibility profile, and the aerodynamic regime primarily determined by wing size and flapping frequency [1, 130]. It is important to remember that biological structures, have been shaped by evolutionary compromises as well as ancestral history. Biological wings do not represent optimal structures with respect to lift production or

aerodynamic efficiency, but are the good enough solution that gave the organism the best chance to survive in its environment. With this in mind, biological wings have been shaped by hundreds of millions of year of evolution and utilize unsteady aerodynamic principles that remain difficult to precisely model. Therefore, biology remains an invaluable tool for determining general design principles specific to a vehicle size and flapping frequency scale. The following sections broadly cover aspects of wing morphology: planform shape, area distribution, flexibility, camber, twist, and venation.

### **4.2.1 Planform Shape**

Weis-Fogh approximated the wing shape of several common insects and birds with characteristic functions in order to better characterize their aerodynamics as seen in Figure 4.1 [42]. The wings appear to be either half ellipse or parabolic, while the shape of the butterfly is considered a triangle with the apex attached to the body. The elliptical planform is well known from classical aerodynamics as minimizes induced drag by reducing drag near the tip and also results in a uniform lift distribution. Differences can be seen in terms of the tapering of the wings toward the base. This modifies the wing area distribution, which will be discussed in the following section. The wasp and hawk moth both have a hind wing that fills in the wing area toward the base. Although this wing area generates less lift due to its lower velocity, it may help augment wing area during the downstroke, while having minimal effects on the upstroke. It may also simply be a vestigial trait. Although the curvature and tapering of biological wings results in beautiful, functional structures, such shapes are often hard to fabricate. For classical aircraft an elliptical planform is often approximated with a tapered shape. For many FWMAV systems and experiments, biological planforms are often copied or simply approximated as a rectangle.

### **4.2.2 Area Distribution**

The effect of wing area distribution on lift generation has been examined in detail by Weis-Fogh for a variety of different insects [42]. He established that the lift production is directly proportional to the moment of the wing area about the wing hinge. In other words, lift production increases as the wing area is distributed further from the base of the wing. Therefore, in order to increase lift, the wingspan can be increased and chord length near the distal areas can be elongated. However, it has been shown that increasing wingspan has limited returns since it produces a proportional increase in the required inertial flapping power [7]. Since the wing areas near the hinge do not contribute significantly to lift generation, they can be narrow provided that they can withstand the bending moment produced due to the inertial and aerodynamic forces acting on the wing.

Ellington continued the study of lift generation through a detailed mathematical analysis of insect morphology [2]. He established that the first moment of area gives the position of the wing centroid. The second moment of area is proportional to the mean lift force for a quasi-steady-state aerodynamic analysis, while the third moment corresponds to the mean profile power. He also determined that the first moment of mass corresponds to the wing center of mass, which is proportional to the inertial force on the flapping wings. The second moment of mass is proportional to the inertia of the wing pair. Ellington established that in many insects for both area

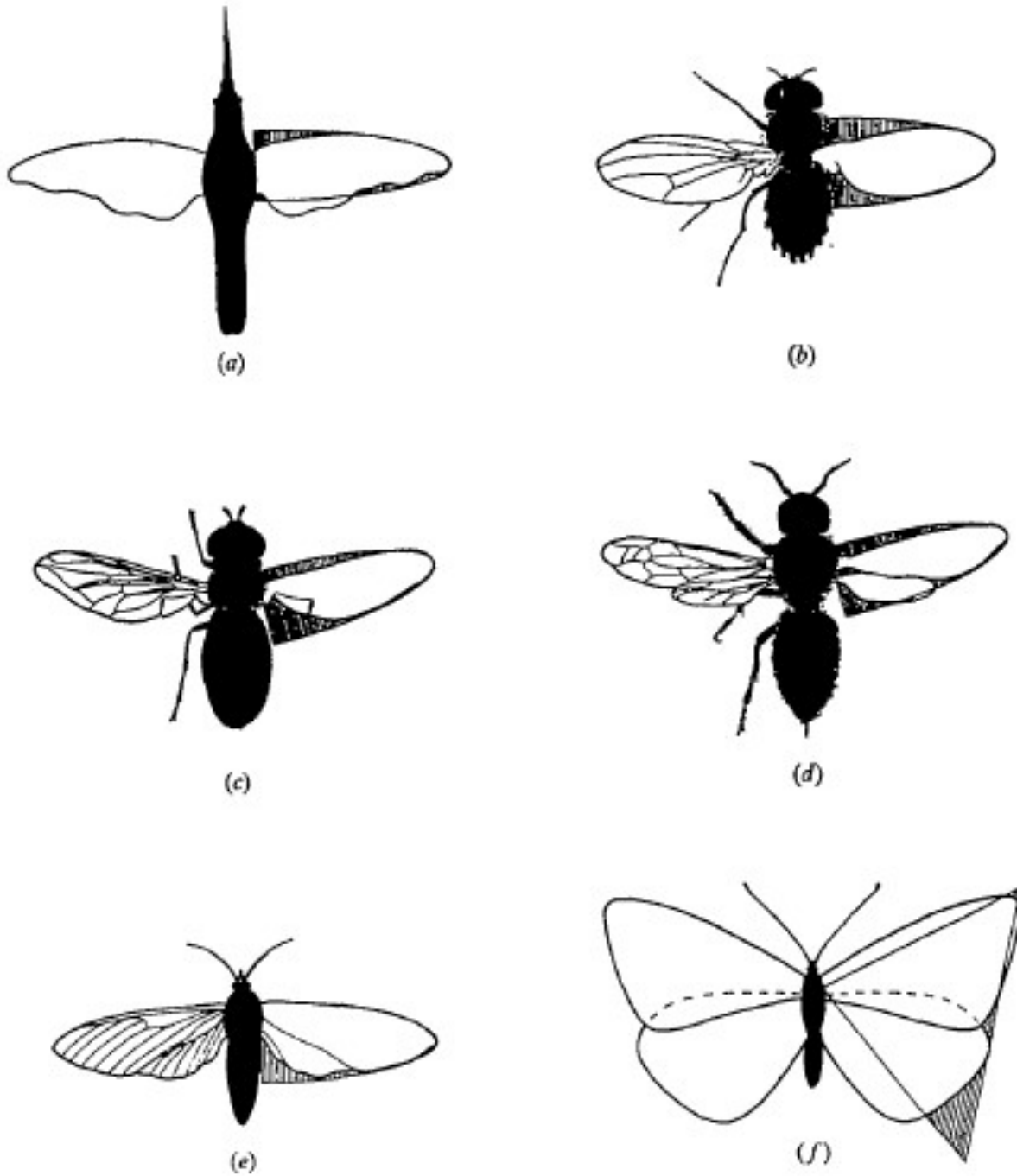


Figure 4.1: Wing shapes of common birds and insects: (a) hummingbird, (b) fruit-fly, (c) hover-fly, (d) wasp, (e) hawk moth, and (f) cabbage white butterfly.

Table 4.1: Aspect Ratios of Biological Wings

Organism	Wing Aspect Ratio
Moths and Butterflies	$2.85 \pm 0.082$
Wasps and Bees	$3.33 \pm 0.080$
Beetles	$3.54 \pm 0.034$
Hummingbirds	$3.70 \pm 0.3$
Lacewings and Mantidflies	$4.23 \pm 0.52$
Flies	$4.48 \pm 0.70$
Dragonflies and Damselflies	$5.01 \pm 1.14$

and mass, the radii of the second and third moments are very closely correlated with the first moment. This indicates that the distribution of wing area about the wing hinge directly affects the lift generation and the required flapping power.

### 4.2.3 Aspect Ratio and Rossby Number

Aspect ratio is another important parameter for describing wing shape. In classical aerodynamics it is the most important parameter for optimizing the performance of an aircraft and high aspect ratio wings operating at low angles of attack are used to maximize efficiency [131, 132]. Aspect ratio is defined as follows

$$AR = \frac{L}{\bar{c}} = \frac{L^2}{A}, \quad (4.2)$$

where  $L$  is the wing length,  $\bar{c}$  is the mean chord length, and  $A$  is the wing area. Biological wings show large variation in aspect ratio, even amount orders, with the largest being 5.01 as seen in Table 4.1 based on data from Ellington and Lentink [2, 35]. Studies of aspect ratio based on revolving model insect wings concluded that variation of aspect ratio has minimal effect on  $C_L$  and  $C_D$  at high angles of attack [133]. However, recent work by Kruyt *et al.* has demonstrates that aspect ratio determined performance based on the operating angle of attack, where an aspect ratio 10 wing performed better under  $20^\circ$  angle of attack, while an aspect ratio 4 wing performed better above  $20^\circ$  angle of attack. The aspect ratio 4 wing achieved the highest lift and aerodynamic efficiency on average above  $20^\circ$  angle of attack over the range of  $Re$  from 9000-25000.

Another important parameter when considering wings with an offset is the Rossby number ( $Ro$ ) defined as follows,

$$Ro = \frac{L + d_w}{\bar{c}} = \frac{(L + d_w)^2}{A}, \quad (4.3)$$

where  $d_w$  is the wing offset. A diagram of our wing with an aspect ratio of 3.6 and Rossby number 8.58 shown in Figure 4.2. Low Rossby number values indicate that rotational accelerations are significant compared to inertial forces and is a critical parameter for determining LEV stability. At equivalent flapping amplitudes high Rossby number wings will undergo primarily translational motion, while low Rossby number wings undergo mainly rotation changing the aerodynamics. Work by Lentink and Dickinson indicates that stable LEVs are generated for

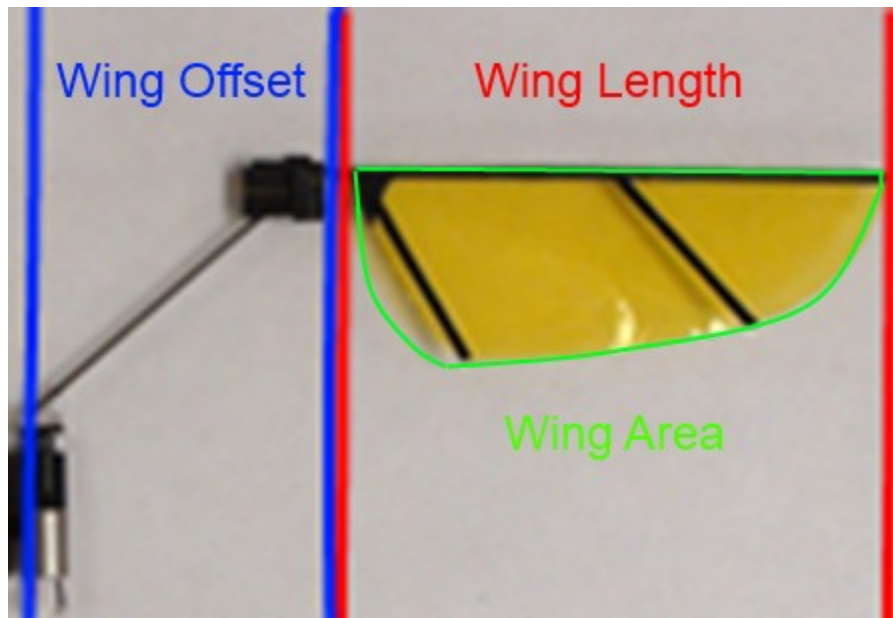


Figure 4.2: Schematic of our wing design with aspect ratio of 3.6 and Rossby number 8.58.

wings with a Rossby number less than 3 or over the sections of a larger wing where the Rossby number is less than 3 over the range of  $Re$  from 100 to 14000 [35]. For most organisms that wing offset is minimal so that aspect ratio and Rossby number can be considered as equivalent.

#### 4.2.4 Flexibility

Biological wings are flexible structures that undergo inertial and aeroelastic deformation throughout the wing stroke as shown in Figure 4.3b [130, 134]. Work by Combes and Daniel demonstrated that bending of the Hawkmoth wing was driven primarily by inertial forces, although rapid stroke reversal may generate additional aerodynamic force to help deform with wing [18]. Figure 4.3a shows that spanwise flexural stiffness is strongly correlated with wing span and the work goes on to show that chordwise stiffness is correlated with chord length. A stiffness anisotropy was present for all wings tested, with spanwise stiffness being 1-2 order of magnitude larger than chordwise stiffness. This indicates that the primary mode of wing deflection is along the chord, such as in cambering or twisting. The scaling of the wing stiffness seems to provide functional similarity such that angular deflections would remain constant over the range of organism sizes. Looking at the scaling of wing strain reveals that chordwise deflection remains proportional to the applied force, while spanwise deflection scales with  $\frac{F}{L}$  indicating that spanwise deflections will decrease for larger wings. However, a generalized scaling argument for the inertial and aerodynamic forces on the wing is difficult to determine due to variations in flapping frequency and kinematics across the large range of organism sizes.

The potential benefits of flexible wings include improved lift production, reduced power needed to flap the wings, and utilization of resonance. Mountcastle and Daniel showed that flexible wings increase the magnitude and orientation of induced flow compared to rigid wings

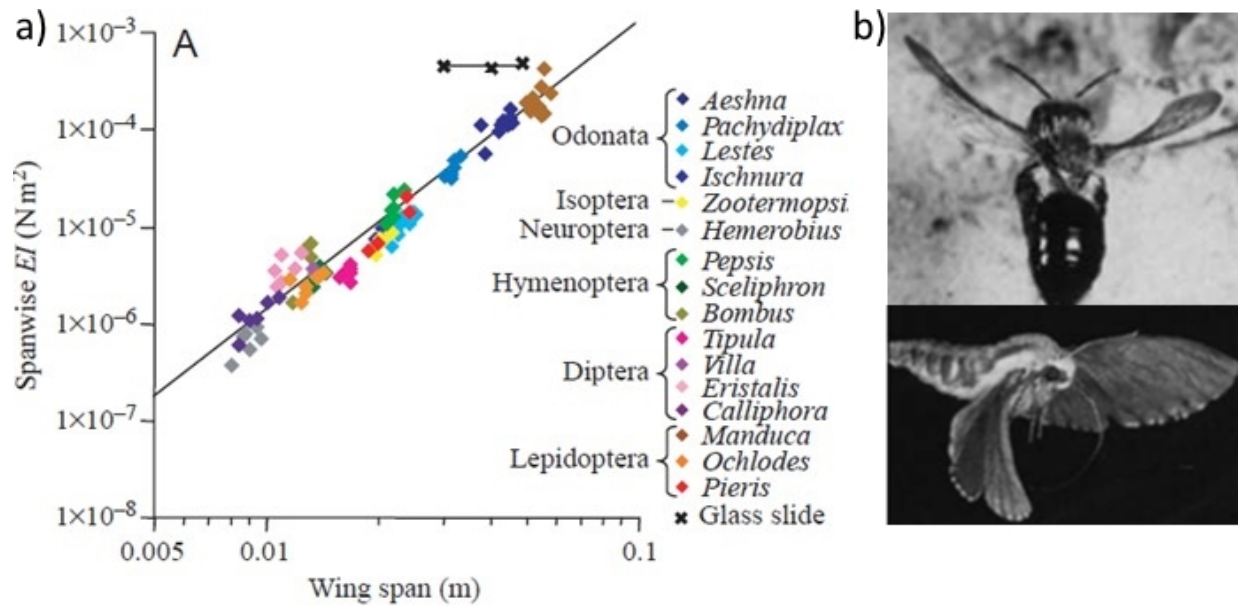


Figure 4.3: a) Measurements of wing flexibility [1], b) wing deformation during flight [2].

improving lift production [135]. Bending of the flexible wing structure can be used to store energy throughout the stroke and increase tip velocity and deflection as this energy is released. When the natural frequency of the wing cantilever structure matches the flapping frequency of the system further improvements could be seen as the stored elastic energy would cancel out any inertial work needed to deform the wing structure. Flexibility also appears to be important for control as it provides high control authority based on tuning of wing kinematics, especially the phase of rotation [135, 136].

Many simulation studies have explored the role of wing flexibility. Some look at the results of flexibility very generally and focus on modeling of the fluid structure interaction. Results from Noda *et al.* demonstrated that a flexible wing improved aerodynamic efficiency ( $\frac{C_L}{C_D}$ ) by 12.75% on average compared to a rigid wing. The main difference was twisting of the flexible wing near the tip, which was suggested to stabilize the LEV. Other studies simplify the wing flexibility and model the wing as two rigid links connected with a torsional spring such as those by Vanella *et al.* and Liu *et al.*, which demonstrates an increase in mean lift by 21% in the case of trailing-edge flexion just prior to shedding of the starting vortex [137, 138].

In a study by Eberle *et al.* the dependence of lift coefficient on flapping frequency, phase of wing rotation, and flexural stiffness is explored [139]. The study finds that when the structural resonance of the wing matches the flapping frequency there is a large increase in the lift coefficient. However, the lift coefficient is shown to have regions of high sensitivity to the tested parameters. For insects with significant sensory information on dynamic wing bending and precise control over flapping frequency and phase it seems possible to tune wing kinematics to maximize lift production through utilization of resonance. On the other hand, this may be difficult to achieve in our system driven in open-loop with passive wing rotation.

Despite flexibility being a common feature of insect wings across all sizes, its benefit at low  $Re$  remain unclear. Although flexibility effects of camber and twist demonstrate clear benefits at

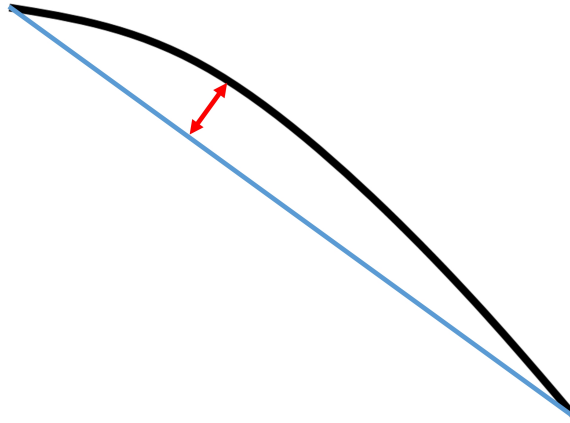


Figure 4.4: The thin cambered airfoil is shown as the black curve. Since the foil is of negligible thickness its shape corresponds to the mean camber line. The chord line shown in blue connects the leading and trailing edges. The red segment indicates the maximum displacement between the chord line and mean camber line.

larger sizes, below  $Re$  of 1500 these wing attributes appear to have negligible or even detrimental effects on translational force production [140, 141]. An experimental study done by Tanaka *et al.* compared the performance of a flexible polymer wing modeled on the hoverfly to a rigid artificial wing at a  $Re$  of approximately 1200. This study found that excessive chordwise deformation of the flexible wing decreased lift production compared to the rigid wing, although drag and aerodynamic efficiency were not quantified and may have shown improvements [142]. Additional simulation studies have shown that flexibility may enhance wake capture at stroke reversal as well as clap and fling force production, which could be significant at small scales [137, 143].

#### 4.2.5 Camber

Wing cambering is a common feature of biological wings seen across a large range of organism scales including the hoverfly, Hawkmoth, and hummingbird [36, 134, 144]. Many of these wings have an inherent camber of approximately 5% due to the wing having a convex upper surface and a concave lower surface. Dynamic camber generated throughout the wing stroke can reach up to 12% and is generated by wing veins that transfer forces along the wing and material properties that generate flexion of the trailing edge in response to inertial and aerodynamic forces. Percent camber refers to the ratio of the distance from the wing chord line to the point of maximum camber to the total chord length as seen in Figure 4.4. A stimulation study based on wing deformation data from free-flying hoverflies concluded that a cambered wing reduced the aerodynamic power required for producing unit lift ( $W/N$ ) by 9.7% on average [144]. Furthermore,  $C_L$  increased by 10.7% and aerodynamic efficiency increased by 3.6%. In addition to improving the aerodynamic of the wing, camber can assist in maintaining a constant angle of attack throughout the stroke and can increase the spanwise stiffness of the wing.

It is important to note a key distinction between biological systems and robotic ones related to airfoil camber. Most organisms have an asymmetric wing stroke with a controlled wing tip

trajectory, which results in a powerful downstroke that generates most of the lift and an upstroke where minimal lift is generated but allows the stroke to be reset. A cambered wing improves lift production during the down stroke and has minimal effect on the upstroke. However, in robotic systems the wing stroke tends to be symmetric with a flat wing tip trajectory, as it is very difficult to generate asymmetric stroke profiles. For the case of symmetric flapping profiles the benefit of an inherently cambered airfoil is negated since during half the stroke the airfoil is positively cambered to improve performance, but during the second half of the stroke it will have negative camber, which decreases performance. A bistable design that generates the appropriate camber dynamically could be used, but difficult to fabricate, especially at small scales.

#### 4.2.6 Wing Twist

Spanwise twist is another common feature of biological wings, observed in many flying insects as well as hummingbirds [27, 87, 87, 133, 145, 146]. Many species demonstrate significant dynamic twist such as  $25^\circ$  in hawkmoths,  $30^\circ$  in locusts, and over  $50^\circ$  in hoverflies [19, 147]. Twisting of an airfoil changes the local angle of attack of individual blade elements as seen in Figure 4.5. In classical aerodynamics, the twist of the airfoil is designed such that the resulting lift distribution is parabolic, which minimizes induced drag, primarily by reducing the angle of attack near the blade tip where the air velocity is the highest [148]. This design principle is used for the blades of rotorcraft due to the increasing velocity along the blade span due to its radial motion, analogous to the case of a flapping wing. The stimulation study based on wing deformation data from free-flying hoverflies concluded that a twisted wing reduced aerodynamic power by 5.9%. Twisting decreased  $C_L$  by 0.3%, but increased aerodynamic efficiency increased by 5.7%. Twisting of the wing near the tip may also help stabilize the LEV [149].

### 4.3 Analytical Generation of Wing Shape

A survey of wing shapes conducted by Ellington concludes that biological wing shapes could be parameterized by a single variable  $\hat{r}_2$ , the second moment of area [2]. For the organisms surveyed this value ranged from 0.5 to 0.6. This value was then used to calculate the first moment of area, the position of the centroid of wing area, using

$$\hat{r}_1 = 1.106\hat{r}_2^{1.366} \quad (4.4)$$

Wing shape was then generated with a beta distribution, where the p and q parameters were based on  $\hat{r}_1$  and  $\hat{r}_2$ . The beta distribution parameters were calculated using the equations 4.5 and 4.6. Once these parameters are calculated, the beta distribution can be generated. Points are then sampled from this distribution to define non-dimensional wing shapes seen in Figure 4.7. The non-dimensional wing shape must be scaled in order to generate an actual wing shape. The scaling parameters are aspect ratio, wing length, and wing offset.

$$p = \hat{r}_1 \left( \frac{\hat{r}_1 (1 - \hat{r}_1)}{\hat{r}_2^2 - \hat{r}_1^2} - 1 \right) \quad (4.5)$$

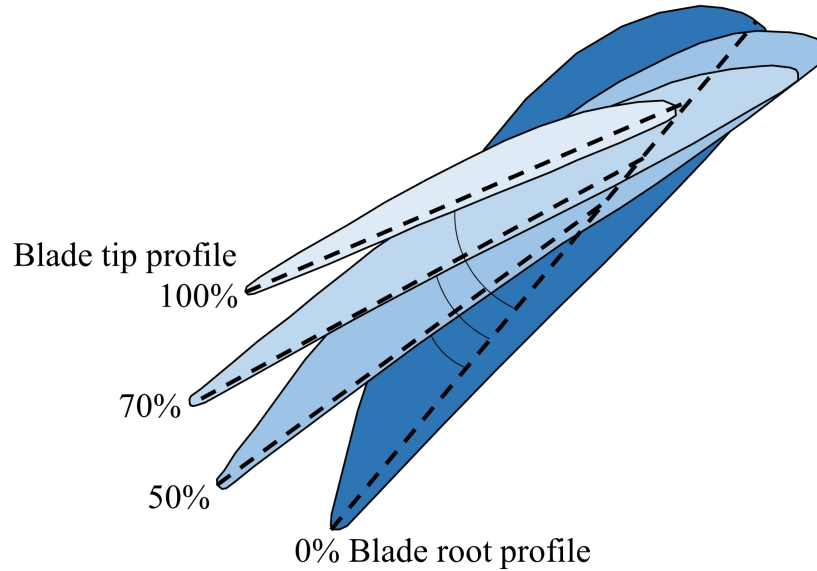


Figure 4.5: Four cross-sections of a twisted propeller blade, each labeled with its position as a percentage of the total length. The largest section is at the base, located at 0%. The next section is located at 50%, half the distance to the tip. Proceeding out, the blade tapers and the chord line (shown as dashed line) rotates decreasing the angle of attack of the cross-sections, which is maximal at the tip (100%).

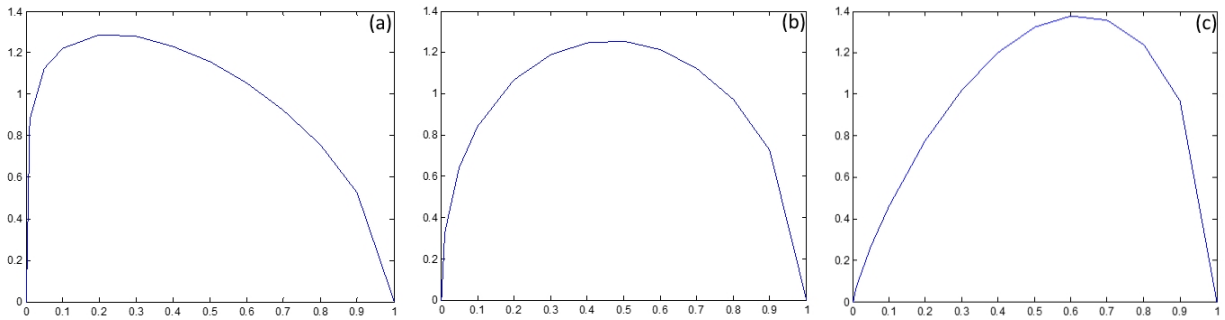


Figure 4.6: a) Beta distribution for  $\hat{r}_2 = 0.5$ ,  $\hat{r}_1 = 0.4291$  using  $p = 1.1664$  and  $q = 1.5519$ , b) Beta distribution for  $\hat{r}_2 = 0.55$ , c) Beta distribution for  $\hat{r}_2 = 0.6$ .

$$q = (1 - \hat{r}_1) \left( \frac{\hat{r}_1 (1 - \hat{r}_1)}{\hat{r}_2^2 - \hat{r}_1^2} - 1 \right) \quad (4.6)$$

## 4.4 Wing Shapes of FWMAs

Despite the plethora of biological wing shapes available to study, design of a wing that provides high performance for a given size, flapping frequency, and actuation technique remains a difficult task. The full system simulation describes in Chapter 2 was not found to be adequate to explore

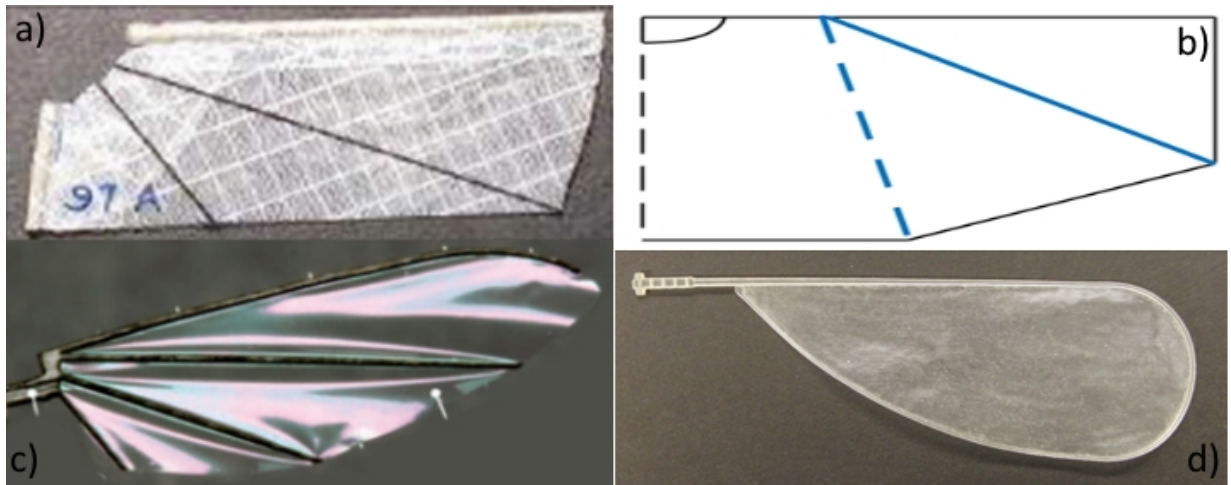


Figure 4.7: Wings of the a) Nano Hummingbird, b) Delfly, c) Robobee, d) Cornell.

variations in wing shape. As is commonly done, our wing shape has been based on previous work and improved by trial and error. For example, in the development of the Nano Hummingbird a computational approach to wing design was found unsuitable and as a result over 300 wing designs were evaluated experimentally. The wing shape also depends heavily on the materials and manufacturing techniques. It is critical to minimize the wing weight and moment of inertia in order for it to be actuated, but it must also be sufficiently stiff to resist excessive deformation in response to aerodynamic and inertial forces.

Wings of current FWMAVs use basic shapes, with relatively low aspect ratios, and varying degrees of flexibility. The Nano Hummingbird uses a rectangular wing with an aspect ratio of 2.5 [50] as seen in Figure 4.7a. The frame consists of a leading edge spar and chordwise root spar made of carbon fiber with a flexible membrane material. Actuation of the root spar angle allows for reliable camber reversal as well as generation of dynamic twist and camber for control.

The wings of the Delfly is also rectangular, but with a single taper near the tip and an aspect ratio of 1.75 as seen in Figure 4.7b [150]. The wings use a  $5 \mu m$  thick Mylar foil that is reinforced by carbon stiffeners with 0.28 mm diameter and stiffened along the leading edges with D shaped carbon fiber rods ( $0.7 \times 1.4$  mm). The large flexible wings allow it to achieve a clap and fling motion to augment lift production by 6% at the start of each wing stroke. Furthermore, optimization of wing stiffener placement to control deformation of the leading edge and wing membrane was observed to improve lift per power by 10% [131].

The wing of the Robobee is based on the wing of the hoverfly as seen in Figure 4.7c, *Eristalis tenax*, with an aspect ratio of 3 and is designed to be fully rigid. The frame is made of ultra-high-modulus carbon fiber reinforced polymer and the membrane is made of a  $1.5 \mu m$  thick polyester film. A similar shape is used by our group as well as the group from Purdue. The shape of the wing from Cornell was determined experimentally and can be seen in Figure 4.7d. The wing is 3D printed using Objet FullCure 720 material. The membrane has a thickness of  $40 \mu m$ , while the thickness of the exterior frame was varied to control wing flexibility.

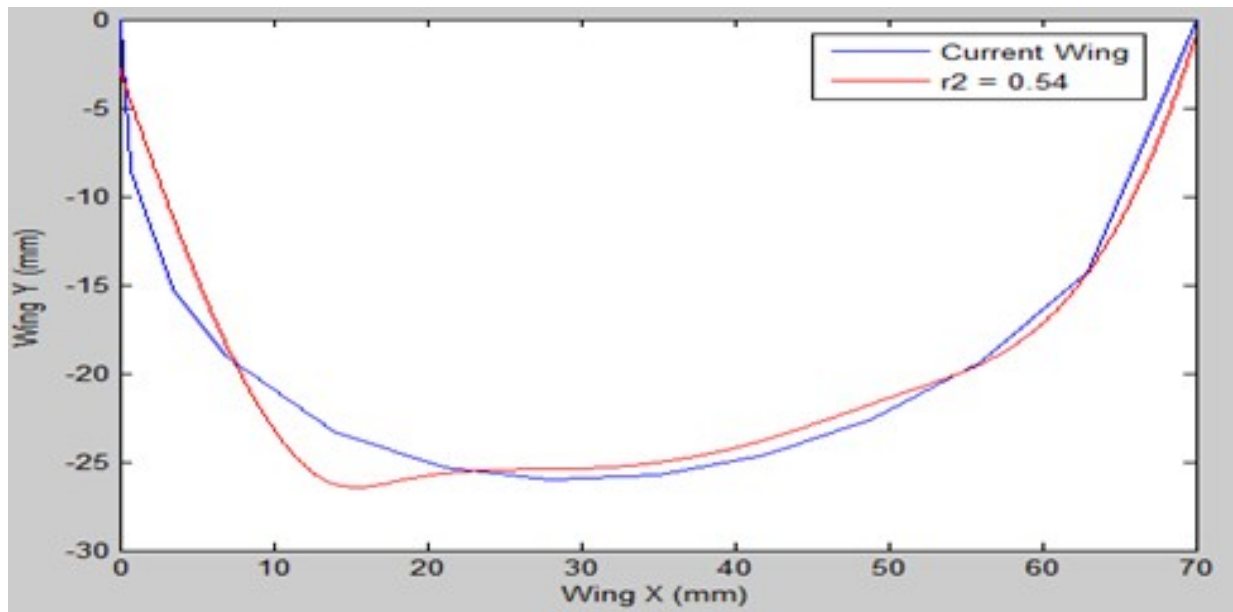


Figure 4.8: Current wing spline compared to the ideal second moment of area of 0.54

## 4.5 Wing Shape Experiments

The wing shape for our vehicle is roughly based on the one used by Campolo *et al.* [53]. Wing size was constrained by the available vacuum chamber and was made as large as possible. The wing has an aspect ratio of approximately 3.5, a second moment of area of approximately 0.54 as seen in Figure 4.8, and a length of 70 mm. The root of the wing is straightened compared to the ideal shape in order to accommodate a straight root spar. Extra material on the side of the spar is not fully supported. The wing offset was then varied experimentally, with an offset of 38 mm found to maximize lift production [54].

In order to test new wing shapes *in silico*, the simulation had to be improved so that the wing inertia matrix could be calculated based on wing shape. Originally the wing inertia matrix had to be calculated from a Solidworks model and input into the simulation. The wing was modeled as a matrix shown in Figure 4.9 indexed by position with the values indicating material thickness, essentially the material mass since the Kapton and carbon fiber used to fabricate the wing have equal densities. However, the predicted mean lift was extremely sensitive to the position of the wing center of gravity and therefore the spar placement tended to determine the results and not the actual shape of the wing. An alternate approach is shown in figure 4.9b where the wing was modeled with a rigid border so it achieved an equivalent mass to a wing reinforced with spars. The location of the center of gravity was then optimized for each particular wing shape. However, the optimized position tended to be on the trailing edge near the mid chord position, which is not possible to fabricate without adding significant weight to the wing to shift the center of gravity. The simulation also tended to predict large rotational lift contributions that did not seem realistic. For these reasons testing of wing shape in simulation was abandoned.

I fabricated several additional wing shapes for testing as shown in Figure 4.10. Three additional wings were fabricated with the same aspect ratio, but varying second moments of area:

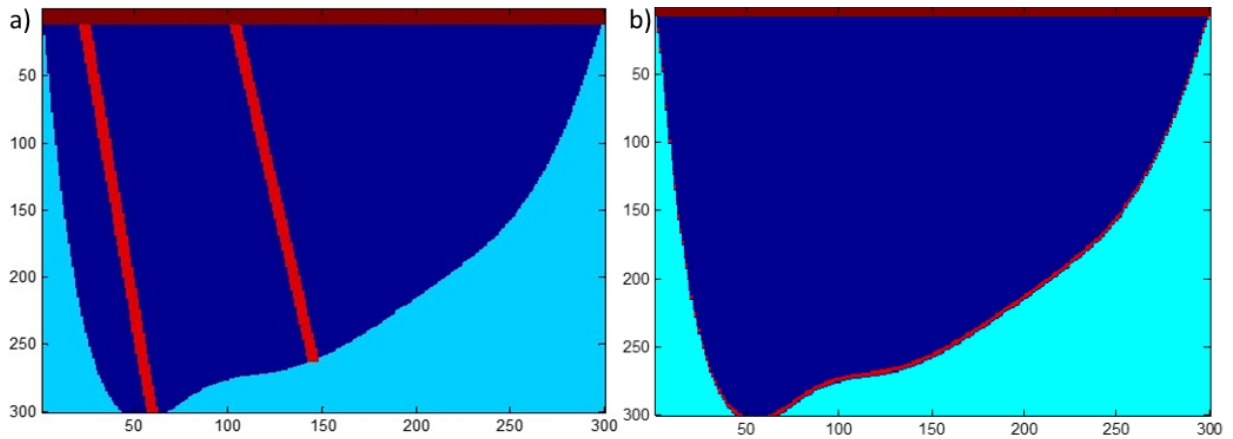


Figure 4.9: Wing mass model a) Using reinforcing spars, b) Using a rigid border.

0.54, 0.57, 0.6, and a rectangular wing. With the use of a newly fabricated larger vacuum chamber I was able to make a wing with aspect ratio close to 2, which had generated good simulation results. However, testing wings on the prototype system did not provide adequate results. Frequent failures of the system, both in the flexure and gearbox, made it difficult to collect consistent results. Stalling of the motor was also seen for some of the wings, especially the largest, in certain test conditions. The large wing had especially poor rotation that decreased its performance, which indicates that the flexure stiffness was not sufficient for the increased size. Testing of varying wing shapes is left as future work, as the current design generates sufficient lift to continue the work and has been redesigned to provide dynamic twisting as is described in the following two sections. Future testing of wings should be conducted as follows. First a frequency sweep at a nominal voltage amplitude should be performed with high speed video to determine the system resonance frequency where the flapping amplitude is maximize. Then high speed video should be taken to examine the wing stroke itself to ensure there is minimal variation in the stroke dynamics and that rotation is symmetric. Issues with rotation can be addressed by changing the flexure stiffness, by changing its length, as well as with stopper placement. Finally the performance of the wing with respect to lift per input power should be quantified and compared to other design. This has been the most common figure of merit for evaluating wing performance in FWMAVs. Tests comparing the original wing to a scaled up design with twice the area, shown in Figure 4.11, demonstrated that both produced similar lift with equivalent total wing length when operated at the same frequency. However, the smaller wing with large offset has lower weight and allows the system to be operated at higher frequencies which could generate more lift and is beneficial for control. Therefore using a significant wing offset is considered as a weight reducing and performance improving technique that is not seen in biological systems since it is enabled by the lightweight and high stiffness carbon fiber rods used.

## 4.6 General Wing Flexibility Experiments

Due to constraints of our manufacturing process and to facilitate system modeling, the wings have until now been built as flat, rigid plates. The wings are fabricated out of unidirectional

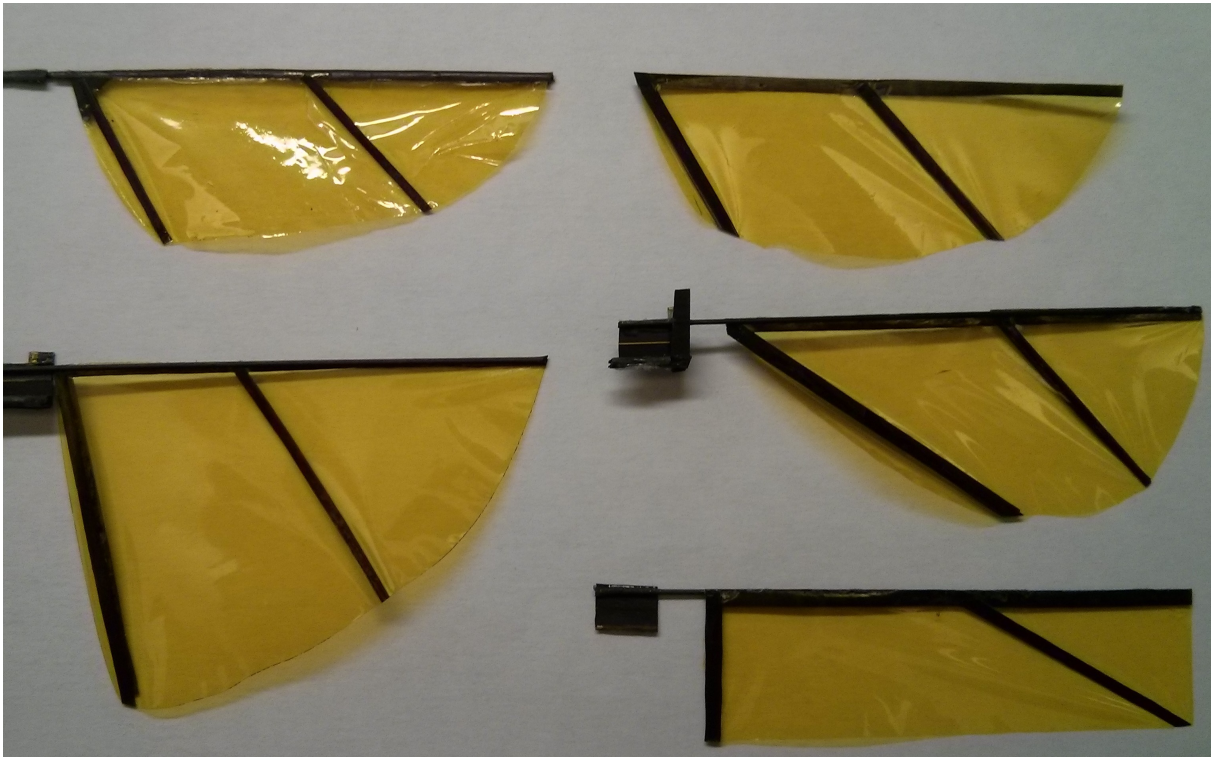


Figure 4.10: a) Current wing design  $AR = 3.5$ ,  $\hat{r}_2 = 0.54$ , b)  $AR = 3.5$ ,  $\hat{r}_2 = 0.57$ , c)  $AR = 3.5$ ,  $\hat{r}_2 = 0.57$ , d)  $AR = 3.5$ , rectangular, e)  $AR = 2$ ,  $\hat{r}_2 = 0.54$ .

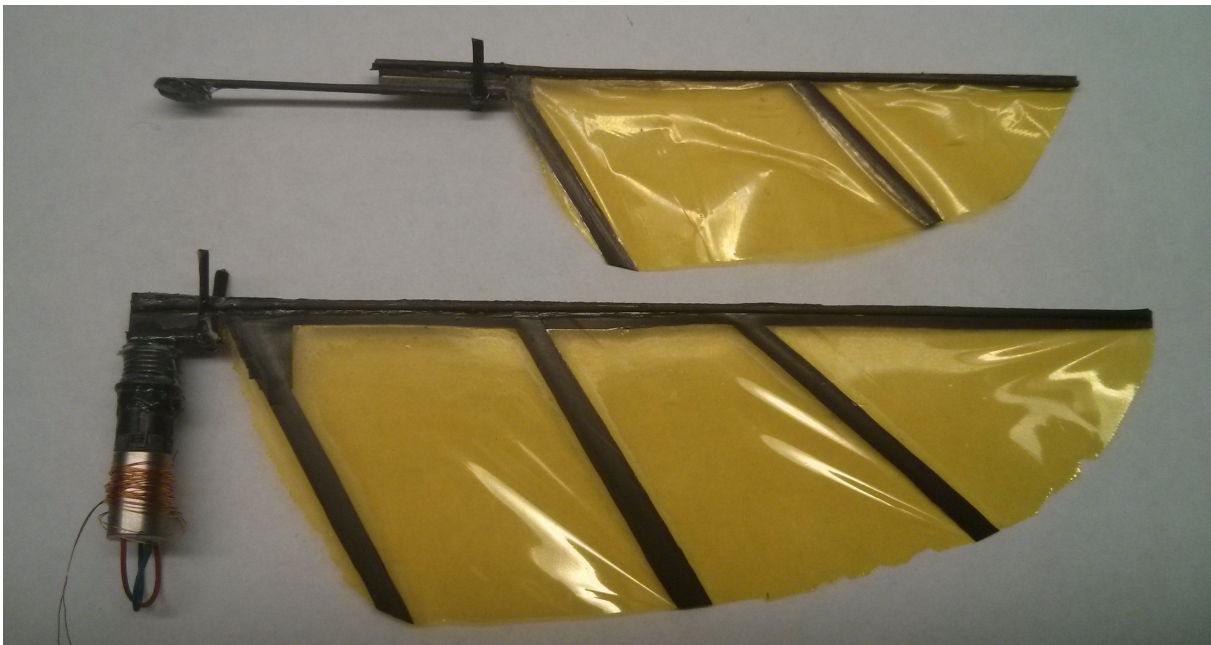


Figure 4.11: Comparison of original wing and larger wing with double the area.

carbon fiber prepreg sheets (M60J with 60% Toray 250 F Epoxy Resin) with a thickness of  $40\ \mu\text{m}$ . A thin layer of Kapton film,  $6\ \mu\text{m}$  thick, is sandwiched in between the carbon fiber layers. The wing was laid up as a composite with Kapton held between structural carbon fiber layers. This assembly is then pressurized in a vacuum chamber at 1 atm and cured at  $180^\circ$  for two hours. The layout typically consists of a leading edge spar along the entire length of the wing and two supporting spars that run diagonally along the wing chord. The position and angle of these rectangular spars is chosen such that the Kapton film is fully supported. Multiple layers of carbon fiber are used in order to ensure the wing is rigid. The leading edge is further supported with a carbon fiber rod that attaches to the gearbox output shaft, through a flexure, and serves to transmit the driving force of the actuator to the wing.

Two main approaches to designing flexible wings. The first approach based on resonance was varying the spanwise stiffness to match the natural frequency of the wing cantilever structure with the flapping frequency. The second aimed at generated dynamic twist varied the chordwise stiffness along a wing with a rigid leading edge. In our original design the wing rotation was limited to  $\pm 45^\circ$ , where lift per drag is close to 1 as shown in Figure from an experiment by Dickinson *et al.* [3]. Decreasing the angle of attack near the tip could allow for a higher lift to drag ratio at this point. Furthermore since the velocity is highest near the tip, any reduction in drag in this area could have a significant effect on overall performance.

#### 4.6.1 Modeling and Design

The use of a 1 mm diameter rod to stabilize the leading edge of the current design could result in a wing with unnecessary rigidity and add extra weight to the wing structure. Therefore, for the initial experiments, rods were not used and flexibility of the wing was based on the carbon fiber and Kapton composite structure alone. Flexibility of the wing was also modified by selecting a new bio-inspired spar pattern (Figure 4.13b) based on dipteran wings shown in Figure 4.13a. Initial testing of these wings showed that they were overly compliant and produced less lift than required for takeoff. Subsequently the leading edge was reinforced with rods of increasing diameter to determine the minimum amount of reinforcement that would result in a sufficiently stiff leading edge.

Initial results showed that unstructured chordwise deformation reduced wing performance, leading to efforts to control this deformation to generate wing twist. To vary the chord-wise deformation behavior, the number of spars along the wing was increased from two to five (including a short segment wrapping around the wingtip). The thickness of each chord spar was adjusted by varying the numbers of carbon fiber layers. The amount of twist should increase along the wing, which requires chord stiffness to decrease along the wing length. Consequently the most layers were used for the root spar and decreasing numbers of layers were used for subsequent spars out to the wingtip. In some cases where the wing appeared overly flexible, reinforcing rods were added at the joint between the leading edge and chord spars.

CAD modeling of the bio-inspired wing was done in order to manufacturing the spar pattern with a laser ablation system (QuikLaze 50ST2). FEA was performed on these CAD models to validate the generation of wing twist by varying chord spar stiffness as seen in Figure 4.14. A uniform loading condition was applied to view the variance of chord-wise compliance. For the original wing design, apart from the deformation accounted for by the leading edge spar, the

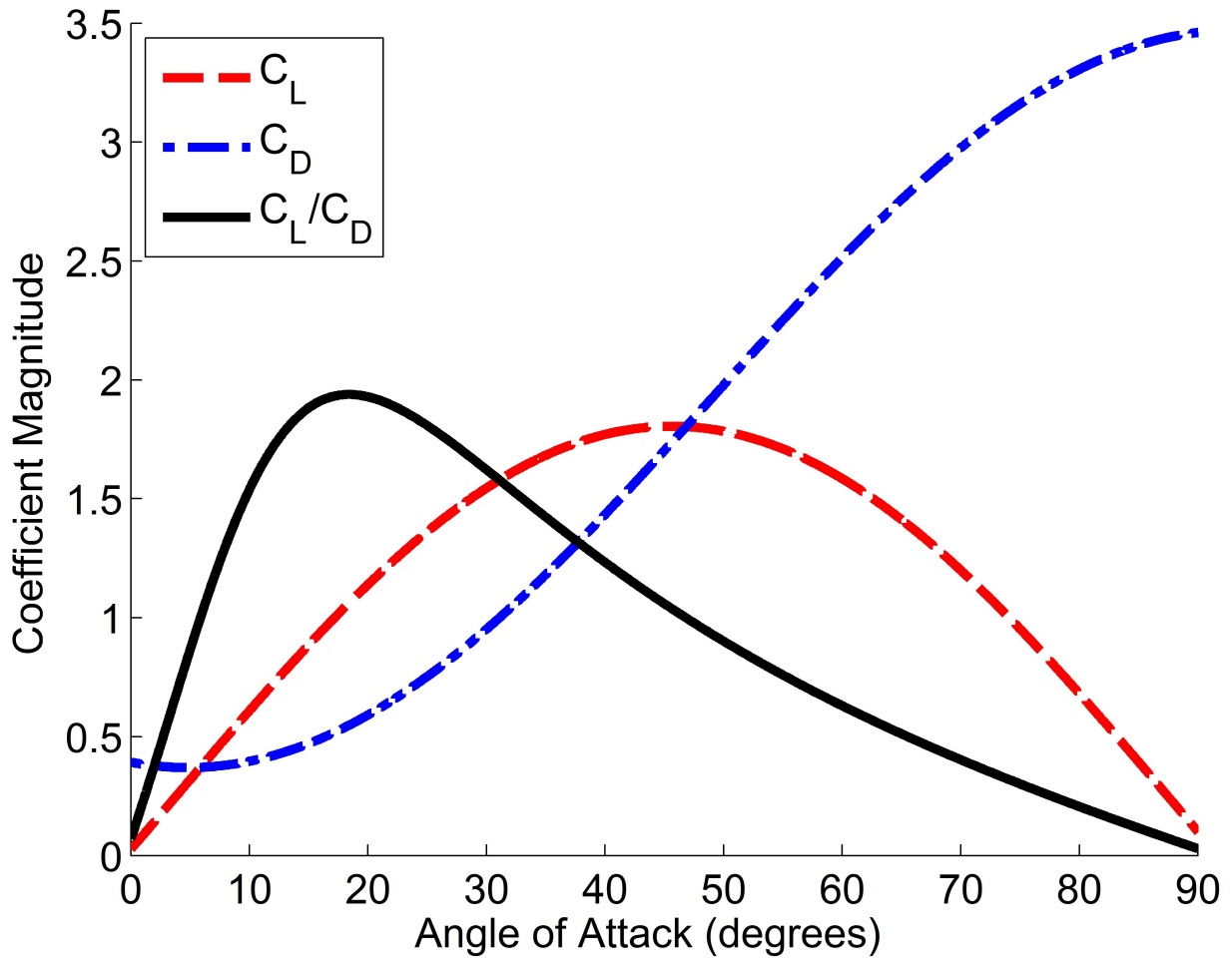


Figure 4.12: Lift and drag coefficients ( $C_L$  and  $C_D$ ) determined from experiments by Dickinson *et al.* [3] as a function of angle of attack. At  $90^\circ$  angle of attack, the wing is perpendicular to the airflow producing no lift and maximal drag. At  $0^\circ$ , the wing is parallel to the airflow.

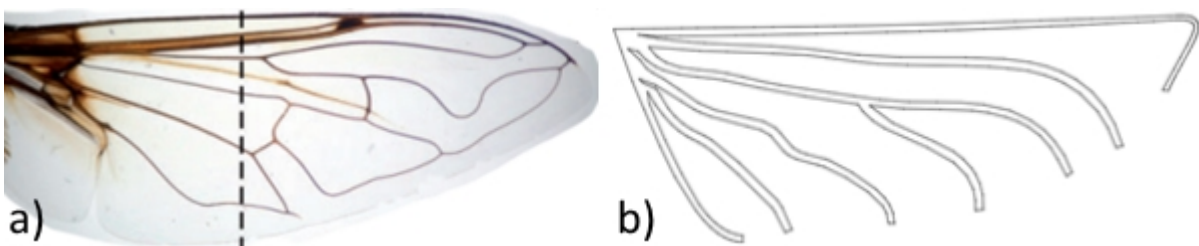


Figure 4.13: a) Right wing of a hoverfly, *Eristalis tenax*, b) our bio-inspired design for tuning overall wing stiffness.

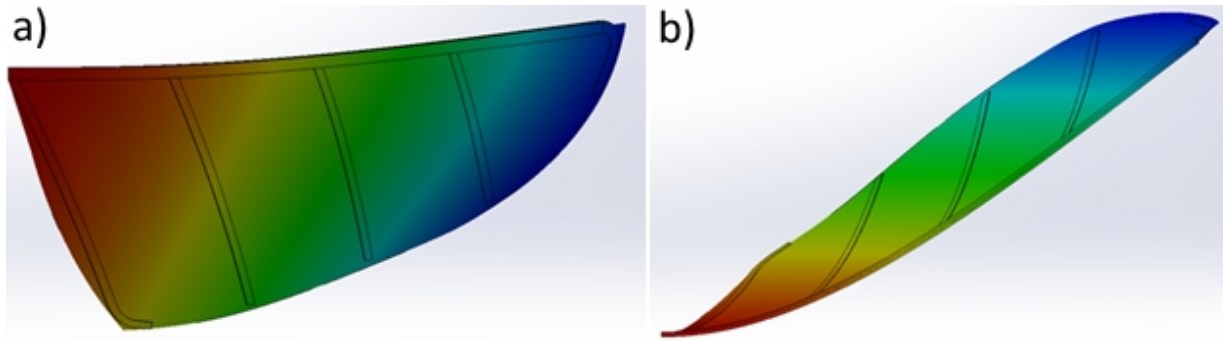


Figure 4.14: Side (a) and top view (b) of twisted wing simulation. Displacement ranges from 0mm (red) to 34mm (dark blue).

chord-wise deformation was uniform. For the twisting wing design, the chord-wise deformation generally increased from the root chord to the tip. These models also provided a convenient way to estimate mass moment of inertia, which was used to calculating a figure of merit for these wings.

Initial work on our system concerned with variation of system parameters found that increasing wing offset increased lift production. This effect is quantified in a study by Lentink *et al.* as the nondimensional Rossby number ( $Ro$ ) and concludes that force augmentation from a leading edge vortex is most prominent for  $Ro < 3$ . Since the wings initially tested had a larger  $Ro$  of between 8 and 9, a new set of wings were made with smaller  $Ro$  (6 and 4.8). Since the previously determined wing length and offset appear to maximize actuator output,  $Ro$  was decreased by increasing mean chord length. Due to the variation in chord length the rotation axis was standardized to 15% of the maximum chord. These wings retained the twist design as initial tests showed improved results over the original rigid design.

## 4.6.2 Wing Fabrication

In order to modulate wing stiffness with as few carbon fiber layers as possible, several layers were pressed together before being cut into the wing frame pattern. For the first set of wings, this consisted of two layers pressed orthogonally (0-90 grain direction) that were then cut with a laser ablation system. Only two layers were used due to limitations of the cut depth of this laser system. Although asymmetric carbon fiber layups generate residual stresses due to the anisotropic thermal expansion (the coefficient is slightly negative in the grain direction, but large and positive orthogonal to the grain), we hoped that the effect would be minimal since the final assembly (0-90-kapton-90-0) would be symmetric. 0-90 and 0-45 layups were used for the hand laid fabrication of the same spar pattern. For the first iteration of the twisted wing (fabricated by hand), a symmetric 0-90-0 layup was used. These wings were cured with the same temperature and pressure as done previously, but the leading edge was reinforced with smaller rods (0.5 or 0.3mm diameter).

For the second fabrication procedure, we attempted to take advantage of the adhesive prepreg to join all wing assembly elements and minimize additional glue weight. For these wings we continued to use the 0-90-0 layup for each layer. Since the curing of the laminate assembly

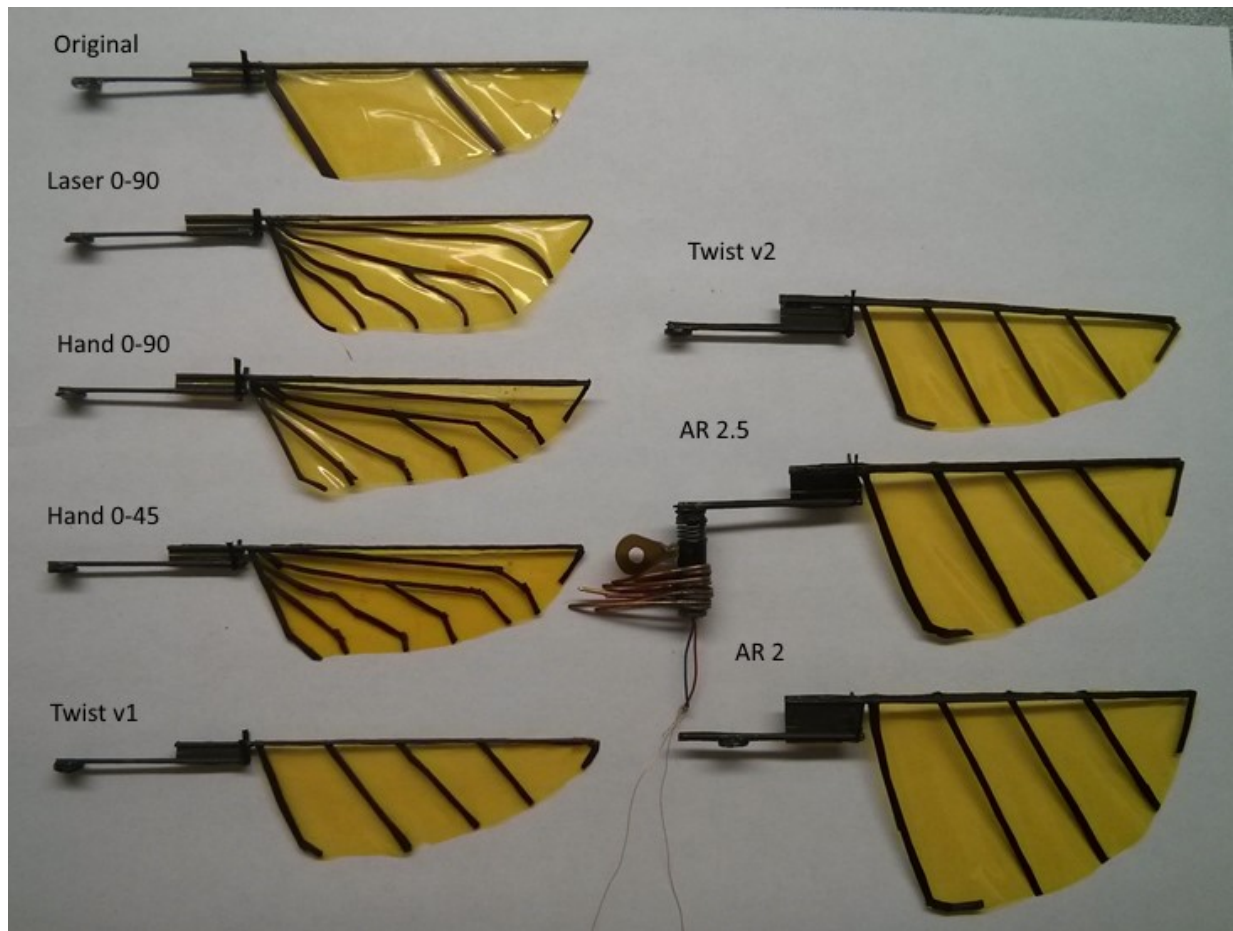


Figure 4.15: Images of fabricated full wing assemblies with labels.

requires it to lay flat, rods could only be included on the top side. After curing of the assembly, rods were glued to the back side of the leading edge and wing offset.

All fabrication results are shown in Figure 4.15, with predicted and actual weights shown in Table 4.2. The predicted and actual weights are of the final tested wings that include all reinforcing modifications. The original wing has a high glue weight fraction due to being repaired several times. This clearly motivates fabrication of new wings instead of repairing wings when possible. Due to the amount of stiffening modification that was done for all wings, it is difficult to evaluate the benefits of the improved manufacturing procedure in terms of minimizing added glue weight.

### 4.6.3 Experimental Setup

For testing of the wings a single motor and wing were used. From previous work with the full two wing system, there did not appear to be any significant wing interference effects when the wing amplitude remained below  $170^\circ$ . A control computer with two DAQ boards (National Instruments PCIe-6353 and PCI-6952e) were used for testing, shown in Figure 2.3. One card generated

Table 4.2: Predicted wing assembly weight vs. measured weights to quantify added glue mass. All weights in milligrams.

Wing:	Original	0-90 Laser	0-90 Hand	Twist v1	Twist v2	AR2	AR2.5
Spar Pattern	93.07	116.88	93.55	80.86	128.79	158.3	200.55
Base	29	29	29	29	29	29	29
Flexure	15.14	15.14	15.14	16.3	27.7	34.6	31.68
Offset	42.56	42.56	42.56	42.56	15.94	59.76	33.5
Stopper	17.13	14.46	20.17	15.67	2.75	3.49	2.95
Predicted Weight	196.9	218.03	200.41	184.39	204.18	285.14	297.68
Actual Weight	283.6	241.6	241	226	239.4	326.8	318
Glue Weight	86.7	23.57	40.59	41.61	35.22	41.66	20.32
Glue Percentage	30.57%	9.75%	16.84%	18.41%	14.71%	12.75%	6.39%

sinusoidal control signals for the motor driver (Dimension Engineering SyRen 10) that powers the motor. The voltage (measured directly as an analog signal) and current (ASC712-30A) output of the driver were measured in order to calculate the input power to the motor. Calculating power as the product of current and voltage has been the most accurate way to measure input power, since heating of the motor leads to changes in winding resistance during the trial. Force was measured with a load cell (ATI Nano17 Titanium) and wing kinematics were extracted from high-speed video (PCO Dimax).

#### 4.6.4 Resonance Testing

The load cell was also used to determine wing natural frequency. The wings were mounted on the cell horizontally and then excited with a mechanical impulse. The resulting force trace was analyzed using FFT to determine the dominant frequency components that correspond to the resonance modes of the structure, shown in Figure 4.16a for the original wing. Leading edge stiffness was also found by displacing the tip of the wing by different amounts and measuring the resulting force on the load cell, shown in Figure 4.16b. Full results are shown in Table 4.3. For these tests only the original wing included reinforcing rods.

#### 4.6.5 Experimental Wing Characterization

Once the wing assembly was completed the wings could be tested. First the wing was tested at a nominal frequency (18 Hz) at a large amplitude (2.4). The force trace was examined to ensure that lift peaks had similar maximum amplitudes (indicating symmetric stopper placement) as well as having consistent troughs (indicative of the quality of wing rotation and flexure integrity). In some cases the stoppers were narrowed past the standard 45 degrees to account for chordwise deflection of the entire wing or twisting of the entire wing assembly. In cases where the deflection of the wing appeared to decrease lift excessively, additional rods were added to the wing to increase stiffness and subsequent lift generation. For example, stiffening the 0-90 laser and AR2

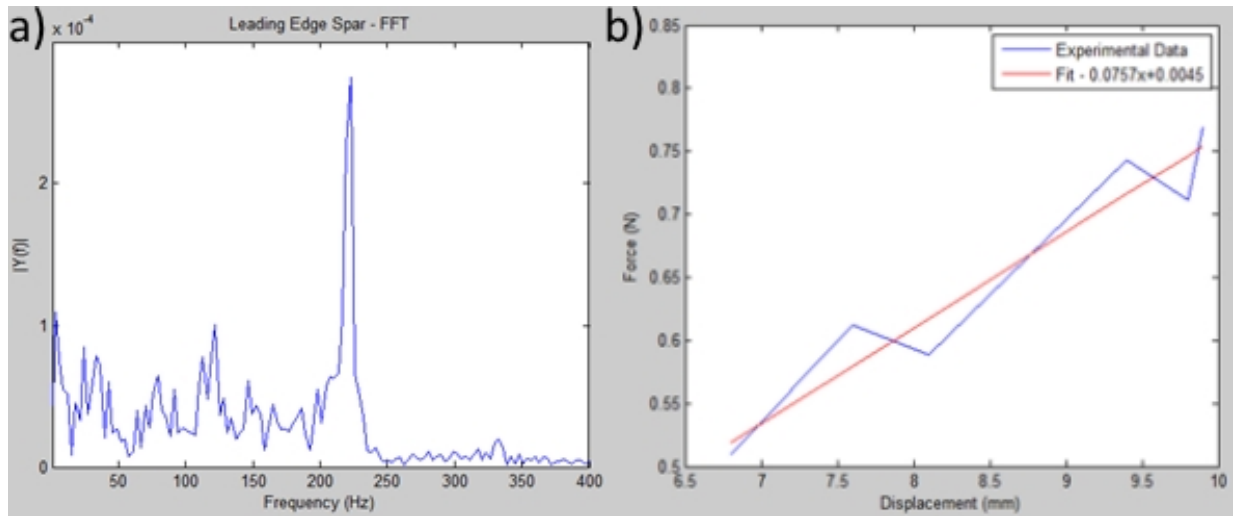


Figure 4.16: a) Determination of wing spanwise resonance mode, and b) leading edge stiffness.

Table 4.3: Resonance and stiffness testing results. A \* indicates the dominant natural frequency, while other recorded peaks were conserved across trial, but appeared at lower magnitudes.

Wing	Leading Edge Natural Frequency (Hz)	Leading Edge Stiffness (N/m)	Chordwise resonance modes (Hz)
Original	221.7	75.7	24.04, 76.57*
0-90 Laser	27.47	0.997	32.96
0-90 Hand Laid	24.41	0.73	24.41, 50.35*
0-45 Hand Laid	24.41	0.572	38.15
Twist v1			38.93

wings resulted in increases in maximum lift production from initial tests by a factor of 2.26 and 2.58 respectively.

Once the configuration of the assembly was finalized, the resonance frequency of the system was determined. The flapping frequency of the system was varied from 16 to 22 Hz at a constant input amplitude of 2.4. The flapping amplitude was measured from the high speed video by averaging the amplitude for wing strokes five through seven from the trial. This was done to make sure the wing achieved full amplitude as it typically takes up to three wing strokes for the wing to do so as energy is added to the spring. While system resonance corresponds with maximum flapping amplitude, from previous experiments it has been determined that maximum lift is usually achieved at a frequency just above resonance. Once the system resonance was determined the system was tested at 1 Hz higher, which will be referred to as the operating frequency.

At the operating frequency the system was tested at six input amplitudes: 0.8, 1.2, 1.6, 2.0, 2.4, 2.8 with the input voltage to the motor driver set to 10 V. The input signal is a sinusoid with the selected amplitude centered at 2.5 V, that is mirrored by the driver and runs the motor in both directions. The input amplitude represents the amplitude of this sinusoidal input to the driver, with the input to the driver capped at 5 V. In the case of input 2.8, the sinusoidal waveform is truncated to the maximum amplitude to generate a ramped square wave signal that is used to generate maximal system performance at a given driver voltage. The input signal to the driver represents the amount of output voltage it should deliver, with an input of 5 V corresponding to an output of 100% of the input voltage, 3.75V to 50%, 2.5V to 0%, 1.25 to -50%, and 0V to -100%.

Lift was measured from the load cell and taken to be the average of wing strokes 4-14. Power data was averaged over the entire trial and the average of three tests was taken. Due to limitations of our setup these two metrics were taken independently. Current and voltage must be sampled at high frequencies since the motor driver generates a 32 kHz pwm signal. Force data was collected at 50 kHz, while current and voltage data were collected at 80 kHz.

## 4.6.6 Results

As expected, the first iterations of the wings with no reinforcing rod along the leading edge underwent significant deflection during the wing stroke as seen in Figure 4.17. Even though the spanwise resonance mode was well matched to the flapping frequency, the deflection of the wing resulted in a significant decrease in lift production. Since the lift obtained was less than the lift required for takeoff, the leading edge was reinforced. One clear issue was that deflection of the wing appeared to interrupt wing rotation, which was more delayed and less smooth than for the original stiff wing. From the high speed video, deformation of the wing in the chordwise direction appears to generate wing displacement orthogonal to the stroke plane. This motion appears to interrupt the smooth operating of the motor, contributing to the issues with wing rotation. This off-axis loading on the output shaft of the gearbox may also lead to degradation of the performance over time.

The experimental results are shown in Figure 4.18 and Table 4.4. A comprehensive table with relevant wing parameters is shown in Table 4.5. There were minimal differences between the laser cut and hand laid spar pattern, but these wings had lower performance than the original

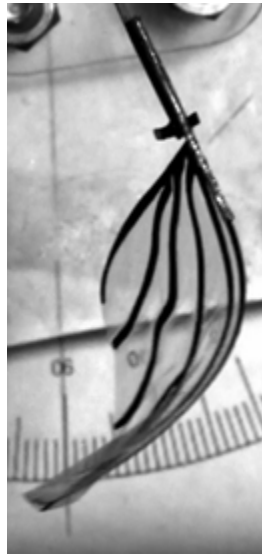


Figure 4.17: Example of wing deflection for 0-90 laser.

Table 4.4: Lift/power (mN/Watt) results for all wings tested.

Wing Design	Lift per Input Power (mN/Watt)
Original	14.9
Hand 0-90	14.2
Laser 0-90	14.4
Twist v1	16.5
Twist v1 (new system)	17.8
Twist v2 (new system)	25.8
AR2 (new system)	18.2

wing design. Data for 0-45 hand laid is not shown since even with additional reinforcement the wing underwent excessive deformation. The first iteration of the twist wing outperformed the original so this design was used for the second iteration of wings. A new motor system was used to test the second iteration of wings. Twist v1 was tested on both these systems, with the newer system having slightly improved performance. This was expected since the motor had a higher unloaded speed in testing (in the range of 2600-2700 rpm, whereas the original had been 2400-2500 rpm). This speed difference reflects a difference in gearbox efficiency, which affects the lift per power fit slope. However, since the same wing was tested on both systems the difference between the slopes could be used to roughly scale all results and compare them directly.

The second iteration twist wing has the best performance, while the larger wing that was tested has similar performance to the initial twist wing. The larger wing has additional disadvantages of being heavier, having more delayed rotation, and operating at a lower frequency. The vertical deflection of the larger wing, and thus off-axis loading on the gearbox, appeared to be larger and the system degraded substantially with subsequent tests of this wing (performance decreased with each test). Upon re-testing the twist v1 wing, the lift production of the system

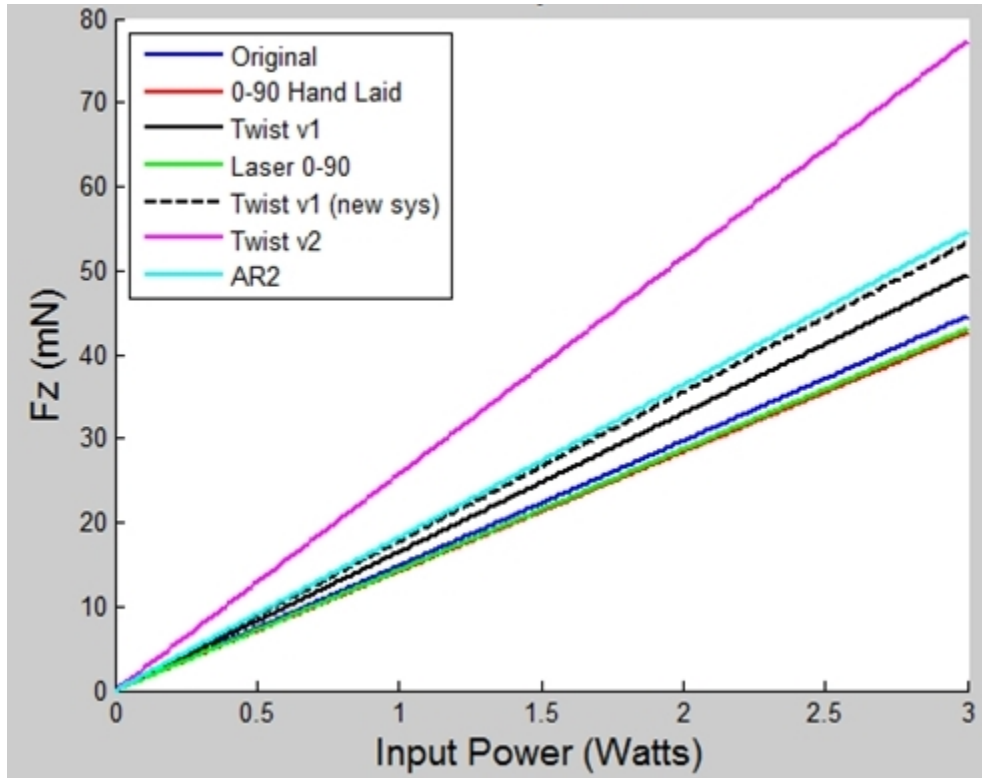


Figure 4.18: Lift per power results of all wings tested.

Table 4.5: Relevant wing information. Lift per wing weight represents a figure of merit. Rotational delay percentage is measured from high speed video and should produce large aerodynamic effects (0% constitutes symmetric rotation, while delayed rotation is considered  $> 8\%$  delay). Wing area is measured for the actual wings. Aspect ratio and Rossby number are for the ideal wing shapes produced in simulation.

Wing Design	Lift per Weight (mN/g)	% Delay (L — R)	Wing Area ( $mm^2$ )	Aspect Ratio	Rossby Number
Original	132.5	3.6 — 7.1	1360	3.6	8.58
Hand 0-90	149.6	3.9 — 3.9	1290	3.8	9.04
Laser 0-90	146.8	6.0 — 6.0	1480	3.31	7.88
Twist v1	168.6	2.0 — 2.0	1300	3.77	8.97
Twist v1 (new)	183.2	2.0 — 0	1300	3.77	8.97
Twist v2	272.9	6.0 — 0	1430	3.43	8.16
AR2	174	10.7 — 7.1	2440	2.01	4.78
AR2.5	n/a	n/a	1930	2.54	6.04

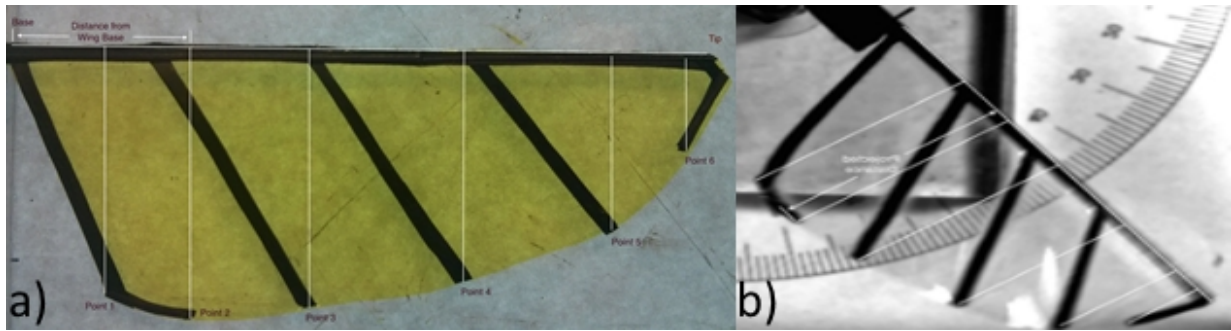


Figure 4.19: a) Flat and b) fully twisted wing image, both with measured chordwise distances shown.

had decreased by 15%. The off-axis loading of the gearbox may play a larger role than expected in determining system performance. The L/P fit lines are based on the last 3 points, as the first 3 points tended to have a higher slope (13.9% higher on average, excluding AR2 which had the opposite trend). This lift per power dependence on amplitude may further indicate reduction of gearbox performance when under high loading. Large wings were seen to have greater vertical deflections that decreased performance, confounding any putative increase in aerodynamic performance due to the lower Rossby number.

In order to quantify the twist profile from these images, two assumptions were made to simplify the quantitative analysis. First, it was assumed that only wing rotation and wing twist change the projected distance from the leading edge to the selected points. Choosing different rotation angles shifts the twist plot up or down, while differing magnitudes of twist alter the gradient of the twist plot. Second, the angle of attack of the fully rotated wing is assumed to be close to 45 degrees. In the case of the larger wings tested, significant twisting of the wing assembly introduced a large shift into the twist data. A sweep of the assumed angle of attack was done to minimize the apparent twist of the first point, which resulted in an assumed angle of attack of 60 degrees, which is reasonable. This was done in order to provide a better comparison of the twist distribution across the wings. For each point, the projected distance at the assumed angle of attack was subtracted from the projected distance measured from the video. The result was averaged over multiple frames that were selected from different wing strokes. This difference was then normalized by the distance measured from the untwisted wing image. This resulted in a plot of percent twist along the wing length shown in Figure 4.20. Since the wings had different spar positions the selected points are not identical across the wings. To make the visualization somewhat easier all wings were assumed to have zero twist at the base. The result was then normalized by the corresponding distance measured from the flat wing.

In order to better compare our results to previous work, we calculated a figure of merit for our wings based on equation 32 from Whitney and Wood,

$$I_w = \frac{\sqrt{W}R^4}{M_1} \quad (4.7)$$

where  $W$  is the maximum lift produced by a wing pair in experiment,  $R$  is the wing length, and  $I_w$  is the wing mass moment of inertia calculated from our CAD model [4]. The original wing

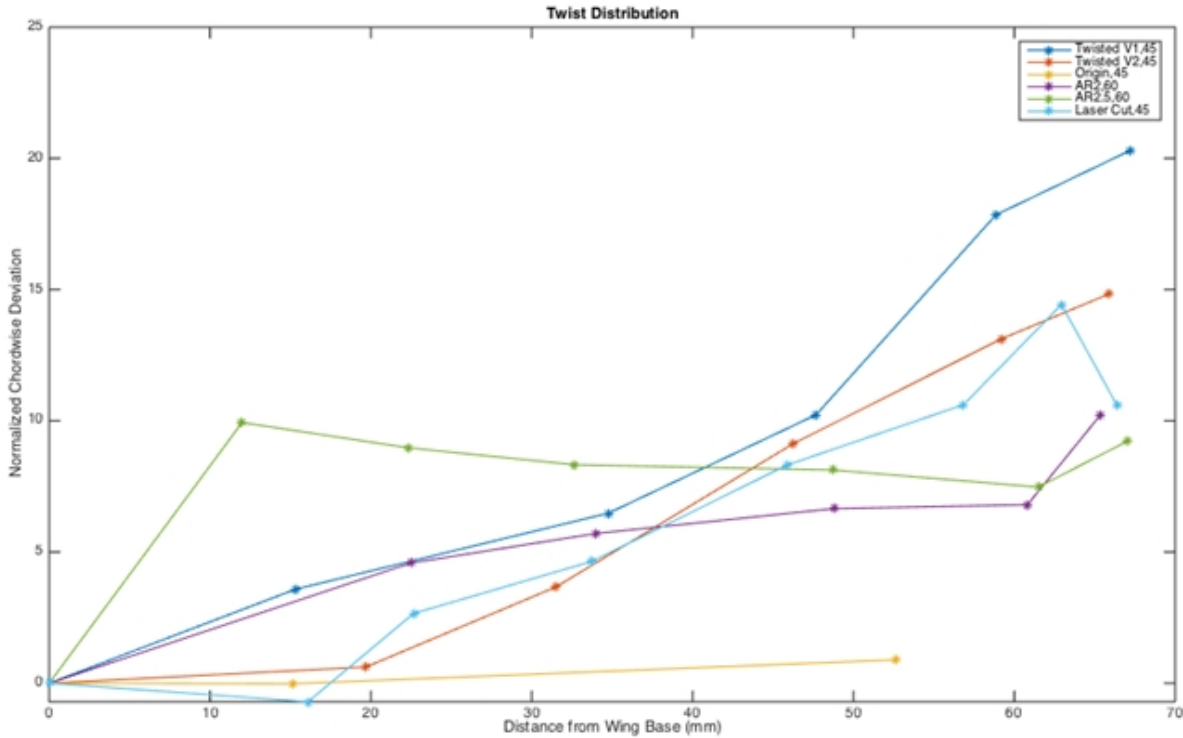


Figure 4.20: Normalized percent wing twist vs. wing length.

has a relatively high figure of merit and is almost identical to the design of the artificial wing as shown in figure 39. However, the other designs have a trend of decreasing performance as their mass moment of inertia increased with their size and complexity. Calculating the figure of merit based on equation 33, would have likely provided more consistent results as it accounts for structural efficiency of the wing structure, but not all necessary parameters could be calculated. This metric motivates the exploration of alternative methods to modulate wing twist without the addition of additional chord spars that increase the mass moment of inertia. This may be possible by varying the number of carbon fiber layers used along the leading edge or tapering the diameter of supporting rods. For the purpose of providing a simple metric to compare the structural performance of the wings studied, lift per wing weight is calculated in table 13. These results show an increase in performance for most of the wing design and highlights twist v2 as clearly having the best results. However, it would be interesting to test a newly fabricated wing of the original design since the one used in this study had a high glue weight due to repairs.

This study concludes that the wing leading edge should be stiff and that chordwise deflections should be structured in order to produce a linear twist distribution for our system driven in open loop. We could not replicated resonance based lift improvements predicted from simulation. Deformation of the wing significantly reduced effective wing area during translation and disrupted rotation at stroke reversal. While resonance improvements may be possible for insects that can precisely tune their flapping kinematics using sensory feedback with high temporal resolution, it was not possible to achieve for our system that is driven in open loop and depends on passive wing rotation. Improvements based on decreasing Rossby number to strengthen the lead-

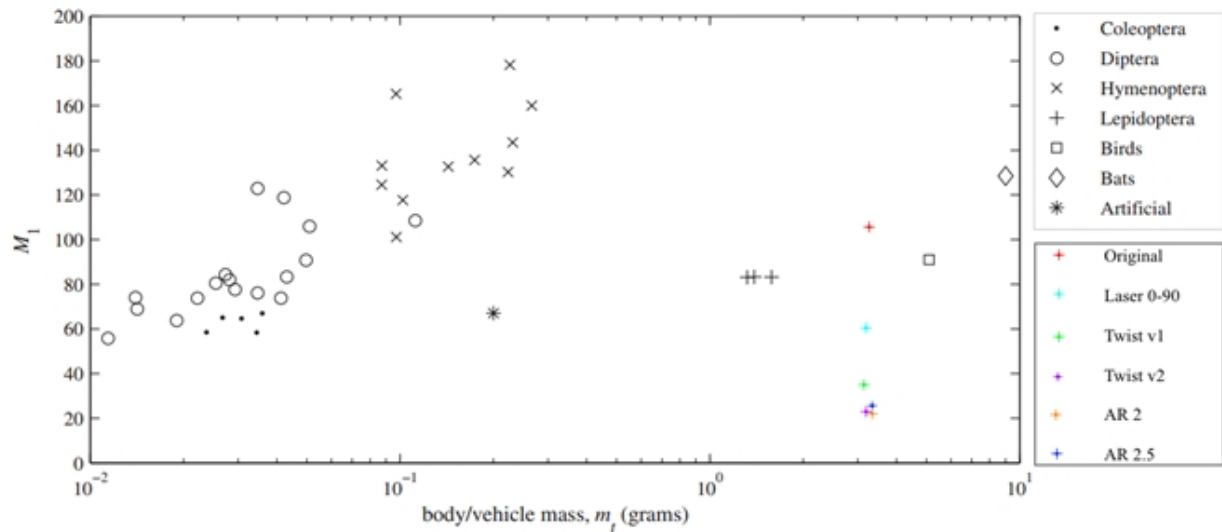


Figure 4.21: Wing structural-inertial efficiency. Figure of merit plot reproduced from [4], with added data for our fabricated wings

ing edge vortex force augmentation could also not be replicated. Since the wing size and offset for our system has resulted in the best lift performance, to modulate Rossby number the mean chord length was increased. This larger wing size increasing vertical stroke plane deflections that decreased performance at large amplitudes.

With respect to lift performance, wing deformation appears to play an important role. Deflection of the wing along the leading edge was found to be undesirable. Results from the bio-inspired wing pattern also indicate that chordwise deflection can be undesirable if not controlled properly. The correct way for the wing to deform appears to be in order to develop a twist profile. The best performance was seen in twist v2, which had the most linear twist profile as shown in Figure 4.20. In order to calculate wing twist, frames were taken from the high speed video showing the full wing length at about 75% of the wing stroke where we expect the wing to be fully twisted. While having an image closer to mid stroke could provide more consistent results, due to the limitations of the image size at high frame rates mid stroke frames did not include the entire wing length. For each wing, points at the base of the spars were selected since they are the easiest to repeatedly identify in the recorded images. The distance between each of these points and the leading edge is measured in both the recorded images (provides a measure of the projected distance) and from a flat, untwisted image of the wing as shown in Figure 4.19.

## 4.7 Wing Twist Experiments and Analysis

Wings used in this set of experiments are shown in Figure 4.22. The length of the wing is 70 mm, with a mean chord of 20.5 mm, and a 38 mm offset is used from the wing base to the motor shaft. The rigid-wing design used two reinforcing spars and a 1 mm diameter carbon fiber rod was added to the leading edge to ensure the wing was fully rigid. For the flexible wing designs, Twist v1 and Twist v2, torsional stiffness had to be decreased such that the aerodynamic forces could

dynamically shape the wing. Twist v1 used only half of a 1 mm rod along its length, while Twist v2 had half of a 1 mm rod for the basal 57% of wing with a 0.3 mm diameter rod supporting the rest of the leading edge to the tip. Furthermore, these designs used five supporting spars in order to provide additional locations where the distributed aerodynamic force on the wing membrane could be transmitted as a torsional load to the leading edge.

Wings were tested using a control computer with two DAQ boards (National Instruments PCIe-6353 and PCI-6952e) as shown in Figure 2.3. One card generated sinusoidal control signals for the motor driver (Dimension Engineering Sabertooth 2x32) that powered the motor. To determine the system resonance, the control signal frequency was varied from 10 to 30 Hz at constant input voltage amplitude of  $4.9 V_{rms}$  for each wing. The resonant operating frequency was selected based on minimum current draw, which also corresponds with the maximum flapping amplitude. The determined frequencies were 21, 22, and 23 Hz for the original, Twist v1, and Twist v2 designs, respectively, with variation due to differences in weight between designs. At the resonant frequency, each wing was tested at four input voltages: 4.9, 5.5, 6.2, and 7.2  $V_{rms}$ . Lift was measured directly from the load cell (ATI Nano17 Titanium) by averaging wing strokes 5 to 125. The raw force data contained contributions from aerodynamic forces and inertial effects due to wing motion, particularly vertical motion during stroke reversal. The data was processed to remove inertial effects. Although this processing changed the magnitude of the measured lift force, the relations between wings remained similar and will be references throughout. Given that the wings were designed with consistent axes of rotation and symmetric rotational dynamics were measured from high-speed video, the contribution of rotational effects on stroke-averaged lift was expected to be negligible. Therefore the stroke-averaged forces were considered to be translational lift only. The voltage (measured directly as an analog signal) and current (ASC714) output of the driver were measured by the second DAQ board and were averaged over the same wing strokes to calculate the input power to the motor. Inertial power was estimated from separate proof mass tests and subtracted from the measured power in order to calculate the aerodynamic power. Flapping amplitude was measured using Matlab image processing of high-speed video (PCO Dimax) images over the same wing strokes. Twist was also characterized from high-speed video images at mid-stroke, where the twist profile was fully developed by measuring the projected distance between points on the trailing edge and the leading edge. The difference between the projected distance measured from the video images and that of the untwisted wing was then used to calculate the local area of attack at each measured point.

### 4.7.1 Results and Discussion

Lift results as a function of the aerodynamic power input are shown in Figure 4.23a. The tested powers corresponds with the nominal operating range of the rigid-wing during hovering of the vehicle, with the lowest point surpassing the takeoff lift requirement of 26 mN. Twist v1 and Twist v2 produced improvements of 41.3% and 22.1%, respectively (44.3% and 17.1% from raw data), over the rigid-wing design with respect to aerodynamic efficiency. These designs also increased translational lift production by 35.3% and 17.7%, respectively (38.1% and 12.9% from raw data), indicating that the twisted shape resulted in increased lift coefficients. Results of the calculated wing twist profiles are shown in Figure 4.23b. The rigid-wing design displayed minimal twist as expected. Twist v1 was highly twisted with a 0.29 degree/mm profile for the

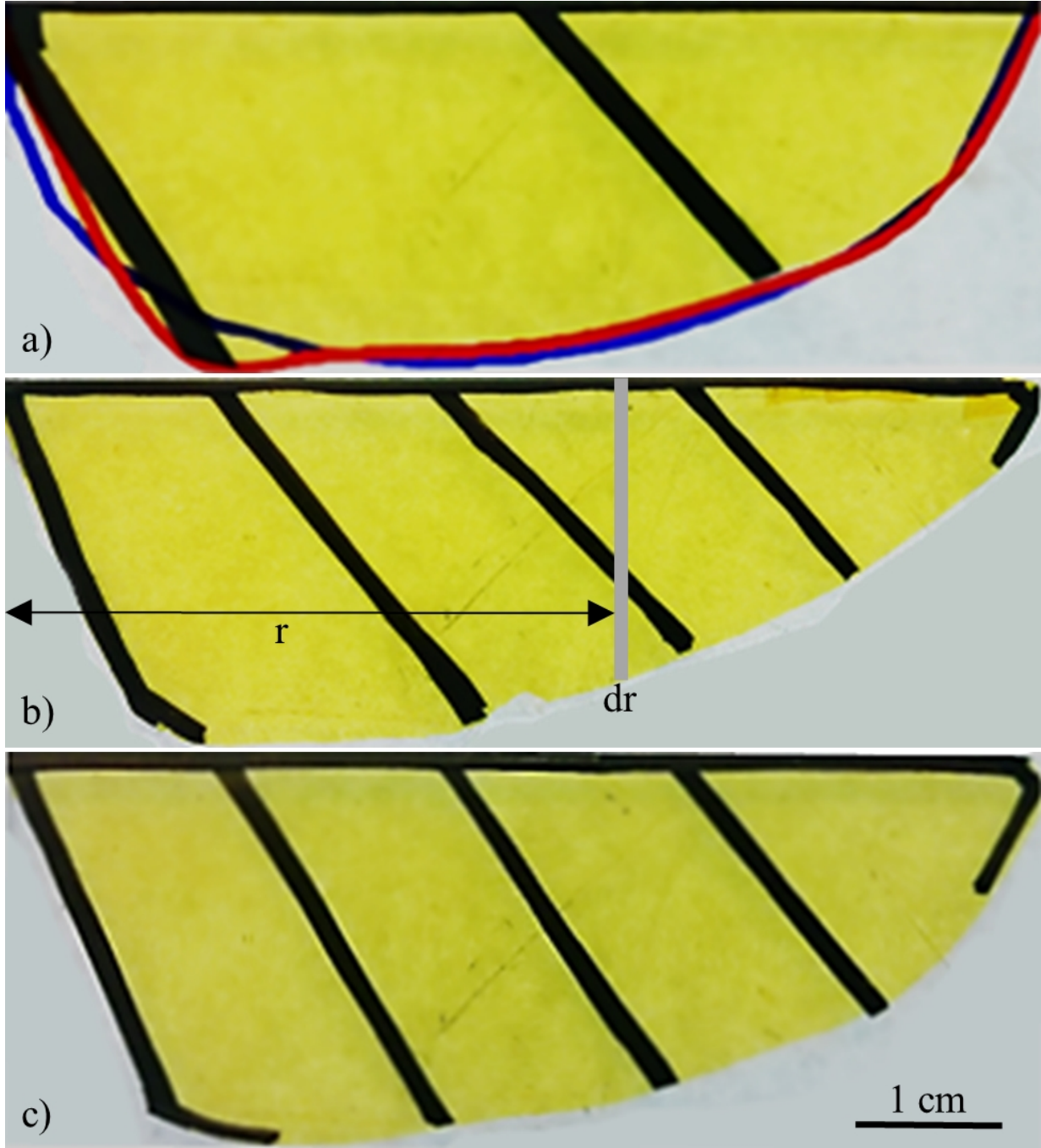


Figure 4.22: (a) Rigid wing with  $\hat{r}_2 = 0.54$  beta distribution shown in blue and the modeled wing spline shown in red, and flexible wing designs, Twist v1 (b) and Twist v2 (c), with distance  $r$  and element  $dr$  shown.

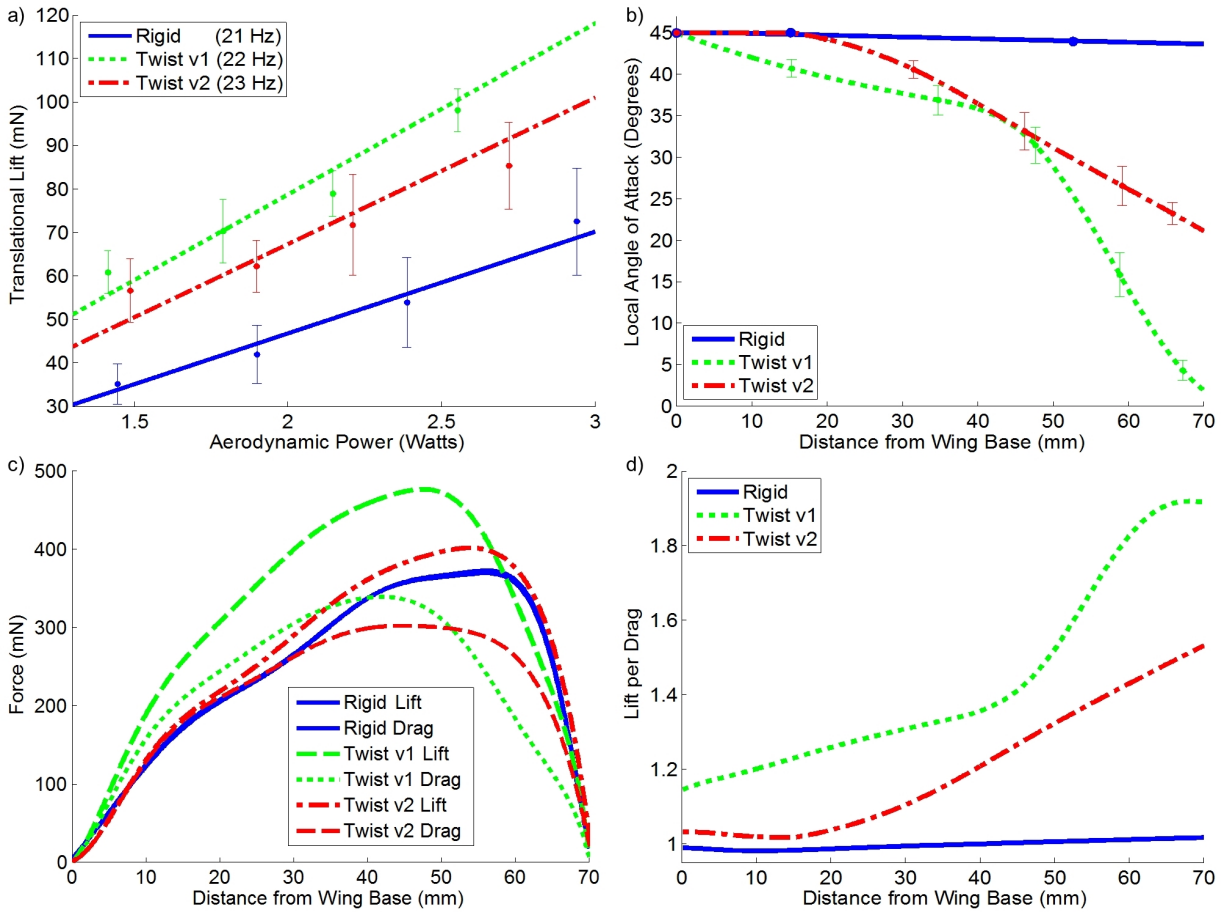


Figure 4.23: (a) Experimental lift results as a function of input aerodynamic power. (b) Calculated twist profiles from experimental high-speed video images. (c) Simulated lift and drag distributions based on twist profiles. Lift and drag are equal for the rigid-wing design, and appear as a single line. (d) Simulated lift per drag, aerodynamic efficiency, along the wing length based on twist profile.

basal 48 mm of the wing and a 1.39 degree/mm profile for the remaining 22 mm. Twist v2 displayed minimal twist for the basal 20 mm and had a constant 0.46 degree/mm profile for the remaining 50 mm of the wing.

These twist profiles were then used to model the stroke-averaged translational lift and drag forces along the wing as shown in Figure 4.23c. The instantaneous half-stroke wing velocity field was modeled based on the wing flapping amplitude, wing rotation, and operating frequency. Dynamic twisting of the wing was included based on high-speed video analysis such that the wing linearly transitioned from flat to fully twisted over the first 20% of the stroke, remained fully twisted for the subsequent 60% of the stroke, and returned to flat over the final 20%. A quasi-steady blade element model was used to estimate the lift and drag forces per segment based on the force coefficients from Figure 4.12, which were then integrated along the wingspan. To estimate changes in force coefficients, the total lift was scaled to match the experimental results. Aerodynamic power was also scaled by the experimental values and then normalized such that

the rigid-wing operated at a constant lift per drag (L/D) of one. The experimental analysis, summarized as follows, allows the effects due to 3D wing flexibility to be quantified in the quasi-steady, blade element simulation framework by using the rigid wing as a baseline.

- Estimate lift and drag forces per segment using quasi-steady blade element and measured experimental wing kinematics
- Rescale lift distribution by a constant factor for each wing so that total simulated lift matches stroke-averaged experimental result. This constant factor represents the change in effective  $C_L$
- Rescale power by a constant factor for each wing so that the total simulated power matches stroke-averaged experimental result. This constant factor represents the change in effective  $C_D$
- Rescale drag distribution by the constant factors determined from power (the effective  $C_D$ )
- Normalize drag distribution of the rigid wing so that total lift and drag are equal (as expected due to 45 degree angle of attack)
- Rescale the drag distribution of the flexible wings by the determined normalization factor

The resulting L/D along the wings is shown in Figure 4.23d. This analysis shows increases in the effective lift coefficient by 63.6% and 13.3%, respectively (67.1% and 8.6% from raw data), for Twist v1 and Twist v2. It is possible that the twisted shape of the wing stabilizes or strengthens the leading edge vortex (LEV) resulting in observed increase in the lift coefficient. This could occur directly due to the 3D shape of wing, increased spanwise flow, or decreased angle of attack near the tip could prevent bursting of the LEV. Such mechanisms for strengthening of the LEV are discussed in work by Lentink *et al.* [35]. The trend of increasing aerodynamic efficiency and lift production is also consistent with computational fluid dynamics (CFD) results by Noda *et al.* for flexible wings [149]. Twist v2 displays a moderate twist profile that improves efficiency along the entire wingspan, primarily through a reduction in drag. Although lift production is slightly improved, the lift distribution remains similar to the rigid-wing design that is biased towards the wing tip. The highly twisted profile of the Twist v1 design greatly improved efficiency along the wing, especially near the tip. The lift and drag distributions are re-shaped to better match the ideal elliptical distribution. This design produces significantly more lift in the center of the wing, while achieving similar drag to the other designs. Lift towards the tip is similar to the other designs, but with significantly reduced drag likely due to a reduction of wing tip vorticity.

Simulation output is summarized in Table 4.6. The scaling factors to match lift and power to experimental data are  $L_{correct} = [0.9074, 1.4851, 1.0280]$  and  $D_{correct} = [2.6192, 3.7068, 2.8451]$  for rigid, twist v1, and twist v2 respectively. The large discrepancy in drag indicates that significant power is consumed by the flapping mechanisms and/or that drag coefficients are not correctly modeled for this Reynolds number regime. The results scaled to match processed experimental data are summarized in Table 4.6 column three, while those scaled to match raw experimental data are summarized in column four. For the raw experimental data  $L_{correct} = [0.6133, 1.0249, 0.6665]$ . We see that removal of the inertial artifacts from the data has minimal effects on the relative performance of the wings. It does however bring the lift values to within 10% of the estimated values, indicating that the procedure for processing experimental data is valid.

Table 4.6: Flexible Wing Simulation Results

	Simulation	Scaled Experiment	Scaled Experiment Raw
Lift Original (mN)	79.899188	72.500000	49.000000
Lift Twist v1 (mN)	66.057401	98.100000	67.700000
Lift Twist v2 (mN)	82.975063	85.300000	55.300000
Drag Original (mN)	114.570124	72.500000	49.000000
Drag Twist v1 (mN)	77.531168	69.433998	46.927806
Drag Twist v2 (mN)	101.634007	69.859554	47.215423
Power Original (W)	1.122889	2.941100	2.941100
Power Twist v1 (W)	0.688783	2.553200	2.553200
Power Twist v2 (W)	0.956215	2.720500	2.720500
LoD Original	0.697382	1.000000	1.000000
LoD Twist v1	0.852011	1.412853	1.442642
LoD Twist v2	0.816410	1.221021	1.171227
Twist v1 increase in CL (%)		63.663518	67.114244
Twist v2 increase in Cl (%)		13.293710	8.673543
Twist v1 increase in CD (%)		41.523717	41.52371
Twist v2 increase in CD (%)		8.622586	8.622586

Now that the performance of our fabricated wings has been characterized, it can be compared to optimal designs predicted by the quasi-steady model. Integrating under the lift curve in Figure 4.23c gives total stroke-averaged lift, while integrating under the L/D curve in Figure 4.23d provides a metric of flapping efficiency. These lift and efficiency metrics were co-optimized using MATLAB *ga* to generate a Pareto frontier that shows all potentially optimal twist profiles for different weightings of lift versus efficiency. The optimization was constrained to strictly increasing twist profiles that take advantage of the increasing oncoming flow velocity along the wing to generate twist. The frontier demonstrates the expected tradeoff between lift production and efficiency. Wing twist, which decreased the average angle of attack, results in a more efficient wing that produces less lift. Furthermore, the simulation results indicate that this tradeoff can be achieved by uniformly changing the angle of attack of the entire wing, effectively adjusting the rotational stoppers for a rigid wing. This could be implemented with the use of additional actuators as is done by the Nano Hummingbird, but ultimately reduces the lift per weight of the vehicle [50]. Our experimental results indicate that the standard quasi-steady model does not account for changes in force coefficients due to 3D twisted wing shapes. Therefore, the simulation was updated to include a 3D shape factor, fit from experimental data, which accounts for the lift augmentation due to increasing wing twist profiles.

The new Pareto frontier is shown in Figure 4.24. This frontier indicates a range of optimal average wing twists between 1.28 and 1.45 lift per drag. The resulting twist profiles are shown in Figure 4.25. Wings producing the most lift have low twist in the basal half of the wing with uniformly increasing twist along the distal portion, similar to the Twist v2 design. However, the lift production compared to Twist v2 is increased by 9.5% by increasing the basal twist from an average of 0.17 degrees/mm to 0.27 and distal twist from 0.51 degrees/mm to 0.83. Wings designed for higher efficiency display a two-stage twist profile similar to Twist v1, although the model falls short of predicting the lift achieved by this design. However, there are some differences in the shapes of these designs. Twist v1 has a nearly uniform twist profile of 0.25 degrees/mm for the basal 45 mm of the wing, whereas the model designs utilize 0.83 degrees/mm for the basal 26 mm of the wing followed by an untwisted section. The distal profile in Twist v1 is 1.27 degrees/mm, while it is 0.79 in the model. The importance of high twist near the wing tip agrees with CFD results by Noda *et al.* [149]. Improved CFD modeling could improve the understanding of the relationships between 3D wing shapes resulting changes in force coefficients, which could be applied to generate better estimates of optimal twisted designs. Furthermore, our results indicate that wing designs with significant twist profiles can provide high performance without active changes in stopper position, which is essential for low mass, underactuated FWMAV systems.

## 4.7.2 Wing Twist Computational Fluid Dynamics Simulation

Since it appears that twisting of the wing modifies its force coefficients, an optimization using the rigid wing drag polar from Dickinson will have limited practical results. For such a simulation to have improved accuracy a correction factor for the overall 3D twisted shape of the wing must be determined. Computational fluid dynamics simulations (CFD) are one possible way of determining this correction. However, the aerodynamics of wings at high angles of attack at low *Re* are difficult to model, in particular due to the effect of the LEV. In addition to any pressure differences generated by the LEV it generates a drag crisis where flow begins to separate from

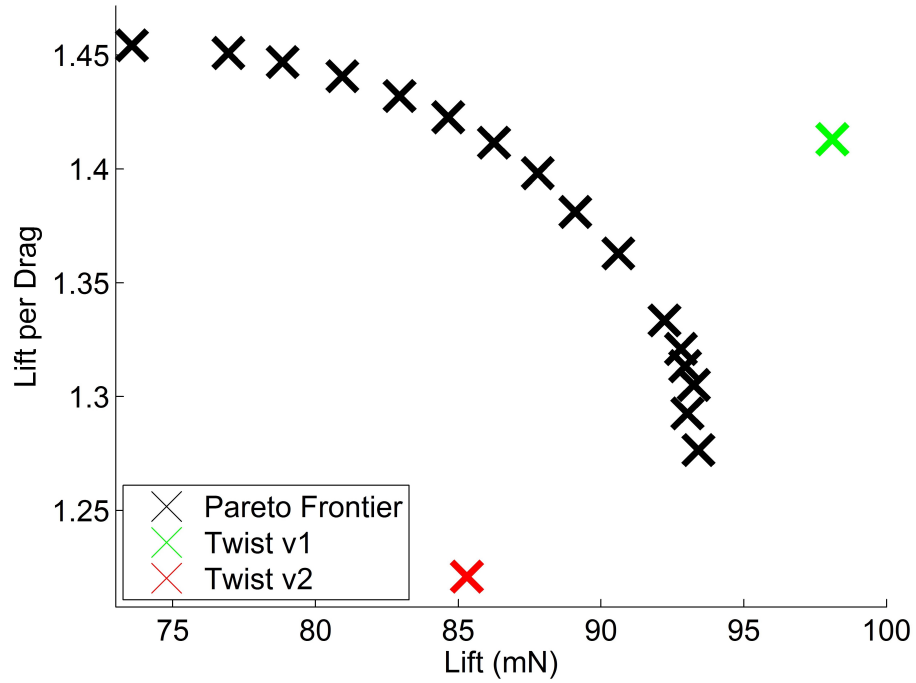


Figure 4.24: Pareto frontier of simulated optimal twisted wing designs.

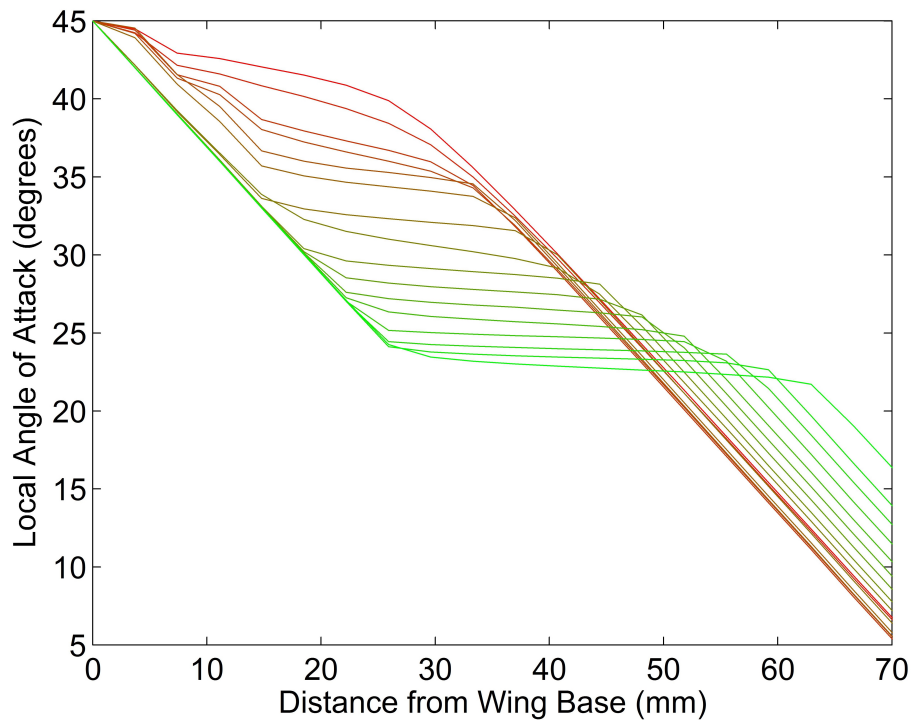


Figure 4.25: Simulated optimal wing twist profiles. Curves go from high lift (top, red) to high efficiency (bottom, green).

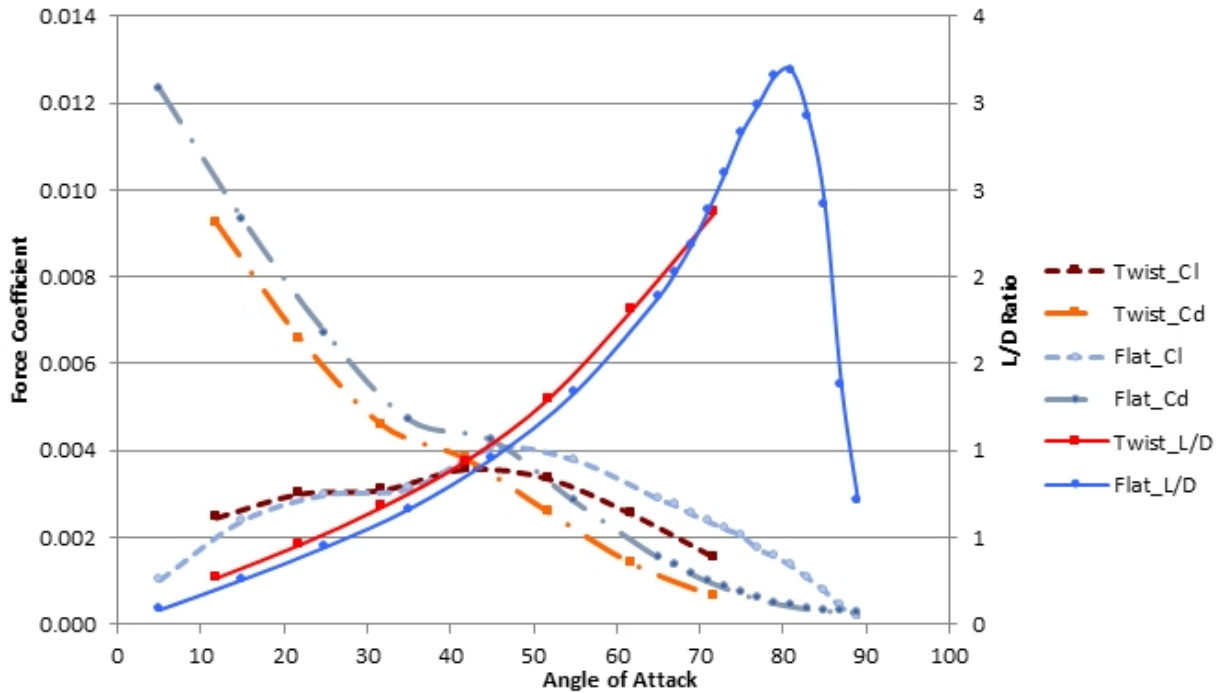


Figure 4.26: Laminar CFD simulation of wing twist.

the wing due to high angle of attack, but due to the generated vorticity the flow is able to re-attach to the wing, decreasing the drag coefficient by reducing the size of the turbulent wake. This behavior effectively generates a laminar flow profile over the wing, so the CFD simulations were chosen to start with a laminar case since it is much more computationally tractable. Results of the laminar CFD simulation are shown in Figure 4.26 comparing the performance of a flat wing and a twisted wing. The wings are compared at the same average rotation angle. The twisted wing can only be operated up to an average rotation angle of 72 since at this point the tip is fully rotated to 90 degrees. The L/D curve has a similar shape to Dickinsons work suggesting that the force coefficient trends are correctly captured. However, the lift and drag coefficients themselves are approximately an order of magnitude lower than expected. The twisted wing shows a marginal improvement in efficiency as its drag coefficient is reduced over the entire range of rotation angles. The lift coefficient of the twisted wing shows minimal improvement over the rigid one for angles of attack under 40, but decreases after this point. While these result do demonstrate efficiency improvements, they do not demonstrate an increase in lift coefficient, which was the main result of our experimental study. A turbulent simulation was also tested in hopes of improved accuracy. Although this simulation did appear to show the formation of an LEV the force coefficient results were very similar to the laminar case. Details of the CFD performed using ANSYS Fluent are provided in table 4.7.

Table 4.7: Details of ANSYS Fluent CFD simulation comparing rigid and twisted wings.

	Transient Polar F&T	Steady Polar F&T
Precision	Double	Single
Solver	Pressure-Based	Pressure-Based
Velocity Formulation	Absolute	Absolute
Time	Transient	Steady
Viscous	Laminar	Laminar
Material	Air	Air
Decouple Scheme	SIMPLE	SIMPLE
Spatial: Gradient	Least Squares Cell Based	Least Squares Cell Based
Spatial: Pressure	Standard	Standard
Spatial: Momentum	Second Order Upwind	Second Order Upwind
Transient Formulation	First Order Implicit	NA
Max Iter/Time Step	30	

### 4.7.3 Particle Image Velocimetry Study of Twisted Wings

Another way to explore the performance of twisted wings is to analyze the flow around the wings. This can be done with the technique of particle image velocimetry (PIV). For PIV small particles, in this case aerosolized olive oil, are injected into the working area. A trigger is used to detect operation of the system, which is followed by two high power laser pulses that are synced with camera exposures. These two images record the reflection of the laser off of particles in a plane of the working volume. The motion of particles between the two successive frames can be analyzed to measure fluid flow. The custom PIV setup, provided by the Bio-Robotics Lab at Purdue, is shown in Figure 4.27. PIV experiments allow the size and strength of the LEV to be analyzed as well as to analyze advective momentum transfer generated by the wing. Initial data processing reveals that despite the high Rossby number of the system, the LEV remains attached along the length of the wing. Figure 4.28 shows shots at approximately 40, 60, and 80% of the wing length.

## 4.8 Conclusion

Biological wings display a huge range of variation with respect to their shape, size, and function. It is up to vehicle designs to derive key aspects of biological wings, such as the flexibility effects of camber and spanwise twist, which can be used as design guidelines for FWMAVs based on size, flapping frequency, and actuator. For successful FWMAVs wings have either been shaped as a rectangle or copied from a model organism. FWMAVs vary in their use of flexibility, with larger systems utilizing large amounts of flexibility for lift augmentation and control, while smaller systems opt for rigid wings, primarily due to small scale fabrication limitations. Limitations of our simulation and initial prototype precluded a study of wing shape for our vehicle.

I demonstrate that a twisted wing design increased aerodynamic efficiency, translation lift, and the effective lift coefficient by 41.3%, 35.3%, and 63.7%, respectively, compared to our

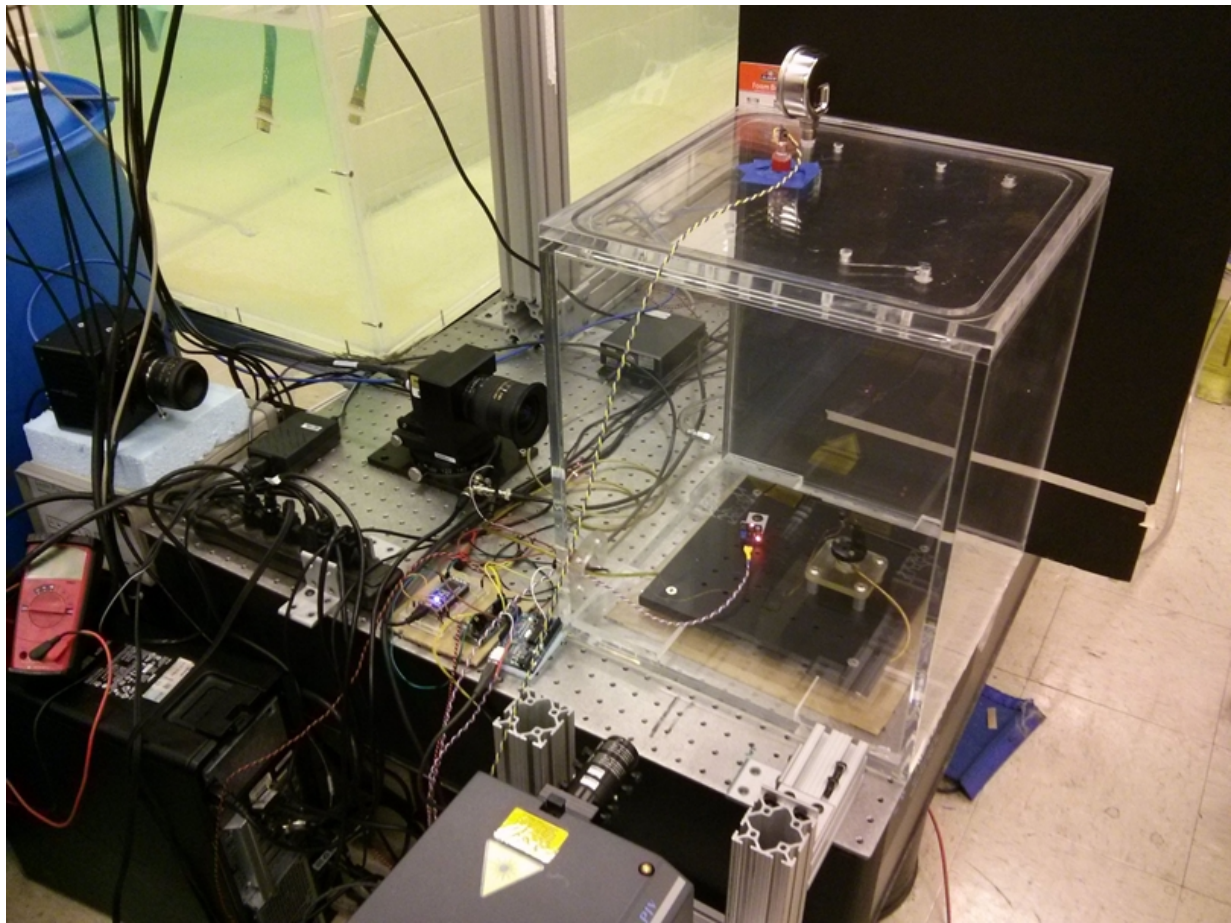


Figure 4.27: Custom PIV setup at the Bio-Robotics Lab.

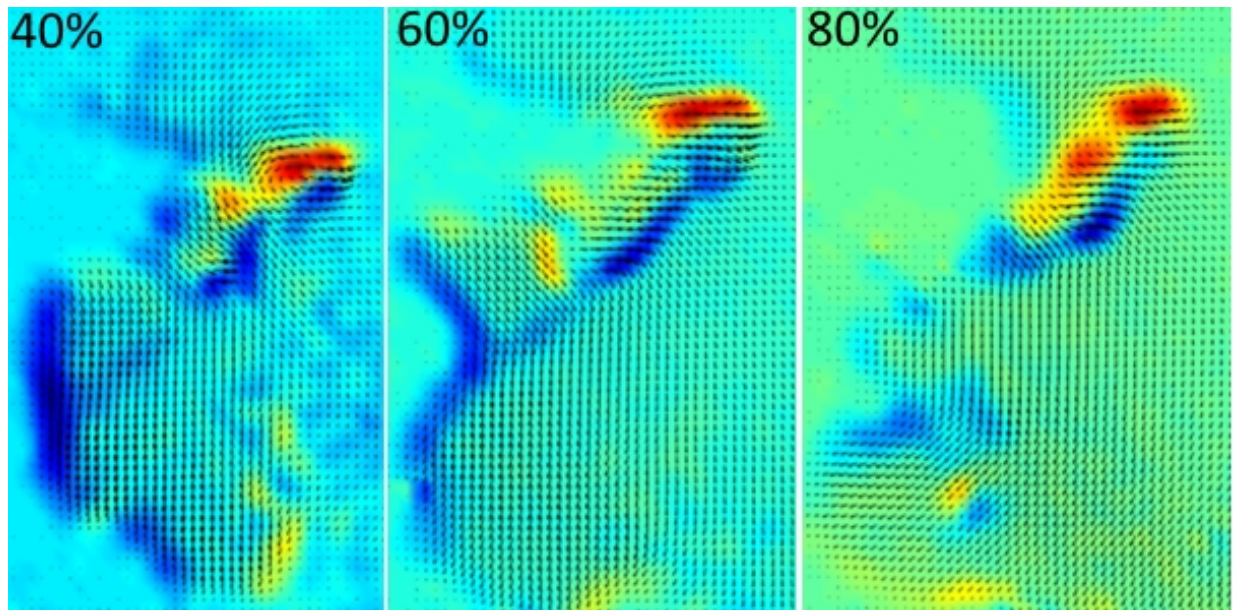


Figure 4.28: Processed PIV images showing vorticity magnitude at approximately 40, 60, 80% of the wing length

rigid-wing design. A quasi-steady blade element model predicted that twisting of the wing could improve efficiency, but at the cost of decreased lift production. This discrepancy between the model and experimental results indicated that the full 3D twisted shape of the wing changed the lift and drag coefficients through unsteady mechanisms, such as LEV augmentation. The quasi-steady model was updated with a 3D shape factor to estimate the lift improvement due to wing twist. The improved simulation was used to optimize twisted wing shapes, resulting in a series of twist profiles similar to the fabricated wings. However, the optimization fell short of predicting the lift achieved in experiments by the highly twisted Twist v1 design. Improved force coefficient estimation for flexible wings remains as an open problem. However, most studies focus on overall flexibility and fluid structure interaction, instead of on specific flexibility results, such as dynamic twisting or cambering. Future work will address wing twisting-based LEV augmentation with particle image velocimetry experiments. Furthermore, improved CFD modeling may provide direct relationships between twist profiles and resulting changes in force coefficients. This would allow vehicle designers to better optimize twisted wing shapes and would serve as a general design principle by which to improve the performance of bio-inspired FWMAVs.

# Chapter 5

## Vehicle Design Improvements

### 5.1 Introduction

In addition to improving our FWMAV through flexible wing design, several general improvements are made to the vehicle to improve lift production, reliability, and controllability. Section 5.2 covers improvements to the actuation, realized primarily through increased resonant spring stiffness. Section 5.3 addressed improvements to flexure lifetime obtained by variation of its geometry. Section 5.4 discusses improving system stability with the use of dampers. Section 5.5 provides an overview of system improvements and a summary.

### 5.2 Improvement of the resonant actuator

As discussed in Chapter 3, the GM15 remains the actuator of choice due to its low weight and high torque density. However, a significant improvement was made by switching from the GM15A, which offered a D shaft output, to the standard version of the GM15 that has a pulley shaft output. It remains straightforward to attach to the output shaft and the difference between the gearboxes is remarkable. The pins connecting the planetary gears to the carrier assembly, Figure 3.4c, have half the diameter of those in the standard version and would often shear off during operation of the system. Switching gearboxes allowed the resonant spring stiffness to be increased from 2.8 to 18 N\*mm/rad. With the A version, the gearbox failed frequently even with such a weak spring. The new gearbox has had no failures indicating that it could potentially tolerate even stiffer springs. However, it does experience wear, seen as a decrease in system lift output over time. It is not clear how much of this wear is due to off-axis loading which is mitigated by supporting the shaft with a bearing or simply the forces generated by operation of the system.

Increasing spring stiffness has allowed for higher frequency resonant operation of the system and improved lift production. Details of the spring variation is provided in Table 5.1 and can be seen in Figure 5.1. The original spring had good reliability due to its high coil count, but had low stiffness due to limitations of the gearbox. System resonance was estimated to be around 7 Hz, although flapping frequency was set to 10 Hz. The second version of the spring allowed the system to achieve 10 Hz resonance, but failed frequently due to low coil count. The final iteration

Table 5.1: Variations in system resonant spring

Spring Version	Wire Diameter (mm)	Coil Diameter (mm)	Number of Coils	Stiffness (mN*mm/rad)	Material
1	0.3	2	5	$2.80 \times 10^3$	Steel
2	0.4	3.5	2	$8.10 \times 10^3$	Steel
3	0.56	6	3	$18 \times 10^3$	1080 Steel



Figure 5.1: Iterations of the resonant spring of increasing stiffness from left to right 2.8, 8.1, 18 N\*mm/rad.

of the spring is custom fabricated and has allowed for resonance up to 23 Hz. This spring features spacing between the coils to minimize friction and grinding of the ends produces flat attachment points where it can be mounted to the end cap and gearbox case. Flat end attachment ensures that the spring deforms uniformly about its center. For version two it can be seen that straightened ends of the spring are attached to the side of the gearbox and cap. This tended to produce off axis deformation of the spring that likely generated off axis loading on the output shaft and decreased performance. The stiffness of the original spring was estimated based on material properties, since the original gearbox was not back drivable so the stiffness could not be directly tested. The stiffness of the successive versions represents the average stiffness since there is an asymmetry when it is loaded in the coiling versus uncoiling direction as shown in Figure 5.2. Loading such springs in the uncoiling direction results in lower stiffness and can significantly decrease lifetime. The spring stiffness is also likely to have non-linear behavior with respect to deflection amplitude although this behavior has not been fully quantified.

The efficiencies of the resulting systems are shown in Figure 5.3 with respect to lift per power. Versions one and two operated at the same frequency, so there should have been minimal differences in aerodynamic effects. Efficiency decreased despite the system operating at resonance. However, this could be due to poor mounting of the spring (generating off axis loading on the gearbox), losses due to spring deformation (due to low coil count), or losses due to increased spring asymmetry. The final two versions of the system utilize the third revision of the spring and display similar efficiency to the 10 Hz resonant system. The 18 Hz version was an unsupported system that may have had decreased performance due to off axis loading. The 21 Hz resonant system combines all design improvements and uses a bearing to reduce loading on the gearbox.

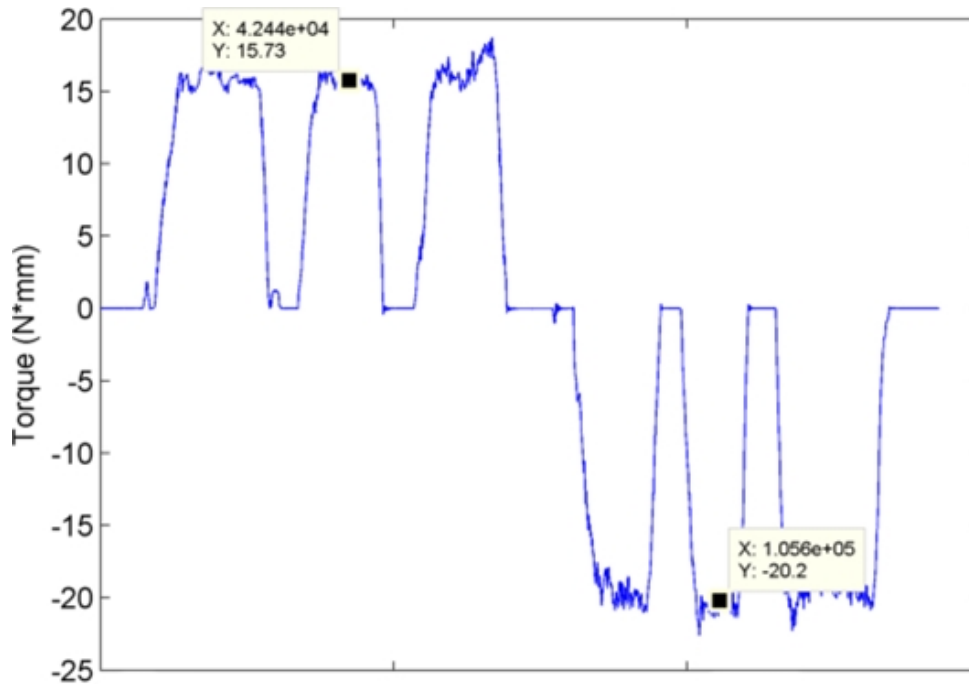


Figure 5.2: Measured torque differs by 22% for a 45 degree deflection of the spring.

The final point deviates from the linear trend indicating that the spring is being driven to the limit of its deflection,  $132^\circ$  in this case. The difference in efficiency between the original 10 Hz system and subsequent revisions are likely due to deformation of the spring and nonlinear behavior due to low coil count and deflection. The spring should be re-designed to achieve similar stiffness with a higher coil count to minimize spring losses and asymmetries.

A bearing was integrated into the system to reduce off-axis loading on the gearbox, decreasing wear and increasing efficiency as shown in Figure 5.4. The assembly has several components. The motor and gearbox holder is 3D printed and ensures correct motor spacing and alignment as well as including press-fit mounting points for the dampers. The shaft coupler is custom fabricated from titanium and is turned down from rod stock on a mini lathe. The bearing is a  $2 \times 5 \times 1.5$  mm open miniature ball bearing from VBX (Kit7420). Stabilizing the output shaft results in consistent wing strokes and less out of plane deviation, which should improve translational lift production as well as rotation. A preliminary comparison of system efficiency for two wings is shown in Figure 5.5. For twist v1 both lift production and efficiency are improved significantly, while for twist v2 performance for the tested points is similar but indicates an efficiency improvement. This indicates that the unstabilized system had significant kinematic differences between the two designs, and in the case of twist v1 deficiencies were significantly improved. Improved robustness of the system has been noticeable, but difficult to quantify. Typically test systems degrade over a set of experiments with losses of lift production on the order of 10%. The output shaft develops significantly more play, which would lead to increased out of plane deviation. The bearing stabilized system has been characterized, used to test a new calibration procedure, undergone a verification of calibration and experiments to offset thermal losses, and has been used to test the controller without significant loss of performance. A proposed improve-

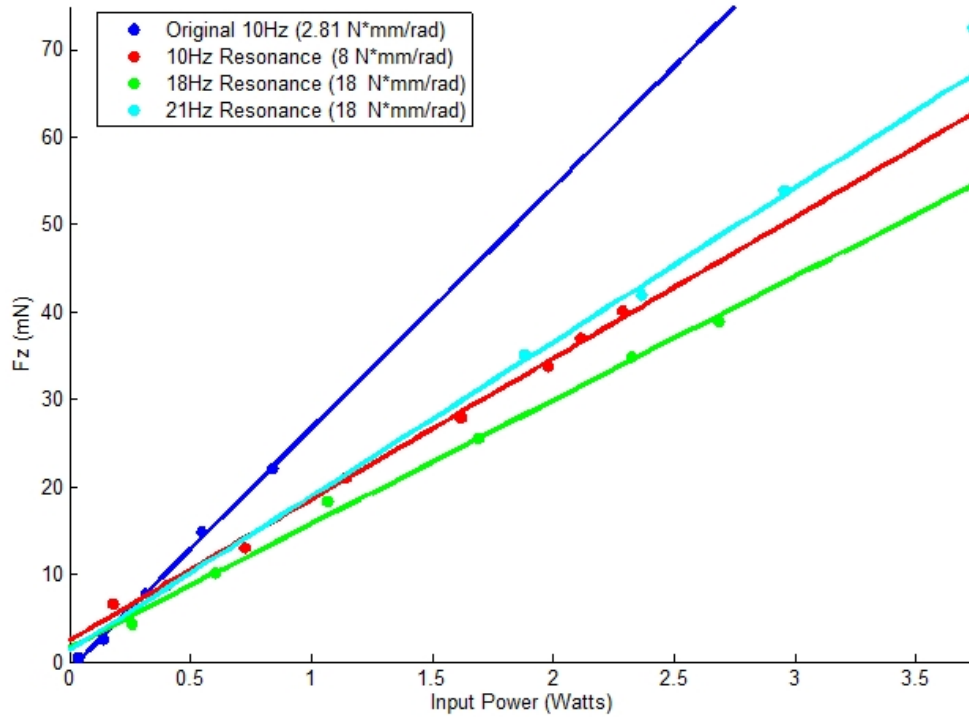


Figure 5.3: Comparison of systems fabricated with various springs with respect to lift per power.

ment to the bearing system in shown in Figure 5.6. This revision is aimed at improving system efficiency by mitigating the spring asymmetry. Springs are placed above and below the wing connector and are coiled in opposite directions so that while one is coiling the other is uncoiling.

### 5.3 Flexure improvements

Another persistent issue with system reliability was the lifetime of the flexure. As the system was improved to generate more lift at higher operating frequencies, flexure lifetime dropped even further to 500-1000 cycles or 28-58 seconds of system operating time. Work by Malka *et al.* discussed flexure design principles to enhance endurance and concluded that lengthening the flexure was the most effective technique for improving lifetime [151]. Based on these results the flexure cut height and length were increased by 20 and 50% respectively. This has resulted in significantly increased lifetime, with no flexure failures occurring during recent experiments. Increase of the cut height was done to reduce the stiffness of the flexure, while lengthening it increased the stiffness. The resulting flexure is 25% stiffer, which has actually improved rotation by providing more restorative force to rotate the wing. Flexure stiffness is given by the equation

$$k = \frac{Et^3L}{12w} \quad (5.1)$$

where E is the Youngs modulus of the fabrication material, t is the material thickness, L is the length of the flexure, and w is the cut height. The length of our current flexure is 20 mm with a

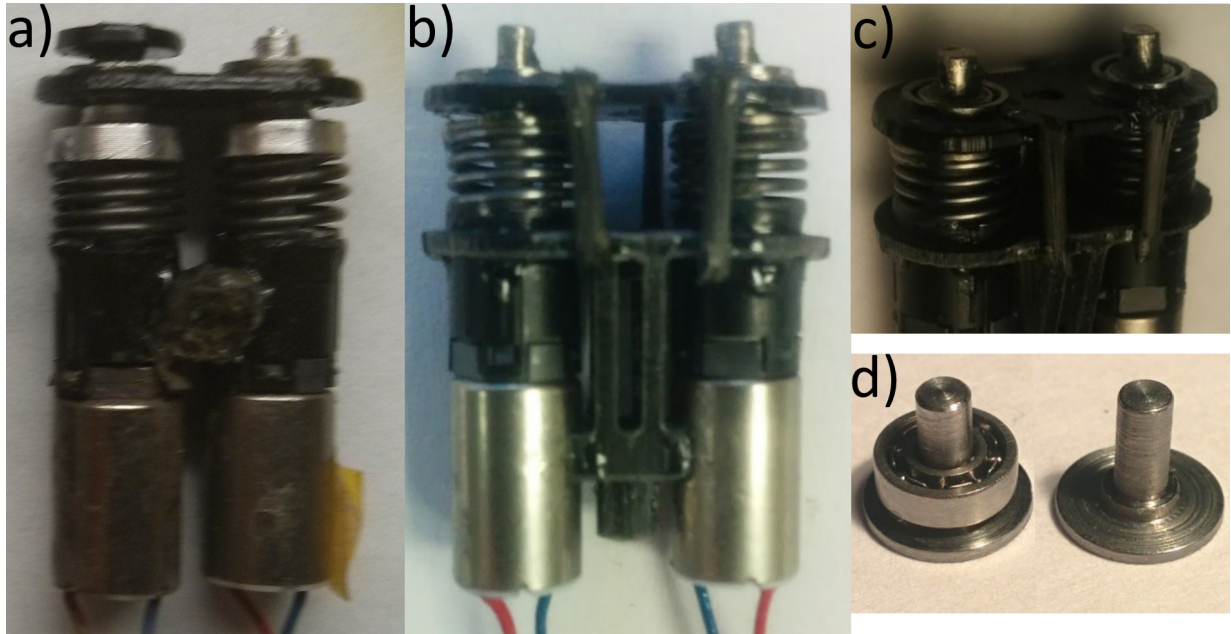


Figure 5.4: Resonant actuator revision that supports gearbox output shaft with a bearing. a) Prototype, b) final version, c) final top view, d) shaft coupler piece.

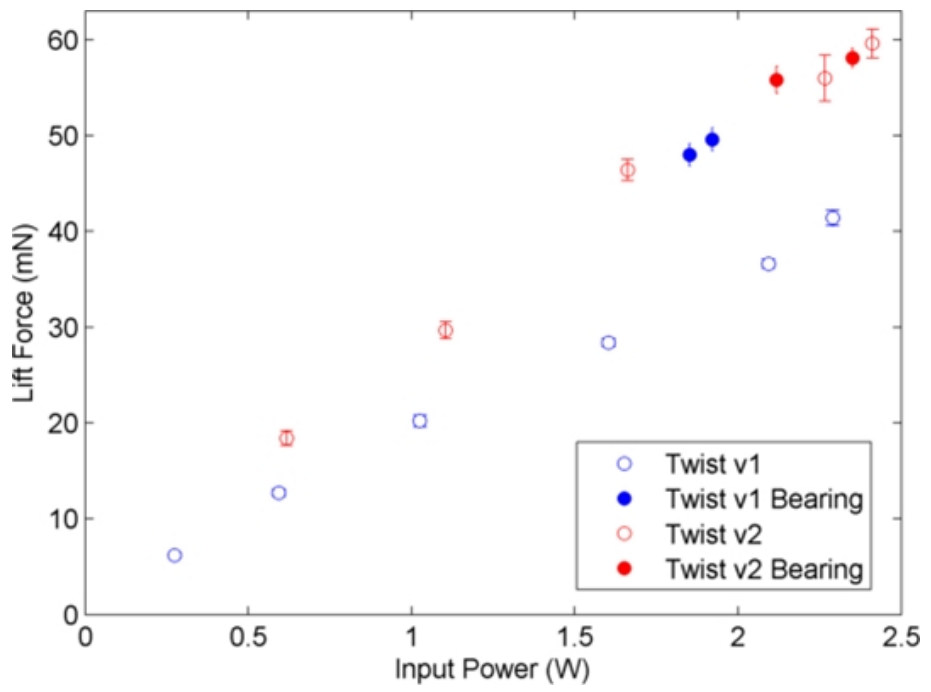


Figure 5.5: Efficiency comparison of the bearing system to an unstabilized system using twist v1 and v2 wings.



## 5.4 Passive Stability

Now that system reliability has been covered, we can address issues with controllability of the system. Control of the system is based on averaging theory, which allows the system to be treated as time-invariant approximation. This approximation is predicated on the condition that the flapping frequency is sufficiently high and the wing forces are sufficiently filtered by the body dynamics. However, due to the low flapping frequency as well as low pitch inertia of the system a significant body oscillation, on the order of  $\pm 50^\circ$ , is generated at the flapping frequency. Oscillations of this magnitude severely reduce system controllability due to significant vectoring of the lift force over the flapping cycle. For vehicle such as the Delfly and Nano Hummingbird, this issue is not present due to increased pitching inertia from the tail and long body. For the Purdue vehicles using custom actuators and the Robobee, the flapping frequency is sufficiently high to be averaged by the body dynamics and no significant pitching oscillation is developed. For organisms with relatively low flapping frequencies such as the hawkmoth and hummingbird, the abdomen and tail have been shown to play a critical role in maintaining pitch stability and control [152, 153, 154]. Increasing the offset between the wing center of pressure and vehicle center of mass can help increase stability [55]. However, the system with any nominal offset remains unstably oscillating and large offsets can even increase pitching oscillations due as they increase the lever arm between the wing center of pressure and vehicle center of mass. A four wing vehicle was also developed that eliminated the pitching oscillation and provided an alternative control scheme. Details of this developed platform are discussed in my work "Liftoff of a motor-driven, flapping-wing microaerial vehicle capable of resonance" [55]. An active tail provides another approach to stabilizing pitch, such a mechanism would substantially increase the weight of our system [155]. Aerodynamic dampers provide a passive mechanism to stabilize pitch that can be achieved with low weight. The damper is chosen to be large enough to eliminate the pitching oscillations and is effective when the center of damping lies above the center of mass [156] and is based on work by Richter and Lipson for the Cornell vehicle and by Teoh *et al.* for the Robobee [51, 83, 157]. The improvement in vehicle stability can be assessed with the Routh-Hurwitz criteria. Dampers were sized based on scaling of those used for the Robobee and are shown attached to the vehicle in Figure 5.8. Unlike previous work, stable flight was achieved using only the top damper, which provides passive stability. However, this top damper shifts the center of mass of the vehicle, which becomes unstable when the center of mass lies above the center of pressure of the wings. Therefore, a bottom damper is added to shift the center of gravity back down and further increase the pitching inertia. The dampers are crossed to also stabilize roll dynamics. The dampers are  $95 \times 95$  mm with a 65 mm offset for the top and 105 mm for the bottom. The dampers are constructed from carbon fiber rods and lightweight foam and each have a weight of 0.63 g.

## 5.5 Full System Summary

The improved system is shown compared to the initial prototype in Figure 5.9. Improvements of the system address reliability, resonant operating frequency, and lift production. Passive stability is also improved to allow for control. Table 5.2 summarizes the system improvements.

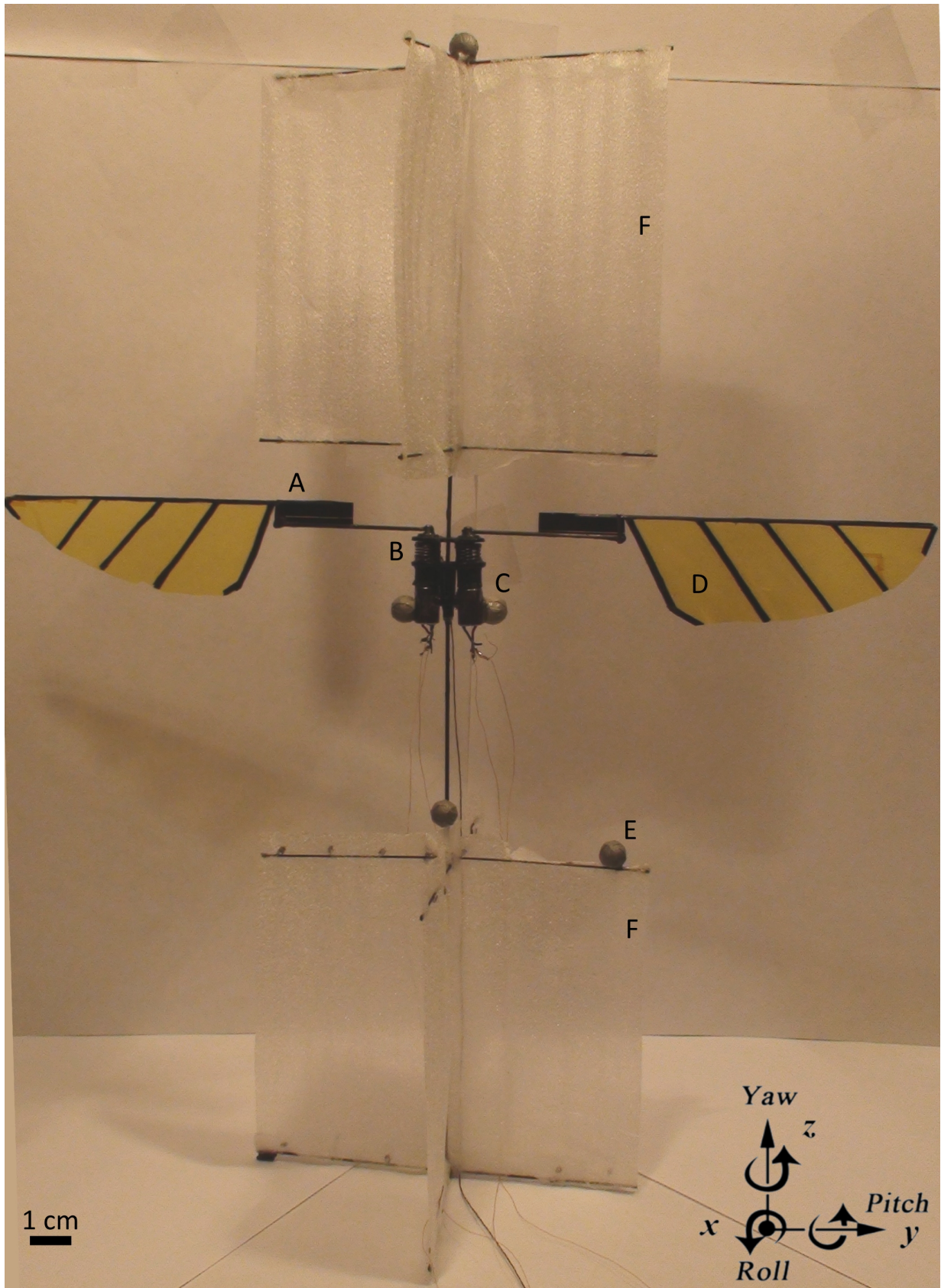


Figure 5.8: Picture of the FWMAV system with attached air dampers and Vicon markers. A) Wing rotation flexure, B) Torsional spring, C) GM15 gearmotor, D) Kapton and carbon fiber wing, E) Vicon marker, F) Air dampers

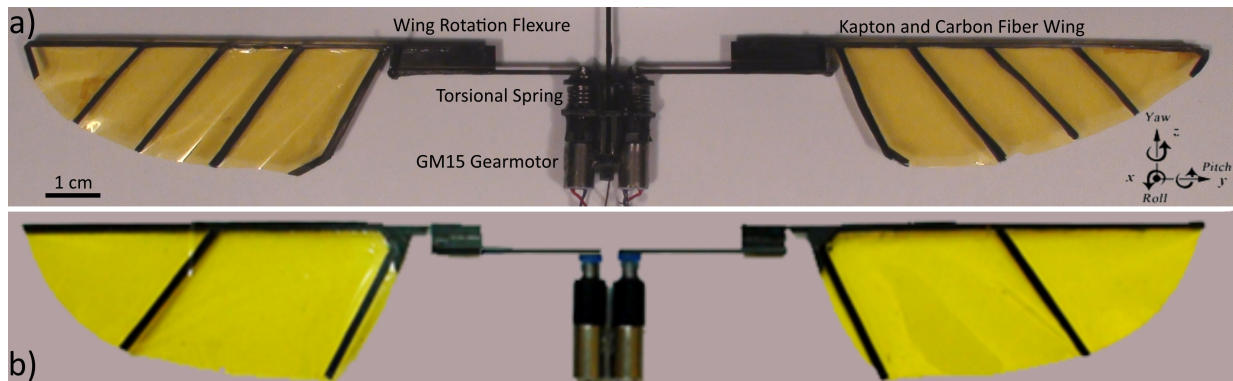


Figure 5.9: a) Developed system compared to b) initial prototype.

Table 5.2: Summary of system improvements

	Prototype	Improved System
Weight /Payload	2.7 g / 1 g (Lift to Weight 1.4)	3.2 g / 8.72 g (Lift to Weight 3.73)
Wing Design	Rigid	Flexible twisting wing increases aerodynamic efficiency, translational lift, and the effective lift coefficient by 41.3%, 35.3%, and 63.7%
Flapping Freq.	10 Hz (7 Hz resonance )	23 Hz (resonant operation)
Spring Stiffness	2.8 N*mm/rad	18 N*mm/rad (custom fabricated)
Reliability	Low (< 2500 cycles)	High (> 50000 cycles)
Actuator	Not backdrivable (GM15A)	Fully backdrivable (GM15) bearing stabilized with 3D printed assembly
Flexure	Lifetime reduced to < 1000 cycles by higher operating frequencies	Length and cut height increased by 50% and 20%
Thermal Effects	Joule heating of motor winding increases resistance and decreases lift	Closed-loop control ensures consistent output and optimized heat sink increases operating time by 102.4%
Passive Stability	Unstable Oscillations	Dampers increase pitch inertia and eliminate wing beat oscillations (0.63 grams each)
Flight Time	10 wing strokes / 1 second (ends by hitting tether)	275 wing strokes / 12 s (control limited)

# Chapter 6

## Closed-Loop Control Framework

Since the important aspects of system design and fabrication have been covered, this final chapter deals with free flight control. Section 6.1 presents a system model that allows for independent controllers to be designed for roll, pitch, and height based on Vicon feedback. Section 6.2 discusses calibration of the system, 6.3 describes the controller framework, section 6.4 covers controller tuning and free flight performance, while 6.5 provides a conclusion.

### 6.1 System Model

The linear transmission of the resonant actuator allows flapping amplitude and mean angle to be controlled directly by varying the sinusoidal input voltage,

$$V_{in,i} = \frac{V_{pp,i}}{2} \sin(2\pi ft + \phi_i) + V_{b,i} \quad (6.1)$$

to each motor  $i$ , where  $f$  is the flapping frequency,  $V_{pp}$  is the peak-to-peak voltage magnitude,  $V_b$  is the voltage bias, and  $\phi$  is the phase offset. The wings are driven out of phase such that  $\phi_1 = \phi_2 + 180^\circ$ , which ensures that the instantaneous yaw torque about the body  $z$  axis is approximately zero. A torque to induce a rolling motion can be created with a difference in  $V_{pp}$  between motors as shown in Figure 6.1. This results in a difference in flapping amplitude and mean lift between each wing. A pitching motion, or rotation about the  $y$  axis, can be created by changing  $V_b$ , which shifts the wing flapping angle. This effectively shifts the aerodynamic center of lift over a wing stroke either in front of or behind the vehicle center of mass. These behaviors can be combined to simultaneously produce pitching and rolling as well as control of  $z$  position. This control paradigm has been applied at small scales by Ma *et al.* [65], but not demonstrated in larger, motor-driven systems.

Lift production is the primary concern when selecting system physical parameters. Wing size, wing shape, and wing offset, have the potential to affect system open-loop flight behavior, but also have a direct impact on lift generated. An added damper or a sail can be chosen such that the system is stable about hover, but if too large can add a significant weight and reduce lift-to-weight ratio while potentially slowing system dynamics to an extent where desired maneuvers are unachievable.

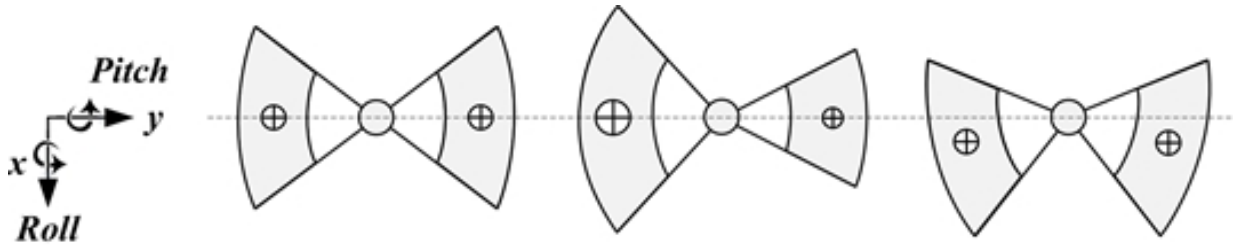


Figure 6.1: Diagram of the independent wing control paradigm. The system is shown from a top-down view with the arc demonstrating the flapping amplitude. The location of the crossed circles indicates the mean angle of the stroke, while their size indicates the amount of lift production which is proportional to the flapping amplitude. The configurations demonstrate stable flight, negative roll torque, and negative pitching torque.

We will now formulate the dynamics model of our flapping wing vehicle in order to understand and simulate its motion as well as develop free-flight controllers. The Newton-Euler equation is used for the dynamics of a translating and rotating rigid body. In the body fixed coordinate frame the equation is

$$\begin{bmatrix} m\mathbf{I} & 0 \\ 0 & \mathbf{J} \end{bmatrix} \begin{bmatrix} \dot{\nu} \\ \dot{\omega} \end{bmatrix} + \begin{bmatrix} \omega \times m\nu \\ \omega \times \mathbf{J}\omega \end{bmatrix} = \begin{bmatrix} f \\ \tau \end{bmatrix} \quad (6.2)$$

where  $m$  is the body mass,  $\mathbf{I}$  is the  $3 \times 3$  identity matrix, and  $\mathbf{J}$  is the body inertia matrix. The translational and angular velocity vectors in the body frame are  $\vec{\nu} = [\nu_x, \nu_y, \nu_z]^T$  and  $\vec{\omega} = [\omega_x, \omega_y, \omega_z]^T$  respectively. The wrench applied to the system  $W = [F, \tau]^T$  is a vector encompassing the external forces and torques about each axis. Both the wrench and inertia matrix  $\mathbf{J}$  are time varying and depend on the flapping wing motion. Here, as the effect of the changing  $\mathbf{J}$  is small, it is assumed to be constant.

The right side of the equation, the body wrench, is broken down into two components due to the effect of gravity as well as the forces and torques produced by the flapping wings as follows

$$\begin{bmatrix} f \\ \tau \end{bmatrix} = \begin{bmatrix} \mathbf{R}_{\mathbf{WB}}mg \\ 0 \end{bmatrix} + \begin{bmatrix} f_w \\ \tau_w \end{bmatrix} \quad (6.3)$$

where  $\mathbf{R}_{\mathbf{WB}}$  is the rotation matrix transformation between the world fixed frame and the body frame.

$$\mathbf{R}_{\mathbf{WB}} = R_{\theta_z} \times R_{\theta_y} \times R_{\theta_x} = \begin{bmatrix} \cos(\theta_z) & -\sin(\theta_z) & 0 \\ \sin(\theta_z) & \cos(\theta_z) & 0 \\ 0 & 0 & 1 \end{bmatrix} \times \begin{bmatrix} \cos(\theta_y) & 0 & \sin(\theta_y) \\ 0 & 1 & 0 \\ -\sin(\theta_y) & 0 & \cos(\theta_y) \end{bmatrix} \times \begin{bmatrix} 1 & 0 & 0 \\ 0 & \cos(\theta_x) & -\sin(\theta_x) \\ 0 & \sin(\theta_x) & \cos(\theta_x) \end{bmatrix} \quad (6.4)$$

The gravity vector,  $g$  is  $[0, 0, -9.8]$  m/s. Wing forces and calculated following 2.3, however in this case the wing cord velocity and angle of attack are updated considering the motion of the

vehicle. The wing forces and torques on the body can be written as

$$\begin{bmatrix} f_w \\ \tau_w \end{bmatrix} = \begin{bmatrix} \mathbf{R}_{\theta,L}F_L + \mathbf{R}_{\theta,R}F_R \\ \mathbf{R}_{\theta,L}(\vec{p}_w \times F_L) + \mathbf{R}_{\theta,R}(\vec{p}_w \times F_R) \end{bmatrix} \quad (6.5)$$

where  $\mathbf{R}_\theta$  is the rotational transformation by the wing flapping angle for each wing (L, R) from the body frame,  $F$  is the total lift force from a wing, and  $\vec{p}_w$  depends on the wing center of lift location as follows  $[0, w_{off} + R_{CL}, h_w - \beta_{CL}]$ .

The flapping system is nonlinear and time varying, which complicates system analysis or later control. As the wing forces and torques are periodic, they can be approximated with their average value resulting in a system approximation that is time-invariant. This approach is accurate only when the wing flapping frequency is considerably higher than the bandwidth of the system, or the magnitude of the applied wrench is low. We make this approximation here in order to use existing design tools, though it does not appear to be valid without the addition of a damper. This approximation is formalized for a general nonlinear system

$$\begin{aligned} \dot{x} &= f(x, u) \\ u &= g(v, t) = g(v, t + nT), \text{ for integers } n \\ \dot{\bar{x}} &= \bar{f}(\bar{x}, \bar{u}) = \frac{1}{\tau} = \int_0^\tau f(x, g(v, t)) dt \end{aligned} \quad (6.6)$$

where  $x$  is the state variable,  $u$  is the open-loop control input, and  $v$  is the feedback control input. The open-loop control has period  $\tau$ . All function up to their second order derivatives must be continuous. If the origin  $\bar{x} = 0$  of the averaged system is an exponentially stable equilibrium point, there exists a  $\tau^*$  and constant  $k > 0$  such that for any  $0 < \tau < \tau^*$ , the error between the instantaneous and averaged system is bounded  $\|x(t) - \bar{x}\| < k\tau$  [78, 158]. The produced wing forces averaged over a wing stroke and in the absence of body motion are

$$\begin{bmatrix} \bar{f}_{w0} \\ \bar{\tau}_{w0} \end{bmatrix} = \begin{bmatrix} \mathbf{R}_{\bar{\theta},L}\bar{F}_L + \mathbf{R}_{\bar{\theta},R}\bar{F}_R \\ \mathbf{R}_{\bar{\theta},L}(\vec{p}_w \times \bar{F}_L) + \mathbf{R}_{\bar{\theta},R}(\vec{p}_w \times \bar{F}_R) \end{bmatrix} \quad (6.7)$$

where  $\bar{F}$  is the stroke averaged wing force and  $\bar{\theta}$  is the average wing flapping angle. Assuming symmetry in the average wing flapping angle  $\theta_{L} = \theta_{R} = \theta$  the body wrench is simplified to.

$$\begin{bmatrix} \bar{f}_{w0,x} \\ \bar{f}_{w0,y} \\ \bar{f}_{w0,z} \\ \bar{\tau}_{w0,x} \\ \bar{\tau}_{w0,y} \\ \bar{\tau}_{w0,z} \end{bmatrix} = \begin{bmatrix} 0 \\ 0 \\ \bar{F}_L, z + \bar{F}_R, z \\ h_{yoff} \cos(\bar{\theta})(\bar{F}_L, z - \bar{F}_R, z) \\ h_{yoff} \sin(\bar{\theta})(\bar{F}_L, z + \bar{F}_R, z) \\ 0 \end{bmatrix} = \begin{bmatrix} 0 \\ 0 \\ F_{z,in} \\ T_{x,in} \\ T_{y,in} \\ 0 \end{bmatrix} \quad (6.8)$$

Now we can write out the entire stroke averaged body wrench as

$$\begin{aligned}
\begin{bmatrix} \bar{f}_x \\ \bar{f}_y \\ \bar{f}_z \\ \bar{\tau}_x \\ \bar{\tau}_y \\ \bar{\tau}_z \end{bmatrix} &= \begin{bmatrix} -\cos(\theta_x)\cos(\theta_z)\sin(\theta_y) + \sin(\theta_x)\sin(\theta_z) \\ -\cos(\theta_z)\sin(\theta_x) + \cos(\theta_x)\sin(\theta_y)\sin(\theta_z) \\ -\cos(\theta_x)\cos(\theta_y) \\ 0 \\ 0 \\ 0 \end{bmatrix} (-9.8)m \quad (6.9) \\
&- \begin{bmatrix} \bar{X} & 0 & 0 & 0 & \bar{X}h_{zoff} & 0 \\ 0 & \bar{Y} & 0 & -\bar{Y}h_{yoff} & 0 & 0 \\ 0 & 0 & \bar{Z} & 0 & 0 & 0 \\ 0 & -\bar{Y}h_{zoff} & 0 & (\bar{Y}h_{zoff}^2 + \bar{L}) & 0 & 0 \\ \bar{X}h_{zoff} & 0 & 0 & 0 & \bar{X}h_{zoff}h_{yoff} + \bar{M} & 0 \\ 0 & 0 & 0 & 0 & 0 & \bar{N} \end{bmatrix} \begin{bmatrix} v_x \\ v_y \\ v_z \\ \omega_x \\ \omega_y \\ \omega_z \end{bmatrix} + \begin{bmatrix} 0 \\ 0 \\ F_{z,in} \\ T_{x,in} \\ T_{y,in} \\ 0 \end{bmatrix}
\end{aligned}$$

The variables  $\bar{X}$ ,  $\bar{Y}$ ,  $\bar{Z}$  are defined as the damping coefficients for the wing pair for each DOF and are dependent on the wing flapping amplitude and frequency as determined by Cheng and Deng [159]. The translational damping coefficients are measured experimentally by recording the damped response of the system mounted to a swinging pendulum, similar to the approach taken by Parks *et al.* [160]. The rotational coefficients,  $\bar{L}$ ,  $\bar{M}$ , and  $\bar{N}$ , are calculated following work by Cheng and Deng.

Setting 6.2 and 6.9 equal results in a set of nonlinear equation of motion for the vehicle in the body fixed frame.

$$\begin{aligned}
\ddot{x} &= \frac{1}{m}(-m(v_z\omega_y - v_y\omega_z) + mg \times gv(1) - \bar{X}(v_x + \omega_y h_{zoff})) \quad (6.10) \\
\ddot{y} &= \frac{1}{m}(-m(v_x\omega_z - v_z\omega_x) + mg \times gv(2) - \bar{Y}(v_y - \omega_x h_{yoff})) \\
\ddot{z} &= \frac{1}{m}(-m(v_y\omega_z - v_x\omega_y) + mg \times gv(3) - \bar{Z}v_z + F_{z,in}) \\
\ddot{\theta}_x &= \frac{1}{J_x}((J_y - J_z)\omega_y\omega_z + \bar{Y}h_{zoff}(v_y - \omega_x h_{zoff}) - \bar{L}\omega_x + T_{x,in}) \\
\ddot{\theta}_y &= \frac{1}{J_y}((J_z - J_x)\omega_x\omega_z - \bar{X}h_{zoff}(v_x + \omega_y h_{yoff}) - \bar{M}\omega_y + T_{y,in}) \\
\ddot{\theta}_z &= \frac{1}{J_z}(-\bar{N}\omega_z)
\end{aligned}$$

where  $gv(n)$  are rows of the first matrix in 6.9. We linearize about the hover condition where  $\vec{x} = 0$  and the vehicle generates enough lift to support its weight. The resulting linearized equations are



while the others must be solved as a system of equations solving  $\ddot{x}$  and  $\ddot{\theta}_y$  as well as  $\ddot{y}$  and  $\ddot{\theta}_x$  simultaneously.

$$\frac{z}{F_{z,in}} = \frac{\frac{1}{m}}{s^2 + \frac{\bar{Z}}{m}s} \quad (6.16)$$

$$\frac{\theta_x}{T_{x,in}} = \frac{ms + \bar{Y}}{J_x ms^3 + \bar{Y}m(h_{zoff}^2 + \bar{L}J_x)s^2 + (\bar{L}\bar{Y})s + barYh_{zoff}gm} \quad (6.17)$$

$$\frac{\theta_y}{T_{y,in}} = \frac{ms + \bar{X}}{J_y ms^3 + (\bar{M}m + \bar{X}h_{zoff}^2m + J_y\bar{X})s^2 + \bar{M}\bar{X}s + \bar{X}} \quad (6.18)$$

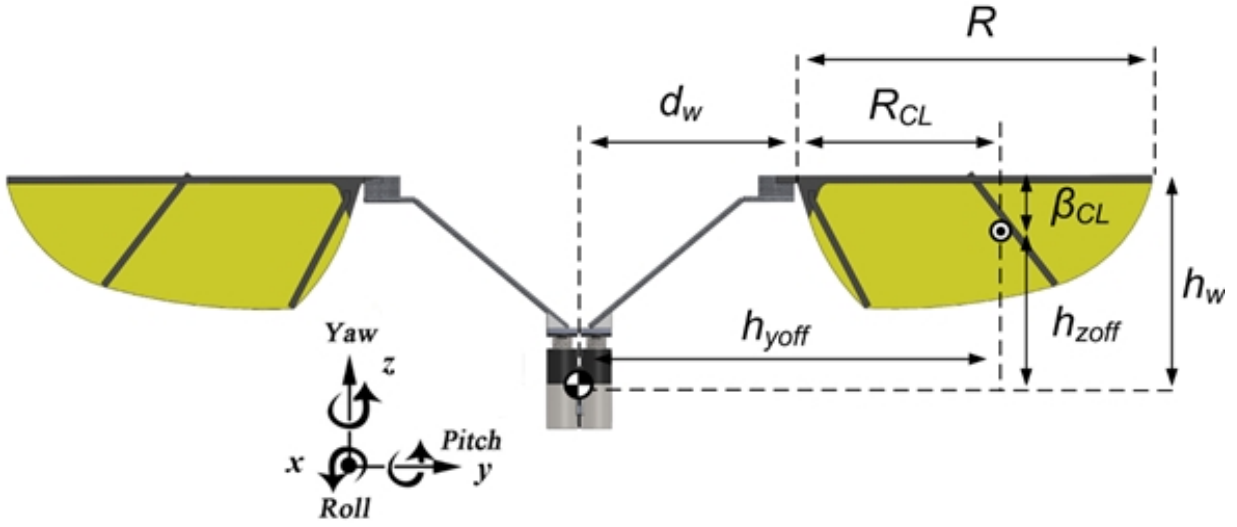


Figure 6.2: 3D printed fixture for attaching robot to the ATI Nano17-Ti sensor.

## 6.2 Calibration

A calibration is needed to characterize the relationship between the input voltage signal to the actuator and the resulting forces and torques on the vehicle. This consists of a mapping between the sinusoidal input signal parameters  $V_{pp,i}$  and  $V_{b,i}$  and the resulting mean wing stroke (time averaged) body forces and torques  $F_z$ ,  $\tau_x$ , and  $\tau_y$  that is determined for each actuator wing pair  $i$ . For calibration the system is mounted to a six axis force torque sensor (ATI Nano17-Ti) with a 3D printed fixture shown in Figure 6.3. The mount is designed to align the y-axis of the robot with the y-axis of the sensor and to eliminate x and y displacements between the center of mass of the sensor and system. The z offset,  $\delta_z$ , must still be accounted for when calculating the body torques based on the measured ones such that  $\tau_x = \tau_x^m + \delta_z F_y$  and  $\tau_y = \tau_y^m - \delta_z F_x$ . Once the calibration data is collected it is fit to a quadratic surface using singular value decomposition.

Due to the actuator being run at high power, significant heating occurs in the motor windings changing their resistance. If the system is run at a constant voltage amplitude, the output torque

Table 6.1: System Physical Parameters

	Parameter	Value	Unit
$f$	flapping frequency	23	Hz
$k_s$	elastic element stiffness	18e3	mN.mm/rad
$d_w$	wing offset	35	mm
$R$	wing length	70	mm
$R_{CL}$	wing CL horz. distance	42	mm
$\beta_{CL}$	wing CL vert. distance	10	mm
$m$	mass	3.2	g
	lift-to-weight ratio	3.7	
$\mathbf{J}$	body inertia [ $J_x, J_y, J_z$ ]*	[ $1.5e^3, 0.45e^3, 1.13e^3$ ]	$g.mm^2$
$h_w$	vertical wing offset	10	mm

\*Diagonal terms in diagonal matrix, predicted from 3D CAD model.

Table 6.2: System Damping Coefficients and Trim Inputs

Parameter	Value	Unit
$\bar{X}$	3.0	nM/m/s
$\bar{Y}$	4.5	nM/m/s
$\bar{Z}$	2.9	nM/m/s
$\bar{L}$	$4.7e^{-3}$ *	mN.m/rad/sec
$\bar{M}$	$4.0e^{-3}$ *	mN.m/rad/sec
$\bar{N}$	$3.2e^{-3}$ *	mN.m/rad/sec

\*Calculated following [159].

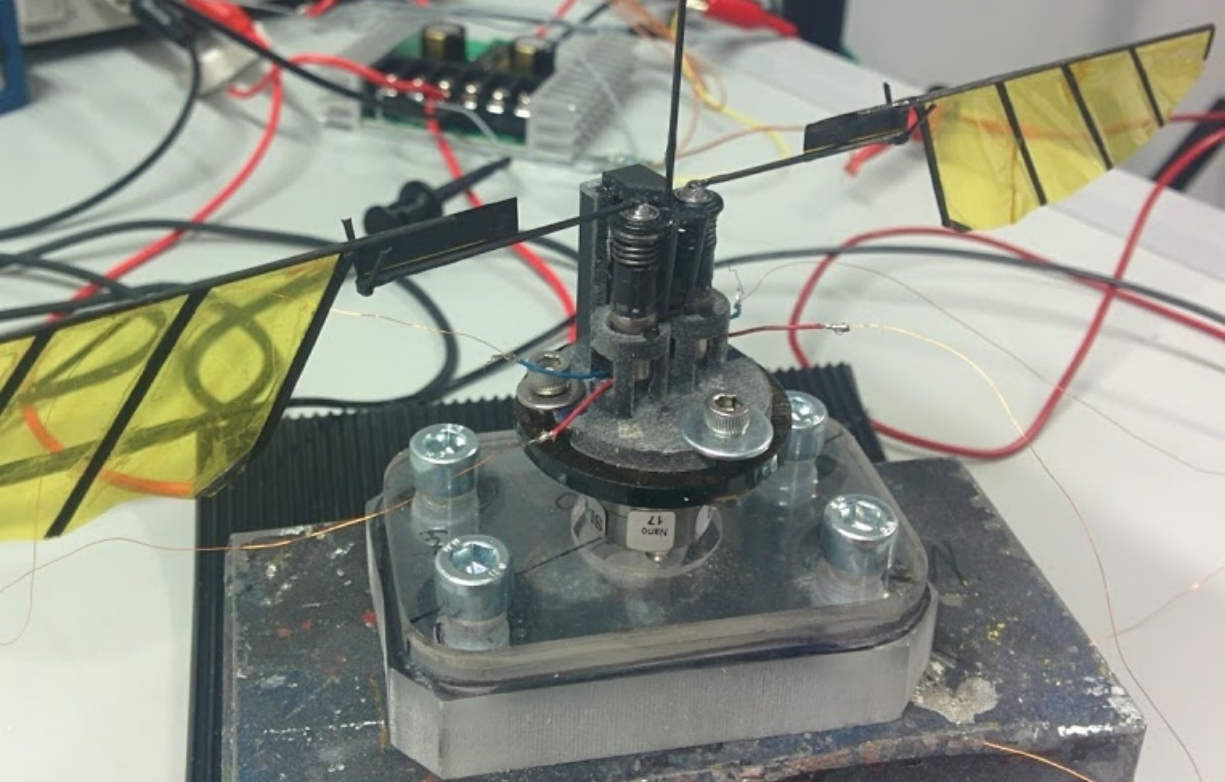


Figure 6.3: Physical parameters of the vehicle along with the coordinate system. The concentric circle symbol denotes the wing center of lift.

and resulting flapping amplitude, decrease over time due to decreasing current draw. Therefore, closed-loop current control was achieved using a proportional-integral controller with gains  $P = 3$  and  $I = 4 \times 10^{-6}$  for current error in amps. The current set point is calculated from the voltage amplitude and motor nominal resistance using Ohms law. The control framework is coded in LabVIEW, which is used to generate sinusoidal signal output between 0-5V with a DAQ board (National Instruments PCIe-6353) to the motor driver (Dimension Engineering Sabertooth 2x32) with a supply voltage of 17.5V. The current sensor (Allegro ACS714) signal is measured with the same DAQ. Load cell measurements are acquired with a separate DAQ (National Instruments PCI-6952e) as shown in Figure 6.4. Position and orientation data from the Vicon array are transmitted via Ethernet.

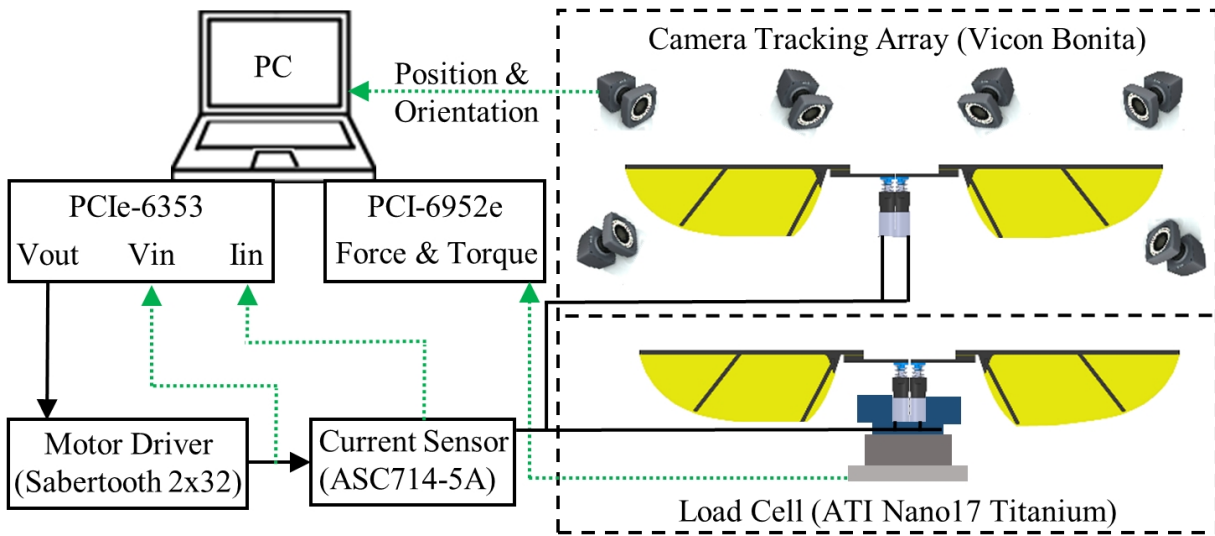


Figure 6.4: Experimental setup with computer, electronics, FWMAV system, load cell, and tracking camera array. The motor control signal is shown with solid lines, while measured data is shown as dotted lines. The dashed box shows the two ways the system is run: fixed to the load cell for calibration, or free flying in the camera array for closed-loop control.

Previous experiments indicated that although wing to wing interactions did not significantly affect lift generation, it did generate significant changes in roll and pitch torques. Therefore, the calibration was performed to take into account this effect. Through a set of initial experiments, a nominal trim amplitude was determined for each wing,  $V_{pp} = V_{trim}$ , where the generated lift was equal to half the weight of the vehicle. Then one wing was operated at this amplitude with no bias and the forces and torques for this condition were recorded. Then the second wing was swept over a range of  $V_{pp}$  and  $V_b$  for the calibration, while the other wing operated at the constant condition. The force and torque results from the constant wing were then subtracted from the measured data. This procedure was found to be sufficient to eliminate significant torque offsets from the two wing calibration, even though it did not account for all possible combinations of wing interactions. Furthermore, a sparse calibration using only 12 points was tested. In previous experiments, more extensive calibrations were used, but found to cause significant wear on the system. This wear altered the force production leading to a less accurate calibration and shorter

system lifetime during experiments.

Each wing was tested at four amplitudes:  $V_{trim}$ ,  $V_{trim} + 0.15$ ,  $V_{trim} + 0.3$ ,  $V_{trim} + 0.45$  for one second each, at three offsets:  $V_b = 2.4, 2.5, 2.6$ . An example calibration trial is shown in Figure 6.5. On the left we see the raw force data from both wings for a single calibration run, four amplitudes at one offset, although some pre-processing has been done to make the data readable. The solid line segments, labeled A-D indicate the different amplitudes being tested and show the windows where the data is averaged, consisting of 38 wing strokes or 0.83 seconds. Dashed sections are ignored, consisting of an initial 13 wing stroke startup transient and 8 stroke transients as the commanded amplitudes are changed. This delay between changes in commanded input and system output has not been well characterized and likely depends on the magnitude of the derivative of the command signal. During closed-loop control, the commanded amplitudes changes more smoothly so no delay was accounted for. Characterizing and accounting for this delay in the controller remains future work.  $F_z$  remains relatively consistent during each of the segments of interest, however a small decrease is seen in the first segment and an increase seen in the second segment as the closed-loop current controller varies the voltage to account for changing resistance. Winding heating, and therefore resistance, changes most rapidly at the start of the trial and then slows as the system reaches a thermal equilibrium.  $\tau_x$  and  $\tau_y$  exhibit higher noise as well as some beating patterns, but their averaged values remain relatively consistent across multiple calibration runs. The right side of the figure shows the full calibration surfaces.  $F_z$  and  $\tau_x$  display the same quadratic trend as they are both proportional to flapping amplitude, but show almost no dependence on offset. Flapping amplitude saturates as increasing voltage drives it towards the maximum deflection angle of the torsional spring. During closed-loop control the operating regime is typically small enough to be considered locally linear.  $\tau_y$  displays an approximately linear dependence on both amplitude and offset.

### 6.3 Controller Framework

Measurements of vehicle position and orientation were obtained with a Vicon Bonita tracking setup with 6 cameras running at 120 Hz shown in Figure 6.6. The positioning of the array provided a sphere of approximately 1 meter radius in which the robot was operated. Five 6.5 mm diameter tracking markers were placed on the robot as seen in Figure 6.7 each with a weight of 0.15 g. The system was tethered for power and control. The wires and physical tether had a weight of 0.35 g, only 6% of the total system weight and were not seen to alter the overall system dynamics.

Previous modeling work of the system dynamics linearized about hover demonstrated that the lateral (side to side), longitudinal (forward backward), heave (up and down), and yaw dynamics are decoupled [55]. Therefore, we designed independent linear PID controllers for our parameters of interest: z position, roll angle, and pitch angle. The control loop diagram of the free flight system is shown in Figure 6.7. The output of each controller is the desired torque ( $\tau_x$ ,  $\tau_y$ ) for the body angles and desired lift force ( $F_z$ ) for the position. A lookup is performed using the calibration surface to determine the appropriate  $V_{pp}$  and  $V_b$  for each wing to achieve these desired commands. As described previously,  $V_{pp}$  is converted to a current set point for the actuator control loop. Since the wing-stroke itself is driven in open-loop, new control inputs could only

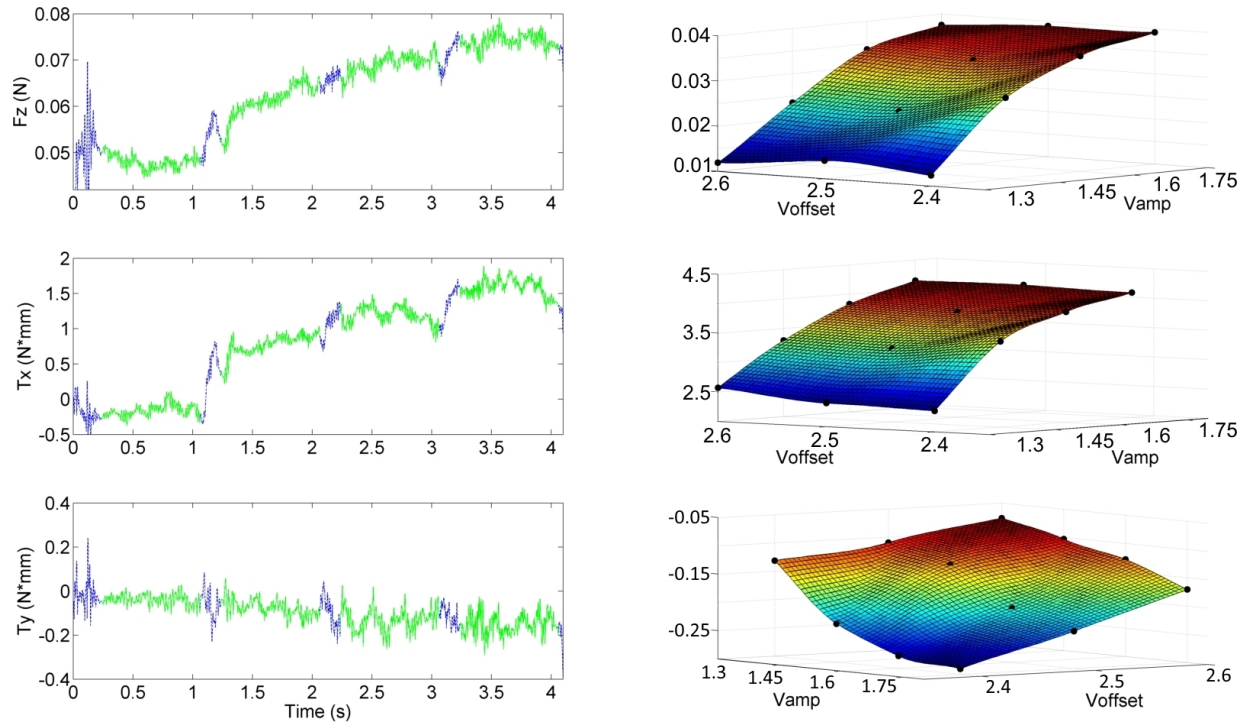


Figure 6.5: Example calibration run. The left side shows raw data for both wings over a single experiment. Solid line sections A-D indicate difference commanded amplitudes over which the data is averaged. The right side shows the full calibration surfaces consisting of the marked points based on averaged data. The quadratic surface is fit to the measured data using singular value decomposition.



Figure 6.6: Vicon Bonita tracking setup.

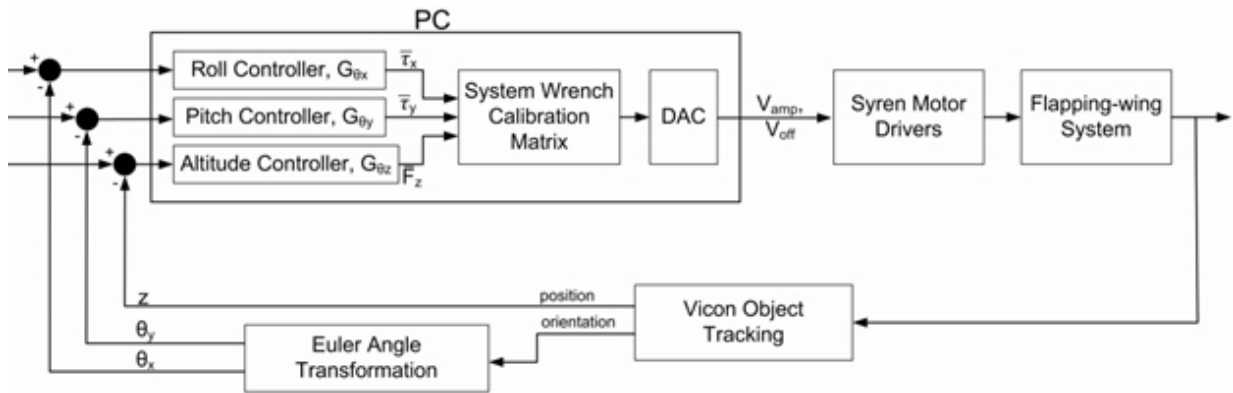


Figure 6.7: Free flight control framework consisting of three independent PID controllers for roll, pitch, and altitude. The Vicon tracking system provides measurements of the system angles and position. Errors are converted by the controllers to desired forces and torques. The calibration matrix converts these to the appropriate actuator driving signal based on the determined  $V_{pp}$  and  $V_b$ .

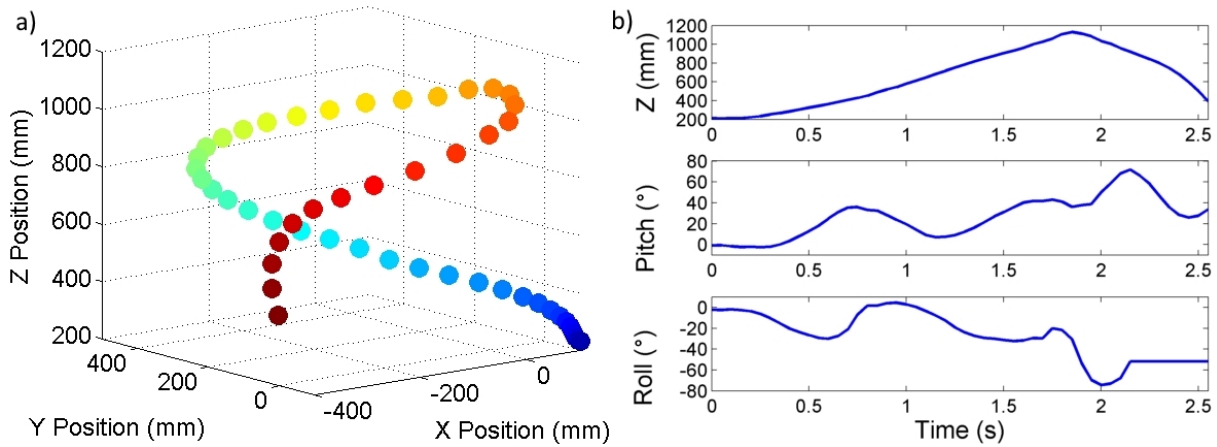


Figure 6.8: Representative open-loop test flight tracking data. The left side shows the 3D position with all axes in mm. The right side shows the time series for the parameters of interest, vertical position as well as pitch and roll angles.

be applied every flapping cycle. Therefore, the control frequency for the system was 23 Hz.

## 6.4 Controller Tuning and Free Flight Results

Experimental training of the controller parameters was performed with the final goal of stable flight of the system. Degrees of freedom were tuned sequentially starting with roll, then adding pitch, and finally vertical position. Roll and pitch were tuned using primarily vertical flight, which resulted in longer trials and increased the effectiveness of the damper. The metric for roll and pitch parameter tuning was minimizing body angle error. The metric for the full controller was flight time, measured as the time the system remained above its initial vertical position from takeoff minus 0.25 seconds to account for the system going unstable at the end of the trial.

First open-loop flight was conducted to check the validity of the calibration matrix and to determine the necessary commanded  $F_z$  that matched the weight of the system. Although the damper eliminated body oscillations, it was not large enough to fully stabilize the lateral and longitudinal dynamics. The open-loop behavior was that the system quickly went down due to deflections in roll and pitch. As the system rotated the thrust from the wings was vectored resulting in decreased lift and translation of the system away from the release point. In some cases the system did fly vertically, but eventual interaction with the tether produced a significant angular perturbation that brought it down. These open-loop tests had an average length of  $2.78 \pm 0.48$  seconds. A representative open-loop flight is shown in Figure 6.8, showing the 3D flight trajectory on the left and parameters of interest on the right. In this trial, the system takes off towards the left, with a roll and pitch perturbation occurring around 0.5 seconds that increases this translation while continuing climbing. Another perturbation causes it to veer to the right, but still climb, Just before 2 seconds a large perturbation causes the body angle to be significant enough that the lift produced is less than the weight of the system causing it to quickly lose altitude. A representative trial video is provided as supplementary material.

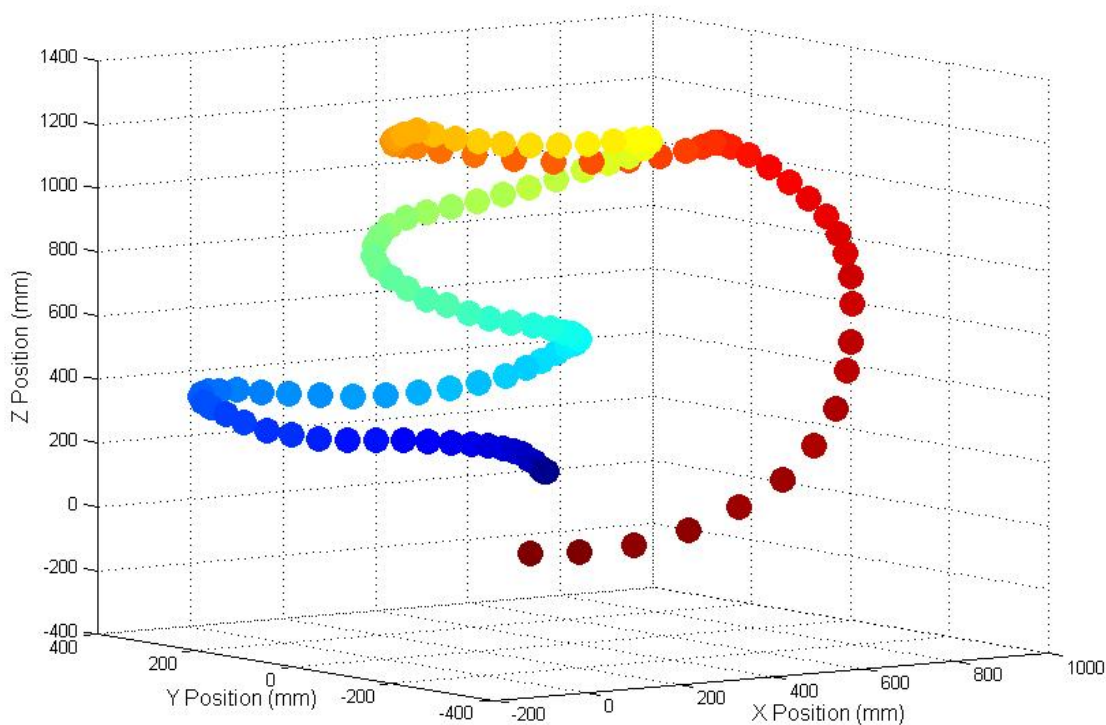


Figure 6.9: Roll control vicon trajectory. The trajectory begins with blue markers and ends with red ones.

Roll was the first degree of freedom to be trained. Gains of  $P = 0.004$  and  $D = 0.002$  were found to reduce the mean squared error (MSE) in roll angle from 873 to 588 compared to open-loop. Trial times were  $4.75 \pm 0.84$  seconds, showing a significant improvement. Uncorrected deflections or drift of the pitch angle caused the system to translate and lose lift as is shown in Figure 6.9 and 6.10. Next pitch was trained with a gain of  $P = 0.002$  being sufficient to reduce MSE in pitch angle from 974 to 287. Trial times were  $4.96 \pm 3.28$  seconds. Although the average time is similar to the previous case, the qualitative behavior of the system was much different. The system consistently flew vertically until reaching the maximum height allowable by the tether. In some cases interaction with the tether caused a perturbation that ended the trial resulting in shorter flights as is shown in Figures 6.11 and 6.12, while in others the system continued flying at the end of the tether for up to 10.38 seconds shown in Figures 6.13 and 6.14.

Finally pitch was trained. Gains of  $P = 0.01$  and  $D = 0.05$  with a Z set point of 800 resulted in increased flight times with an average of  $5.68 \pm 2.56$  seconds. Relatively high gain was found to be needed to bring the system to the vertical set point. Although the derivative term reduced overshoot, the system often went unstable when the control term went negative, decreasing lift and resulting in overall poor height control as seen in Figures 6.15 and 6.16. An integral term was added to the framework to improve performance. This allowed the strength of the PD to be decreased, while using an integral gain to slowly pull the system towards the set point. The

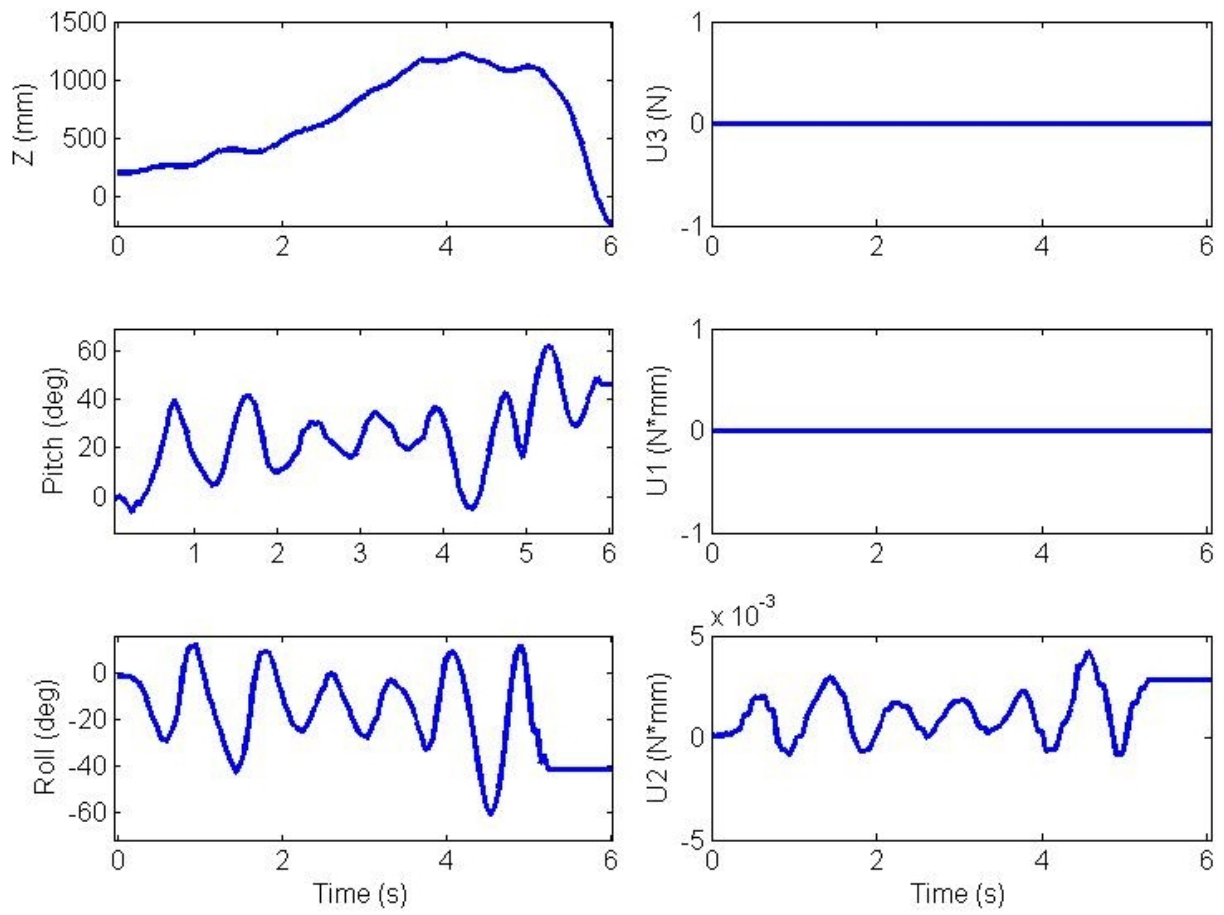


Figure 6.10: Roll control showing vertical position, pitch angle, roll angle, and roll control signal.

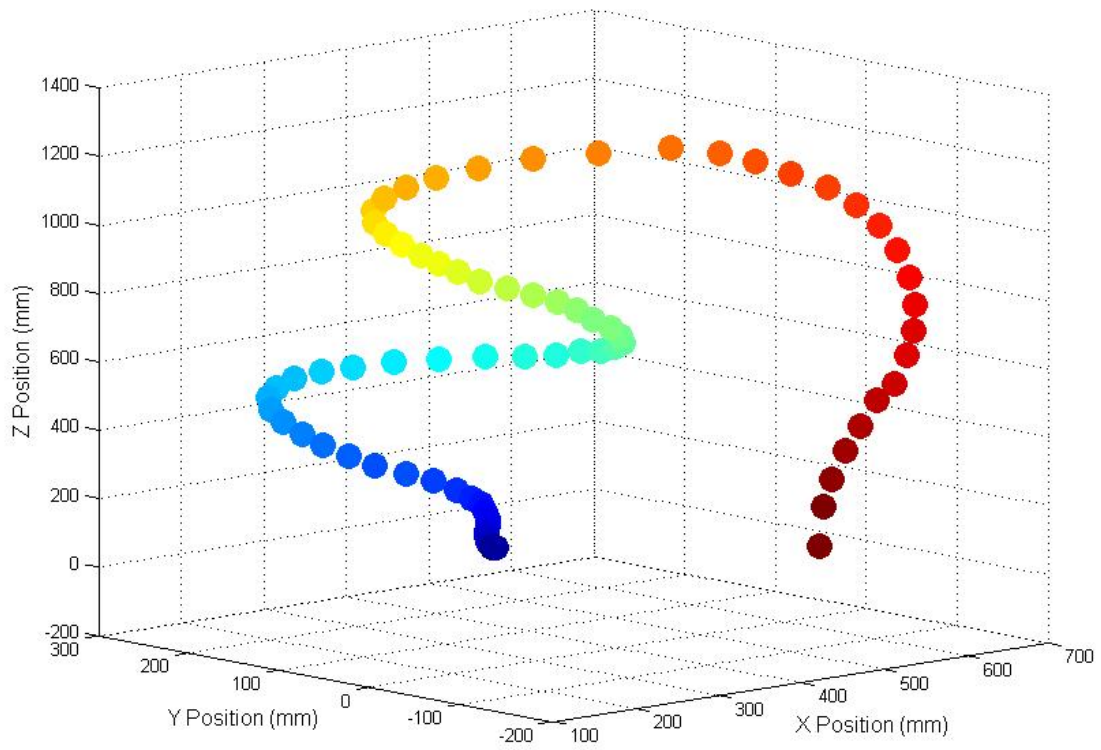


Figure 6.11: Pitch and roll control vicon trajectory showing short flight due to tether interaction. The trajectory begins with blue markers and ends with red ones.

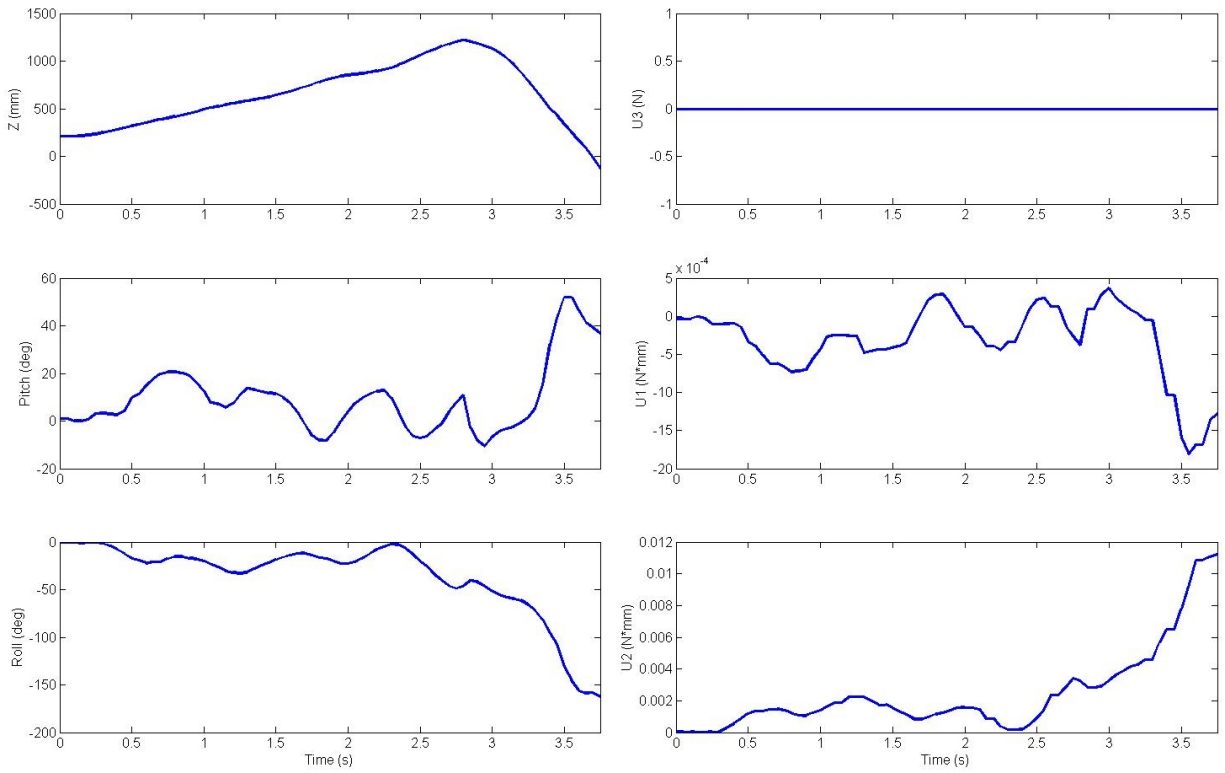


Figure 6.12: Pitch and roll control time series for vertical position, pitch angle, roll angle as well as pitch and roll control signal for short flight due to tether interaction.

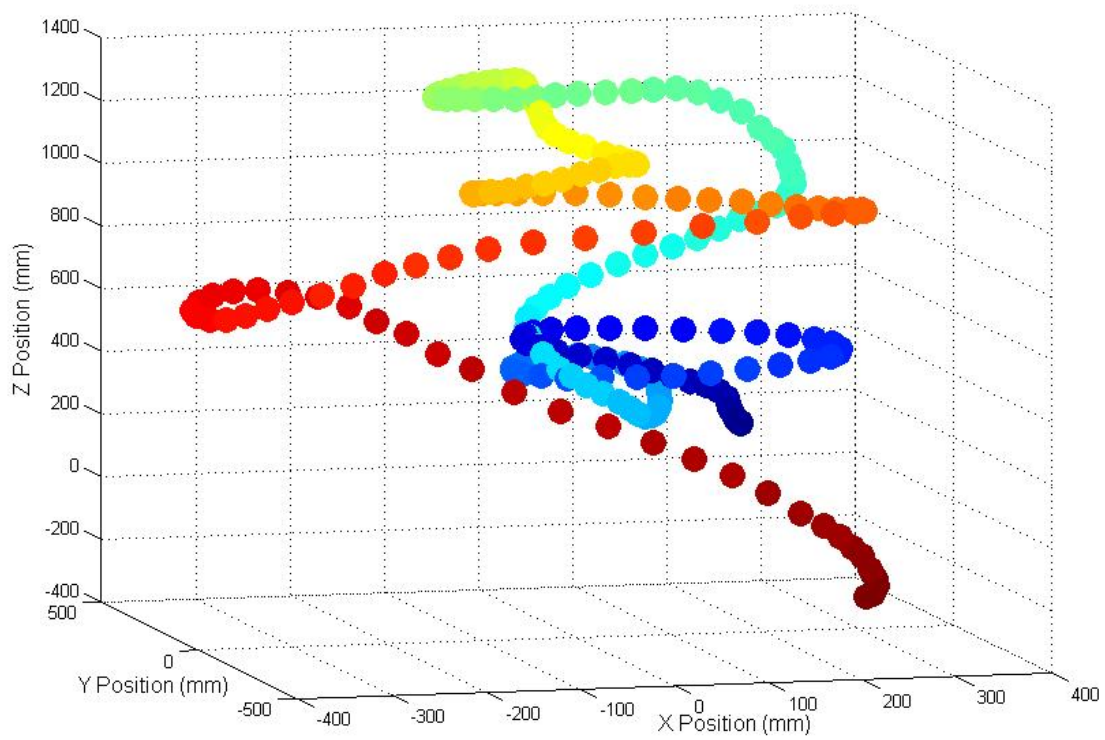


Figure 6.13: Pitch and roll control vicon trajectory showing long flight staying on tether. The trajectory begins with blue markers and ends with red ones.

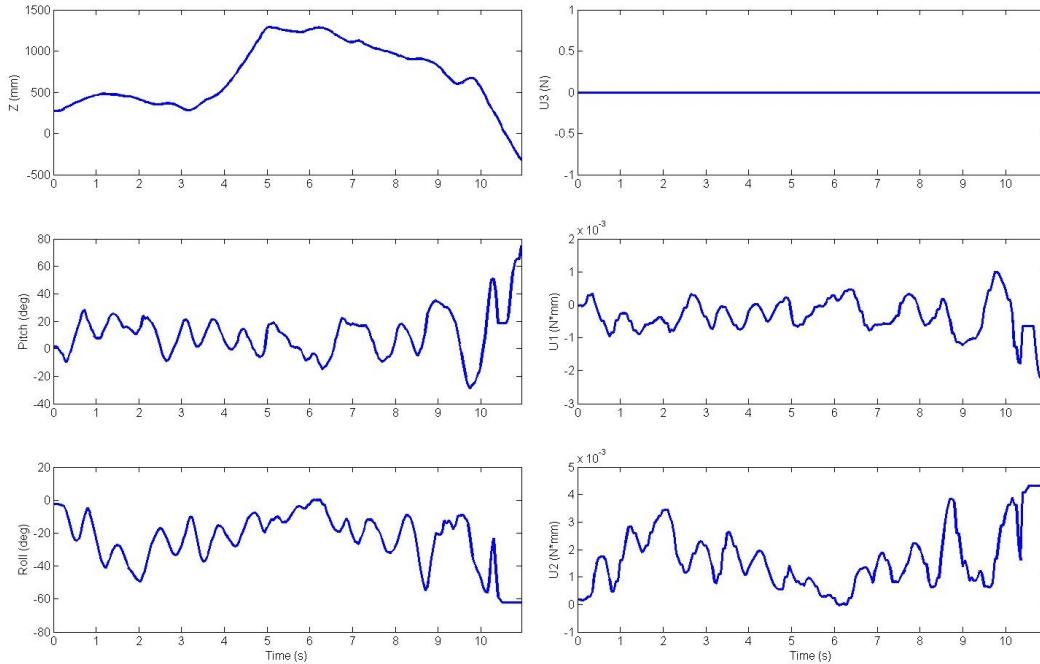


Figure 6.14: Pitch and roll control time series for vertical position, pitch angle, roll angle as well as pitch and roll control signal for long flight staying on tether.

roll angle also tended to drift necessitating integral control for this degree of freedom as well. An integral gain  $I = 1 \times 10^{-6}$  was added to roll, while the other gains were unchanged. For pitch the re-tuned gains were  $P = 0.005$ ,  $D = 0.003$ ,  $I = 4 \times 10^{-5}$  and the  $Z$  set point was lowered to 600 to decrease the likelihood that the system would interact with the tether. The fully tuned system results in low roll and pitch MSE, 255 and 166 respectively, with adequate vertical control. A representative flight trajectory is shown in Figure 6.17, with accompanying data plots shown in Figure 6.18. In this trial, the system begins by climbing vertically. As it passes the vertical set point the rate of climbing decreases, but significant overshoot still occurs. Small attitude deflections, primarily due to oscillations in the pitch angle, caused the system to spiral while it remained controlled. The system then settles towards the vertical set point. A large attitude perturbation occurred after seven seconds that caused the system to lose altitude and rapidly translate to the right ending the trial. The average flight times were  $6.09 \pm 1.17$  seconds. Controller results are summarized in Table 6.4 with transfer functions and set points show in 6.19. A representative trial video is provided as supplemental material. These results clearly demonstrate that the independent wing control paradigm is effective for control of motor driven systems at larger scales. Furthermore, the final flight time is the longest reported in the literature for this control paradigm. Building off this work, improved control frameworks and flight behaviors can be developed for such systems.

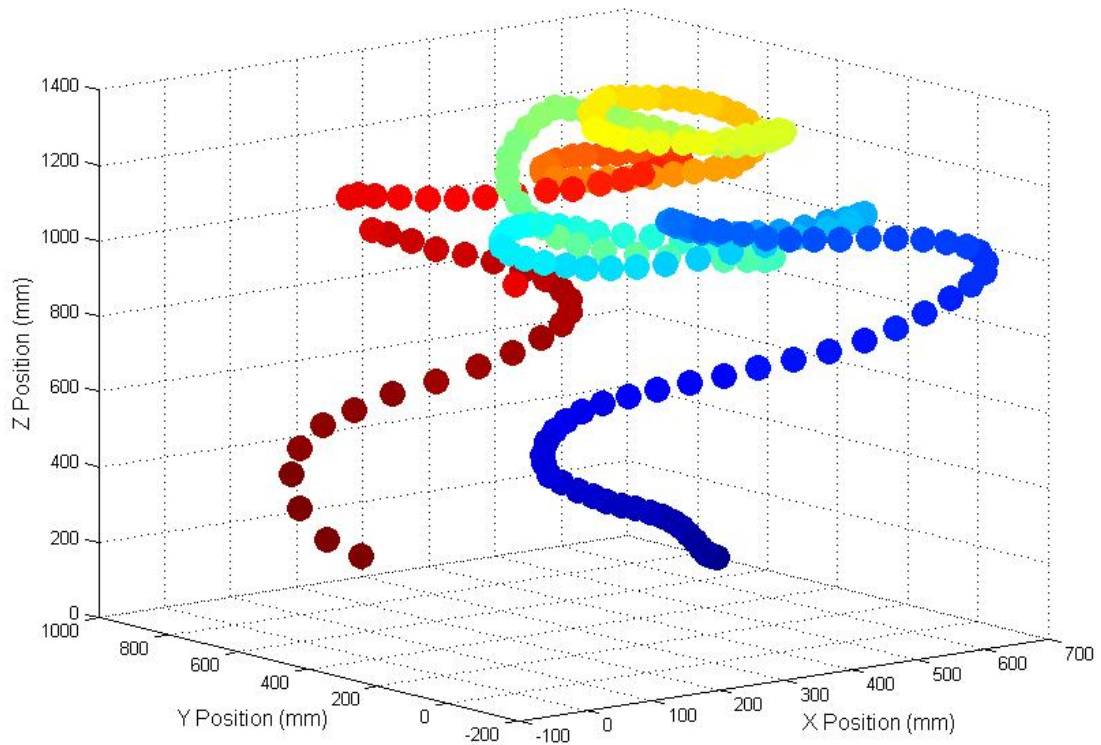


Figure 6.15: Full PD control vicon trajectory. The trajectory begins with blue markers and ends with red ones.

Table 6.3: Closed-loop Control Results

	Open-loop	Roll	Roll, Pitch	Roll, Pitch, Z
Flight time (s)	$2.78 \pm 0.48$	$4.75 \pm 0.84$	$4.96 \pm 3.28$	$6.09 \pm 1.17$
Roll MSE	873	588	769	255
Pitch MSE	974	935	287	166

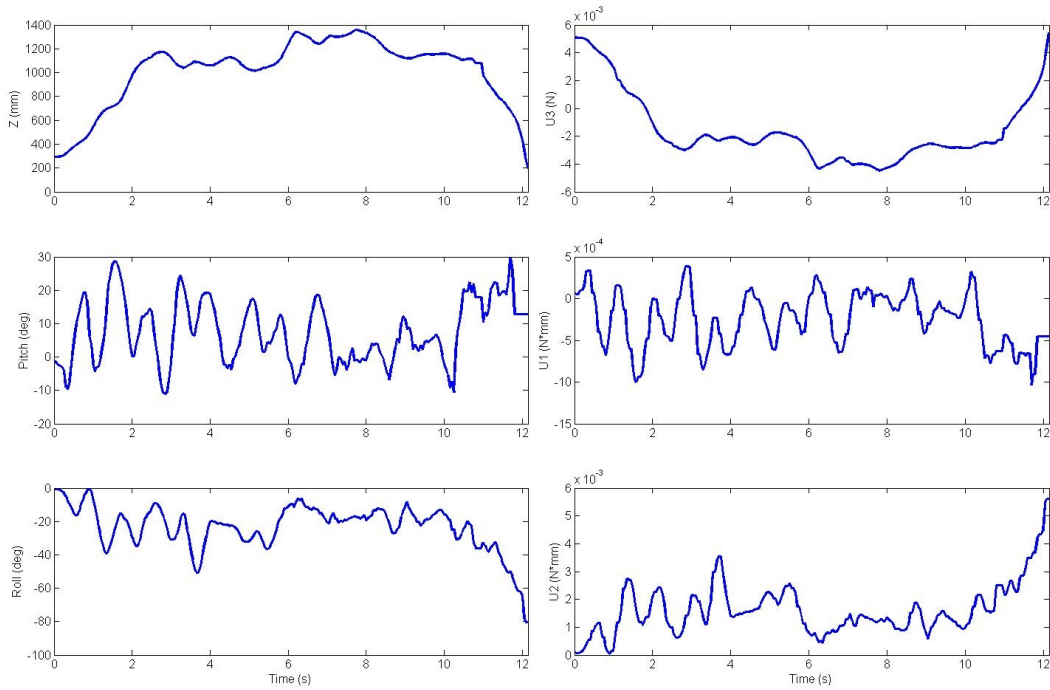


Figure 6.16: Full PD control time series for vertical position, pitch angle, roll angle as well as pitch, roll, and height control signal.

$$\frac{T_y}{\theta_{y, err, rad}} = 0.002 \quad (6.19)$$

$$\theta_{y, des} = 0$$

$$\frac{T_x}{\theta_{x, err, rad}} = \frac{0.002s^2 + 0.004s + 1 \times 10^{-6}}{s}$$

$$\theta_{x, des} = 0$$

$$\frac{F_z}{Z_{err, mm}} = \frac{0.005s^2 + 0.01s + 4 \times 10^{-5}}{s}$$

$$Z_{des} = 600$$

The current system has several limitations that are compounded to reduce performance, particularly for vertical control. The off-line calibration procedure cannot account for changes in trim conditions due to wear of the system, which results in decreased flight performance until the system is re-calibrated. In particular, the commanded  $F_z$  had to be frequently increased so that it continued to match the system weight, a necessary condition for the linearization of the system dynamics about hover to be valid. The resulting commanded  $F_z$  was often too small, with the difference being made up with the tuning of the controller, otherwise choosing  $F_z$  to be too large

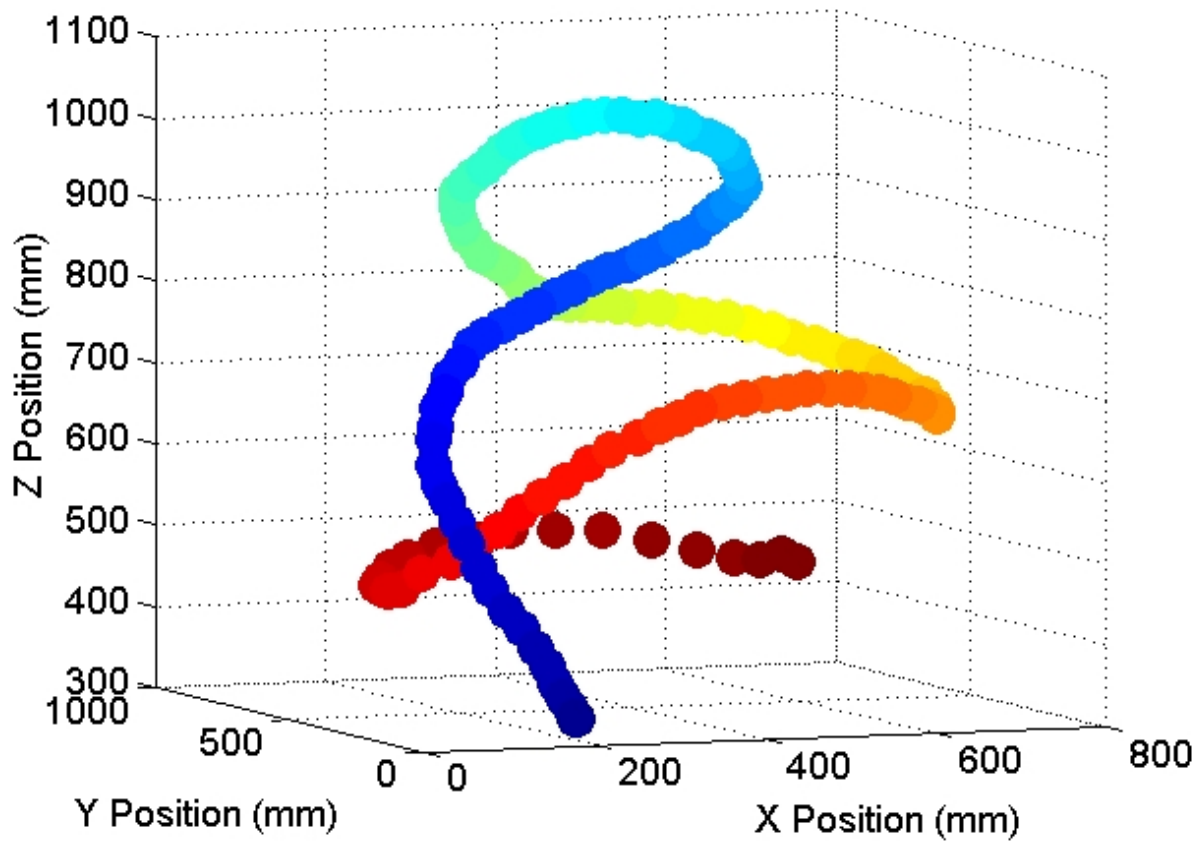


Figure 6.17: Representative closed-loop test flight tracking data for a trail lasting 8 seconds. The 3D trajectory is shown with all axes in mm.

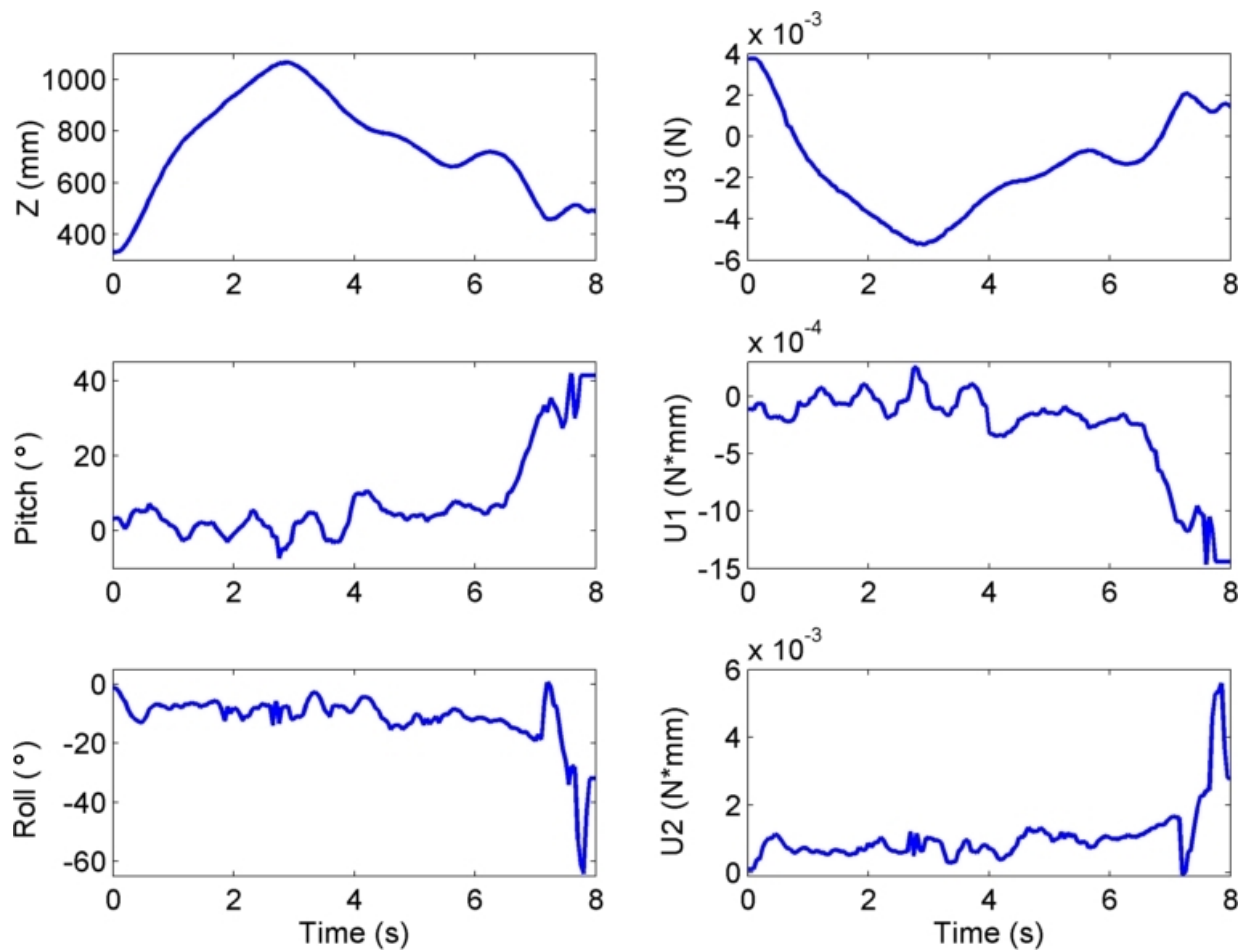


Figure 6.18: Representative closed-loop experiment. The left side shows the controlled degrees of freedom, vertical position as well as the pitch and roll angles. On the right side, the control inputs applied to these degrees of freedom are shown.

resulted in the system quickly climbing vertically and hitting the tether. However, such tuning of the controller resulted in greater overshoot of the vertical set point. Another limitation was the small control volume relative to vehicle size due to tethering of the system. In addition to generating torques to correct angular errors, wing thrust should be increased so that lift remains at the commanded value. However, since angular errors resulted in translation of the system and increasing thrust resulted in faster translation this approach often caused the system to interact with the tether. Future work will focus on adaptive control that relies on free-flight data to populate and update the calibration matrix continuously. Another focus will be system autonomy, integration of the motor driver hardware and an on-board power source. Such an autonomous system is able to operate in a larger control volume and perform active maneuvers that are not possible with the tethered system.

## 6.5 Conclusion

In this chapter I demonstrate the implementation of linear PID control for stable flight of our FWMAV based on independent wing control, which had previously not been demonstrated in motor-driven systems. Independent wing control was realized with a resonant actuator allowing the system to be fully controlled with one actuator per wing, resulting in a vehicle that is lighter, has higher lift to weight capability, and with decreased power consumption compared to other motor-driven systems. We utilize an air-damper as a passive mechanism to reduce pitching oscillations and improve stability compared to previous work. An off-line calibration procedure was used to characterize the relationship from the periodic actuator input signal to the resulting stroke-averaged forces and torques on the vehicle. The resulting sparse calibration accounted for wing-wing interaction and eliminated time-dependent behavior due to heating of the actuator with closed-loop current control. The free flight control framework consisted of three controllers for pitch, roll, and z position that used feedback from the camera tracking system. These controllers were iteratively tuned based on experimental results. Initially vertical flight was used to train the pitch and roll controllers by measuring the reduction of mean squared error through the trials. Vertical control was then trained based on increasing flight time. The tuned controller produced average flight times of  $6.09 \pm 1.17$  seconds, with the longest trial lasting 11.96 seconds. These results provides a stable platform to study free-flight system dynamics and to improve the control framework. The primary limitations that reduce the accuracy of vertical control and flight time are wear of the system that is not accounted for by the off-line calibration as well as a small control volume due to tethering. Future work will focus on adaptive control that relies on free-flight data to continuously update the calibration as well as hardware integration that would result in an untethered system.

# Chapter 7

## Contributions and Concluding Remarks

The major contribution of this work is the development of an efficient, reliable, and controllable FWMAV platform that is capable of controlled flight and has the potential to be fully integrated. In summary, this work presents contribution to system modeling, actuator design, flexible wing design, system robustness, and control. The contributions are:

- Transformed a simple prototype into a robust flapping wing micro aerial vehicle tested with a flapping frequency of 23 Hz, weight of 3.2 g, and peak lift to weight of 3.7 with reliability exceeding 50,000 cycles
- Developed a DC gearmotor based resonant actuator that increases torque and power density by 161.1% and 666.8% respectively, compared to just the motor, while decreasing current draw 25.8%
- Modeled actuator thermal performance, experimentally identifying novel parameters for micro motors, to predict safe operating parameters for the system and to optimize a heatsink that increased operating time by 102.4%
- Fabricated and tested flexible wings that increase translational lift production by 35.3%
- Extended a quasi-steady, blade element aerodynamic simulation to account for wing flexibility demonstrating that the flexible design increases aerodynamic efficiency by 41.3% and the effective lift coefficient by 63.7%
- Implemented control framework stabilizes the vehicle allowing for controlled flight experiments surpassing 10 second in duration

Publication summary:

- D. Colmenares, M. Sitti, Control of a Flapping Wing Micro Air Vehicle for Stable Flight Based on Independent Wing Motion, *International Journal of Advanced Robotic Systems*. In review.
- D. Colmenares, R. Kania, W. Zhang, M. Sitti, Bio-inspired Flexible Twisting Wings Increase Lift and Efficiency of a Flapping Wing Micro Air Vehicle, *Journal of Micro-Bio Robotics*. In review.
- D. Colmenares, R. Kania, M. Liu, M. Sitti, Characterization and Thermal Management of a DC Motor-Driven Resonant Actuator for Miniature Mobile Robots with Oscillating

Limbs, *IEEE/ASME Transactions on Mechatronics*. In review.

- D. Colmenares, R. Kania, W. Zhang, M. Sitti, Compliant Wing Design for a Flapping Wing Micro Air Vehicle, *Proc. Of the IEEE/RSJ Conference on Intelligent Robots and Systems*, Hamburg, Germany, September 2015. pp. 32-39.
- L. Hines, D. Colmenares, M. Sitti, Platform Design and Tethered Flight of a Motor-driven Flapping-wing System, *Proc. Of the IEEE International Conference on Robotics and Automation*, Seattle, WA, May 2015. pp. 5838-5845.

## 7.1 Future Work

The development of a controllable FWMAV capable of controlled free-flight greatly opens up possibilities for future work and development. Currently the primary limitations that reduce the accuracy of vertical control and flight time are wear of the system that is not accounted for by the off-line calibration as well as a small control volume due to tethering. Future work should focus on adaptive control that relies on free-flight data to continuously update the calibration as well as hardware integration that would result in an untethered system. Several tasks that could be realized for improvement of the system are as follows based on subsystem.

### **Actuator Design:**

- Custom motor design and gear ratio selection. Survey available motors using improved workflow:
  - Identify candidate motors using first principles, torque/power density, and/or use of GM15 gearbox
  - Characterize components (motor/gearhead) and select best
  - Measure increased torque/power output due to resonant actuation
  - Impedance matching simulation with measured values to select wing size
- Re-design spring and/or spring assembly to increase coil count, reduce deflection/losses and non-linear/asymmetric behavior
- Mechanical interlocking of spring into mechanism (upper gearbox surface / lower shaft coupler surface)

### **Flexible Wing Design and Modeling:**

- Develop consistent procedure for twisting wing fabrication
- Acquire improved material and equipment (heated press)
- Additional experiments and testing methodologies (PIV / CFD) to characterize improvements due to twist
- Update simulation with determined 3D flexibility effects
- Generate and test optimized twisted wing designs

### **Vehicle Design:**

- Wing below flexure could reduce rotation asymmetries
- Integrate flexure and wing assembly to reduce manufacturing defects and reduce glue weight
- 3D print actuator, vehicle, damper assembly to reduce weight
- Increasing the rigidity of the system to reduce vertical deflections of the wing stroke plan would ensure consistent force generation.
- Driving system with an H-bridge and integrating closed-loop current control could reduce hardware complexity and weight, as a step towards onboard hardware integration.

**Control:**

- Model free control based on flight experiments using on-line calibration could significantly improve model accuracy and allow experimental determination of flight model parameters
- Adaptive control framework could adapt to system wear
- Robust controller design from non-linear dynamics
- Full integration of system hardware allowing untethered flight
- Improved vertical control using larger control volume
- Explore underactuated control of wing rotation utilizing fast/slow dynamics
- Other mechanisms to actively control wing rotation would significantly improve vehicle maneuverability
- Improved control framework to fully utilize two wing control
  - Set amplitude based on orientation and desired lift
  - Bias wings symmetrically based on desired pitch torque
  - Vary L/R lift percentage based on desired roll torque

# Bibliography

- [1] Stacey Anne Combes. *Wing flexibility and design for animal flight*. Thesis, 2002. (document), 4.2, 4.3
- [2] CP Ellington. The aerodynamics of hovering insect flight. ii. morphological parameters. *Philosophical Transactions of the Royal Society of London. B, Biological Sciences*, 305(1122):17–40, 1984. (document), 4.2.2, 4.2.3, 4.3, 4.3
- [3] Michael H Dickinson, Fritz-Olaf Lehmann, and Sanjay P Sane. Wing rotation and the aerodynamic basis of insect flight. *Science*, 284(5422):1954–1960, 1999. (document), 1.2, 2.3, 4.6, 4.12
- [4] JP Whitney and RJ Wood. Conceptual design of flapping-wing micro air vehicles. *Bioinspiration & biomimetics*, 7(3):036001, 2012. (document), 4.6.6, 4.21
- [5] Elisabetta Chiappini and John Huber. *Fairyflies (Hymenoptera: Mymaridae)*, pages 1407–1409. Springer, 2008. 1.1
- [6] Robert C Lasiewski, Wesley W Weathers, and Marvin H Bernstein. Physiological responses of the giant hummingbird, patagona gigas. *Comparative biochemistry and physiology*, 23(3):797–813, 1967. 1.1
- [7] Robert Dudley and York Winter. Hovering flight mechanics of neotropical flower bats (phyllostomidae: Glossophaginae) in normodense and hypodense gas mixtures. *Journal of Experimental Biology*, 205(23):3669–3677, 2002. 1.1, 1.2, 4.2.2
- [8] Steven N Fry, Rosalyn Sayaman, and Michael H Dickinson. The aerodynamics of free-flight maneuvers in drosophila. *Science*, 300(5618):495–498, 2003. 1.1, 2.4
- [9] Matteo Mischiati, Huai-Ti Lin, Paul Herold, Elliot Imler, Robert Olberg, and Anthony Leonardo. Internal models direct dragonfly interception steering. *Nature*, 517(7534):333–338, 2015. 1.1
- [10] Introduction to the odonata. 1.1
- [11] Robert Wood, Radhika Nagpal, and Gu-Yeon Wei. Flight of the robobees. *Scientific American*, 308(3):60–65, 2013. 1.1
- [12] C Galiski and R bikowski. Some problems of micro air vehicles development. *Technical Sciences*, 55(1), 2007. 1.1
- [13] Michael Karpelson, Gu-Yeon Wei, and Robert J Wood. A review of actuation and power electronics options for flapping-wing robotic insects. In *Robotics and Automation, 2008. ICRA 2008. IEEE International Conference on*, pages 779–786. IEEE. 1.1, 1.2.2

- [14] Franck Ruffier and Nicolas Franceschini. Visually guided micro-aerial vehicle: automatic take off, terrain following, landing and wind reaction. In *Robotics and Automation, 2004. Proceedings. ICRA'04. 2004 IEEE International Conference on*, volume 3, pages 2339–2346. IEEE. 1.1
- [15] Steven N Fry, Rosalyn Sayaman, and Michael H Dickinson. The aerodynamics of hovering flight in drosophila. *Journal of Experimental Biology*, 208(12):2303–2318, 2005. 1.2
- [16] Michael H Dickinson. Muscle efficiency and elastic storage in the flight motor of drosophila. *Science*, 268(5207):87–90, 1995. 1.2
- [17] Akira Mamiya and Michael H Dickinson. Antennal mechanosensory neurons mediate wing motor reflexes in flying drosophila. *The Journal of Neuroscience*, 35(20):7977–7991, 2015. 1.2
- [18] Stacey A Combes and Thomas L Daniel. Into thin air: contributions of aerodynamic and inertial-elastic forces to wing bending in the hawkmoth *manduca sexta*. *Journal of Experimental Biology*, 206(17):2999–3006, 2003. 1.2, 4.2.4
- [19] Alexander P Willmott and Charles P Ellington. The mechanics of flight in the hawkmoth *manduca sexta*. i. kinematics of hovering and forward flight. *The Journal of Experimental Biology*, 200(21):2705–2722, 1997. 1.2, 4.2.6
- [20] ALEXANDER P Willmott and CHARLES P Ellington. The mechanics of flight in the hawkmoth *manduca sexta*. ii. aerodynamic consequences of kinematic and morphological variation. *The Journal of experimental biology*, 200(21):2723–2745, 1997. 1.2, 3.4
- [21] Alexander P Willmott, Charles P Ellington, and Adrian LR Thomas. Flow visualization and unsteady aerodynamics in the flight of the hawkmoth, *manduca sexta*. *Philosophical Transactions of the Royal Society B: Biological Sciences*, 352(1351):303–316, 1997. 1.2
- [22] Michael H Dickinson. Motor control: How dragonflies catch their prey. *Current Biology*, 25(6):R232–R234, 2015. 1.2
- [23] Akira Azuma, Soichi Azuma, Isao Watanabe, and Toyohiko Furuta. Flight mechanics of a dragonfly. *Journal of experimental biology*, 116(1):79–107, 1985. 1.2
- [24] JM Wakeling and C Pt Ellington. Dragonfly flight. i. gliding flight and steady-state aerodynamic forces. *Journal of Experimental Biology*, 200(3):543–556, 1997. 1.2
- [25] JM Wakeling and CP Ellington. Dragonfly flight. ii. velocities, accelerations and kinematics of flapping flight. *Journal of experimental biology*, 200(3):557–582, 1997. 1.2
- [26] JM Wakeling and CP Ellington. Dragonfly flight. iii. lift and power requirements. *Journal of Experimental Biology*, 200(3):583–600, 1997. 1.2
- [27] Bret W Tobalske, Douglas R Warrick, Christopher J Clark, Donald R Powers, Tyson L Hedrick, Gabriel A Hyder, and Andrew A Biewener. Three-dimensional kinematics of hummingbird flight. *Journal of Experimental Biology*, 210(13):2368–2382, 2007. 1.2, 4.2.6
- [28] Douglas L Altshuler and Robert Dudley. Kinematics of hovering hummingbird flight along simulated and natural elevational gradients. *Journal of Experimental Biology*,

206(18):3139–3147, 2003. 1.2

- [29] Douglas L Altshuler, Robert Dudley, and Jimmy A McGuire. Resolution of a paradox: hummingbird flight at high elevation does not come without a cost. *Proceedings of the National Academy of Sciences of the United States of America*, 101(51):17731–17736, 2004. 1.2
- [30] Tyson L Hedrick, Bret W Tobalske, Ivo G Ros, Douglas R Warrick, and Andrew A Biewener. Morphological and kinematic basis of the hummingbird flight stroke: scaling of flight muscle transmission ratio. *Proceedings of the Royal Society of London B: Biological Sciences*, page rspb20112238, 2011. 1.2
- [31] Steven P Thomas and RODERICK A SUTHERS. The physiology and energetics of bat flight. *Journal of Experimental Biology*, 57(2):317–335, 1972. 1.2
- [32] SP Thomas. The physiology of bat flight. *Recent advances in the study of bats*, pages 75–99, 1987. 1.2
- [33] Anders Hedenström, LC Johansson, Marta Wolf, R Von Busse, Y Winter, and GR Spedding. Bat flight generates complex aerodynamic tracks. *Science*, 316(5826):894–897, 2007. 1.2
- [34] Tatjana Y Hubel, Nickolay I Hristov, Sharon M Swartz, and Kenneth S Breuer. Time-resolved wake structure and kinematics of bat flight. *Experiments in fluids*, 46(5):933–943, 2009. 1.2
- [35] David Lentink and Michael H Dickinson. Rotational accelerations stabilize leading edge vortices on revolving fly wings. *Journal of Experimental Biology*, 212(16):2705–2719, 2009. 1.2, 1.3, 4.2.3, 4.2.3, 4.7.1
- [36] Jan W Kruyt, GertJan F van Heijst, Douglas L Altshuler, and David Lentink. Power reduction and the radial limit of stall delay in revolving wings of different aspect ratio. *Journal of The Royal Society Interface*, 12(105):20150051, 2015. 1.2, 4.2.5
- [37] Philip C Withers. An aerodynamic analysis of bird wings as fixed aerofoils. *Journal of Experimental Biology*, 90(1):143–162, 1981. 1.2
- [38] Mark Cutler, N Kemal Ure, Bernard Michini, and Jonathan P How. Comparison of fixed and variable pitch actuators for agile quadrotors. In *AIAA Conf. on Guidance, Navigation and Control, Portland, OR*. 1.2
- [39] TL Hedrick and TL Daniel. Flight control in the hawkmoth *manduca sexta*: the inverse problem of hovering. *The journal of experimental Biology*, 209(16):3114–3130, 2006. 1.2
- [40] Charles P Ellington. The novel aerodynamics of insect flight: applications to micro-air vehicles. *Journal of Experimental Biology*, 202(23):3439–3448, 1999. 1.2, 1.2.1, 4.2
- [41] CP Ellington. Limitations on animal flight performance. *Journal of Experimental Biology*, 160(1):71–91, 1991. 1.2
- [42] Torkel Weis-Fogh. Quick estimates of flight fitness in hovering animals, including novel mechanisms for lift production. *Journal of Experimental Biology*, 59(1):169–230, 1973. 1.2, 4.2.1, 4.2.2
- [43] Tony Maxworthy. Experiments on the weis-fogh mechanism of lift generation by insects

- in hovering flight. part 1. dynamics of the fling. *Journal of Fluid Mechanics*, 93(01):47–63, 1979. 1.2
- [44] Zachary John Jackowski. *Design and construction of an autonomous ornithopter*. Thesis, 2009. 1.2
- [45] David Billingsley, Geoff Slipper, Jared Grauer, and James Hubbard. Testing of a passively morphing ornithopter wing. *AIAA Paper*, 1828, 2009. 1.2
- [46] T Nick Pornsin-Sirirak, YC Tai, H Nassef, and CM Ho. Titanium-alloy mems wing technology for a micro aerial vehicle application. *Sensors and Actuators A: Physical*, 89(1):95–103, 2001. 1.2
- [47] Stanley S Baek, Fernando L Garcia Bermudez, and Ronald S Fearing. Flight control for target seeking by 13 gram ornithopter. In *Intelligent Robots and Systems (IROS), 2011 IEEE/RSJ International Conference on*, pages 2674–2681. IEEE. 1.2
- [48] Domenico Campolo. Motor selection via impedance-matching for driving nonlinearly damped, resonant loads. *Mechatronics*, 20(5):566–573, 2010. 1.2.1, 3.2, 3.2, 3.4, 3.4
- [49] GCHE De Croon, KME De Clercq, R Ruijsink, B Remes, and C De Wagter. Design, aerodynamics, and vision-based control of the delfly. *International Journal of Micro Air Vehicles*, 1(2):71–97, 2009. 1.2.1, 3.2, 3.3, 3.4
- [50] Matthew Keennon, Karl Klingebiel, Henry Won, and Alexander Andriukov. Development of the nano hummingbird: A tailless flapping wing micro air vehicle. In *AIAA Aerospace Sciences Meeting*, pages 1–24. 1.2.1, 1.1, 1.2.3, 3.2, 4.4, 4.7.1
- [51] Charles Richter and Hod Lipson. Untethered hovering flapping flight of a 3d-printed mechanical insect. *Artificial life*, 17(2):73–86, 2011. 1.2.1, 1.1, 3.2, 3.6, 5.4
- [52] Muhammad Azhar, Domenico Campolo, Gih-Keong Lau, Lindsey Hines, and Metin Sitti. Flapping wings via direct-driving by dc motors. In *Robotics and Automation (ICRA), 2013 IEEE International Conference on*, pages 1397–1402. IEEE. 1.2.1, 3.2, 3.4
- [53] Domenico Campolo, Muhammad Azhar, Gih-Keong Lau, and Metin Sitti. Can dc motors directly drive flapping wings at high frequency and large wing strokes? *Mechatronics, IEEE/ASME Transactions on*, 19(1):109–120, 2014. 1.2.1, 3.4, 3.4, 4.5
- [54] Lindsey Hines, Domenico Campolo, and Metin Sitti. Liftoff of a motor-driven, flapping-wing microaerial vehicle capable of resonance. *Robotics, IEEE Transactions on*, 30(1):220–232, 2014. 1.2.1, 1.1, 1.4, 2.1, 3.4, 3.6, 4.5
- [55] Lindsey Hines, David Colmenares, and Metin Sitti. Platform design and tethered flight of a motor-driven flapping-wing system. In *Robotics and Automation (ICRA), 2015 IEEE International Conference on*, pages 5838–5845. IEEE. 1.2.1, 1.4, 5.4, 6.3
- [56] Colmenares David, Kania Randall, Zhang Wang, and Sitti Mettin. Compliant wing design for a flapping wing micro air vehicle. *Proc. Of the IEEE/RSJ International Conference on Intelligent Robots and Systems, Hamburg, Germany*, 2015. 1.2.1, 1.1, 1.4, 3.4
- [57] Jian Zhang, Bo Cheng, Jesse Roll, Xinyan Deng, and Bin Yao. Direct drive of flapping wings under resonance with instantaneous wing trajectory control. In *Robotics and Automation (ICRA), 2013 IEEE International Conference on*, pages 4029–4034. IEEE. 1.2.1,

1.2.3, 3.3

- [58] Jian Zhang, Bo Cheng, Bin Yao, and Xinyan Deng. Adaptive robust wing trajectory control and force generation of flapping wing mav. In *Robotics and Automation (ICRA), 2015 IEEE International Conference on*, pages 5852–5857. IEEE. 1.2.1, 1.1, 1.2.3, 3.3
- [59] Jesse Roll, Bo Cheng, and Xinyan Deng. An electromagnetic actuator for high-frequency flapping-wing microair vehicles. *Robotics, IEEE Transactions on*, 31(2):400–414, 2015. 1.1, 1.2.1
- [60] Gih-Keong Lau, Yao-Wei Chin, Joel Tian-Wei Goh, and Robert J Wood. Dipteran-insect-inspired thoracic mechanism with nonlinear stiffness to save inertial power of flapping-wing flight. *Robotics, IEEE Transactions on*, 30(5):1187–1197, 2014. 1.2.1, 3.4
- [61] Stanley S Baek, Kevin Y Ma, and Ronald S Fearing. Efficient resonant drive of flapping-wing robots. In *Intelligent Robots and Systems, 2009. IROS 2009. IEEE/RSJ International Conference on*, pages 2854–2860. IEEE. 1.2.1, 3.2, 3.4
- [62] S Deng, BW Van Oudheusden, BDW Remes, M Persin, H Bijl, and HM Ruijsink. Experimental investigation of the flapping performance on ‘delfly micro’. In *IMAV 2013: Proceedings of the International Micro Air Vehicle Conference and Flight Competition, Toulouse, France, 17-20 September 2013*. 1.1
- [63] Christophe De Wagter, Sjoerd Tijmons, Bart DW Remes, and Guido CHE de Croon. Autonomous flight of a 20-gram flapping wing mav with a 4-gram onboard stereo vision system. In *Robotics and Automation (ICRA), 2014 IEEE International Conference on*, pages 4982–4987. IEEE. 1.1
- [64] Robert J Wood. The first takeoff of a biologically inspired at-scale robotic insect. *Robotics, IEEE Transactions on*, 24(2):341–347, 2008. 1.2.2, 1.2, 3.4
- [65] Kevin Y Ma, Pakpong Chirarattananon, Sawyer B Fuller, and Robert J Wood. Controlled flight of a biologically inspired, insect-scale robot. *Science*, 340(6132):603–607, 2013. 1.2.2, 1.2, 3.4, 6.1
- [66] Zhi Ern Teoh and Robert J Wood. A bioinspired approach to torque control in an insect-sized flapping-wing robot. In *Biomedical Robotics and Biomechatronics (2014) 5th IEEE RAS and EMBS International Conference on*, pages 911–917. IEEE. 1.2.2
- [67] Noah T Jafferis, Michael J Smith, and Robert J Wood. Design and manufacturing rules for maximizing the performance of polycrystalline piezoelectric bending actuators. *Smart Materials and Structures*, 24(6):065023, 2015. 1.2.2
- [68] Sawyer B Fuller, Michael Karpelson, Andrea Censi, Kevin Y Ma, and Robert J Wood. Controlling free flight of a robotic fly using an onboard vision sensor inspired by insect ocelli. *Journal of The Royal Society Interface*, 11(97):20140281, 2014. 1.2.2
- [69] E Farrell Helbling, Sawyer B Fuller, and Robert J Wood. Pitch and yaw control of a robotic insect using an onboard magnetometer. In *Robotics and Automation (ICRA), 2014 IEEE International Conference on*, pages 5516–5522. IEEE. 1.2.2
- [70] Sawyer B Fuller, E Farrell Helbling, Pakpong Chirarattananon, and Robert J Wood. Using a mems gyroscope to stabilize the attitude of a fly-sized hovering robot. In *IMAV 2014*:

*International Micro Air Vehicle Conference & Competition 2014, Delft, The Netherlands, August 12-15, 2014.* Delft University of Technology. 1.2.2

- [71] S Felton, M Tolley, E Demaine, D Rus, and R Wood. A method for building self-folding machines. *Science*, 345(6197):644–646, 2014. 1.2.2
- [72] Pratheev Sabaratnam Sreetharan, John Peter Whitney, and Robert J Wood. Monolithic fabrication of three-dimensional structures, 2014. 1.2.2
- [73] Xinyan Deng, Luca Schenato, Wei Chung Wu, and S Shankar Sastry. Flapping flight for biomimetic robotic insects: Part i-system modeling. *Robotics, IEEE Transactions on*, 22(4):776–788, 2006. 1.2, 1.2.2
- [74] Xinyan Deng, Luca Schenato, and S Shankar Sastry. Flapping flight for biomimetic robotic insects: Part ii-flight control design. *Robotics, IEEE Transactions on*, 22(4):789–803, 2006. 1.2.2
- [75] Ronald G Polcawich, Jeffrey S Pulskamp, Sarah Bedair, Gabriel Smith, Roger Kaul, Chris Kroninger, Eric Wetzel, Hengky Chandrahilim, and Sunil Bhawe. Integrated piezomems actuators and sensors. In *Sensors, 2010 IEEE*, pages 2193–2196. IEEE. 1.2.2
- [76] JS Pulskamp, G Smith, R Polcawich, C Kroninger, and E Wetzel. Two degree of freedom pzt mems actuated flapping wings with integrated force sensing. In *Proc. of*, pages 390–391. 1.2, 1.2.2
- [77] Christopher T Orlowski and Anouck R Girard. Dynamics, stability, and control analyses of flapping wing micro-air vehicles. *Progress in Aerospace Sciences*, 51:18–30, 2012. 1.2.3
- [78] Luca Schenato, Domenico Campolo, and Shankar Sastry. Controllability issues in flapping flight for biomimetic micro aerial vehicles (mavs). In *Decision and Control, 2003. Proceedings. 42nd IEEE Conference on*, volume 6, pages 6441–6447. IEEE. 1.2.3, 6.1
- [79] A Roshanbin, Christophe Collette, and Andr Preumont. Mathematical modelling of insectlike flapping wings for application to mavs. In *International Symposium on Light Weight Unmanned Aerial Vehicle Systems and Subsystems*, pages 11–13. 1.2.3
- [80] Andrea Serrani. Robust nonlinear control design for a minimally-actuated flapping-wing mav in the longitudinal plane. In *Decision and Control and European Control Conference (CDC-ECC), 2011 50th IEEE Conference on*, pages 7464–7469. IEEE. 1.2.3
- [81] Zaeem Khan and K Agrawal. Control of longitudinal flight dynamics of a flapping-wing micro air vehicle using time-averaged model and differential flatness based controller. In *American Control Conference, 2007. ACC'07*, pages 5284–5289. IEEE. 1.2.3
- [82] Matej Karsek, Alexandre Hua, Yanghai Nan, Mohamed Lalami, and Andr Preumont. Pitch and roll control mechanism for a hovering flapping wing mav. *International Journal of Micro Air Vehicles*, 6(4):253–264, 2014. 1.2.3, 3.3
- [83] Zhi Ern Teoh, Sawyer B Fuller, Pakpong Chirarattananon, NO Prez-Arancibia, Jack D Greenberg, and Robert J Wood. A hovering flapping-wing microrobot with altitude control and passive upright stability. In *Intelligent Robots and Systems (IROS), 2012 IEEE/RSJ International Conference on*, pages 3209–3216. IEEE. 1.2.3, 5.4

- [84] Nstor O Prez-Arancibia, Pierre-Emile J Duhamel, Kevin Y Ma, and Robert J Wood. Model-free control of a flapping-wing flying microrobot. In *Advanced Robotics (ICAR), 2013 16th International Conference on*, pages 1–8. IEEE. 1.2.3
- [85] Nstor O Prez-Arancibia, Pierre-Emile J Duhamel, Kevin Y Ma, and Robert J Wood. Model-free control of a hovering flapping-wing microrobot. *Journal of Intelligent & Robotic Systems*, 77(1):95–111, 2015. 1.2.3
- [86] Pakpong Chirarattananon, Kevin Y Ma, and Robert J Wood. Adaptive control for takeoff, hovering, and landing of a robotic fly. In *Intelligent Robots and Systems (IROS), 2013 IEEE/RSJ International Conference on*, pages 3808–3815. IEEE. 1.2.3
- [87] L Zheng, T Hedrick, and R Mittal. A comparative study of the hovering efficiency of flapping and revolving wings. *Bioinspiration & biomimetics*, 8(3):036001, 2013. 1.3, 4.2.6
- [88] Infrared helicopter nano-falcon world’s smallest size. 1.3
- [89] Estes 4606 proto x nano r/c quadcopter. 1.3
- [90] Pd-100 black hornet prs. 1.3
- [91] The crazyflie nano quadcopter. 1.3
- [92] Yash Mulgaonkar, Gareth Cross, and Vijay Kumar. Design of small, safe and robust quadrotor swarms. In *Robotics and Automation (ICRA), 2015 IEEE International Conference on*, pages 2208–2215. IEEE. 1.3
- [93] Theodore L Bergman, Frank P Incropera, and Adrienne S Lavine. *Fundamentals of heat and mass transfer*. John Wiley & Sons, 2011. 1.3, 3.6, 3.6
- [94] Sanjay P Sane and Michael H Dickinson. The aerodynamic effects of wing rotation and a revised quasi-steady model of flapping flight. *Journal of Experimental Biology*, 205(8):1087–1096, 2002. 1.4, 2.1, 2.3
- [95] Colmenares David, Kania Randall, Liu Miao, and Sitti Mettin. Characterization and thermal management of a dc motor-driven resonant actuator for miniature mobile robots with oscillating limbs. *IEEE/ASME Transactions on Mechatronics*, 2017 (In review). 1.4
- [96] Colmenares David, Kania Randall, Zhang Wang, and Sitti Mettin. Bio-inspired flexible twisting wings increase lift and efficiency of a flapping wing micro air vehicle. *Journal of Micro-Bio Robotics*, 2017 (In review). 1.4
- [97] Colmenares David and Sitti Mettin. Control of a flapping wing micro air vehicle for stable flight based on independent wing motion. *International Journal of Advanced Robotic Systems*, 2017 (In review). 1.4
- [98] Veaceslav Arabagi, Lindsey Hines, and Metin Sitti. A simulation and design tool for a passive rotation flapping wing mechanism. *Mechatronics, IEEE/ASME Transactions on*, 18(2):787–798, 2013. 2.4
- [99] T Wu. Hydromechanics of swimming propulsion. part 1. swimming of a two-dimensional flexible plate at variable forward speeds in an inviscid fluid. *Journal of Fluid Mechanics*, 46(02):337–355, 1971. 2.4

- [100] Ravi Ramamurti. Computational study of 3-d flapping foil flows ravi ramamurti and william c. sandberg. 2001. 2.4
- [101] Kevin C Galloway, Galen Clark Haynes, B Deniz Ilhan, Aaron M Johnson, Ryan Knopf, Goran A Lynch, Benjamin N Plotnick, Mackenzie White, and Daniel E Koditschek. X-rhex: A highly mobile hexapedal robot for sensorimotor tasks. 2010. 3.2
- [102] Paul Birkmeyer, Kevin Peterson, and Ronald S Fearing. Dash: A dynamic 16g hexapedal robot. In *Intelligent Robots and Systems, 2009. IROS 2009. IEEE/RSJ International Conference on*, pages 2683–2689. IEEE, 2009. 3.2, 3.4
- [103] Steven Floyd and Metin Sitti. Design and development of the lifting and propulsion mechanism for a biologically inspired water runner robot. *IEEE transactions on robotics*, 24(3):698–709, 2008. 3.2
- [104] MJ Spenko, G Clark Haynes, JA Saunders, Mark R Cutkosky, Alfred A Rizzi, Robert J Full, and Daniel E Koditschek. Biologically inspired climbing with a hexapedal robot. *Journal of Field Robotics*, 25(4-5):223–242, 2008. 3.2
- [105] David B Doman, Michael W Oppenheimer, and David O Sigthorsson. Wingbeat shape modulation for flapping-wing micro-air-vehicle control during hover. *Journal of guidance, control, and dynamics*, 33(3):724, 2010. 3.2
- [106] Portescap - workings of a brush dc motor. 3.2
- [107] Gm15 25:1 6mm planetary gear pager motor. 3.2, 3.4
- [108] Dimension engineering - syren 10a regenerative motor driver. 3.2
- [109] Jesse A Roll, Bo Cheng, and Xinyan Deng. An electromagnetic actuator for high-frequency flapping-wing microair vehicles. *IEEE Transactions on Robotics*, 31(2):400–414, 2015. 3.4
- [110] McMaster-carr - torsion springs. 3.4
- [111] Faulhaber - series 06/1 planetary gearhead specification. 3.4
- [112] Peng Chai and David Millard. Flight and size constraints: hovering performance of large hummingbirds under maximal loading. *Journal of experimental biology*, 200(21):2757–2763, 1997. 3.4
- [113] RD Stevenson and ROBERT K JOSEPHSON. Effects of operating frequency and temperature on mechanical power output from moth flight muscle. *Journal of Experimental Biology*, 149(1):61–78, 1990. 3.4
- [114] Fritz-Olaf Lehmann and Michael H Dickinson. The changes in power requirements and muscle efficiency during elevated force production in the fruit fly *drosophila melanogaster*. *The Journal of experimental biology*, 200(7):1133–1143, 1997. 3.4
- [115] Jim Vigoreaux. *Nature’s Versatile Engine:: Insect Flight Muscle Inside and Out*. Springer Science & Business Media, 2007. 3.4
- [116] Robert J Full. Invertebrate locomotor systems. *Comprehensive Physiology*, 1997. 3.4
- [117] Darrell R Stokes, Jean G Malamud, and Derek A Schreihofer. Gender specific developmental transformation of a cockroach bifunctional muscle. *Journal of Experimental*

*Zoology Part A: Ecological Genetics and Physiology*, 268(5):364–376, 1994. 3.4

- [118] Z. J. Liu, D. Howe, P. H. Mellor, and M. K. Jenkins. Thermal analysis of permanent magnet machines. In *1993 Sixth International Conference on Electrical Machines and Drives (Conf. Publ. No. 376)*, pages 359–364, 1993. 3.6
- [119] Yves Bertin, Etienne Videcoq, Sophie Thieblin, and Daniel Petit. Thermal behavior of an electrical motor through a reduced model. *IEEE Transactions on energy conversion*, 15(2):129–134, 2000. 3.6
- [120] Dave Staton, Aldo Boglietti, and Andrea Cavagnino. Solving the more difficult aspects of electric motor thermal analysis. In *Electric Machines and Drives Conference, 2003. IEMDC'03. IEEE International*, volume 2, pages 747–755. IEEE, 2003. 3.6
- [121] Avik De, Goran Lynch, Aaron Johnson, and Daniel Koditschek. Motor sizing for legged robots using dynamic task specification. In *Technologies for Practical Robot Applications (TePRA), 2011 IEEE Conference on*, pages 64–69. IEEE, 2011. 3.6
- [122] Salomon Trujillo and Mark Cutkosky. Thermally constrained motor operation for a climbing robot. In *Robotics and Automation, 2009. ICRA'09. IEEE International Conference on*, pages 2362–2367. IEEE, 2009. 3.6, 3.6.1
- [123] David A Howey, Peter RN Childs, and Andrew S Holmes. Air-gap convection in rotating electrical machines. *IEEE Transactions on Industrial Electronics*, 59(3):1367–1375, 2012. 3.6, 3.6.1
- [124] Aldo Boglietti, Andrea Cavagnino, David Staton, Martin Shanel, Markus Mueller, and Carlos Mejuto. Evolution and modern approaches for thermal analysis of electrical machines. *IEEE Transactions on industrial electronics*, 56(3):871–882, 2009. 3.6
- [125] Leif Ristroph and Stephen Childress. Stable hovering of a jellyfish-like flying machine. *Journal of The Royal Society Interface*, 11(92):20130992, 2014. 3.6
- [126] Serge Kernbach. Swarmrobot. org-open-hardware microrobotic project for large-scale artificial swarms. *arXiv preprint arXiv:1110.5762*, 2011. 3.6
- [127] Maxon motor - thermal behavior dc motors. 3.6
- [128] Robert L Boylestad. *Boylestad's circuit analysis*. Toronto: Pearson Prentice Hall, 2004. 3.6.2
- [129] B Venkataraman, B Godsey, W Premerlani, E Shulman, M Thaku, and R Midence. Fundamentals of a motor thermal model and its applications in motor protection. In *Protective Relay Engineers, 2005 58th Annual Conference for*, pages 127–144. IEEE, 2005. 3.6.4
- [130] Stacey A Combes. Materials, structure, and dynamics of insect wings as bioinspiration for mavs. *Encyclopedia of Aerospace Engineering*, 2010. 4.2, 4.2.4
- [131] Oskar Karl Gustav Tietjens. *Applied hydro-and aeromechanics: based on lectures of L. Prandtl*, volume 2. Courier Corporation, 1957. 4.2.3
- [132] J Gordon Leishman. *Principles of Helicopter Aerodynamics with CD Extra*. Cambridge university press, 2006. 4.2.3
- [133] James R Usherwood and Charles P Ellington. The aerodynamics of revolving wings

- ii. propeller force coefficients from mayfly to quail. *Journal of Experimental Biology*, 205(11):1565–1576, 2002. 4.2.3, 4.2.6
- [134] SA Combes and TL Daniel. Flexural stiffness in insect wings i. scaling and the influence of wing venation. *Journal of experimental biology*, 206(17):2979–2987, 2003. 4.2.4, 4.2.5
- [135] Andrew M Mountcastle and Thomas L Daniel. *Aerodynamic and functional consequences of wing compliance*, pages 311–320. Springer, 2010. 4.2.4
- [136] AM Mountcastle and TL Daniel. Vortexlet models of flapping flexible wings show tuning for force production and control. *Bioinspiration & biomimetics*, 5(4):045005, 2010. 4.2.4
- [137] Marcos Vanella, Timothy Fitzgerald, Sergio Preidikman, Elias Balaras, and Balakumar Balachandran. Influence of flexibility on the aerodynamic performance of a hovering wing. *Journal of Experimental Biology*, 212(1):95–105, 2009. 4.2.4
- [138] Yun Liu, Bo Cheng, Sanjay P Sane, and Xinyan Deng. Aerodynamics of dynamic wing flexion in translating wings. *Experiments in Fluids*, 56(6):1–15, 2015. 4.2.4
- [139] AL Eberle, PG Reinhall, and TL Daniel. Fluidstructure interaction in compliant insect wings. *Bioinspiration & biomimetics*, 9(2):025005, 2014. 4.2.4
- [140] W Nachtigall. Die aerodynamische polare des tipula-flugels und eine einrichtung zur halbautomatischen polarenaufnahme. *The Physiology of Movement: Biomechanics*, pages 347–52, 1977. 4.2.4
- [141] Michael H Dickinson and Karl G Gotz. Unsteady aerodynamic performance of model wings at low reynolds numbers. *The Journal of Experimental Biology*, 174(1):45–64, 1993. 4.2.4
- [142] Hiroto Tanaka, John P. Whitney, and Robert J. Wood. Effect of flexural and torsional wing flexibility on lift generation in hoverfly flight. *Integrative and Comparative Biology*, 2011. 4.2.4
- [143] Laura A Miller and Charles S Peskin. Flexible clap and fling in tiny insect flight. *Journal of Experimental Biology*, 212(19):3076–3090, 2009. 4.2.4
- [144] Gang Du and Mao Sun. Effects of wing deformation on aerodynamic forces in hovering hoverflies. *The Journal of experimental biology*, 213(13):2273–2283, 2010. 4.2.5
- [145] Robin J Wootton. Functional morphology of insect wings. *Annual review of entomology*, 37(1):113–140, 1992. 4.2.6
- [146] A Roland Ennos. The importance of torsion in the design of insect wings. *Journal of Experimental Biology*, 140(1):137–160, 1988. 4.2.6
- [147] Simon M Walker, Adrian LR Thomas, and Graham K Taylor. Photogrammetric reconstruction of high-resolution surface topographies and deformable wing kinematics of tethered locusts and free-flying hoverflies. *Journal of The Royal Society Interface*, page rsif.2008.0245, 2008. 4.2.6
- [148] LJ Clancy. Aerodynamics, sections 5.17, 5.25, and 8.14, 1975. 4.2.6
- [149] Ryusuke Noda, Toshiyuki Nakata, and Hao Liu. Effects of wing deformation on aerodynamic performance of a revolving insect wing. *Acta Mechanica Sinica*, 30(6):819–827,

2014. 4.2.6, 4.7.1, 4.7.1

- [150] JV Caetano, MB Weehuizen, CC de Visser, GCHE de Croon, C De Wagter, B Remes, and Max Mulder. Rigid vs. flapping: The effects of kinematic formulations in force determination of a free flying flapping wing micro air vehicle. In *Unmanned Aircraft Systems (ICUAS), 2014 International Conference on*, pages 949–959. IEEE. 4.4
- [151] Ronit Malka, Alexis Lussier Desbiens, Yufeng Chen, and Robert J Wood. Principles of microscale flexure hinge design for enhanced endurance. In *Intelligent Robots and Systems (IROS 2014), 2014 IEEE/RSJ International Conference on*, pages 2879–2885. IEEE. 5.3
- [152] Jonathan P Dyhr, Noah J Cowan, David J Colmenares, Kristi Morgansen, and Thomas L Daniel. Autostabilizing airframe articulation: Animal inspired air vehicle control. In *Decision and Control (CDC), 2012 IEEE 51st Annual Conference on*, pages 3715–3720. IEEE. 5.4
- [153] DJ Colmenares, JP Dyhr, KA Morgansen, and TL Daniel. Agile airframes ii: closing the loop on abdominal actuation. In *INTEGRATIVE AND COMPARATIVE BIOLOGY*, volume 53, pages E38–E38. OXFORD UNIV PRESS INC JOURNALS DEPT, 2001 EVANS RD, CARY, NC 27513 USA. 5.4
- [154] Jian-Yuan Su, Shang-Chieh Ting, Yu-Hung Chang, and Jing-Tang Yang. A passerine spreads its tail to facilitate a rapid recovery of its body posture during hovering. *Journal of The Royal Society Interface*, 9(72):1674–1684, 2012. 5.4
- [155] Ivan Penskiy, P Samuel, James Sean Humbert, and Sarah Bergbreiter. A bio-inspired active tail control actuator for nano air vehicles. In *Robotics and Automation (ICRA), 2012 IEEE International Conference on*, pages 4635–4640, 2012. 5.4
- [156] Floris Van Breugel, William Regan, and Hod Lipson. From insects to machines. *IEEE robotics & automation magazine*, 15(4), 2008. 5.4
- [157] Sawyer B Fuller, Zhi Ern Teoh, Pakpong Chirarattananon, Néstor O Pérez-Arancibia, Jack Greenberg, and Robert J Wood. Stabilizing air dampers for hovering aerial robotics: design, insect-scale flight tests, and scaling. *Autonomous Robots*, pages 1–19, 2017. 5.4
- [158] HK Khalil. Nonlinear systems (3rd) prentice hall. *Upper Saddle River, NJ*, 7458, 2002. 6.1
- [159] Bo Cheng and Xinyan Deng. Translational and rotational damping of flapping flight and its dynamics and stability at hovering. *Robotics, IEEE Transactions on*, 27(5):849–864, 2011. 6.1, 6.2
- [160] Perry Parks, Bo Cheng, Zheng Hu, and Xinyan Deng. Translational damping on flapping cicada wings. In *Intelligent Robots and Systems (IROS), 2011 IEEE/RSJ International Conference on*, pages 574–579. IEEE. 6.1